UNIVERSIDAD NACIONAL AUTÓNOMA DE MÉXICO

PROGRAMA DE MAESTRÍA Y DOCTORADO EN INGENIERÍA

INGENIERÍA CIVIL – HIDRÁULICA

ANCLAJE DE TURBINAS SUMERGIDAS Y FLOTANTES PARA OBTENCIÓN DE ENERGÍA DE CORRIENTES MARINAS EN REGIONES DE FONDOS INCLINADOS

TESIS

QUE PARA OPTAR POR EL GRADO DE:

DOCTOR EN INGENIERÍA

PRESENTA:

MICHAEL RING

TUTOR PRINCIPAL:

DR. EDGAR GERARDO MENDOZA BALDWIN, INSTITUTO DE INGENIERÍA, UNAM

COMITÉ TUTOR:

DR. MOISÉS BEREZOWSKY VERDUZCO, INSTITUTO DE INGENIERÍA, UNAM

DR. RODOLFO SILVA CASARÍN, INSTITUTO DE INGENIERÍA, UNAM

DR. ÓSCAR POZOS ESTRADA, INSTITUTO DE INGENIERÍA, UNAM

DR. ISMAEL DE JESÚS MARIÑO TAPIA, ENES-MÉRIDA, UNAM

CIUDAD UNIVERSITARIA, CD. MX., 06 2023

JURADO ASIGNADO:

Presidente:	Dr. Berezowsky Verduzco Moisés
Secretario:	Dr. Silva Casarín Rodolfo
1$^{er.}$ Vocal:	Dr. Mendoza Baldwin Edgar Gerardo
2$^{do.}$ Vocal:	Dr. Pozos Estrada Óscar
3$^{er.}$ Vocal:	Dr. Mariño Tapia Ismael De Jesús

Lugar o lugares donde se realizó la tesis: CIUDAD DE MÉXICO, MÉXICO

TUTOR DE TESIS

DR. EDGAR GERARDO MENDOZA BALDWIN

_____

FIRMA

Acknowledgments

To my wonderful wife Paola, thank you for your unwavering support and patience during this time.

I could not have completed this work without the relentless support of my tutor Dr. Edgar Gerardo Mendoza Balwin and the head of the department Dr. Rodolfo Silva Casarín, who always had time and patience for questions, no matter how trivial they seemed to be, for the credit of trust, and for introducing me to the topic.

The assistance provided by the personal of the laboratory during experiments was greatly appreciated.

I am grateful to Julio Candela and Julio Sheinbaum for permission to use their empirical data, and to the CEMIE-Océano, in particular to Dr. Ismael de Jesús Mariño Tapia, for gathering and processing valuable data during the research expedition CEMIE-1 on board B.O. Justo Sierra.

I would also like to thank my family, especially my parents, who were always supportive and believed in me whichever path I took.

To my friends who were always there to remind me to have fun even in the most stressful times, thank you.

I also appreciate very much the financial support provided by the *Consejo Nacional de Ciencia y Tecnología* (CONACyT) and the CEMIE-Océano.

Contents

List of Figures

List of Tables

Nomenclature - Latin Letters

Symbol	Description
A_S	Swept area by turbine rotor
A_s	Side surface area, outer surface area of the shaft
A_{blst}	Cross-sectional area of a ballast tank
a_{blst}	Apothem of the cross-section of a ballast tank
A_c	Cross sectional area
$\tilde{B}$	Net buoyancy force
C_P	Power coefficient
C_Q	Torque coefficient
C_T	Thrust coefficient
C_D	Drag coefficient
c_{MBL}	Coefficient for minimum breaking load
c_{shell}	Minimal clearance between outer shell and internal components
c_{struc}	Minimal clearance between structure and other components
d	Diameter
d_h	Hamming distance
d_a	Diameter of the anchor
d_{blst}	Outer diameter of rounded section of a ballast tank
d_{bt}	Outer diameter of a buoyancy tank
D_F	Expected annual fatigue damage of component
D_F	Design factor
$D_{F,i}$	Expected annual fatigue damage of component per environmental state i
d_H	Outer diameter of the hulls
d_I	Outer diameter of longitudinal members in the hull's space frame (i.e., structural member type I)
d_{II}	Outer diameter of diagonal members in the hull's space frame (i.e., structural member type II)
$d_{i,j}$	Euklidian distance between i and j

Symbol	Description
E	Young's modulus of the material used
w_i	Weight for parameter i
EA	Axial stiffness per unit length
e_{abs}	Absolute error
E_{ir}	Initial Young's modulus of rock
e_{rel}	Relative error
E_s	Young's modulus of steel
f_i	Fitness of an individual for parameter i
f	Fitness or performance of an individual
f	Frequency
f	Generic function
F_d	Design load
F_k	Characteristic load
F_A	Anchor holding capacity
$\vec{F}_A$	Residual force on anchor
f_A	Factor for considering alteration of rock
F_B	Force due to buoyancy of the object
F_D	Drag force
f_D	Factor for considering rock quality designation
$\vec{F}_E$	External force on object
$\vec{F}_{E,i}$	External force i on object
f_{exp}	Value of experimental observations
$\bar{f}_{exp}$	Mean value of experimental observations
$\bar{f}_{exp,0}$	Mean value of experimental observations for repetitions in static equilibrium
$\vec{F}_F$	Residual force on fairlead
$\vec{F}_{F,i}$	Residual force on i-th fairlead
F_h	Horizontal load
$f_{i,lf}$	Zero up-crossing frequency of the tension spectrum in environmental stat i
F_{MBL}	Minimum breaking load
$\vec{F}_{ML,i}$	Residual force of mooring line i at one end
f_n	Natural frequency
f_{num}	Value of numerical calculations
$f_{num,0}$	Value of numerical calculations for repetitions in static equilibrium
$\vec{F}_R$	Residual force on the object
$\vec{F}_{R,ML0}$	Residual force on mooring line at end 0
$\vec{F}_{R,ML1}$	Residual force on mooring line at end 1

Symbol	Description
F_v	Vertical load
F_W	Force due to weight of the object
g	Gravitational acceleration
H	Wave height
h	Spacing between adjacent nodes of a uniform grid
h	Outstand of shear key
h	Water depth
I	Second moment of area
i	Variable for iteration
J	Entry of the inertia matrix
j	Variable for iteration
J_1	Moment of inertia about its first principal axis
J_2	Moment of inertia about its second principal axis
J_3	Moment of inertia about its third principal axis
$\boldsymbol{K}$	Global stiffness matrix
k	Intercept of T-N curve for fatigue life of mooring components
k	k-factor of genetic algorithm
k_{ir}	Initial linear stiffness of the rock according to p-y curves
r_{rm}	Constant describing properties of rock
L	Characteristic length
l	Length
L'_{BST}	Ratio between length of the ballast tanks and length of buoyancy tanks
L_e	Embedded length of anchor
L_{BST}	Length of the ballast tanks
L_{BT}	Length of the buoyancy tanks
L_F	Fatigue life in years
L_N	Length of nose section
L_{OA}	Length over all
l_s	Stretched length of the mooring line
L_S	Length of the structure inside the hulls
L_T	Length of tail section
l_{us}	Unstretched length of the mooring line
m	Slope of T-N curve for fatigue life of mooring components
m	Mass
M_0	Moment at groundline
m_{MLs}	Mass of all mooring lines
m_{PL}	Mass of platform

Symbol	Description
$\vec{M}_R$	Residual force on the body
n	Shape parameter of nose section
n	Number/count
n	Sample size
n_{BLLST}	Number of ballast tanks
n_k	Number of positives/occurrences in sample
n_{gen}	Number of the generation
n_H	Horizontal coefficient of subgrade reaction
$n_{i,lf}$	Number of low frequency tension cycles per year for environmental state i
n_o	Number of the objectives for optimization
$\vec{P}$	Vector of external forces of linearized equation system
P	Mechanical power at the turbines shaft
$\vec{p}$	Position in global reference frame
p	Power factor for inverse distance weighted interpolation
$\vec{p}_{0z}$	z-position of end point 0 of the mooring line
$\vec{p}_{1z}$	z-position of end point 1 of the mooring line
$\vec{p}_A$	Position of anchor
$\vec{p}_F$	Position of fairlead
P_i	Probability of occurrence of load case
$\vec{p}_{RB}$	Position of rigid body in global reference frame
p_{ur}	Ultimate resistance of the rock
p_{vs}	Vertical pressure for sinking in rock
Q	Torque
Q_f	Ultimate holding capacity due to friction of the shaft
Q_{ha}	Ultimate axial holding capacity of the anchor
Q_{hl}	Lateral holding capacity of the anchor
Q_{sa}	Ultimate structural capacity of the anchor in axial direction
Q_{sl}	Ultimate structural capacity of the anchor in lateral direction
$q_{t,r}$	Tensile strength of rock
$q_{u,g}$	Unconfined compressive strength of grout
$q_{u,r}$	Compressive strength of rock
$\boldsymbol{R}$	Rotation matrix
R	Ratio of tension range (double amplitude) to reference breaking strength
$\vec{r}$	Position in local reference frame
R	Radius of rotor at blade's tip
R_d	Design resistance

Symbol	Description
R_k	Characteristic resistance
$\vec{r}_{cob}$	Position of center of buoyancy
$\vec{r}_{cog}$	Position of center of gravity
$\vec{r}_{E,i}$	Position of external force i
$\vec{r}_{F,i}$	Position of fairlead i
r_i	Inner radius
R_n	Reynolds number
r_n	Node radius of the space frame of the hulls
r_N	Nose radius
r_o	Outer radius
r_T	Tail radius
S	Final fitness score
s	Lithoclase spacing of the rock
s	Spacing or pitch height of shear keys
S_k	Characteristic load effect
S_{ASF}	Adjusted safety factor
S_{bt}	Outer surface of a buoyancy tank
s_c	Scale of k-factor of genetic algorithm
S_F	Safety factor as required by the limit sate
S_H	Surface of a hull
$R_{i,lf}$	Ratio of low frequency standard deviation tension range to reference breaking strength
s_{pe}	Height above groundline of the pad eye
s_t	Stretch of k-factor of genetic algorithm
v_∞	Undisturbed velocity
T	Thrust
t_a	Wall thickness of the anchor
t'_a	Adjusted wall thickness of the anchor
T_i	Time spent in environmental state i
$\tilde{d}_i$	Crowding distance
$T_{lf,h}$	Tension in mooring line during low frequency cycle for fatigue damage corresponding to higher current
$T_{lf,l}$	Minimum tension in mooring line during low frequency cycle for fatigue damage corresponding to lower current
t_{shell}	Thickness of outer shell
u	Current speed
u	Threshold for generalized Pareto distribution
$\vec{u}_{FA}$	Unit vector from fairlead to anchor

Symbol	Description
u_h	Higher current for calculating tension range of low frequency cycle for fatigue damage
$\hat{u}_k$	Amplitude of the current corresponding to component k of the discrete Fourier transformation
u_l	Lower current for calculating tension range of low frequency cycle for fatigue damage
$u_{LC,i}$	Current corresponding to the analyzed load case i
$\vec{u}_{ML01}$	Direction of mooring line from end point 0 to end point 1
$\vec{u}_{ML10}$	Direction of mooring line from end point 1 to end point 0
V	Displaced volume
$\widehat{V}$	Coefficient of variation
$\hat{v}$	Mean rate of occurrence
v_{bot}	Current speed at the bottom of the water column
V_{bt}	Displaced volume of a buoyancy tank
V_H	Volume of a hull
V_{BLLST}	Displaced volume of a ballast tank
V_{MLs}	Displaced volume of all mooring lines
V_{PL}	Displaced volume of platform
$\vec{W}$	Submerged weight
w'	Submerged weight per unit length
W_{ML}	Submerged weight of the mooring line
W_P	Submerged weight of the pile anchor
$\vec{x}$	Global position vector of linearized equation system
x	Random variable
x	X-position
x_0	Desired minimum or maximum value of the i-th property, whichever is further away from current value
$\bar{X}$	Mean
x'_{BST}	Relative x-position of the ballast tanks
$\hat{x}$	Quantile
x_{BLLST}	Position of the ballast tanks in x-direction
x_i	Value of the i-th property
X_k	Coefficients of the discrete Fourier Transform
x_{max}	Maximum desired value of the i-th property
x_{min}	Minimum desired value of the i-th property
x_{opt}	Desired optimum value of the i-th property
y	Lateral deflection of pile
y_0	Lateral deflection of pile at groundline
y_g	Gumbel reduced variate

Symbol	Description
y_A	Elastic limit deflection of the rock
$y_{A,0}$	Elastic limit deflection of the rock at groundline
z	Depth below surface

Nomenclature - Greek Letters

Symbol	Description
α	Shape parameter of probability distributions
α_r	Strength reduction factor of the rock
α	Angle between principal axis of inertia and reference axis
β	Power law coefficient for current profile
β	Scale parameter of probability distributions
β'	Adjusted scale parameter of probability distributions
χ_h	Fineness ratio of hull
χ_{RQD}	Rock quality designation in percent
ε	Strain of the mooring line
ε_i	Initial strain of the mooring line
γ_f	Load factor
γ_M	Material factor
Γ	Gamma function
$\gamma_{F,FLS}$	Single safety factor for fatigue limit state
λ	Tip speed ratio
ν	Cinematic viscosity
ω	Angular velocity
φ	Heel of floating body
ϕ_r	Resistance factor
ψ	Heading of floating body
ρ_B	Average density of water
ρ	Density
ρ_w	Density of water
σ	Scale parameter of generalized Pareto distribution
σ_{cr}	Critical shear stress of the material in use
σ_{lf}	Low frequency standard deviation tension
σ_{wf}	Wave frequency standard deviation tension
σ_y	Yield strength of the material in use
τ_B	Return period

Symbol	Description
τ_f	Maximum stress due to skin friction
θ	Tail angle, that is half the included angle at the tail's tip
θ	Trim of floating body
ξ	Shape parameter of generalized Pareto distribution

Abbreviations

ADCP	acoustic doppler current profiler
ALS	accidental limit state
AR	acoustic release
ASD	allowable stress design
ASF	adjusted safety factor
AUV	autonomous underwater vehicle
CI	confidence interval
COB	center of buoyancy
COG	center of gravity
DFT	discrete Fourier transform
DOF	degree of freedom
ECMWF	European Centre for Medium-Range Weather Forecasts
EVT	extreme value theory
FLS	fatigue limit state
GPD	generalized Pareto distribution
HMPE	high modulus polyethylene
HYCOM	Hybrid Coordinate Ocean Model
IDW	inverse distance weighted interpolation
IEC	International Electrotechnical Commission
LRFD	load resistance factor design
MBL	minimum breaking load
MCEC	marine current energy converter
MEC	marine energy converter
MOGA	multi objective genetic algorithm
NHC	National Hurricane Center
NOAA	National Oceanic and Atomspheric Administration
OCT	ocean current turbine
POT	peaks-over-threshold
PSFD	partial safety factor design

RMS	root mean square
RQD	rock quality designation
SLS	serviceability limit state
SOGA	single objective genetic algorithm
TEC	tidal energy converter
TSR	tip speed ratio
ULS	ultimate limit state
UNAM	National Autonomous University of Mexico
WEC	wave energy converter

Abstract

In the Mexican Caribbean, the Island Cozumel is separated from the mainland by a channel with a width of approximately 18 km. This channel was found to have a relatively persistent current with a heading in the northeastern direction. This current is part of the ocean-wide circulation and converts later to the loop current in the Gulf of Mexico and the Gulf Stream after passing through the stretch between Florida, USA and Cuba. It rarely reverses its direction and if it does, it does so with very low magnitude. Due to its confinement between the island and mainland a very low directional variation is reported. The rocky sea floor, steep slopes of approximately 10% degrees on the channel's side, and a wide and deep valley at its center with a depth of 400 m make this region challenging for harnessing the energy contained in the ocean current.

In this work and as part of the requirements to obtain the degree of *Doctor en Ingeniería*, a platform and mooring system was designed to fix a submerged, floating ocean current turbine at a specific depth in the water column. To speed up the design process, a Python module for quasi-static analysis of submerged offshore mooring systems with taut lines was created. It was shown that especially the expected tensions in the mooring lines can be reliably predicted with this tool. In conjunction with a Python module for evolutionary optimization, its performance was confirmed with the 10^{th}-order Griewank-function, the module for quasi-static analysis was used to generate one mooring system design concept based on three anchors, and one concept based on four anchors. Both design concepts were further optimized through a parametric design study, while the three-anchor mooring concept was finally chosen for further evaluation. A dynamic mooring analysis on all relevant load cases was performed with ProteusDS, to analyze involved stresses, tensions, and deflection. Additionally, the model in ProteusDS was used to execute a free decay test for estimating the system's natural frequency. The fatigue life of the mooring lines was calculated based on international design codes. Due to the absence of loads during operation originating from higher frequency sources such as waves and wind, it was found that the fatigue life is not of concern for submerged floating ocean current turbines. A reviewed methodology based on the literature for designing pile anchors grouted to rock was presented and applied to two designs: one proposal with and one without shear keys. The shear keys are designed to be a simple welding bead with 2.4 mm in height and helped to significantly reduce the required dimensions of the pile anchor from 115 mm in diameter to just 60 mm. For the design without shear keys, the limiting factor was the friction between grout and steel, while the capacity of the pile with shear keys was limited by the lateral structural capacity. The final design shows good agreement with the relevant design codes and guidelines. At the moment, the design is based on the expected properties of an ocean current turbine, thus it serves as a good starting point for adjusting the design to a turbine that is ready for deployment. Even for different arrangements such as two vertical axis turbines side by side, the efficient design methodology presented in this work is expected to produce a new design ready for certification and fabrication within a few weeks.

Resumen

En el Caribe mexicano, la isla de Cozumel está separada del continente por un canal con un ancho de aproximada 18 km. En este canal se encontró una corriente relativamente persistente con dirección noreste. Esta corriente forma parte de la circulación de todo el océano y se convierte posteriormente en la corriente de bucle del Golfo de México y en la Corriente del Golfo tras atravesar el tramo entre Florida (EE. UU.) y Cuba. En los raros casos que se invierte su dirección lo hace con muy baja magnitud y variación direccional debido a su confinamiento entre la isla y tierra firme. El fondo marino rocoso, las fuertes pendientes de aproximadamente 10% en los lados del canal y un amplio y profundo valle de 400 m en su centro hacen esta región un reto para el aprovechamiento de la energía contenida en la corriente oceánica.

En este trabajo y como parte de los requisitos para obtener el grado de *Doctor en Ingeniería*, se diseñó una plataforma y un sistema de amarre para fijar una turbina de corriente oceánica sumergida y flotante a una profundidad específica en la columna de agua. Para acelerar el proceso de diseño, se creó un módulo Python para el análisis cuasi-estático de sistemas de amarre sumergidos con líneas tensas. Se demostró que, sobre todo, las tensiones esperadas en las líneas de amarre pueden predecirse de forma fiable. Ese módulo se usó junto con un módulo de Python para la optimización evolutiva, cuyo rendimiento fue confirmado a través de la función Griewank de décimo orden, para generar un concepto de un sistema de amarre basado en tres anclas, y un concepto basado en cuatro anclas. Ambos conceptos de diseño se optimizaron posteriormente mediante un estudio de diseño paramétrico y finalmente se eligió el concepto de amarre con tres anclas para su subsecuente evaluación. Con el programa ProteusDS se realizó un análisis dinámico del sistema de amarre en todos los casos de carga relevantes, evaluando los esfuerzos, tensiones y deflexiones. Además, el modelo en ProteusDS se empleó para ejecutar una prueba de decaimiento libre para estimar la frecuencia natural del sistema completo. La resistencia a fatiga de las líneas de amarre se calculó basándose en los códigos de diseño internacionales. Debido a la ausencia durante operación de cargas originadas por fuentes de mayor frecuencia, como las olas y el viento, se comprobó que la resistencia a fatiga no es preocupante para las turbinas de corrientes oceánicas sumergidas. Se presentó una metodología revisada basada en la bibliografía para diseñar anclas de pilotes en roca y se aplicó a una propuesta con y otra sin chavetas de cizallamiento. Las chavetas se diseñaron como un simple cordón de soldadura de 2.4 mm de altura y ayudaron a reducir significativamente las dimensiones requeridas del pilote de 115 mm de diámetro a solo 60 mm. Para el diseño sin chavetas, el factor limitante era la fricción entre el concreto y el acero, mientras que la capacidad del pilote con chavetas estaba limitada por la capacidad estructural lateral.

El diseño final muestra una buena concordancia con los códigos y directrices de diseño pertinentes. El diseño se basa en las propiedades esperadas de una turbina de corrientes oceánicas, por lo que sirve como un buen punto de partida para ajustar el diseño a una turbina lista para su despliegue. Incluso para disposiciones diferentes, como dos turbinas de eje vertical, una al lado de la otra, se espera que la eficiente metodología de diseño presentada en este trabajo produzca un nuevo diseño listo para su certificación y fabricación dentro de pocas semanas.

Chapter 1

Introduction

In recent decades, the production of electrical energy based on low-carbon energy sources such as wind, and solar radiation has gained traction. Both sources have proven to be able to provide significant amounts of electricity to the grid; however, they are not suitable for all regions around the world due to several reasons such as sociological, geographical, or meteorological factors. This has led to the endeavor to explore alternative renewable energy sources for the production of low-carbon electricity. Various countries are actively funding research to develop new technology capable of harnessing other sources. In Mexico, the *centro de investigación en energía del océano* (Spanish for ocean energy research center) or short *CEMIE-O* – a consortium of Mexican universities and Mexican industrial partners founded by the Mexican government – took the challenge to explore ocean thermal energy conversion, wave energy conversion, energy conversion based on saline gradient, and ocean current conversion. All of those four energy sources are available within the Mexican territory and can provide reliable energy of varying degree [50, 49].

A region with great potential of ocean currents is the Cozumel Channel, located offshore the Caribbean coast of Mexico between the mainland and the island Cozumel (see figure 1.1). The channel extends between the latitudes N20°15′ and N20°50′ and between the longitudes W86°40′ and W87°20′, oriented at roughly 40° azimuth [99]. A recent study was performed to validate the energy potential [9]. A relatively steady, mono-directional current was found with a magnitude of approximately $1\,\mathrm{m\,s^{-1}}$ [1] which makes it suitable to harness the energy of the ocean current. From a technical point of view regarding energy extraction, the ocean current found at this site is similar to tidal currents, with the main difference in cyclic bi-directional behavior and predictability of tidal currents. Several confined tidal currents have been or are currently explored around the world regarding their potential to produce low-carbon electric energy. Projects were deployed in different key regions, such as in the Bay of Fundy, Canada [109, 71, 66, 107, 57], the Orkney Islands, UK [2, 14], and the Kyoto stream, Japan [102]. In contrast to the ocean current found in the Cozumel Channel, the tidal currents currently explored are much more energetic, presenting peak velocities up to five times higher. Additionally, most of the used turbines are designed for cut-in velocities for velocities that are barely encountered in the Mexican Caribbean, making it impossible to use

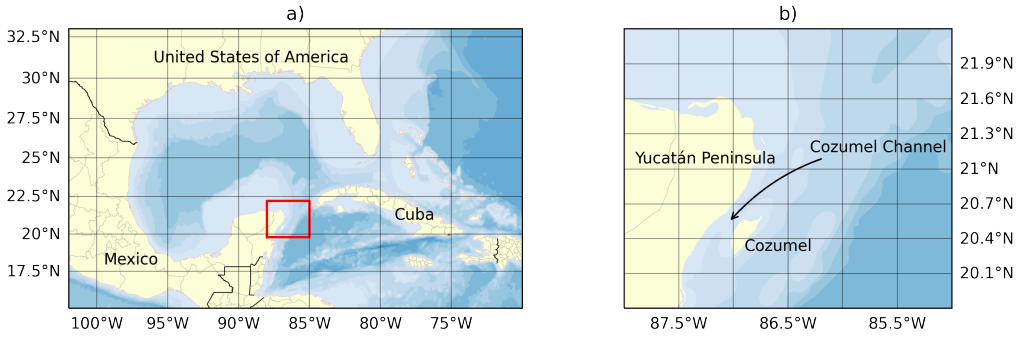

Figure 1.1: Location of the Cozumel Channel within the Mexican Caribbean. **a)** Location in Northwestern Caribbean; **b)** Mexican Caribbean. Data on bathymetry, landmass, and political borders are based on the data set provided by NaturalEarth.

existing technology [127]. At the University of Strathclyde, UK, a turbine specifically for low energetic ocean currents such as they can be found in the Mexican Caribbean or the Philippines is under active development [37], but it is in a very early design phase. Similarly, the Institute of Engineering of the National Autonomous University of Mexico is designing a turbine capable of harnessing low-energy ocean currents, which has demonstrated its capability in various laboratory and real-world experiments.

To harness the power of the current, turbines must be placed at a specific height in the water column. Various concepts have been used or proposed for tidal turbines, such as floating at the surface [43] or mounted directly to the sea floor [126]. Other concepts involve placing turbines on a platform that floats in the middle of the water column [79]. For instance, the PLAT-O platform developed by Sustainable Marine Energy [58, 59] and the KAIRYU platform developed by the IHI corporation [102, 52, 116] follow this concept. However, some recently developed projects are inactive nowadays, such as the submerged, floating *PLAT-O* device which seems to be paused in favor of a surface floating platform [111].

The PLAT-O and the KAIRYU prototypes are both submerged floating platforms but follow different concepts. While both have two turbines mounted on a platform consisting of three cylindrical hulls, there are a few key differences. The PLAT-O prototype places the turbines between the hulls and mounts them at the top of the platform to a structure that connects to the strut. The turbines can be rotated around the transversal axis for easier access during maintenance. The platform is fixed to the sea floor using several mooring lines and anchors. In contrast, the KAIRYU prototype places the turbines directly inside the outer hulls on either side of the platform. The turbines can adjust their pitch and rotate in different directions, the latter to counteract the reaction moment generated. The platform is equipped with an altitude control device to maintain the platform at the design depth. This is necessary because the platform is moored to a single anchor which enables passive weathervaning of the complete system.

The mooring system for floating renewable energy converters poses a unique challenge. In contrast to floating offshore oil and gas facilities, where the mooring system typically accounts for

2% to 3% of the total budget, the mooring system for ocean current energy converters can consume up to 30% [63, 121] of the budget. Additionally, the slope found in the Cozumel Channel imposes limitations on the choice of the anchors suitable for installation [104].

1.1 Objectives

The objective of this work is to develop an optimized mooring system for a submerged turbine that is designed to harness mono-directional ocean currents, as they can be found in the Mexican Caribbean. The turbine should be fully submerged, except for maintenance, installation and dismantling. Additionally, the platform should be free-floating, restrained only by the mooring lines that are connected to the platform.

More specifically, the following objectives should be met:

- Elaborate recommendations for anchoring ocean current turbines (OCTs) for the bathymetric profile found in the Cozumel Channel.
- Develop a methodology to efficiently evaluate early concepts for mooring systems, taking into consideration sloped sea floors.
- Study the dynamics of a mooring system for sloped sea floors.
- Design a mooring system suitable for an OCT to harness the ocean currents in the Cozumel Channel

1.2 Structure of the Document

The structure of the document and a brief summary of the chapters can be found in the following:

- Chapter 2: An overview of mooring systems with a focus on OCT is provided. The information is derived from the offshore oil and gas sector and adapted for offshore renewable energy devices. Various mooring configurations, materials, and anchors are discussed.
- Chapter 3: The design process and principles used in this work are described. This includes the basic formulae used to evaluate the integrity of the structure, its fatigue life, and the load capacity of the anchor. The required limit states according to the relevant design codes are described and the commercial software used in this work is presented.
- Chapter 4: The Python package developed to analyze subsurface, offshore mooring systems based on taut lines is described in detail. The numeric model is described, verified with simple calculations, and validated with two experimental series and data available in the literature on full-scale experiments with a spherical buoy.
- Chapter 5: The genetic algorithm which was used to optimize design proposals is explained. This algorithm was evaluated with the Griewank-function as the benchmark.

- Chapter 6: The possible construction site in the Cozumel Channel is characterized. The data sources and the methods for the extreme value analysis are described as well as the results regarding extreme winds, waves, and currents. The currents were analyzed at the water surface and a depth of 50 m, while the extreme wind speeds are based on hurricanes and data provided by reanalysis. Information on the bathymetry is given and geotechnical information available in the literature is reviewed.
- Chapter 7: The general choices on the system design, relevant load cases, and two potential concepts are presented.
- Chapter 8: The optimization of the system design is performed for both concepts, and the results are provided. The optimization is performed for both concepts, which were then manually tweaked to find the optimum configuration for the given parameter.
- Chapter 9: The optimized design concept is evaluated for compliance with relevant design codes. This includes dynamic mooring analysis, estimation of fatigue life, selection and design of an appropriate anchor, and selection of the required mooring equipment.

The conclusions can be found in chapter 10.

Chapter 2

Mooring Systems

Moorings can be broadly categorized into two types: surface moorings and subsurface moorings. The main difference between them is that while the subsurface mooring remains entirely underwater during operation, the surface mooring has a visible part at or above the surface, typically in the form of a buoy or a platform. For the surface mooring, the platform provides buoyancy and restoring forces for heave, roll, and pitch, while the mooring lines provide restoring forces for surge, sway, and yaw of the vessel [115].

Although certain applications require a surface mooring, a subsurface mooring is preferred as it imposes less fatigue-related requirements on the system due to smaller environmental loads. In addition, subsurface moorings benefit from being less visible, resulting in less problems with surface vessels and vandalism [115].

A typical mooring system consist of three component groups: The flotation device or platform at the upper end which in this case is connected to the marine current energy converter (MCEC), the mooring line which transmits the loads from the platform to the anchor, and the anchor which transmits the loads to the sea bed [115]. To achieve the desired safety level and dynamic behaviour, mooring lines are often segmented, which is especially useful for inverse catenary moorings, where positive and negative submerged weighed segments can be used to design the false bottom. The lowest part of the mooring, which is connected to the anchor, is subject to high wear due to potential contact with the sea bed, and is typically made up of steel chain. This means that wire rope or fiber rope mooring lines will be segmented at least once [124].

2.1 Configuration

The mooring configuration typically refers the profile of the individual lines and the pattern in which they are set up, including the number of lines. The length of the lines is derived from other factors, among which is the line profile.

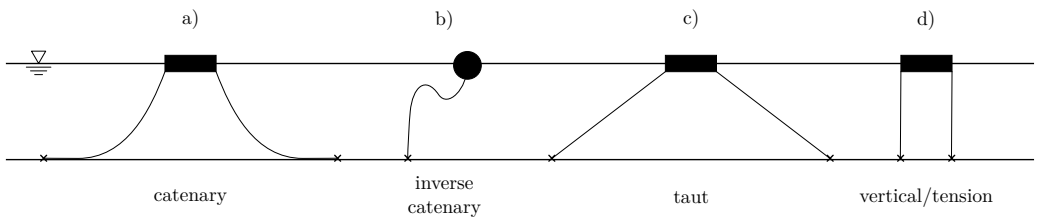

Figure 2.1: Typical profiles of mooring lines. **a)** Catenary profile; **b)** inverse caternay profile; **c)** taut profile; **d)** vertical or tension leg profile. The positions of the anchors are marked with a cross.

2.1.1 Line Profile

For the mooring, a great variety of different mooring lines can be used to achieve the desired behavior of the structure, yet, the line's shapes can be traced back to a few basic profiles. Mooring lines are classified as compliant or rigid [56], and the most common mooring systems are depicted in figure 2.1. Catenary, inverse catenary, and taut moorings are used for compliant mooring systems, while vertical moorings are categorized as rigid. Each of those types has its purpose and serves the special needs of the individual site conditions. When it comes to mooring systems for MCEC, only compliant systems are considered applicable, as noted by Weller et al. [121].

Catenary

Catenary moorings (see figure 2.1 a)) follow a simple design where the mooring line takes on a catenary curve from the fairlead (the attachment point to the vessel) to the anchor. The section of the line that connects to the anchor is intended to lie flat on the sea floor and should only be lifted completely when the line is loaded to its breaking load [82]. Therefore the anchor is not loaded vertically, which increases the variety of suitable anchors as the requirements are quite low [27].

These lines provide low horizontal stiffness to the system, while the vertical stiffness is provided by the shape of the vessel. As the vessel moves horizontally, the line lifts partially from the ground, resulting in more suspended line and restoring forces on the vessel [56]. Catenary lines are tolerant to uncertainties in water depth and use low-cost materials like steel chains [27]. However, the suspended section of the mooring line increases with greater water depths and larger mooring offsets, leading to very heavy lines. The constant contact with the sea floor can cause damage to both the sea floor and the mooring line.

In the offshore oil and gas industry, catenary moorings are used for depths of up to 500 m, followed by a transitional depth where both catenary and taut profiles are used. For greater depths, catenary profiles become too heavy, and taut moorings are mainly used. However, these rules of thumb may not be applicable to MCEC, especially submerged MCEC, which have different requirements that need to be reviewed.

Inverse Catenary

Inverse catenary moorings (see figure 2.1 b)) follow an S-curve to provide the great compliance to the vessel, which is achieved with clump weights and buoys connected at different arc lengths to the line, or ropes of different weights [27]. This line profile is often used for buoys which are required to ride the surface, such as wave buoys, and where the mooring offset is not a significant concern. However, they may not be suitable for very large sea states and are difficult to operate under low-tension conditions that can introduce shock loads. Strong currents can also reduce their geometric compliance [27].

Taut

In contrast to a catenary mooring, a taut line (see figure 2.1 c)) is designed to avoid contact with the sea floor [56]. These moorings are typically used for deep water moorings [27]. Vertical forces are directly transferred to the anchor, while compliance is achieved by elasticity of the mooring line material [56].

Taut mooring lines are typically made up of steel wire rope or synthetic rope such as nylon, polyester, polypropylene, or polyolefin [27]. The mooring lines are design to be always loaded with a minimum force, remaining in tension and reducing risk of snap loading [27]. They have minimal impact on the sea floor since they do not make contact, but their design requires accurate knowledge on the local bathymetry and are more challenging compared to catenary or inverse catenary moorings.

Vertical Mooring

Vertical moorings or tension leg moorings (see figure 2.1 d)) are similar to taut moorings, but they differ in that their mooring lines are considered very stiff due to their large dimensions [56]. Restoring forces result mainly from pretension and length of the mooring lines, with the pretension typically around 20% the vessel's displacement [56]. Therefore they are mostly suitable for large vessels floating on the surface.

Vertical moorings are not well suited for subsurface moorings as horizontal displacement of the vessel can only be counteracted by a geometric shift of the mooring line. This is not the case for surface vessels since horizontal displacement introduces additional hydrostatic forces.

2.1.2 Pattern

For platforms used in the offshore oil and gas sector, moorings lines are often grouped together to provide more space for risers and enhances dynamic behavior in case of mooring line damage [56]. The number of lines depends on various factors, especially if the condition of line loss has to be met while still remain functioning. Achieving this with four or fewer lines is difficult, wherefore mooring lines might be added and grouped. Typically they are named regarding the number of groups and the number of mooring lines in each group [68]. For example, a vessel moored with five groups and

two mooring lines in each group would be called a 5 x 2 pattern. A snapped line in a 5 x 2 mooring pattern transfers nearly all its load to the other mooring line in its group, which could lead to the consecutive failure of the remaining line. This can be avoided by increasing the lines per group to the disadvantage of higher cost due to increased material and more installations. Therefore, in general, the mooring lines are homogeneously spread around the platform, leading to a single angle between different mooring lines. In this case, a 10 x 1 mooring patter would be preferred over a 5 x 3 mooring pattern, as the loads are more likely to be spread over more lines while still maintaining the same number of material and installations.

2.2 Mooring Line Composition

The composition of a mooring line is an essential aspect that determines its behavior and performance. A mooring line's composition is determined by its nominal diameter and the material used, which can be chain, wire rope, or synthetic rope, depending on the desired properties such as stiffness, corrosion resistance, and abrasion resistance. Accessories such as weights, buoyant parts, and connectors that might be fitted to the mooring lines are discussed in section 2.3.

2.2.1 Chain

Chains have been used in the offshore industry and naval architecture for many years and are available in various shapes and grades. The grades of chains, which are made of steel, are defined by DNV GL [31], which range from low to high strength: R3, R3S, R4, R4S, and R5. The grade determines the chain's minimum breaking load (MBL) for a given nominal diameter, which is the diameter of the bar used to form the individual links.

The chain's links can have so called studs, which form a connection of the opposing sides of the same link. Those links are welded in place and prevent the chain from tangling when handling. Stud link chains are mainly used for temporary moorings or moorings of ships, while studless chains are preferred for permanent moorings due to better fracture toughness especially at the weld of the studs.

Due to its greater resistance to abrasion and easier securing, chains are often used for the segments of the mooring line that connect to the fairlead and the anchor, regardless of the material used for the sections in between. Depending on the requirements, such as frequent change in length or when ground contact can be precluded, it might be useful to refrain from the use of chain at one or both ends of the line.

2.2.2 Wire Rope

In comparison to chains with same minimum breaking load (MBL), wire ropes are much lighter with a higher elasticity. They are made by interweaving individual wires to form a strand, which can be combined with more strands to form the rope or taken solely as a single strand rope, also known as a spiral strand. The structure of wire ropes is an important consideration when selecting

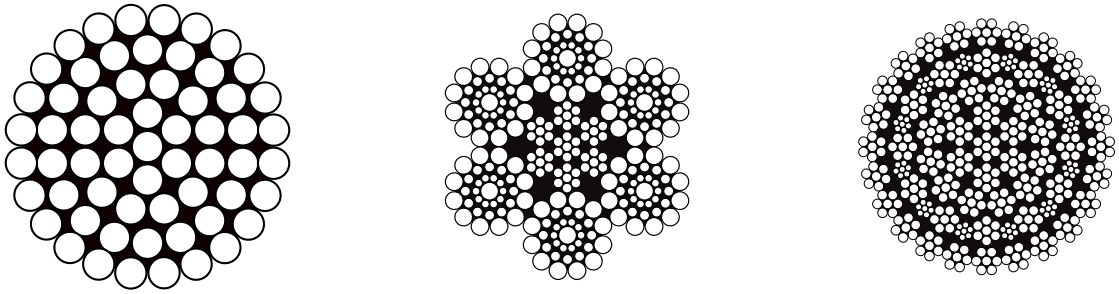

(a) Spiral strand (b) Six strand (c) Multi strand

Figure 2.2: Common layouts of strands in wire ropes.

a mooring line, as it affects the line's behavior under load. Wire strands can be arranged as spiral strand, six strand, eight strand, or multi-strand, following the definition of IEC 62600-10 [53] and as shown in figure 2.2. Depending on the manufacturer, different variations of the multi-strand layout are available, such as *7-wires*, *Seale*, *Filler* and *Warrington-Seale* in the case of Bridon-Bekaert Ropes Group [13]. This inner structure of wire rope defines its tendency to spin or twist under load. Wire ropes with high tendency to spin or twist may form loops in unloaded conditions, which can weaken the material when loaded again, and should be avoided if possible [115]. Six or eight strand ropes, which have a pronounced tendency to spin or twist, are much more flexible and easier to handle than spiral strand ropes and therefore typical for temporary moorings. In cases where low rotation is required in the mooring system, typically multi-strand ropes are selected as they are resistant to rotation due to their inner arrangement. Alternatively, the tendency to rotate under load can be minimized by using different left and right handed layers or the ends of the mooring line can be fitted with swivels.

Another differentiation between wire ropes is their rope lay, which is defined by the direction the fibers are wound around the strands. The most common rope lays are *Ordinary* (sometimes also called *Regular*) and *Lang's* (or *Langs*). In Ordinary lays, the fibers are wound in opposite directions as the strands are (sZ for right handed and Zs for left handed wires), where as for Lang's lays, the fibres are wound in the same direction (zZ for right handed and sS for left handed wires). Those terms are also abbreviated with s and z, as the middle stroke of the letter indicates the direction the strand or wire is laid: following from bottom to top, s goes from right to left and z from left to right. Lang's lay ropes have greater wear resistance than Ordinary lay ropes [13].

Fatigue bending resistance is an important factor to consider when designing a mooring line that involves a significant number of sheaves or is frequently stored on a drum. The size of the wire can increase the fatigue resistance as well as a smoothed surface of the outer strands [13]. A smoothed surface additionally reduces the abrasive wear on the rope when being in contact with itself or other parts of the system.

Protection against Corrosion

To protect against corrosion, there are different techniques available for wire ropes. One common method is to galvanize the wire rope. Another technique is to apply a plastic jacket or sheath made up of Polyvinyl chloride, Polypropylene, or High-Density Polyethylene. The jacket might be kept in yellow for increased visibility [115, 68]. Some wire ropes also include zinc wires and a special grease in the strands to providing a sacrificial anode and prevent water ingress, further enhancing their resistance to corrosion

2.2.3 Synthetic Fiber Rope

Although wire rope is less stiff than chains, using it in taut mooring systems can weaken or even reverse this effect. In the 1990s, synthetic fiber rope became popular for deep waters, as it provides the necessary compliance without the need for catenary moorings [68]. Synthetic rope also provides good compliance as it improves the payload and the platforms offset due to its reduced weight [124]. However, synthetic rope is less stiff than wire rope and may be prone to fish bite, which is a common problem in synthetic materials at depths up to 2000 m [115]. Therefore it is recommended only for line segments below 100 m, while the upper sections should be composed of chain or wire rope [68].

The code IEC 62600-10 [53] allows for the use of Polyester, Aramid, or Dyneema. But also nylon and high modulus polyethylene (HMPE) might be suitable, depending on the desired properties. The synthetic yarn is typically interwoven to different strands, which are joined into a subrope. The final rope is composed of several subropes, covered by a filler element and a jacket. The filler element stops ingress of sediment while the jacket protects the rope against abrasion and helps maintain the rope's geometric shape. Within the subrope, the strands can be aligned parallel, and can be braided or laid, each with its own purpose. While parallel and braided construction is torque free, laid constructions will rotate under load. The improved contact between the strands in laid subropes enhances its fatigue life [68].

Compared to wire ropes, synthetic fiber ropes provide a non-linear relation between tension and strain, and exhibit construction stretch. Mooring lines made up of synthetic material will be greater in length once installed than when they were manufactured. This plastic stretch further increases after the first higher loading event on the line [68]. This is mainly due to the arrangement of the yarns and strands within the rope as they tend to align themselves under load. Another factor can be material creep, which increases the platform's mean offset, and must be taken into account when designing a mooring system based on synthetic ropes.

2.3 Mooring Line Accessories

A variety of accessories are available for mooring lines, including connectors, shackles, clump weights, buoyancy aids, and acoustic releases.

2.3.1 Acoustic Release

An acoustically commanded anchor release or simply acoustic release (AR) is primarily used to disconnect the mooring line from the anchor, especially for subsurface moorings, allowing for equipment recovery. ARs can also be used for localizing the anchors exact position, which can be challenging for subsurface moorings [115].

2.3.2 Clump Weights and Buoyancy Aids

Clump weights and buoyancy aids can be added to alter the characteristics of mooring lines. Both can be used as concentrated or distributed loads. However, it is important to consider their potential negative effects, such as ground contact, increased wear due to sharp angles at the support, and increased drag [53].

Buoyancy aids are often made of hollow steel spheres, glass spheres with a protective plastic layer, or synthetic foam spheres. The latter material have several advantages over steel or glass floats as they can be molded into different shapes to reduce drag. Steel floats have a depth limitation of around 1000 m due to excessive pressure [115]. The ability to create shapes with less drag makes synthetic foam spheres an attractive option for high current environments.

2.4 Anchors

The offshore oil and gas sector and offshore renewable energy sector have developed various anchor types that have been proven in different projects. Experience has been gained for design, installation, operation, and decommissioning, if required. The guidelines IEC 62600 [54, 53] were developed by the International Electrotechnical Commission (IEC) to provide information specifically for marine energy converters (MECs) since the conditions for MECs are different from those in the maritime oil and gas industry. Factors such as safety levels, environmental loads, and profit margins differ significantly.

At most construction sites, sand or clay can be found although the region which this work focuses on is known for rocky sea bed made up of lime stone. Typically, sediment has settled over the years building up a sufficiently thick layer of sand or clay, allowing the anchor only to interact with said material. In regimes with higher current, this layer of sediment may be much smaller or even not existent, evoking the requirement of an anchor suitable for different kinds of rocks. Many anchors are well proven for sand or clay and accepted design methods for rocky sea beds are frequently non existent.

Some of the anchors suggested in IEC 62600-10 [53] are discussed below in more depth, keeping in mind the high current and rocky sea bed at the site of interest.

2.4.1 Drag Embedment Anchor

Drag embedment anchors are installed by anchor handling tugs which pull them horizontally after placing them on the seabed. Due to their special shape, the anchor penetrates the sediment and generates the desired holding capacity. However, their capacity is only valid for loads in direction of installation with no or negligible vertical load component. IEC 62600-10 [53] differentiates further between stockless anchors and high holding power anchors. High holding power anchors have a much higher holding capacity but the downside is installation and recovery of such anchors. They also require much higher precision in positioning before installation while the higher capacity complicates their recovery.

2.4.2 Pile Anchor

Pile anchors are typically slender pipes which are widely used in the offshore oil and gas industry and thus are well understood. The installation methods depend highly on the conditions found on the construction site and range from hammering and vibrating into soil to drilling and grouting into rock.

These anchors can withstand both, vertical and horizontal loads, but their design requires great knowledge of the soil conditions in order to achieve the desired holding capacity and installation depth, as stated in IEC 62600-10 [53]. Testing the design at full-scale is recommended when installed in rock to gain detailed knowledge of their behavior and ultimate capacity [15].

2.4.3 Micropile anchor

Micropiles are widely used for onshore applications such as slope stabilization with their application in offshore construction still being subject to investigation. A concept has been developed by Meggitt et al. [74] with the focus on marine renewable energy. They suggest using a group of three to four micropiles, drilled into the ground from a seabed drilling rig. For floating platforms they suggest a plate which is fixed with several micropiles to the seabed, with the mooring line connected to the plate instead to the actual anchor.

2.4.4 Suction Anchor

Suction anchors can vary heavily in their aspect ratio, from very slender, somewhat similar to pile anchors, to short anchors with aspect ratios of 2:1. The installation to required depth is mainly performed by generating a pressure differential between the inside of the anchor and the surrounding sea. This facilitates precise positioning on the seabed and relatively easy decommissioning. However, they require soil which is easy to penetrate such as sand or clay and work best in soils with low permeability.

2.4.5 Gravity Installed Anchor

Gravity installed anchors rely on their own momentum to penetrate the seabed, generated by dropping them from a sufficient height. The typical drop height of 100 m makes this anchor type unsuitable for construction sites with low water depths. These anchors are effective at resisting both horizontal and vertical loads, and work well in soft soils such as sand or clay.

2.4.6 Dead Weight Anchor

Dead weight or gravity anchors are not designed to penetrate the seabed but they are placed on top of it. Prior treatment of the soil is commonly required to generate the designed holding capacity, which is a combination of the anchors submerged weight and friction between it and the sea bed. For increasing the holding capacity, shear keys fitted to the bottom of the anchor may be considered. These keys penetrate the sea bed and mobilize shear within the soil or rock rather than friction on its surface [88]. A simple form of these anchors is a dead weight made up of dense material such as steel or concrete, or a box filled with heavy material after positioning. The box would be made up of steel or concrete and filled with sand found in place or heavier material such as iron ore. For small oceanographic moorings, metal pieces such as used train wheels can be used.

Modified versions of gravity anchors, known as *grillage and berm anchors*, use a grillage buried under heavy material such as a rock-fill or an iron ore berm. For anchors with a predominant loading direction, the grillage is buried on the back end of the berm, requiring the whole berm to be moved in case of grillage failure [88]. Berm anchors are suitable for predominantly horizontal loading conditions, which might not be the case for MCEC as it would require long and heavy catenary mooring lines.

2.4.7 Screw Anchor

Screw anchors can withstand both horizontal and vertical loads, but are typically used only for special applications and particular sediments. These anchors derive their holding capacity from the friction generated with the seabed and from the reaction against the anchor's structure.

2.5 Relevant Design Codes

The mooring system of MCEC should be analyzed in accordance with IEC 62600-10 [53] with similar information available in DNVGL ST-0164 [33] and the general process of certification described in DNVGL SE-0163 [30]. More general recommendations and requirements for mooring systems can be found in API RP-2SK [5] and DNVGL OS E301 [32]. General information on foundations is given in DNV CN-30.4 [20] and API RP-2GEO [6]. DNV RP-E303 [21] describes design and installation of suction anchors in clay, whereas DNVGL OS-E302 [31] describes the requirements on offshore mooring chains and accessories attached to those. Design of piles for marine structures in different types of soils can be found in ROM 0.5-05 [86].

Guidance on design and analysis of platforms for wave energy converters (WECs) and MCECs is given in IEC 62600-2 [54], whereas information on the design of tidal energy converters is given in DNV OSS-312 [22]. General recommendations on fixed offshore platforms can be found in API RP-2A-WSD [4] or DNVGL OS-C101 [34]. Design regarding buckling of structures in general and tubular members is provided by DNVGL CG-0128 [29] and DNV RP-C202 [25], respectively. Information on environmental conditions in the southern Gulf of Mexico can be found in the code PEMEX NRF-003:2000 [83] as it extends the API RP-2A-WSD by design values for fixed offshore oil and gas platforms in this region. Although safety levels and dimensions might differ for platforms of a different purpose, the return values are useful information during design phase. The recommended practice for estimating environmental conditions and loads in general can be found in DNV RP-C205 [23], while the fatigue design of offshore steel structures in described in DNV RP-C203 [24].

Chapter 3

Design Methodology

3.1 Design Process

The design of a mooring system typically begins with determining the project specifications and general system information, followed by defining the environmental conditions and the load case matrix [68]. This process is illustrated in figure 3.1. The next step involves analyzing the platform and the mooring system to ensure compliance with the national and international codes, as well as the specified design criteria.

An appropriate anchor is selected based on the defined criteria such as the sea floor conditions, mooring line profile, available installation equipment, and overall costs. Based on the loads determined in the mooring analysis, the dimensions of the anchor can be defined, and the involved stresses and deformations evaluated. Based on the results, the mooring components and required equipment is selected.

3.1.1 Mooring Systems

The design of the mooring system itself starts by defining the specific configuration, including the line profile, mooring pattern, and length of the lines. This involves defining the position of the anchors, spread angle between the mooring lines, and their grouping, if applicable. The mooring line composition, such as diameter and material, is selected and the loads are calculated based on load cases specified in the load case matrix. The assumption is made that there is no distortion or movement of the anchors. The design proposal is then evaluated based on relevant design codes, and the principal data of the system are adjusted to optimize it with respect to involved loads and the cost of material, installation, and maintenance, among other criteria.

Especially for submerged and floating platforms, their design significantly impacts the loads experienced by the mooring lines. Therefore, the design of the platform and the mooring system is performed simultaneously. The mooring system is analyzed with a quasi-static approach. The result are then used as input for the structural analysis performed with Abaqus. After optimization,

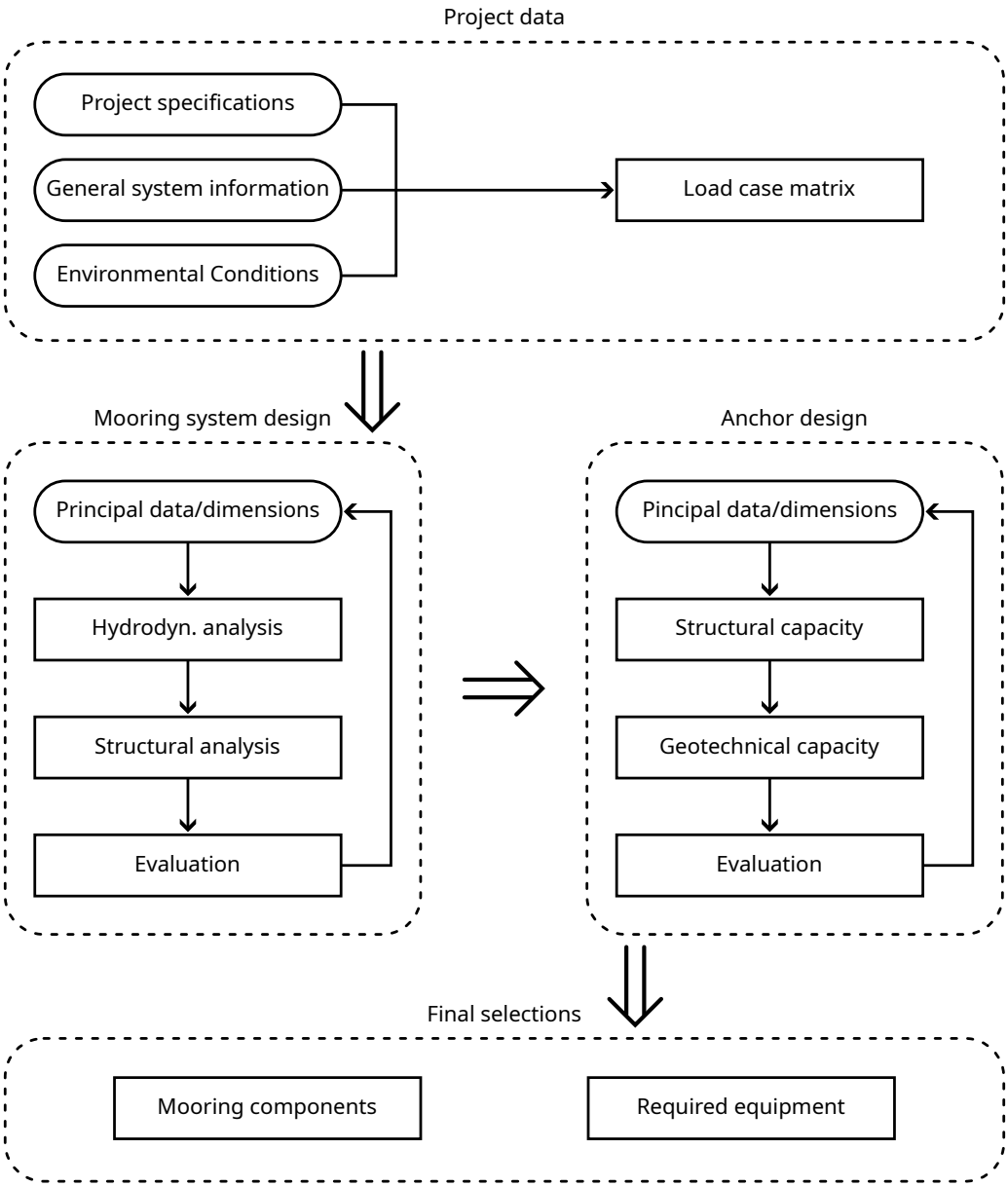

Figure 3.1: Flow chart of general design procedure.

a hydrodynamic mooring analysis is conducted with the software ProteusDS (see section 3.3.1). Subsequently, a structural model of the platform is created in Abaqus, taking into account the loads estimated by ProteusDS.

3.1.2 Anchors

Many different anchor types suitable for permanent moorings have been developed in the past decades due to the vast activity in the offshore oil and gas sector. A selection of anchor types is discussed in section 2.4, each with its unique advantages and disadvantages that must be evaluated based on the project's specific requirements. Bathymetry and geological and geotechnical conditions should also be taken into account when selecting a specific type. Skop [104] provides some selection guidelines for anchors, dividing them into four groups: Drag embedment anchors, gravity anchors, pile anchors, and direct embedment anchors. For regions with an inclined sea floor, pile anchors or direct embedment anchors are a viable option. Both work well for a broad range of sea bed material, except for hard boulders and in case of pile anchors for mud or soft clay. Gravity anchors are suitable for all types of sea bed material, but not recommended for sloped sea floors such as those found around Cozumel Island (see section 6.3.4). The same is true for drag embedment anchors, which are not designed to withstand vertical loads and do not work on rocky sea beds. Detailed information is given in table 3.1.

Regardless of the anchor type, their design typically involves assessing the structural and geotechnical (or holding) capacity separately. These are further divided into horizontal and vertical capacity (or axial and lateral capacity for cylindrical anchors), which are all evaluated individually due to the common assumption of uncoupled behavior between vertical and horizontal load capacity of the soil (i.e uncoupled interaction between soil and structure in horizontal and vertical direction) [88]. Drag embedment and direct embedment anchors are often proprietary designs that are selected based on their load capacity. Gravity and pile anchors are typically custom-made to the specific requirements of the project. After defining their principal data, their capacity can be evaluated on many design guidelines available in literature and international design codes. A design procedure for pile anchors in weak rock is described in section 9.1.4.

3.2 Design Principles

The design of the position keeping system of an ocean current turbine consists of two different parts: designing the platform according to IEC 62600-2 [54], and designing the mooring system including the mooring lines and the anchor according to IEC 62600-10 [53].

3.2.1 Structural Design of Platform

The structural design of the platform for a MCEC can be done using various methods, as per the guidelines IEC 62600-2 [54]. These include the load resistance factor design (LRFD) method, the partial safety factor design (PSFD) method, the allowable stress design (ASD) method, or direct

Table 3.1: Selection guidelines for anchors, after Skop [104].

Parameter	Drag embedment	Gravity	Pile	Direct embedment
Sea bed material:				
Sand or gravel	•	•	•	•
Mud or soft clay	•	•	○	•
Stiff clay	•	•	•	•
Very stiff clay or glacial till	○	•	•	•
Soft rock or coral	–	•	•	•
Hard, monolithic rock	–	•	○	○
Boulders	–	•	–	–
Sea bed topography:				
$< 10°$ slope	•	•	•	•
$> 10°$ slope	–	–	•	•
Loading direction:				
Unidirectional	•	•	•	•
Omnidirectional	–	•	•	○
Large vertical component	–	•	•	•
Horizontal load range:				
$< 45\,\mathrm{kN}$	•	•	○	•
$45\,\mathrm{kN} - 450\,\mathrm{kN}$	•	○	•	○
$> 450\,\mathrm{kN}$	–	–	•	–

• functions well

○ normally not a good choice

– does not function

evaluation of limit states regarding the reliability. All these methods use the same limit states to define acceptable ultimate, accidental, service, and fatigue conditions. Following the international standards such as IEC 62600-2 [54] or DNV GL OS C101 [34], the LRFD method is widely used and accepted by the industry and will be used in this work. The design may also be assisted by testing, while additionally a probability based design method may be used [34].

Load Resistance Factor Design Method The basic concept of the LRFD method demands the design resistance R_d of material and structure to exceed the design loads (F_d), as defined in IEC 62600-2 [54] and DNV GL OS C101 [34]:

$$F_d \leq R_d \tag{3.1}$$

The design load is the sum of the characteristic load effects S_{ki} and the corresponding load factor γ_{f_i} by

$$F_d = \sum_{i=1}^{n} \left(\gamma_{f_i} S_{ki}\right) \quad . \tag{3.2}$$

The design resistance is calculated by the characteristic resistance (R_k) and a resistance factor (ϕ_r) as

$$R_d = \phi_r R_k \quad , \tag{3.3}$$

with the resistance factor defined by

$$\phi_r = \frac{L}{\gamma_M} \quad , \tag{3.4}$$

where L denotes the characteristic length of the structural member such as stiffener span and γ_M the material factor. According to IEC 62600-2 [54], the characteristic length can be set to 1. DNV GL OS C101 [34] provides more detailed information on the material factors and specifies slightly more conservative values than IEC 62600-2 [54]. However, this standard is developed with a wider scope for offshore structures made up of steel in general, while IEC 62600-2 [54] focuses specifically on MEC.

3.2.2 Design of the Mooring System

The design of the mooring system is described in IEC 62600-10 [53] and follows a much simpler approach by comparing the achieved safety factor to the adjusted safety factor (ASF). For both required limit states, the ULS and the accidental limit state (ALS), a safety factor (S_F) is defined based on the type of analysis conducted. Quasi-static calculations generally require a higher safety factor than dynamic mooring analyses. The safety factors for holding capacity of different anchor types such as anchor piles and gravity anchors are provided for intact conditions and redundancy checks. This safety factor is multiplied by the design factor (D_F) to obtain the ASF (S_{ASF}) as follows

$$S_{ASF} = S_F D_F \quad . \tag{3.5}$$

According to IEC 62600-10 [53], the mooring lines must then satisfy the following condition

$$S_{ASF} < \frac{F_{MBL}}{F_d} \quad , \tag{3.6}$$

where F_{MBL} is the MBL in corroded state and F_d the design tension. The condition which has to be satisfied by the anchors follows a similar definition and is defined by

$$S_{ASF} < \frac{F_A}{F_d} \quad , \tag{3.7}$$

where F_A is the holding capacity of the anchor and F_d the design tension at the anchor.

3.2.3 Fatigue Life

Different approaches to estimate the fatigue life of offshore structures and mooring systems can be found in common design codes such as API RP-2SK [5], DNVGL OS-E301 [32], or ISO 19902 [55]. Most widely used is Minor's rule for fatigue assessment. In this work, estimation of the fatigue life (L_F) of all components is based on Minor's rule which is defined by

$$L_F = \frac{1}{\gamma_{F,FLS} D_F} \quad , \tag{3.8}$$

where $\gamma_{F,FLS}$ is the safety factor for the fatigue limit state and with the expected annual fatigue damage of the analyzed component (D_F) given by

$$D_F = \sum D_{F,i} \quad , \tag{3.9}$$

where $D_{F,i}$ is the annual fatigue damage per environmental state.

3.2.4 Limit States

Modern design philosophies are base on limit states, which define the frame of acceptable range of loads and displacements for the installed device and its equipment, such as mooring lines and anchors. Exceeding these limit states may cause failure as the established design requirements are no longer satisfied. In the case of safety factors for evaluating the holding capacity of anchors, IEC 62600-10 [53] distinguishes between intact conditions and conditions for redundancy checks, but does not strictly differentiate between different load cases.

Ultimate Limit State

The load combinations of the ULS define the loads a structure should be able to ultimately resist. For floating MCEC, the ULS includes loss of platform stability, yielding of critical components (e.g., the platform structure, mooring lines, and anchors), buckling of structural members, loss of station-keeping, and sinking of the structure, as defined by IEC 62600-2 [54] and IEC 62600-10 [53].

Permanent loads, variable functional loads, environmental loads, and deformation loads are combined with particular load factors into two different combinations. The load factors are specified in table 7.3 as defined by in DNV OS-J101 [26]. In accordance with the standard, the load factor for combined environmental loads was reduced to 1.15 as the structure is unmanned.

The required safety factors vary depending on the design category for the specific load case and the component that is reviewed. For the platform, partial load safety factors can be found in IEC 62600-2 [54, p. 29], while the necessary safety and design factors for the mooring lines and anchors are available in IEC 62600-10 [53, p. 39f.].

Accidental Limit State

The ALS consideres accidental loads that may occur during installation and operation of the structure. In case of a floating MCEC, this includes the loss of a mooring line, flooding of compartments and assessment of stresses in the components and whether the platform retains its ability to raise to the surface. For loads on the platform, IEC 62600-2 [54] suggests a partial load safety factor of 1.0, while the safety factors for the mooring lines and anchors are given in IEC 62600-10 [53, p. 39f.].

Fatigue Limit State

Under the fatigue limit state (FLS) the cumulative damage caused by repetitive loads is taken into consideration. IEC 62600-10 [53] recommends using Minor's rule for evaluating the systems fatigue life. According to IEC 62600-2 [54], welded joints and stress concentrations should be assessed for fatigue following ISO 19902 [55]. General information on the fatigue design of offshore structures based on S-N curves can be found in DNV RP-C203 [24]. In case of the MCEC, exciting frequencies may arise from from various sources such as vortex induced vibrations on mooring lines, the rotational frequency of rotor, interaction of tip vertices with structure, waves and wind (during maintenance), fluctuations in current, and the number of maintenance cycles.

Serviceability Limit State

In case of MCEC, the serviceability limit state (SLS) is used for evaluating the accelerations, displacements, and distortions affecting the performance of the system [54]. In case of the platform design in this work, the displacements from neutral position in all 6 degree of freedom (DOF) are reviewed.

3.3 Commercial Software

The commercial software used in this work is limited to *ProteusDS* for the dynamic mooring analysis and to *Abaqus* for the structural analysis.

3.3.1 ProteusDS

ProteusDS is developed by DSA Ocean and is used generally for marine dynamic analysis. The effect of the environment such as wind, waves, currents, and the sea floor on floating and submerged objects can be assessed in the time domain. The software models mooring lines with cubic finite-elements that are able to interact with the air, water, the sea floor, and other objects in the model.

Environment

Several profiles are available for modeling environmental effects such as current, wind, and waves. The temporal onset of the environmental effects can be set for each effect individually or for all effects at the same time. This parameter is called `ramp time` and is mainly used to give the model time to settle before environmental effects take place and this way possibly avoid unwanted spikes in loads.

Current The current can be represented with a uniform profile, linear shear current, a power-law current profile, and a custom profile. For all currents, heading and nominal speed can be controlled. The uniform profile applies the current speed to the complete water column, while the linear shear current linearly decreases the current speed from its nominal speed at the water surface to zero at the sea bed. The power-law is defined by

$$u(z) = u\left(\frac{h-z}{h}\right)^{\beta} \quad , \tag{3.10}$$

where h is the water depth, $u(z)$ the current speed at depth below surface z, β the power law coefficient, and u the nominal current speed [36]. The power law can either be applied to the hole depth or to just a lower fraction of the water column which is defined by the parameter `CurrentPowerLawPercentDepth`. In the latter case, the upper section is covered with a uniform current.

Waves Waves can be modeled based on Airy-wave theory, Stokes second order waves, Stokes fifth order waves, a Pierson-Moskowitz wave spectrum, and a JONSWAP wave spectrum [35]. The definition of the Stokes wave model of fifth order can be found in [39].

Wind Constant wind, the Ochi-Shin spectrum and the Froya/NPD spectrum are available as wind types, while the profile can be modeled with a uniform profile, a logarithmic profile, and a power law-profile, among others. For more information, see the manual of ProteusDS [36].

Mooring Lines

In ProteusDS, mooring lines are modeled with 1-dimensional finite-elements with cubic shape functions. The mooring lines, referred to as *Cable* in ProteusDS, can be segmented into different materials. Each cable is discretized into several lumped masses along its arc length with two Frenet

frames. One in axial direction and one fixed to the cable's cross section to determine its elastic torsion. Lumping the mass of the elements to its adjacent nodes neglects the curvature inertia in favor of computational efficiency. The hydrodynamic drag is calculated at the nodes of each element and linearly interpolated along the element. It is based on the normal and tangential drag coefficient of the line's material and hydrodynamic load coefficients, that consider the angle between the normal and tangential current components. The added mass of each element is calculated based on the hydrodynamic mass coefficient in the normal direction while the tangential component is neglected. It is then added to the physical mass to resolve acceleration. For more detailed information refer to the manual of the software [35].

Added Mass

ProteusDS is capable of calculating the added mass of all wetted surfaces; however, it does not account for the added mass and their added mass inertia of surfaces with their normal vector perpendicular to the flow. Additionally, the software is unable to calculate frequency dependent added mass, which has greater effect on large, surface piercing objects.

3.3.2 Abaqus

The structural analysis of the platform was performed using the finite-element feature of the widely accepted commercial software suite *Abaqus*. To model space frames, Abaqus offers a range of different beam and pipe element, such as 2-node linear beams (B31), 3-node quadratic beams (B32), 2-node cubic beams (B33), and 3-node quadratic pipes (PIPE32), among others. These beam elements are mostly based on the Timoshenko beam theory, although several elements are also available in Euler-Bernoulli formulation. As the use of Abaqus is prevalent in the industry, a detailed description of the software and its features is not provided in this work. For more information, the reader is encouraged to consult the user manual of the software [19].

Chapter 4

Quasi-Static Mooring Analysis

Several commercial software is available for detailed mooring analysis, such as *ProteusDS* (see section 3.3.1) or OrcaFlex, with the focus on dynamic simulation of the object in question and its connected mooring lines.

While these software packages are accurate, ProteusDS was found to to slightly overestimate the loads in the mooring lines [12, 58, 128]. Their main disadvantage, however, is the required and significant computational time. In early design stages, and especially when working with evolutionary algorithms, time efficient computation is crucial. During the first design steps, a quasi-static mooring analysis is performed using linear-elastic straight springs with zero compressive stiffness to replace the mooring lines.

To address this need for time-efficient computation, the Institute of Engineering of the National Autonomous University of Mexico has developed a Python module called *OffshorePy*. This tool is specifically designed for submerged systems with taut lines that can be approximated by straight lines. By using a quasi-static approach, OffshorePy provides an efficient and accurate method for analyzing the mooring system during the initial design stages.

4.1 Object Types for Modeling the Mooring System

The mooring system is modeled with 3 different base types of objects: Rigid bodies, points and (taut) lines. The points themselves are divided into three sub types of points, which are fairleads, anchor points, and floats.

4.1.1 Rigid Body

Rigid bodies in OffshorePy are different from the other objects in that they posses 6 DOF, and have a designated center of gravity (COG) and center of buoyancy (COB), at which their weight and buoyancy forces are applied. External forces, such as thrust and moment of turbines or drag forces of the body, can be added as external forces along with their point of application. The definition

of external forces is given in the global reference frame while their point of application is specified relative to the local reference frame, i.e., with respect to the position and orientation of the rigid body. As a result, the force vector remains unchanged upon translation or rotation of the rigid body, while the point of application moves along with body. Rigid bodies interact with the mooring system solely through `Fairleads`, which must be added to the rigid body. The residual force ($\vec{F}_R$) on the `RigidBody` is calculated by

$$\vec{F}_R = \begin{bmatrix} 0 \\ 0 \\ 1 \end{bmatrix} V \rho_w g - \begin{bmatrix} 0 \\ 0 \\ 1 \end{bmatrix} mg + \sum \vec{F}_{E,i} + \sum \vec{F}_{F,i} \tag{4.1}$$

and the residual moment ($\vec{M}_R$) by

$$\vec{M}_R = \begin{bmatrix} 0 \\ 0 \\ 1 \end{bmatrix} V \rho_w g \times \vec{r}_{cob} - \begin{bmatrix} 0 \\ 0 \\ 1 \end{bmatrix} mg \times \vec{r}_{cog} + \sum \vec{F}_{E,i} \times \vec{r}_{E,i} + \sum \vec{F}_{F,i} \times \vec{r}_{F,i} \quad , \tag{4.2}$$

where V is the body's displaced volume, m its mass, ρ_w the density of water, g the gravitational acceleration, $\vec{F}_{E,i}$ the external force i, $\vec{F}_{F,i}$ the residual force on the i-th fairlead, $\vec{r}_{cob}$ the position of the COG, $\vec{r}_{cob}$ the position of the COB, $\vec{r}_{E,i}$ the point of application of the i-th external force, and $\vec{r}_{F,i}$ the position of the i-th fairlead. All positions are assumed to be in the local reference frame of the rigid body and the operator $\times$ denotes the cross product. To transform coordinates from the local reference frame of the rigid body into the global reference frame of the mooring system, the rotation matrix is used, which is defined by

$$\boldsymbol{R} = \begin{bmatrix} \cos\theta\cos\psi & \sin\varphi\sin\theta\cos\psi - \cos\varphi\sin\psi & \cos\varphi\sin\theta\cos\psi + \sin\varphi\sin\psi \\ \cos\theta\sin\psi & \sin\varphi\sin\theta\sin\psi + \cos\varphi\cos\psi & \sin\psi\sin\theta\cos\varphi - \sin\varphi\cos\psi \\ -\sin\theta & \sin\varphi\cos\theta & \cos\varphi\cos\theta \end{bmatrix} \quad , \tag{4.3}$$

where φ is the heel of the platform, θ is the trim of the platform, and ψ is the heading of the platform. The final transformation is than performed by the dot product as follows:

$$\vec{p} = \boldsymbol{R}\vec{r} + \vec{p}_{RB} \quad , \tag{4.4}$$

where $\vec{p}$ is the position in the global reference frame (i.e., the mooring system), $\vec{r}$ the position in the local reference frame (i.e., the rigid body), and $\vec{p}_{RB}$ the position of the rigid body in the global reference frame.

4.1.2 Points

Points have no expansion in space and do not account for their mass and volume. However, external forces can be added to all type of points. `Floats` can move freely in all three DOFs and

the submerged weight can be specified. `Fairleads` are also able to move in three direction but their movement is coupled to a rigid body, meaning that their position does not contribute to the global DOF-vector. Their position is defined in the local reference frame of the coupled rigid body rather then in terms of the global coordinate system. Anchor points (`AnchorPoint`) are fixed in space and do not move. While technically external forces can be added, they have no effect on the mooring system and are simply used as reference point for mooring lines. Since points have three DOFs, only the residual force ($\vec{F}_R$) needs to be calculated, which is defined by

$$\vec{F}_R = \vec{F}_E + \vec{W} + \sum \vec{F}_{ML,i} \quad , \tag{4.5}$$

where $\vec{F}_E$ is an external force on the point, $\vec{W}$ the submerged weight of the point (if applicable), and $\vec{F}_{ML,i}$ the residual force of the i-th mooring line at the end it is connected to the point.

4.1.3 Lines

Mooring lines are modeled as linear-elastic springs and require two connection points. They follow a straight line between those points. If the distance between those two points is shorter than the unstretched length of the line, the stiffness of the mooring line is set to zero. The pretension of the mooring line can be adjusted using the initial strain (ε_i) of the line, that is defined by

$$\varepsilon_i = \frac{l_s}{l_{us}} - 1 \quad , \tag{4.6}$$

where l_s is the stretched length of the line (i.e., the distance between the adjacent points) and l_{us} the unstretched length of the line. The submerged weight of the line is carried by the adjacent point with greater z coordinate or is equally shared between both if their height is equal. The residual force on the mooring line at end point 0 ($\vec{F}_{R,ML0}$) is given by

$$\vec{F}_{R,ML0} = \vec{u}_{ML01}\,(l_s - l_{us})\,EA + \begin{cases} \begin{bmatrix} 0 & 0 & 1 \end{bmatrix}^T l_{us} w' & \text{for } \vec{p}_{0z} > \vec{p}_{1z} \\ \begin{bmatrix} 0 & 0 & 1/2 \end{bmatrix}^T l_{us} w' & \text{for } \vec{p}_{0z} = \vec{p}_{1z} \\ 0 & \text{for } \vec{p}_{0z} < \vec{p}_{1z} \end{cases} \tag{4.7}$$

and at end point 1 ($\vec{F}_{R,ML1}$) by

$$\vec{F}_{R,ML1} = \vec{u}_{ML10}\,(l_s - l_{us})\,EA + \begin{cases} \begin{bmatrix} 0 & 0 & 1 \end{bmatrix}^T l_{us} w' & \text{for } \vec{p}_{1z} > \vec{p}_{0z} \\ \begin{bmatrix} 0 & 0 & 1/2 \end{bmatrix}^T l_{us} w' & \text{for } \vec{p}_{1z} = \vec{p}_{0z} \\ 0 & \text{for } \vec{p}_{1z} < \vec{p}_{0z} \end{cases} \quad , \tag{4.8}$$

where $\vec{u}_{ML01}$ is the unit vector from end point 0 of the mooring line to end point 1, $\vec{u}_{ML10}$ the unit vector in opposite direction, EA the mooring line's axial stiffness per unit length, w' ist submerged weight per unit length, $\vec{p}_{1z}$ the z-position of end point 0, and $\vec{p}_{0z}$ the z-position of end point 1.

4.1.4 Material

Objects are provided to store the material properties for line segments. These properties include the nominal diameter, its axial stiffness per unit length, the MBL, the submerged weight per unit length, and the normal and tangential drag coefficient. The drag coefficients and MBL are currently not used by the software but help the user to keep track of those values. In case specific material properties are not available, they can be estimated by the following formulae as they are published by Ma et al. [68]. The MBL (F_{MBL}) in N is calculated by

$$F_{MBL} = \begin{cases} c_{MBL}\, d^2 \left(44 \times 10^{-6} - 8 \times 10^{-11} d\right) & \textbf{for chain,} \\ 9 \times 10^{-7} d^2 & \textbf{for wire rope,} \\ 2.5 \times 10^{-7} d^2 & \textbf{for polyester rope} \end{cases}, \tag{4.9}$$

where d is the nominal diameter given in m, and c_{MBL} is the coefficient for considering the chain's strength. The coefficient c_{MBL} is 22.6 for chains of grade R3, 24.9 for chains of grade R3S, 27.4 for grade R4, 30.4 for grade R4S, and 32.0 for grade R5. The submerged weight per unit length (w') in $\mathrm{N\,m^{-1}}$ is given by

$$w' = \begin{cases} 187 \times 10^{-9} d^2 & \textbf{for stud chain,} \\ 171 \times 10^{-9} d^2 & \textbf{for studless chain,} \\ 43 \times 10^{-9} d^2 & \textbf{for wire rope,} \\ 1.7 \times 10^{-9} d^2 & \textbf{for polyester rope,} \end{cases}, \tag{4.10}$$

where the nominal diameter (d) is given in m. The axial stiffness per unit length (EA) in N is defined by

$$EA = \begin{cases} 101 \times 10^{-3} d^2 & \textbf{for stud chain,} \\ 85.4 \times 10^{-3} d^2 & \textbf{for studless chain,} \\ 88.7 \times 10^{-3} d^2 & \textbf{for wire rope,} \\ 1.1 \times 10^{-3} d^2 & \textbf{for polyester rope,} \end{cases}, \tag{4.11}$$

where the nominal diameter (d) is given in m.

4.2 Linearized Equation System

The global stiffness matrix ($\boldsymbol{K}$) is created using the central difference scheme with a default perturbation of 1×10^{-5}. The unit for rotation of the rigid body is radians while distances are unitless. The vector of external forces ($\vec{P}$) is composed of the resulting forces on all floats and rigid bodies. Fairleads, anchor points, and lines are ignored in terms of the DOFs of the system but are considered regarding the forces acting on them. Lines exert a force on the adjacent points whereas fairleads transmit the forces acting on them to the coupled rigid body via a force and a moment

with respect to the origin of the rigid body. Anchor points only serve the purpose as reference point for the stretched length and direction of a line, and to evaluate the forces at this point. The equation system can be represented by

$$\boldsymbol{K}\vec{x} = \vec{P} \quad , \tag{4.12}$$

where $\vec{x}$ is the change in position, and which is solved using the function `numpy.linalg.lstsq` which is part of the `numpy`-Package for Python 3.9 and was used in version 1.22.4. In case the matrix is of full rank, the numerically exact solution for $\vec{x}$ is returned, otherwise this function minimizes $||\vec{P} - \boldsymbol{K}\vec{x}||$ and returns the minimum value of $||\vec{x}||$ in case of various solutions, where $||\vec{a}||$ denotes the Euclidean 2-norm of a vector (see Harris et al. [48]).

4.3 Verification

The software has been verified with a simple mooring system which can be calculated by hand. A spherical subsurface buoy is moored to the sea floor with a single mooring line while the current speed (i.e. load on the buoy) is varied between $0.0\,\mathrm{m\,s^{-1}}$ and $2.0\,\mathrm{m\,s^{-1}}$ in $0.5\,\mathrm{m\,s^{-1}}$ increments. In the second case the buoy is held in place with four mooring lines. The software was validated with model scale experiments and full scale experiments published in literature, its documentation can be found below in section 4.4.

External Forces The drag force (F_D) of the body can be calculated by

$$F_D = {}^1\!/_2 C_D \rho u^2 A \quad , \tag{4.13}$$

where C_D is the specific drag coefficient, u the speed and A the reference area of the body, in this case the projected area parallel to the direction of the current. A formula for estimating the drag coefficient of a sphere as a function of the Reynolds number is defined by Morrison [76] as

$$C_D = \frac{24}{R_n} + \frac{2.6\frac{R_n}{5.0}}{1 + \left(\frac{R_n}{5.0}\right)^{1.52}} + \frac{0.411\left(\frac{R_n}{263000}\right)^{-7.94}}{1 + \left(\frac{R_n}{263000}\right)^{-8.0}} + \frac{0.25\frac{R_n}{10^6}}{1 + \frac{R_n}{10^6}} \tag{4.14}$$

with the Reynolds number (R_n) defined by

$$R_n = \frac{uL}{\nu} \quad , \tag{4.15}$$

and where u denotes the relative speed between (undisturbed) fluid and body, L the characteristic length of the body, and ν the cinematic viscosity of the fluid. The buoyant force (F_B) on the sphere is calculated by

$$F_B = \rho_w g V \quad , \tag{4.16}$$

where V is the displaced volume of water, ρ_w the density of water, and g the gravitational acceleration. Since the sphere is completely submerged, its displaced volume can be calculated by $V = \frac{\pi}{3}d^3$, where d is the diameter of sphere. The weight of the buoy (F_W) can be calculated by simply substituting the density of the water in equation (4.16) by the buoys average density (ρ_B):

$$F_W = \rho_B g V \tag{4.17}$$

Considering the direction of the forces, the vector of external force ($\vec{F}_E$) on the buoy can be assembled to

$$\vec{F}_E = \begin{bmatrix}1\\0\\0\end{bmatrix} F_D + \begin{bmatrix}0\\0\\1\end{bmatrix} F_B - \begin{bmatrix}0\\0\\1\end{bmatrix} F_W \quad . \tag{4.18}$$

The current is assumed to be parallel to the channel's floor, thus has only a horizontal component. The buoyant force acts in positive z-direction while the weight acts in the opposite direction. Although the cases are completely 2-dimensional, 3-dimensional vectors are used since it simplifies the calculation of the moment around the y-axis using the cross product.

Mooring Line The mooring line is modeled as linear elastic spring, connecting both end points, the anchor point and the fairlead, with a straight line. The strain (ε) of the mooring line is defined as

$$\varepsilon = \frac{\|\vec{p}_F - \vec{p}_A\|}{l_{us}} - 1 \quad , \tag{4.19}$$

where $\vec{p}_F$ is the position vector of the fairlead, $\vec{p}_A$ the position vector of the anchor, and l_{us} is the unstretched length of the mooring line. The submerged weight of the mooring line (W_{ML}) is assumed to be completely carried by the higher end point (i.e., the fairlead) and is estimated by $W_{ML} = w' l_{us}$, where w' is the weight per unit length. The unit vector in direction of the mooring line from fairlead to anchor ($\vec{u}_{FA}$) is defined by

$$\vec{u}_{FA} = \frac{\vec{p}_A - \vec{p}_F}{\|\vec{p}_A - \vec{p}_F\|} \quad . \tag{4.20}$$

The force on the anchor point ($\vec{F}_A$) can be calculated by

$$\vec{F}_A = -\vec{u}_{FA} \frac{EA}{l_{us}} (l_s - l_{us}) \quad , \tag{4.21}$$

where EA denotes the mooring lines stiffness per unit length and l_s the stretched length of the mooring line (i.e., the distance between anchor point and fairlead). The force on the fairlead ($\vec{F}_F$) is given by

$$\vec{F}_F = \vec{u}_{FA} \frac{EA}{l_{us}} (l_s - l_{us}) - \begin{bmatrix}0\\0\\1\end{bmatrix} w' l_{us} \quad . \tag{4.22}$$

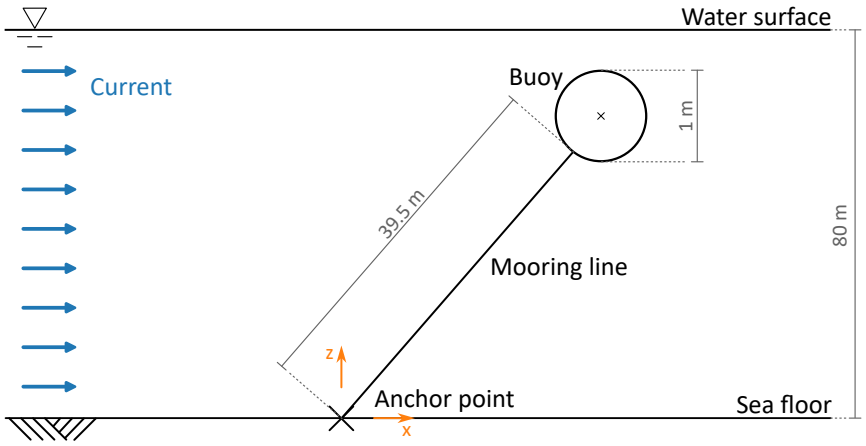

Figure 4.1: Concept of single lline mooring case for verification of quasi-static mooring analysis package OffshorePy. Not to scale.

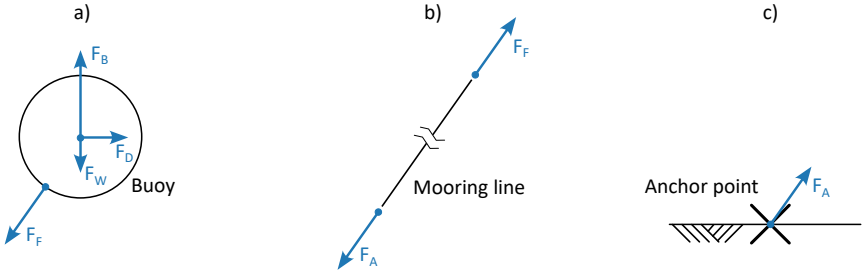

Figure 4.2: Free body diagram of objects of single line mooring case. **a**: Free body diagram of buoy; **b**: Free body diagram of mooring line; **c**: Free body diagram of anchor point. Not to scale.

If no data are given, the stiffness (EA) in $\mathrm{Pa\,m^2}$ and the submerged weight per unit length (w') in $\mathrm{N\,m^{-1}}$ of the wires can be estimated with equations (4.10) and (4.11), following Ma et al. [68].

Single Line Mooring

The buoy is placed initially at half the local water depth of 80 m. The anchor point is at the center line and is assumed to remain fixed to the sea floor. The buoy has a diameter of 1 m and the mooring line is connected directly to its outer shell. The principal arrangement is illustrated in figure 4.1. For demonstration purposes, the sketch is not to scale. Although the current is depicted as uniform over the whole height of the water column, only the buoy experiences drag forces, not the mooring line. The corresponding free body diagrams for the anchor point, mooring line, and the buoy can be seen in figure 4.2. The buoyancy force F_B, the weight F_W, the drag force due to the current F_D and the force of the mooring line at fairlead $\vec{F}_F$ are acting on the buoy. The former three are acting on the COG and COB, respectively, which are at the same position in this case. The force of the mooring line is acting at the position of the fairlead $\vec{p}_F$. The input data for the

Table 4.1: Input data for calculations of single line mooring case.

Water depth (h)	80	m
Water density (ρ_w)	1025	$\mathrm{kg\,m^{-3}}$
Water viscosity (ν)	1.0023×10^{-6}	$\mathrm{m^2\,s^{-1}}$
Diameter of buoy (d_B)	1	m
Average density of buoy (ρ_B)	200	$\mathrm{kg\,m^{-3}}$
Unstretched length of line (l_{us})	39.5	m
Diameter of line (d_{ML})	0.02	m
Stiffness of line (EA)	3.548×10^{7}	$\mathrm{Pa\,m^2}$
Submerged weight per unit length (w')	1.72	$\mathrm{N\,m^{-1}}$

Table 4.2: Relative error of numerical calculation with respect to analytical calculation of single line mooring case.

Current speed	$0.0\,\mathrm{m\,s^{-1}}$	$0.5\,\mathrm{m\,s^{-1}}$	$1.0\,\mathrm{m\,s^{-1}}$	$1.5\,\mathrm{m\,s^{-1}}$	$2.0\,\mathrm{m\,s^{-1}}$
x position of buoy	0.00^*	6.70×10^{-8}	2.81×10^{-9}	2.49×10^{-11}	0.00
z position of buoy	3.38×10^{-15}	4.56×10^{-13}	6.02×10^{-13}	3.80×10^{-14}	0.00
y rotation of buoy	0.00^*	2.66×10^{-10}	3.26×10^{-11}	1.35×10^{-14}	0.00
Stretched length	3.42×10^{-15}	0.00	0.00	0.00	0.00
Strain	3.26×10^{-11}	3.14×10^{-13}	2.49×10^{-13}	1.38×10^{-12}	1.15×10^{-12}
Tension	2.83×10^{-11}	3.65×10^{-15}	6.02×10^{-13}	5.22×10^{-13}	4.96×10^{-13}

* Absolute error

calculations are shown in table 4.1; the code used to create the OffshorePy-model can be found in section A.1.3.

4.4 Experimental Validation

For validation, a spherical buoy was moored in an open circulation tank with four mooring lines. Two experimental series were conducted due to findings in previous experiments, which were similar in terms of setup. The first series involved a vertical section of the mooring line as shown in figure 4.3, but without the load cell. Due to excessive deflection of the vertical section, a second series was conducted without the vertical section and with the lines being connected directly to the channel's floor instead. Due to the elasticity of the mooring lines, the buoy was closer to the water surface in equilibrium than in initial condition. A current meter was positioned at the center line of the channel 1.2 m upstream of the buoy. On one side of the channel a high speed camera was set up together with two to three LED light sources to capture the scene. The circulation tank is equipped with three pumps, their frequency was varied through out the experimental series.

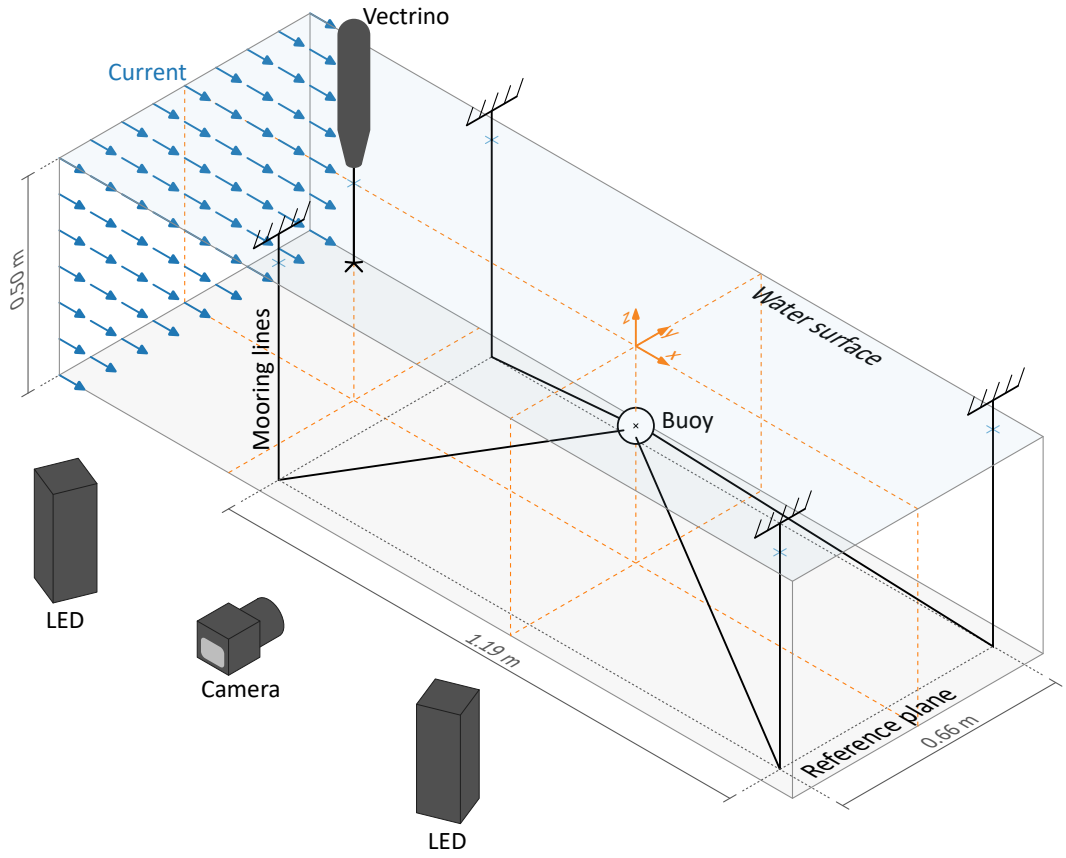

Figure 4.3: General experimental setup for validation of numerical mooring analysis.

The buoy had a diameter of 0.08 m and was mainly 3D printed with glycol-modified polyethylene terephthalate (*PETG*). It was covered with white paint to properly seal the surface and generate a smooth finish. Depending on the experimental series, the eye bolts or some precisely defined points on the buoy's hull were painted black to be visible against a white background and the buoy's surface.

4.4.1 Equipment

The current was measured with a *Nortek Vectrino* which is able to measure the current speed at a point just below the probes in all three directions via the Doppler effect. The sampling rate was set to 80 Hz with a nominal velocity range of $\pm 1.0\,\mathrm{m\,s^{-1}}$. The transmit length was set to 1.8 mm, the sampling vol. to 7.0 mm and the Power level to *HIGH+*.

The position of the buoy was recorded with the high speed camera *HiSpec 2G Mono* by *Fastec Imaging* at 80 frames per second and a shutter time of 800 µs. The lens used was the NAVITAR 50mm F0.95 TV with the aperture set to F8. The images were processed with *ImageJ/Fiji* (Schindelin et al. [95]) and the plugin *Trackmate* (Tinevez et al. [114] and Ershov et al. [38]).

Table 4.3: Measurements of for determining elasticity of mooring line.

Force	Pixels	Deformation
0.000 N	448	0.1677 m
1.956 N	551	0.2062 m
3.912 N	654	0.2448 m

The resulting trajectories of the fairleads as well as the current data obtained via the *Vectrino* were analyzed with Python 3 and the modules NumPy in version 1.22.4 [48], and Pandas in version 1.4.3 [112, 72].

4.4.2 Material of Mooring Line

Monofilament fishing line was used as mooring line material with a nominal diameter of 0.3 mm and that was later determined to 0.32 mm with a digital caliper. The weight per unit length was measured as $9.862\,500 \times 10^{-5}\,\mathrm{kg\,m^{-1}}$ with the analytical balance *Ohaus Pioneer PX224*. The fishing line is sold in Mexico under the brand name *Mustad* and has a nominal strength of 4.6 kg.

Elasticity The elasticity of the line was measured with 2 calibration masses of 200 g each. The deformation of the line with known length was captured with a digital camera and later analyzed with a raster image manipulation software. With the known length of the mount, the relation between pixels and length was determined and a deformation could be assigned to each load. The measurements can be found in table 4.3. The function `stats.linregress` of the Python module SciPy in version 1.8.0 [120] was used to calculate the linear regression for the three points. The stiffness of the samples was calculated to $5.0741 \times 10^{1}\,\mathrm{N\,m^{-1}}$ with a corresponding r-value of 1.0000. The stiffness per unit length (EA) was then estimated to $1.138\,634 \times 10^{2}\,\mathrm{Pa\,m^{2}}$.

4.4.3 Methodology

The absolute error (e_{abs}) between the mean of the experimental observations ($\bar{f}_{exp}$) and the numerical calculation (f_{num}) is defined by

$$e_{abs} = f_{num} - f_{num,0} - \bar{f}_{exp} + \bar{f}_{exp,0} \tag{4.23}$$

and the relative error (e_{rel}) is defined by

$$e_{rel} = \frac{f_{num} - f_{num,0}}{\bar{f}_{exp} - \bar{f}_{exp,0}} - 1 \quad , \tag{4.24}$$

where $f_{num,0}$ and $\bar{f}_{exp,0}$ are the mean position of the first three repetitions (e.g., A01F1_A, A02F1_B and A03F1_C). In case of the experimental observations, the mean position for the corresponding experiment is taken, which is indicated by the bar on top of the symbol.

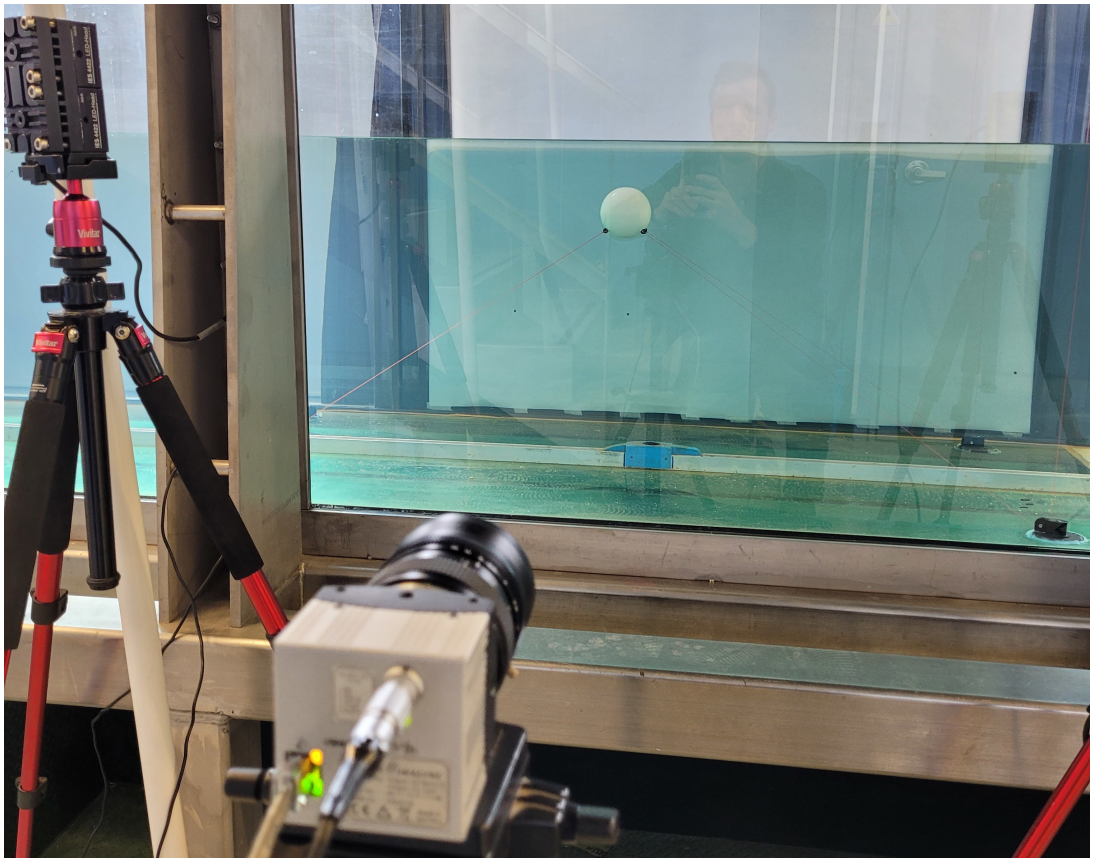

Figure 4.4: Experimental setup for series A.

4.4.4 Experimental Series A

The experimental setup is shown in figure 4.3. In figure 4.4, a photo of the setup before the experiments started can be seen, clearly displaying the black painted eye bolts, that serve as fairleads, as well as two of the four anchor points at the lower right side of the image. After passing through roller and swivel of the anchor point, a vertical section of a mooring line is visible at the right side of the image. The black marks on the background below the the buoy are reference points with known height for determining the buoys vertical position. Initially, the buoy was placed at the channels center line, 0.2 m above the reference plane. The distance between the virtual anchor point and the fairleads was 0.68 m. The frequency of the pumps was changed between 0 Hz and 60 Hz in 10 Hz increments. With three repetitions, 21 experiments were conducted in total. The complete matrix can be found in table 4.4. The mooring lines were attached to metallic, black eye bolts. To account for the vertical section, which cannot be modeled with `OffshorePy`, the apparent stiffness per unit length (EA') was calculated to 39.3096 Pa m^2.

Table 4.4: Experiment matrix series A for validation of numerical mooring analysis software.

Experiment	F_P Hz	**Experiment**	F_P Hz	**Experiment**	F_P Hz
A01F1_A	0	A08F3_B	20	A15F5_C	40
A02F1_B	0	A09F3_C	20	A16F6_A	50
A03F1_C	0	A10F4_A	30	A17F6_B	50
A04F2_A	10	A11F4_B	30	A18F6_C	50
A05F2_B	10	A12F4_C	30	A19F7_A	60
A06F2_C	10	A13F5_A	40	A20F7_B	60
A07F3_A	20	A14F5_B	40	A21F7_C	60

Current Speed

The histogram of the current speeds measured for each experiment with current are shown in figure 4.5. Unfortunately, the measurements of the vectrino were very poor for the first three experiments (A01F1_A, A02F1_B and A03F1_C), resulting in the detection of a non-existent current. For the simulations, these measurements were disregarded and the current was assumed to be zero. For all other experiments, the mean current speed of the respective repetition was used. For the experiments A13F5_A and following, the distribution presents a much greater standard deviation. While the standard deviation was below $0.020\,\mathrm{m\,s^{-1}}$ for all repetitions before A13F5_A, it ranges from $0.024\,\mathrm{m\,s^{-1}}$ to $0.36\,\mathrm{m\,s^{-1}}$ for the experiments A13F5_A to A21F7_C (see table A.1).

Position of Buoy

The position and the rotation of the buoy was calculated from the position of the fairleads. The numerical model predicted the x-position of the buoy very accurately (see figure 4.6 a)) up until a current speed of $0.42\,\mathrm{m\,s^{-1}}$. However, the corresponding absolute error in figure 4.6 b) indicates that the simulation slightly overestimates the x-position until this threshold, followed by a significant underestimation. The relative error was highest for the second lowest current speeds which can be attributed to the low absolute values. For the two following current speeds, the relative error is at maximum 0.151 (see table A.2). Similarly, the rotation around the y-axis (see figure 4.6 d)) was accurately predicted by the numerical model for low current speeds, but showed a clear overestimation of rotation for higher current speeds. This discrepancy was less pronounced than for the x-position. The error ranged between 0.25 and 0.35 for the current speeds of $0.21\,\mathrm{m\,s^{-1}}$ and $0.32\,\mathrm{m\,s^{-1}}$. However, the z-position of the buoy shows a huge error (see figure 4.7). While the simulation predicts nearly no change in the z-position, a clear decrease of 0.005 m was observed during the experiments.

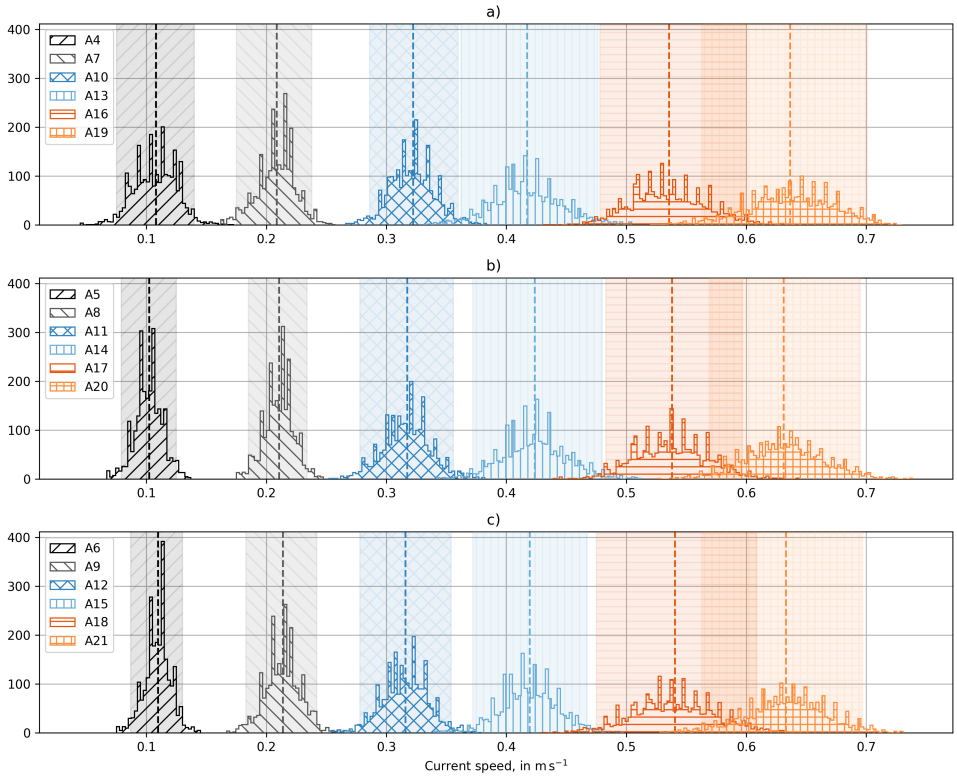

Figure 4.5: Current speeds measured during experiment series A. The 2.5$^{\text{th}}$ and the 97.5$^{\text{th}}$ quantile (shaded area) as well as the mean current speed (dashed line) are shown for each experiment. **a)** First repetitions; **b)** Second repetitions; **c)** Third repetitions.

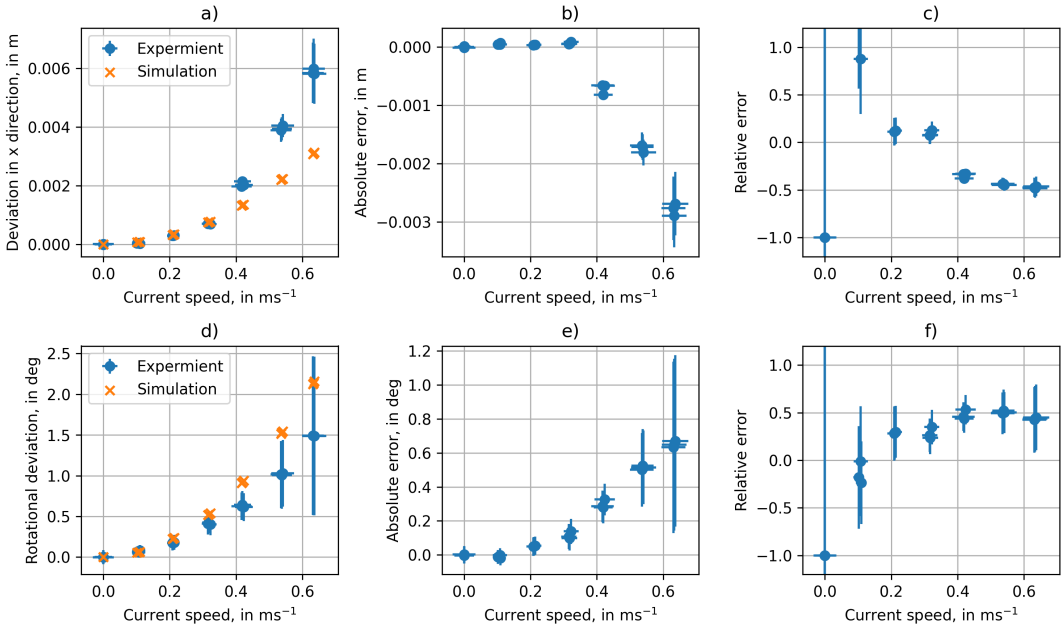

Figure 4.6: Comparison between numerical prediction of buoy position and experimental observation for experiment series A: **a)-c)** Deviation in x-direction, and corresponding absolute and relative error; **d)-f)** Rotation around y-axis, and corresponding absolute and relative error;

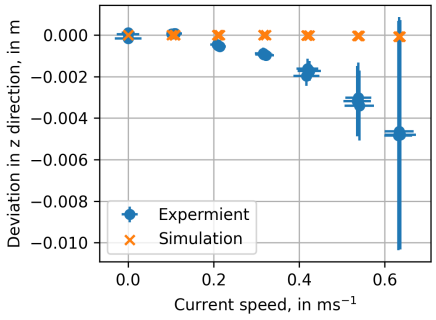

Figure 4.7: Deviation of z-position of the buoy as predicted by numerical prediction and observed in experiments for experiment series A

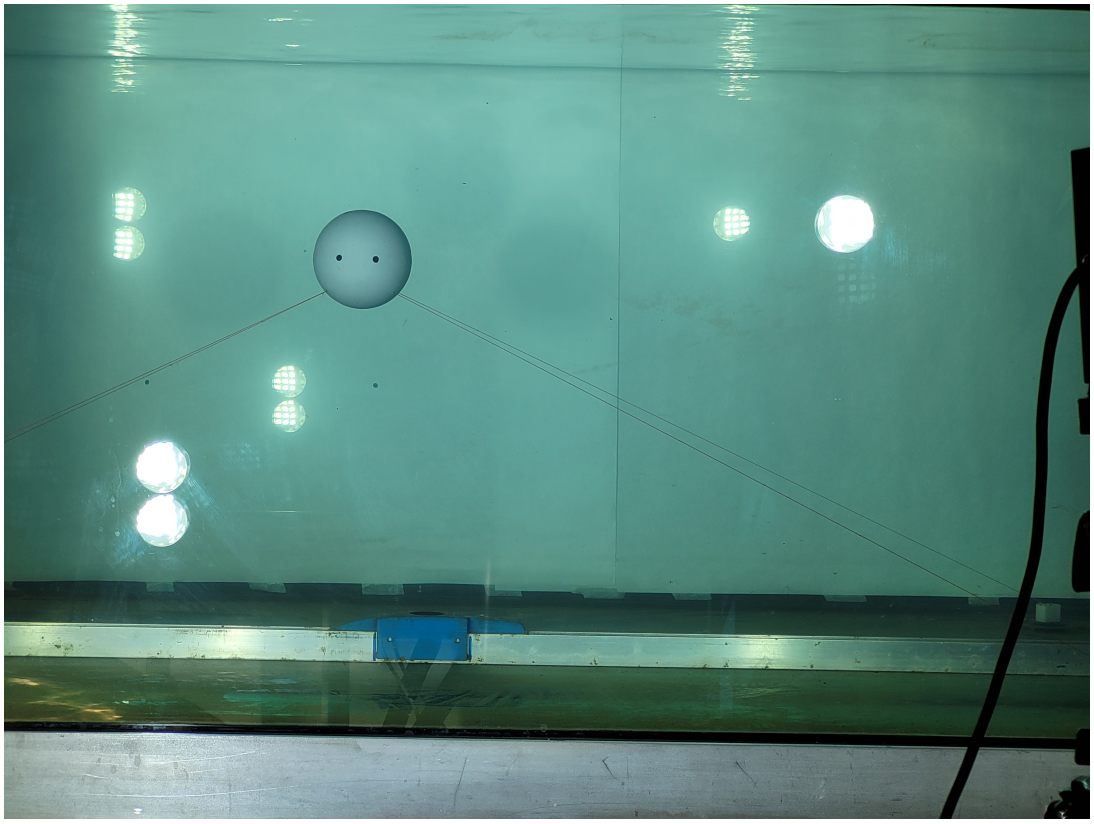

Figure 4.8: Experimental setup for series B, taken during experiments with the pumps at 35 Hz.

4.4.5 Experimental Series B

The experimental series B featured a different mooring configuration than series A, with the mooring lines directly attached to the channel's bottom via the anchor. However, the general setup was similar to that shown in figure 4.3. In figure 4.8, the four mooring lines are visible as well as one anchor point at the lower right corner (white box), slightly obscured by a cable. Despite the image being taken at the maximum pump frequency (i.e., maximum current speed), the mooring lines remained straight between the anchor point and the fairleads. Since the mooring lines were directly glued to the holes inside the buoy, dedicated fairleads similar to experimental series A were unnecessary. Instead, two black dots were painted on the surface of the buoy at a distance of 0.03 m arc length to aid in determining the buoy's position and orientation. The same reference points used in experimental series A to calculate the buoy's vertical position were also used in series B, visible as the black dot on the background below the buoy. The scene was illuminated with 5 light emitting diodes, their reflection is visible in the image. Similar to series A, the buoy was placed at half the water depth of 0.5 m at the channel's center line, resulting in a line length of 0.6937 m. The frequency of the pumps was changed between 0 Hz and 30 Hz in 5 Hz increments. With three repetitions, 21 experiments were conducted in total, leading to the experiment matrix shown in

Table 4.5: Experiment matrix series B for validation of numerical mooring analysis software.

Experiment	F_P Hz	**Experiment**	F_P Hz	**Experiment**	F_P Hz
B01F1_A	0	B08F3_B	10	B15F5_C	20
B02F1_B	0	B09F3_C	10	B16F6_A	25
B03F1_C	0	B10F4_A	15	B17F6_B	25
B04F2_A	5	B11F4_B	15	B18F6_C	25
B05F2_B	5	B12F4_C	15	B19F7_A	30
B06F2_C	5	B13F5_A	20	B20F7_B	30
B07F3_A	10	B14F5_B	20	B21F7_C	30

table 4.5. The roller at the anchor points and the subsequent vertical sections of the mooring lines were omitted by gluing the lines to the anchor points.

Current Speed

The measured current speeds during this series are presented in figure 4.9. The mean of the current changes significantly between repetitions especially for experiments B04F2_A, B05F2_B and B06F2_C. The correlation as reported by the Vectrino (see table A.3) seems to have great influence on the standard deviation of the measured current. For some experiments, the measured 95% confidence interval (shadows in figure 4.9) does overlap for adjacent experiments (e.g. B17F6_B and B20F7_C, see figure 4.9 c)). Noticeable is also the steady increase in standard deviation with increasing pump frequency (i.e., current speed), with the exception of the experiments without current and experiments B05F2_B and B06F2_C, which showed a much higher standard deviation than expected. Similar to the experimental series A, the measurements for the experiments without current seem to be inaccurate (B01F1_A, B02F1_B and B03F1_C), as currents were detected in the range of roughly $-0.1\,\mathrm{m\,s^{-1}}$ to $0.1\,\mathrm{m\,s^{-1}}$. For the simulations, these measurements were ignored and the current was set to zero while for all other experiments, the mean current speed was chosen.

Position of Buoy

The position of the buoy was determined by analyzing the relative position of the dots painted on the buoy's surface. To minimize errors due to camera tilt, misalignment of dots, or minimal differences in line lengths, the position of the buoy was compared to its initial position. The deviation in x direction and the rotation around the y-axis, together with their respective absolute and relative error, can be seen in figure 4.10, and the exact values of the signed relative error can be found in table A.4. The numerical model underestimates the deviation in x-direction by approximately 0.5 for the repetitions of current speeds $\geq 0.1\,\mathrm{m\,s^{-1}}$ (07F3_A and higher). For the first repetition

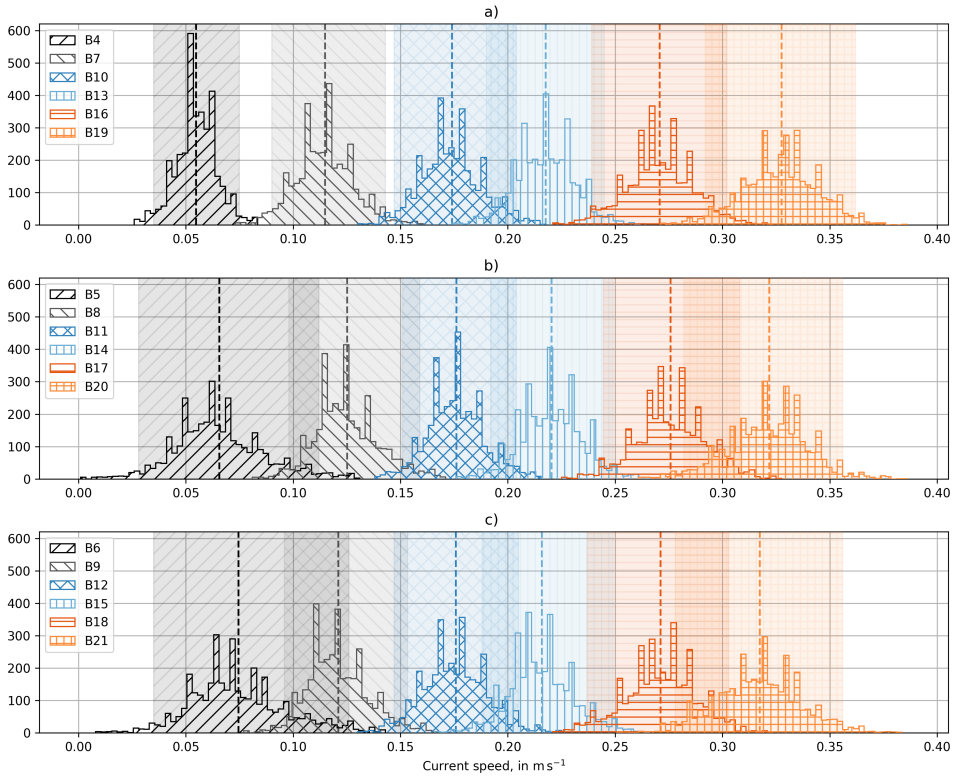

Figure 4.9: Current speeds measured during experiment series B. The 95% confidence interval is indicated by the shadows and the mean current speed by the dashed line, while the colors correspond to the experiment. **a)** First repetitions; **b)** Second repetitions; **c)** Third repetitions.

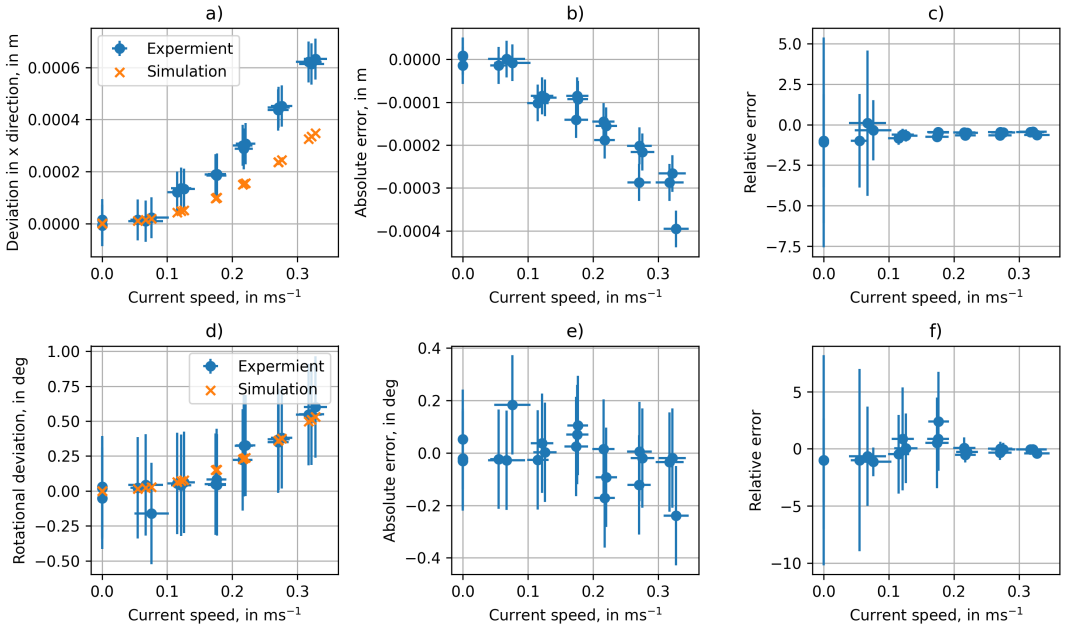

Figure 4.10: Comparison between numerical prediction of buoy position and experimental observation for experiment series B: **a)-c)** Deviation in x-direction, and corresponding absolute and relative error; **d)-f)** Rotation around y-axis, and corresponding absolute and relative error;

of each experiment the error is increased. For the first three repetitions, the error is one as the numerical model naturally does not predict a deviation from its initial position. The repetitions for the second experiment (04F2_A through 06F2_C) present a great variation of errors. However, for the first six repetitions, the 95%-confidence interval crosses zero, wherefore no qualified statement can be made for low current speeds.

For higher current speeds, the numerical model shows a much better fit on the rotation around the y-axis. However, a similar pattern as for the x-deflection can be found, where the first repetition of the experiments shows a significantly higher error. For example for the last experiment, the first repetition shows a relative error of -0.4, while the relative error of the second and third repetition were reported to be -0.04 and -0.06 respectively. For the first four experiments ($u \leq 0.2\,\mathrm{m\,s^{-1}}$) a very large 95%-confidence interval was reported (see figure 4.10 c)). However, the for the majority of the repetitions, the absolute error was found close to 0, while the 95%-confidence intervals are significantly larger (see figure 4.10 c)), suggesting that the errors reported for lower currents might be the result of the experimental setup.

The deviation in z-direction is shown separately in figure 4.11, as the predictions of the numerical model are far off of the observed deviations. With increasing current speed, the buoy moved upwards, reaching the maximum position at around $0.2\,\mathrm{m\,s^{-1}}$ before it begins to slowly drop again. In contrast, the numerical model predicts a deflection of 3 µm towards the bottom of the channel.

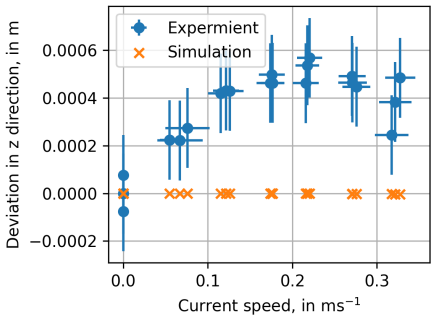

Figure 4.11: Comparison of z-position of the buoy between numerical prediction and experimental observation for experiment series B.

4.5 Validation of Line Tensions

Accurately predicting tensions in mooring lines is crucial for designing effective mooring systems. Since during the experimental validation, the tensions were not measured, the python module is compared to data found in literature. Specifically, data from full-scale experiments conducted by Berteaux et al. [11], who moored a spherical subsurface buoy to the sea floor at a depth of 27.5 m using wire rope with a nominal diameter of 5/16 in. The diameter of the buoy was 48 m, while its buoyancy was varied between 400 lb, 800 lb, and 1050 lb. The mass of the buoy was adjusted to match the buoyancy for a perfectly spherical buoy with the given diameter. The initial depth was set to 5 m below the surface. To compare the prediction by OffshorePy to the reported tensions, the properties of the wire rope were calculated based on equations (4.10) and (4.11), provided by Ma et al. [68]. The results of the calculations can be seen in figure 4.12, with the relative error defined by

$$e_{rel} = \frac{f_{num}}{f_{exp}} - 1 \quad , \tag{4.25}$$

where f_{num} refers to the tension as predicted by OffshorePy and f_{exp} to the value from literature. It should be noted, that the values reported in [11] for the experiment (here called *Dynamoor*) are the mean tensions. The tension ranges were reported to 573 lb, 780 lb, and 786 lb, respectively, fully embracing the predictions by OffshorePy and SSMOOR. As can be seen in figure 4.12, OffshorePy overestimates the tensions with respect to SSMOOR, and underestimates the tensions with respect to the measurements. The mean relative error with respect to SSMOOR was calculated to 0.040 0.04 and the mean error with respect to the measurements (i.e., Dynamoor) are -0.073.

4.6 Discussion

The impact of current speed on the quality of the current measurements is evident from the results presented in figures 4.5 and 4.9. As the current speed increases, particularly for the experiments A13F5_A and following with pump frequencies exceeding 30 Hz, the current quality deteriorates.

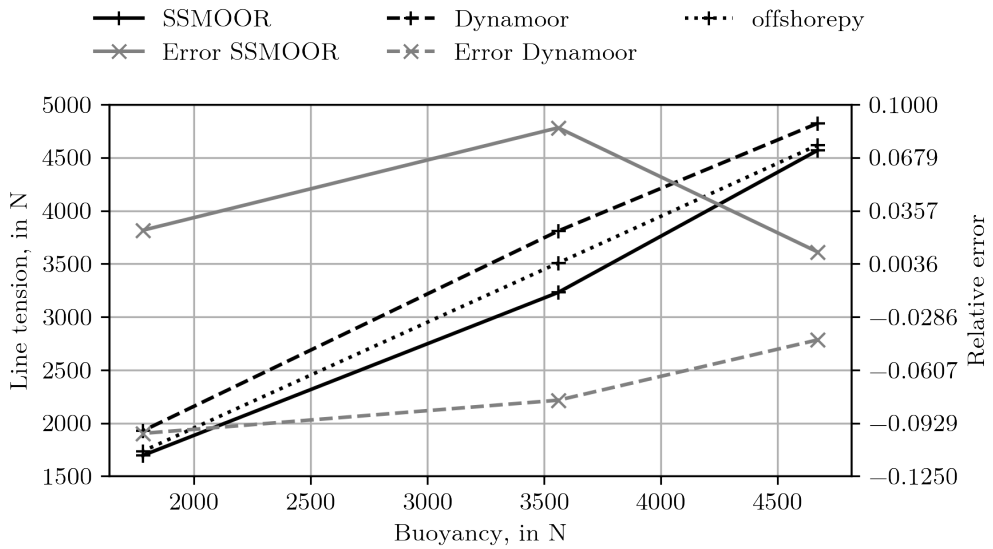

Figure 4.12: Comparison of line tensions between Dynamoor and OffshorePy.

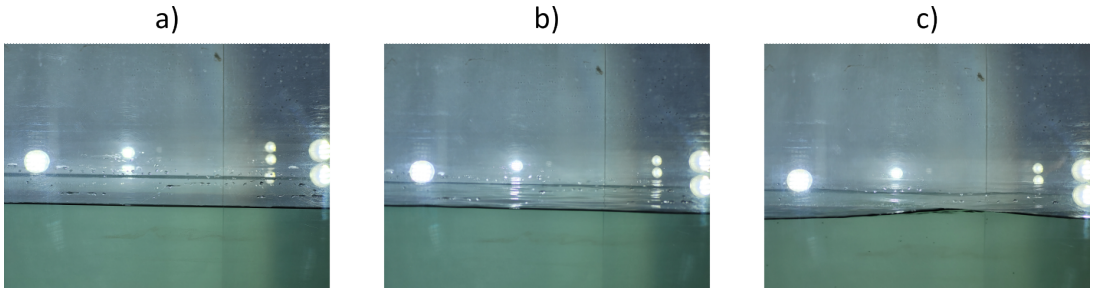

Figure 4.13: Water surface of the channel for different pump frequencies. **a)** 20 Hz; **b)** 40 Hz; **c)** 60 Hz. The surface appears to be inclined due to the perspective of the photos.

This behavior may be attributed yo the quality of the current in the channel as shown in figure 4.13. The surface appears to be completely flat at 20 Hz, but as the frequency rises, small ripples appear at 40 Hz, and eventually a noticeable disturbance is observed at 60 Hz. Since the current is the only environmental influence on the water, this indicates a decrease in the alignment of the stream lines. Previous studies have reported a significant vertical profile of the current flow in this channel, where the vertical position of the peak velocity varies with the frequency of the pumps. However, since the current speed was only measured at a single point upstream of the buoy at the same depth during the experiments, the vertical profile of the current during the experiments remains unknown.

Regarding the experimental series A, it is important to note that the numerical model does not include the fairleads (i.e., eye bolts of the buoy) and their effect on the buoy. The fairleads are positioned at the bottom of the buoy and their drag force generates a opposing moment to the

moment of the drag force of the buoy itself. This effectively reduces the rotation around the y-axis, which could explain the overestimation of the pitch angle as seen in figure 4.6 c). Additionally, the reduced quality of the current could be the source of the error for currents above $0.42\,\mathrm{m\,s^{-1}}$. During the experiments, a significant deflection of the vertical section of the mooring lines was noted, effectively shortening the diagonal part of the mooring line. This resulted in lowering the position of the buoy, as it was observed during the experiments (see figure 4.6 b)). However, this effect cannot be represented by the mooring software as such mooring configuration is rather untypical.

For the above mentioned reasons, a second experiment series, series B, was performed; to address the limitations of the first series and to eliminate the fairleads and the vertical sections of the mooring lines. In the series B the buoy was positioned slightly higher than in the experimental series A. Noticeable is the unexpected behavior of the buoy to first raise its position with increasing velocity and to drop again after reaching its maximum height at roughly $0.22\,\mathrm{m\,s^{-1}}$. A similar behavior was observed in preliminary experiments at this height, suggesting that it may be linked to the vertical position of the buoy above the channel's floor. The influence of this effect on the x-position of the buoy is unclear, but the fact that the relative error during series A was much lower for the x-position suggests a possible link. Nonetheless, the agreement regarding the trim of the buoy is much better. The numerical model showed a high relative error for some repetitions and good agreement for others, indicating the need for further investigation.

Both experimental series showed high standard deviations for position and rotation of the buoy, especially at lower current speeds. It is possible that some of the reported deviations could be attributed to the camera sensor noise since the observed deflections are at the order of magnitude of a pixel. For future experiments a higher elasticity of the mooring system is recommended to reduce the error due to spacial resolution of the sensor. However, during preliminary experiments with a single mooring line the buoy never reached quasi-static equilibrium and oscillated with an amplitude of several diameters perpendicular to the current. As shown in the experimental series B, the estimation of the tilt of the buoy was very good, while the horizontal position was underestimated by approximately 0.5. It remains unclear, weather this is an error of the numerical model or due to the experimental setup. Nonetheless, for the purpose of the software developed in this work, the angle is of much greater importance than the mooring offset. Additionally, the error of the tensions in comparison to the software SSMOOR and measurements of the Dynamoor experiments was very, with a relative error of 0.04 and -0.073, respectively. This suggests that the tensions in subsurface mooring lines can be predicted reliably with `OffshorePy`.

Chapter 5

Genetic Algorithm

For the concept design of the position keeping system a multi objective genetic algorithm is used as they are described by Zhou et al. [125]. In this chapter the genetic algorithm is explained while its application can be found in chapter 8. This approach has been successfully applied by several authors in the past. For example Xu et al. [123] proposed a design methodology based on the non-dominated sorting algorithm for very large floating structures. Xia et al. [122] optimized a single point mooring system based on static equilibrium model with a multi-objective genetic algorithm. Shafieefar and Rezvani [101] proposed a design procedure to optimize parameters such as heading and mooring pattern of floating structures with the help of a genetic algorithm. Another work has been presented by Pillai et al. [84], who optimized the mooring system for a floating offshore wind turbine. Therefore, the problem is generalized and simplified, only described by a few parameters, which are registered and joined in the *genome* of the system. During the optimization process, the algorithm modifies the parameters and evaluates the obtained position keeping system until the termination criterion is met. A brief description of the overall principle is given in figure 5.1. The process beings with the initialization, where the first generation is randomly created, obtaining a wide spread gene pool. Each set of parameters (i.e. genome) represents one variation of the position keeping system (i.e. individual). In the next step, all variations (i.e. the whole generation) are evaluated and sorted according to their individual fitness. The fitness can be evaluated with respect to a single objective or multiple objectives. Single objective genetic algorithms (SOGAs) optimize the problem for a single objective which can include multiple objectives via a fitness function, that reduces the fitness to a single score, and is discussed in more detail in section 5.1. Multi objective genetic algorithms (MOGAs) typically aim to find the Pareto-Optimized Front, which is not bound to a specific weighting between the different objectives, as described in section 5.2. The individuals are sorted and only a few individuals are selected to serve as breeders for the next generation. For the selection, many different algorithms can be selected, where tournament-selection and roulette-wheel-selection are among the most used for genetic algorithms. These breeders are randomly recombined to create new individuals and mutation is applied to maintain a wide spread gene pool. If elitism is used, the next generation is mixed with the previous generation and cut down to the size

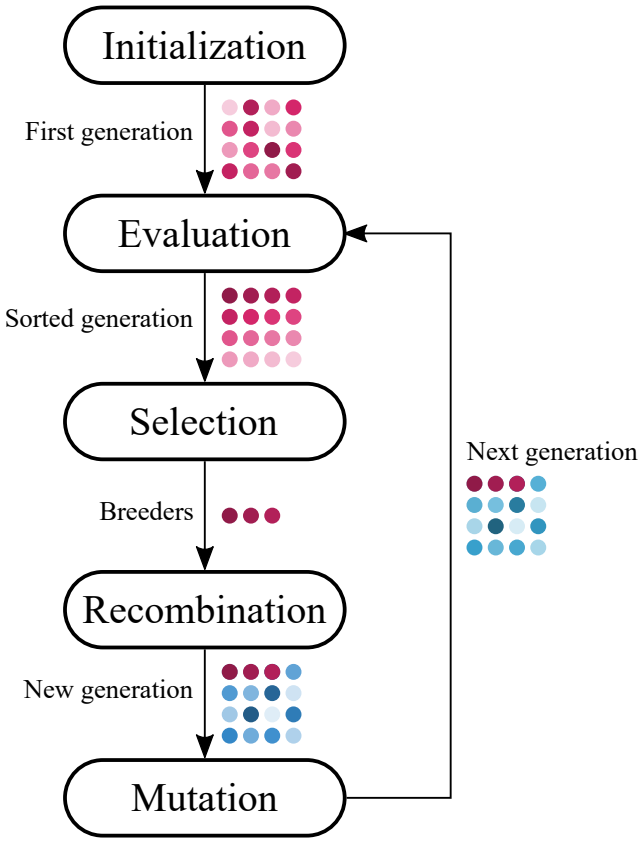

Figure 5.1: Process of optimization with a single objective genetic algorithm.

of the original generation size by discarding the worst performing individuals. This helps maintain a good set of information within the gene pool until better individuals are found which outperform their breeders.

5.1 Single Objective Optimization

The fitness function aims to evaluate the performance of an individual in a given situation by considering multiple properties, which are assigned different weights based on their relative importance. Each evaluated property has a minimum, maximum and desired optimum value and an associated weight. To calculate the fitness score for a given individual, the fitness function applies a mathematical formula that takes into account the values of each property, their associated weights, and the chosen function type (quadratic or sinusoidal). This process results in a single value that represents the overall quality of the individual's performance in the evaluated situation. The used genetic algorithm provides either a quadratic function or a sinusoidal function.

The quadratic function is defined by

$$f_i = \begin{cases} 0 & \text{for } x_i < x_{min} \\ \left(\frac{-1}{(x_0 - x_{opt})^2}\left(x_i - x_{opt}\right)^2 + 1\right) & \text{for } x_{min} \leq x_i \leq x_{max} \\ 0 & \text{for } x_i > x_{max} \end{cases} , \tag{5.1}$$

where x_i denotes the value of the property, x_0 the min or max x-value, whichever is further away from the optimum value, x_{opt} the optimum value and x_{min} and x_{max} the minimum and maximum value, respectively. The function has its apex at the desired optimum and a simple zero at the minimum or maximum value, whichever is further away from the optimum value.

The sinusoidal function is given by

$$f_i = \begin{cases} 0 & \text{for } x_i < x_{min} \\ 1/2\left(\cos\left(\frac{x_i - x_{opt}}{x_{min} - x_{opt}\pi}\right) + 1\right) & \text{for } x_{min} \leq x_i < x_{opt} \\ 1/2\left(\cos\left(\frac{x_i - x_{opt}}{x_{max} - x_{opt}\pi}\right) + 1\right) & \text{for } x_{opt} \leq x_i \leq x_{opt} \\ 0 & \text{for } x_i > x_{max} \end{cases} , \tag{5.2}$$

where the variables are reserved for the same value as in equation (5.1). The function is bell shaped with its maximum at x_{opt} and zero at x_{min} and x_{max}, while the shape in between is sinusoidal.

Outside the acceptable range of the property, the fitness is set to zero, while the ordinate of the quadratic function of its apex is the weight (w_i) of the specific property. The values of the property's fitness (f_i) are added up and then normalized by the total weight in order to limit the maximum fitness to 100:

$$f = \frac{100}{\sum w_i} \sum w_i f_i \quad , \tag{5.3}$$

where w_i is the weight associated to the property.

5.1.1 k-Factor

The k-factor (k) is an additional factor which is added to the fitness of an individual to obtain its overall score. It is used to promote a wide spread gene pool particularly in the first generations by the use of the scale factor (s_c), the stretch factor (s_t), and the hamming distance (d_h) between the individual and the whole generation, that is how different the individual is from its generation based one the entries in its genome. Thus, the score S is calculated by

$$S = f + kd_h \quad , \tag{5.4}$$

with

$$k = s_c \frac{s_t + 1}{n_{gen}} \quad , \tag{5.5}$$

where n_{gen} denotes the number of generation.

5.1.2 Recombination and Mutation

The recombination process involves selecting the best breeder as a pattern, and then randomly selecting a value for each parameter from the pool of available breeders.

To introduce variability and avoid convergence to local optima, a mutation step is applied to each parameter with a probability determined by the globally specified mutation rate. Depending on the parameter type, the mutation strength is taken into account or not. For list types, a random item is selected from the list, which may be the same or different. For integers and floating point numbers, a random value between 0 and the mutation strength times the original value is added or subtracted from the current value. If the new value falls outside the acceptable range for the parameter, the procedure is up to 100 times repeated until a valid value is found or the value remains unchanged.

5.2 Multi Objective Optimization

In multi-objective optimization, it is often beneficial to avoid aggregating the different objectives into a single score, as is typically done in single-objective optimization. Instead, a Pareto-Optimized front can be searched, which consists of individuals that represent the best possible trade-off between different objectives. The Pareto front is defined as the set of individuals whose improvement in one objective comes at the cost of a degradation in another objective. This means that any individual on the Pareto front represents the best possible trade-off between the different objectives, and further optimization of one objective would necessarily lead to a deterioration in performance with respect to the other objectives.

5.2.1 Sorting

In comparison to the single objective evaluation, no absolute value can be given to determine whether an individual is superior to another or not. MOGAs usually sort the individuals by their rank and use the crowding distance to order individuals of equal rank.

Rank A rank-based fitness assignment gives each individual a rank based on the number of individuals it is dominated by. An individual is considered to be dominated (i.e. it is inferior) if there exists another individual that is at least as good as it in all objectives, and strictly better in at least one objective. If all objectives are fulfilled equally good by two compared individuals, neither of both individuals is dominated by the other (i.e. non-inferiority) [41].

There are different ways to define the rank of an individual, depending on the specific algorithm used. One common definition is based on the work of Fourman [42], who defines the rank of an individual as the number of individuals which are superior elevated by one. For example, individuals of the Pareto optimal set have rank 1, as they are dominated by no other individual. Individuals of rank 2 would only be dominated by one other individual and so on. Another definition for the rank, proposed by Golberg [45], defines the rank as the number of individuals of different ranks, which dominated the individual in question. For example, an individual dominated by two individuals of rank 1 would be of rank 3 following Fourman and of rank 2 following Golberg.

Crowding Distance The crowding distance of an individual is a measure of its diversity with respect to the other individuals in the population for a particular objective. Specifically, it is calculated as the difference in performance for that objective (j) between the two adjacent individuals ($f_{i+1,j}$ and $f_{i-1,j}$) when sorted regarding their performance for the objective and normalized by the range of performance values between for that objective in the population. The total crowding distance of an individual i is the simple sum of the crowding distance for each objective. Those individuals which only have one neighbor, which are the best and the worst performing individuals regarding the analyzed objective, have an infinite crowding distance.

$$\tilde{d}_i = \sum_{j=1}^{n_o} \frac{f_{i+1,j} - f_{i-1,j}}{f_{max,j} - f_{min,j}} \quad , \tag{5.6}$$

where n_o is the total number of objectives, $f_{max,j}$ the fitness of the best performing individual, and $f_{min,j}$ the fitness of the worst performing individual in the same population.

5.2.2 Creating Next Generation

The breeder for the recombination are selected through Round Robin tournaments, where individuals are selected randomly from the complete gene pool. The best individual from each tournament is selected regarding rank and crowding distance, and chosen as breeder.

All individuals of the last generation are then copied to the new generation. An equal number of new individuals is then generated through recombination of the breeders and mutation of the

newly generated individuals. For recombination, each parameter is copied from a randomly selected breeder. This process is performed for each parameter and each new individual independently, increasing the probability of a unique combination. Afterwards, a random number between 0 and 1 is drawn for each parameter of the newly generated individuals. If this number is smaller or equal to the specified mutation rate, the value of the parameter is mutated. In case the parameter is a list of values, a random value of the list is drawn. If the parameter is an integer or a floating point number, a second number between 0 and 1 is randomly drawn, multiplied by the mutation strength and the current value of this parameter. The sign of the value is also set randomly before being added to the current value. If the new value falls outside the permitted range for the parameter, this procedure is repeated up to 100 times until mutation of this value is abandoned.

After mutation, the newly generated individuals are evaluated by an external function that must be provided during initialization of the gene pool. Since the current generation contains double the desired number of individuals per generation, they are sorted regarding rank and crowding distance and the inferior half is discarded.

5.3 Implementation

The pattern of the genome is defined in an XML file, which is given as input to the `GenePool` Python class responsible for managing genetic optimization. The `GenePool` class parses the XML file and uses the information to generate the initial population of individuals and to determine the parameters for the genetic optimization algorithm. The XML document begins with information on the XML version and encoding, followed by the root element `genome`, as can be seen in the following example:

```
<?xml version="1.0" encoding="UTF-8"?>
<genome v="0.1">
</genome>
```

Within the `genome` element, the parameters subject to change are defined by providing the name of the parameter, its type, and the range. The name is used to reference to the specific parameter within Python. The type of the parameter can be integer, indicated by `int`, a floating point number, indicated by `float`, and a comma separated list, indicated by `list`. The range attribute defines the possible range of values, the parameter may reproduce. The min and max value are separated by a dash "-" and the direction of the square bracket indicates if the boundary is part of the range (enclosing bracket) or not (faced away from boundary), as can be seen in the following listing:

```
<?xml version="1.0" encoding="UTF-8"?>
<genome v="0.1">
  <parameter name="line numbers" type="int" range="[1-5]"/>
  <parameter name="line diameter" type="float" range="]0.005-0.2["/>
  <parameter name="line material" type="list" range="dyneema,steel"/>
</genome>
```

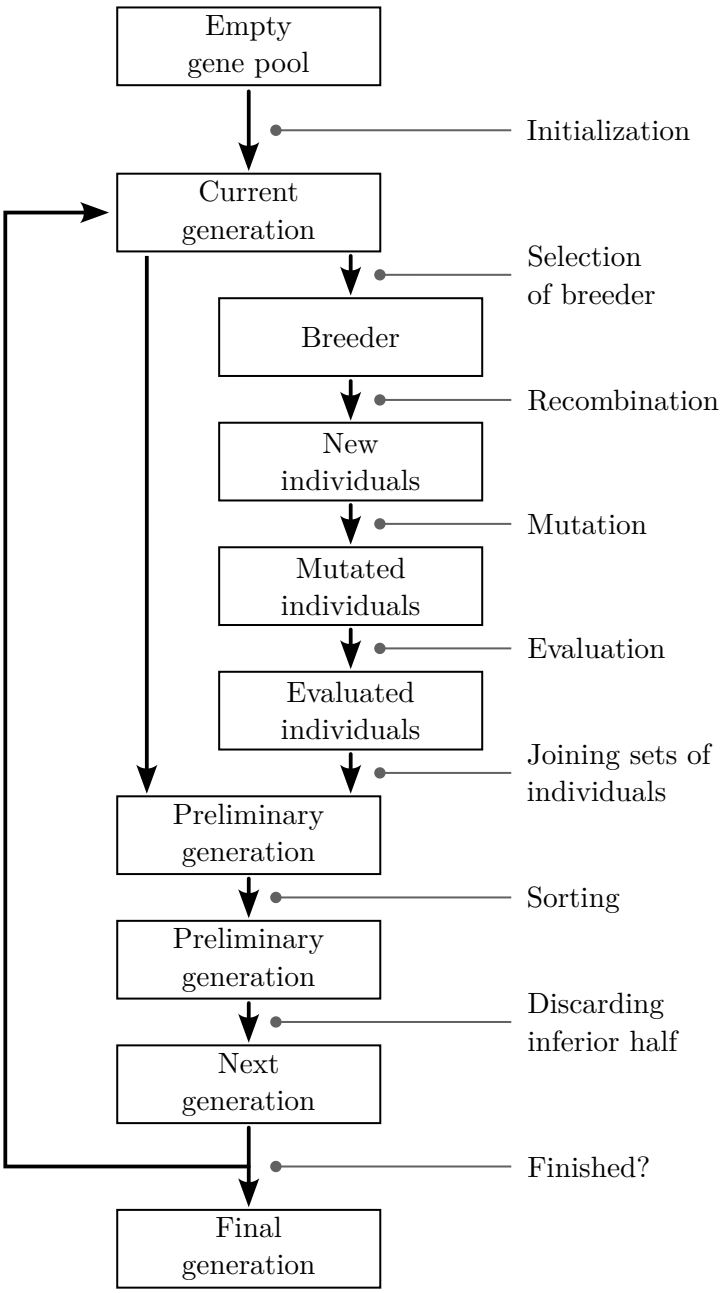

Figure 5.2: Process of optimization with a multi objective genetic algorithm.

The parameter "line numbers" is an integer and ranges from one to five, including the boundary, whereas the parameter "line diameter" is a floating point number ranging from 0.005 to 0.2, not including the boundaries. The line material may be one of "dyneema" or "steel".

Sometimes one or more parameter define one object which can be used multiple times in different appearances. To obtain this behavior, the corresponding parameter are child elements of a `block` element.

```
<block name="hulls" prefix="hull" range="[1-3]">
  <parameter name="diameter" type="float" range="]0.1-1]"/>
  <parameter name="length" type="float" range="]0.1-5["/>
</block>
```

The number of objects can be accessed via the name, in this case "hulls", which always is of type integer. The prefix is used to get access to the objects, follow by an underscore, the serial number of the object, a dot, and finally the parameter's name. For example, to obtain the diameter of the second hull, the string `"hull_1.diameter"` has to be used. The range and type attributes of both, the `block` element and the `parameter` elements of the object, follow the same rules as described above.

5.3.1 Performance

The performance of the algorithm was evaluated with the Griewank-function of 10-th order as suggested by Digalakis and Margaritis [28]. The function (f) is given by

$$f = 1 + \sum_{i=1}^{10} \frac{x_i^2}{4000} - \prod_{i=1}^{10} \cos \frac{x_i}{i} \quad , \tag{5.7}$$

where x_i is the i-th parameter. As can be observed, the function attains its absolute minimum at 0 when each parameter is also 0. The optimization process involved 150 generations, each with 50 individuals, a mutation rate of 0.6, a mutation strength of 1.0, and a randomly generated initial generation. Each parameter was restricted to 6 decimal digits. The maximum parameter value per generation is shown in figure 5.3 a) while figure 5.3 b) illustrates the function value. Both maximum parameter and the function values approach zero rapidly. However, the absolute minimum is not reached until the 102$^{\text{nd}}$ generation.

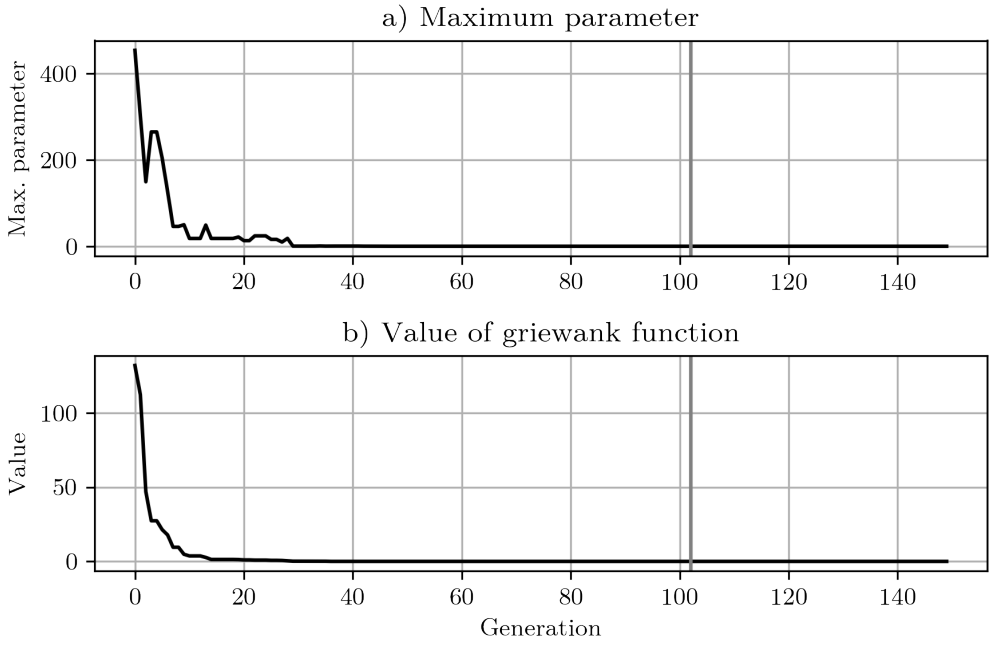

Figure 5.3: Evaluation of genetic algorithm with Griewank-function. **a)** Maximum parameter; **b)** Value of Griewank-function. The vertical line marks the 102$^{\text{nd}}$ generation at which the absolute minimum was reached.

Chapter 6

Site Characterization

For the design process, comprehensive data on the construction site are essential to reliably predict required dimensions of the mooring system, select suitable anchors, and estimates the loads occurring during operation and maintenance. These data should cover meteorological and oceanographic conditions, water depth, geotechnical conditions, seismicity, biology, and human activities [33]. However, since this work concentrates on the design of the mooring system and the platform for mounting the turbine, not all topics will be addressed. Previous research has already been conducted on topics such as selecting a suitable location and estimating power potential [1]. This chapter concentrates on the extreme values to be expected regarding wind, waves and currents. The data sources used are described in section 6.1, while the methodology applied for estimating extreme return levels can be found in section 6.2. The values obtained from the extreme value analysis are presented in section 6.3. Despite the lack of data specifically for the potential construction site, a brief review of the geological and geotechnical characteristics of the region can be found in section 6.4.

6.1 Data Sources

For the extreme value analysis, data on the currents have been taken from the Hybrid Coordinate Ocean Model (HYCOM) Consortium, data regarding wind and waves from the ERA 5 database, and hurricane data from the HURDAT2 database. Data from the research expedition CEMIE-1 was used for the bathymetric analysis. In the following, all sources are explained in detail.

6.1.1 Research Expedition CEMIE-1

The research expedition *CEMIE-1* on board the research vessel *B.O. Justo Sierra* took place from the 25th April 2019 and the 5th may 2019. The primary objective of this expedition was to gather information around Cozumel on the soil composition, the currents, the bathymetry and various biological parameters. The following systems were used during the campaign for the parameter

with importance for this work:

- Sub-bottom profiler Kongsberg TOPAS PS 120 used for the soil composition
- Multibeam echo sounder Kongsberg ES 302 used for bathymetry and soil composition of uppermost layer
- Acoustic doppler current profiler (ADCP) by Teledyne-RDI used for current profile

In this work, the most important data was obtained during three transects crossing the Cozumel Channel, which were carried out roughly from the 200 m isobath on the island's coast to the 200 m isobath on the continental coast. As depicted in figure 6.1, three transects were carried out, starting at the channel's north and finishing at the channel's south end. The transects are arranged in an alternating pattern, perpendicular to the prevailing current and therefore in southeastern (transect one and three) and northwestern (transect two) direction. During the transects, current, soil composition, and bathymetry were measured. However, during the connection passages, only current and bathymetry measurements were carried out, as determining soil composition was not possible in due to the pronounced slopes in these areas.

6.1.2 HYCOM Consortium

The HYCOM consortium develops and evaluates a *hybrid isopycnal-sigma-pressure (generalized) coordinate ocean model*. For the Gulf of Mexico including the Cozumel Channel, they provide information on the northward and eastward water velocity, salinity, temperature, surface elevation and temperature, among others. The consortium provides the data based on reanalysis in different projects, each with specific spacial and temporal coverage as well as resolution. For this work, the data of the model HYCOM + NCODA GOMNu0.04 experiment 50.1 were used, which are are publicly available in `https://www.hycom.org/data/gomu0pt04/expt-50pt1`. The model provides data for the Gulf of Mexico and parts of the Mexican Caribbean, covering 1st January 1993 to 31st December 2012. The temporal resolution is three hours and the spatial resolution is 0.04°, while the data are reported for 40 discrete depths.

6.1.3 CANEK Research Project

Measurements have been taken of the current in the Cozumel Channel by the CANEK project [16]. The *Centro de Investigación Científica y Educación Superior de Ensenada* coordinated the CANEK research project since its foundation in 1996, also named *Estudio de la circulación y el intercambio a través del Canal de Yucatán* (Study of circulation and exchange through the Yucatan Canal). A stationary, long-range acoustic Doppler current profiler at N20°32.218′ W87°2.738′ was anchored at a depth of approximately 400 m to obtain the data. The measurements were recorded every half hour, from 9th April 2009 to 14th May 2011 at 16 vertical cells. The cell closest to the surface was located at a depth of 49 m.

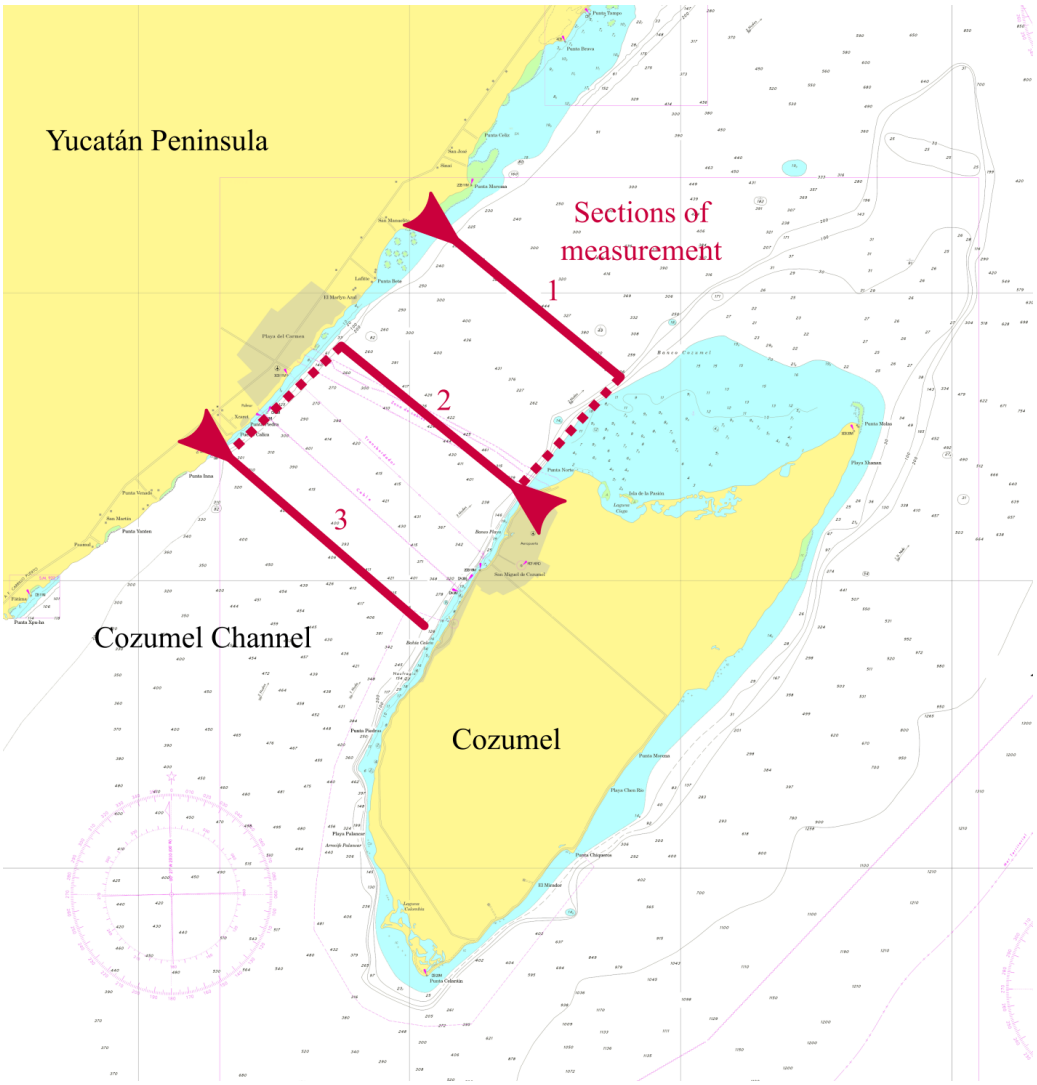

Figure 6.1: Sections of measurement within the the Cozumel Channel carried out during research expedition *CEMIE-1*, based on nautical chart S.M. 922 by Secretaria de Marina [99]. A solid red line indicates transects, while a dotted red line indicates the trajectory for connecting different transects.

6.1.4 ERA 5 Database

The ERA 5 database is based on reanalysis and provided by the European Centre for Medium-Range Weather Forecasts (ECMWF) [51]. At time of analysis, the data covered the complete earth from 1978 up to date and were later updated to include data from 1950 and later. The values are reported on an hourly basis and a grid with a spacial resolution of 0.25° for atmospheric and land-surface parameter (such as the wind) and 0.5° for (ocean) wave parameter.

6.1.5 HURDAT2 Database

The HURDAT2 database is a valuable resource for the analysis of tropical cyclones. The database is compiled by the National Hurricane Center (NHC) after the cyclone has passed, as real-time data may not be available for all aspects of the storm. The database is constantly updated and reevaluated with modern methodologies, particularly for older records. At time of analysis, the database contained data on all recorded tropical cyclones from 1851 up to date [64], including information such as the central pressure, position, intensity (i.e. wind speeds) and the storms' spacial extend. The data are recorded every six hours with interpolation performed for records earlier than 1956, for which raw data are only available on a 12-hour basis. Furthermore, newer records may contain asynoptic points to mark important events (e.g. landfall). It is important to note, that the database is not complete and does not contain all tropical cyclones occurred since 1851. The reporting stations and ships that provide data were limited in number in the early years, and satellite-based imagery was not available. Therefore, some events may be missing in the database or are not fully documented.

Studies have been performed to improve understanding of the uncertainty associated with hurricane detection in the years before 1965. These studies have suggested that the apparent increase in hurricane frequency in the HURDAT2 database may be partly due to increased detection capability [119]. The failure to detect some hurricanes, particularly those of category 4 and 5, can result in overestimation of the return period of hurricanes and underestimating the correct design wind speeds.

6.2 Estimation of Extreme Values

For estimating extreme values corresponding to a specific return period, the application of extreme value theory (EVT) is necessary. EVT can follow two different procedures: Counting extreme values in a certain time span (i.e. block), known as *Block Model*, or counting the extreme values above a certain threshold, known as *Threshold Model* or peaks-over-threshold (POT) [92, 46]. The block model is widely used for analyzing metocean data, where annual maxima, minima or averages are computed by selecting a block size of one year. However, it neglects the typical temporal spread of extreme events as only one value is picked, which can lead to biased results. For variables with temporal spread, the POT-model is a better choice, which establishes a threshold and considers all values above it [92]. The selection of a suitable threshold is crucial for the accuracy of the results.

Regardless of the chosen model, the obtained extreme values need to be fitted by a suitable distribution function. Distributions for normalized maxima can be of different types. Mallor et al. [69] suggest three different types:

Type I Gumbel distribution

Type II Fréchet distribution

Type III Weibull distribution

However, the choice of distribution should be based on the best fit of the data. The selected distribution is then used to estimate the value corresponding to a specific return period.

Besides those two widely adopted methods of the EVT, specific methods have been developed using the whole sample for predicting extreme values rather than just a selection of the sample. Various methods for evaluating extreme values are available in the relevant literature. For example, for extreme wind speeds due to hurricanes a specific methodology is presented below while for extreme wave heights a methodology is available in [17].

6.2.1 Peaks over Threshold

A general methodology for an extreme value analysis is the POT approach, which involves fitting an extreme model to all peaks above a certain threshold. Typically, a generalized Pareto distribution (GPD) is chosen as excess model. However, the selection of a suitable threshold has a significant influence on the results. In this methodology, an automated threshold selection method is used which was originally published by Thompson et al. [113]. This is to reduce the influence and possible bias of the person conducting the analysis. This methodology was modified and extended to suit the specific requirements of this work and is described in detail in Ring et al. [90]. The GPD used is defined following Liang et al. [67] by

$$F(x) = \begin{cases} 1 - \left(1 + \xi \frac{x-u}{\sigma}\right)^{-1/\xi} & \text{for } \xi \neq 0 \\ 1 - \exp\left(-\frac{x-u}{\sigma}\right) & \text{for } \xi = 0 \end{cases} \quad \text{, with } x \geq u \quad , \tag{6.1}$$

where x represents the random variable, u the threshold, ξ the shape parameter, and σ the scale parameter. Due to the temporal resolution of the time series, the data cannot be considered as truly random and the data is filtered with a moving time window. The window length is determined by a sensitivity study. To identify and eliminate outliers in the univariate dataset, the quartile method suggested by Laurikkala et al. [65] is applied. For identification of a suitable threshold, potential thresholds are equally spaced between the 25^{th} and 98^{th} percentile. For each of the potential thresholds, a reparameterized scale parameter and its difference to this value of the next higher threshold is determined. A normal distribution with zero mean is fitted through the determined differences, eliminating one difference after another, starting with the difference corresponding to the lowest potential threshold. As soon as the p-value corresponding to the normal distribution is above the significance level of 5%, this threshold is selected as suitable for the extreme value

analysis. More details and information regarding the estimation of the extreme values and the corresponding confidence intervals can be found in Ring et al. [90, chapter 2.3], which can also be found in appendix C.

6.2.2 Extreme Annual Wind Speeds due to Hurricanes

Extreme wind speeds result from low pressure centers such as storms, hurricanes, or typhoons, depending on the geographical region. The estimation of the wind speed due to hurricanes with a certain return period can be challenging as the number of hurricanes is typically too low for this type of analysis. However, taking certain assumptions for distributions makes it possible to reduce this to a relatively simple procedure which was suggested by Salvadori et al. [92]. The data required is the number of hurricanes (n_k, i.e. occurrences in the sample) within a certain time span of years (n, i.e. sample size). Furthermore, the mean wind speed ($\bar{X}$) and the coefficient of variation ($\widehat{V}$) need to be calculated for the sample. The mean rate of occurrence ($\hat{v}$) is then calculated by

$$\hat{v} = \frac{n_k}{n} \quad . \tag{6.2}$$

Assuming Pareto distributed wind speeds, the shape parameter (α) is defined by

$$\alpha = 1 + \sqrt{1 + \frac{1}{\widehat{V}^2}} \tag{6.3}$$

and the scale parameter (β) by

$$\beta = \frac{\bar{X}\,(\alpha - 1)}{\alpha} \quad . \tag{6.4}$$

The annual maximum wind speed is modeled with a Fréchet distribution, its parameters can be obtained from the Pareto distribution. The shape parameter (α) remains the same, while the scale parameter (β) should be adjusted according to

$$\beta' = \beta \hat{v}^{1/\alpha} \quad . \tag{6.5}$$

The Gumbel reduced variate (y_g) is defined as

$$y_g = -\ln\left[-\ln\left(1 - {\tau_B}^{-1}\right)\right] \quad , \tag{6.6}$$

where τ_B is the return period for which the wind speed is calculated. The quantile ($\hat{x}$) of the maximum annual wind speed corresponding to the return period (τ_B) is calculated by

$$\hat{x} = \beta' \exp\left(\frac{y_g}{\alpha}\right) \quad . \tag{6.7}$$

6.2.3 Expected Wave Frequency

Extreme waves are calculated regarding their wave height with the methodology described above. According to relevant literature and design codes such as DNV OS-J101 [26] and IEC 62600-2 [54], the wave period corresponding to the wave height is in the range of

$$11.1\sqrt{\frac{H}{g}} \leq T \leq 14.3\sqrt{\frac{H}{g}} \quad , \tag{6.8}$$

where H is the wave height and g the gravitational acceleration. Depending on the purpose of the calculation, the conservative wave period is chosen.

6.2.4 Spacial interpolation

Several methodologies are available for geo-spacial interpolation [75]. One commonly used method is the inverse distance weighted interpolation, which involves calculating the values at the surrounding nodes and weighing them according to their inverse distance and a specific power factor. Typically, this method considers 10 to 30 surrounding nodes and uses a power factor of 2 [75]. The depth (h_j) at the new point j is calculated by

$$h_j = \frac{\sum h_i \left(d_{i,j}\right)^{-p}}{\sum \left(d_{i,j}\right)^{-p}} \quad , \tag{6.9}$$

where $d_{i,j}$ denotes the Euclidean distance between the point j and node i, p the power factor, and h_i is the water depth at node i.

6.3 Meteorological and Oceanographic Data

The results of the extreme value analysis for the wind speed, significant wave height, and ocean currents are presented below. Furthermore, the bathymetry derived from the expedition data is described and values for storm surge, tides, and sea level rise are reported based on available literature.

6.3.1 Extreme Wind Speed

The extreme wind speeds are estimated based on the hurricanes found in this region and based on data provided by the HURDAT2 database. Additionally, the wind speeds at 10 m height, as they are reported by the ERA5 reanalysis model, are analyzed.

Hurricanes

Due to the geographical location, Cozumel Island and the Cozumel Channel are hit by hurricanes with significant severity. To analyze the hurricanes which have passed near Cozumel, the HURDAT2

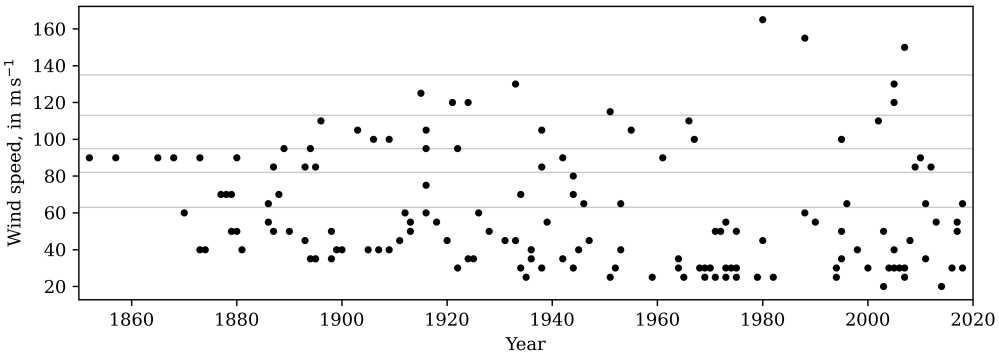

Figure 6.2: Storms and hurricanes considered for statistical analysis.

Table 6.1: Return periods of extreme wind speeds due to hurricanes.

Return period, in years	2	5	10	15	20	25	50	75	100
Wind speed, in m s^{-1}	22.63	32.53	41.37	47.38	52.09	56.04	70.20	80.02	87.79

database elaborated by the National Oceanic and Atomspheric Administration (NOAA) was used [64]. Hurricanes and tropical storms which passed the location within 2° with wind speeds $\geq 34\,\mathrm{kt}$ were considered in the analysis. The results of this analysis are shown in figure 6.2, where the horizontal lines delimit the threshold for the different categories of tropical depressions. The data reveals that in the early years, there were very few hurricanes, particularly those with higher wind speeds. As mentioned in section 6.1, this could potentially be attributed to the methods used for data acquisition during this period, which differs significantly from the methods employed nowadays. From 1851 to 2018, 1893 hurricanes were registered in the HURDAT2 database in the Atlantic basin, 152 of which passed close to Cozumel. The mean wind speed during passage was $30.511\,\mathrm{m\,s^{-1}}$ with a standard deviation of $16.290\,\mathrm{m\,s^{-1}}$. The rate of occurrence was estimated to 0.910 and shape and scale parameter to 3.123 and 20.742, respectively, resulting in an adjusted scale parameter of 20.127. More information on the parameters can be found in section 6.2.2. The obtained extreme wind speeds due to hurricanes for selected return periods are presented in table 6.1.

Wind at a Height of 10 meters

The numerical data are provided by the ERA5 reanalysis model were developed by the ECMWF. For the following analysis the node at N20.418° W87.114° was selected as it is the closest node to a potential site [1] for which both, wind and wave data exist.

The results of the study regarding the time window length can be seen in figure 6.3. The relative difference in figure 6.3 b) dips for the first time below the 5% mark at a time window length of 9 days, which is equivalent to 216 (numerical) observations. All identified peaks are shown in figure 6.4. Vertical lines indicate the occurrence of a hurricane within the distance of 2° with the color intensity related to the maximum wind speed. The horizontal dashed lines indicate

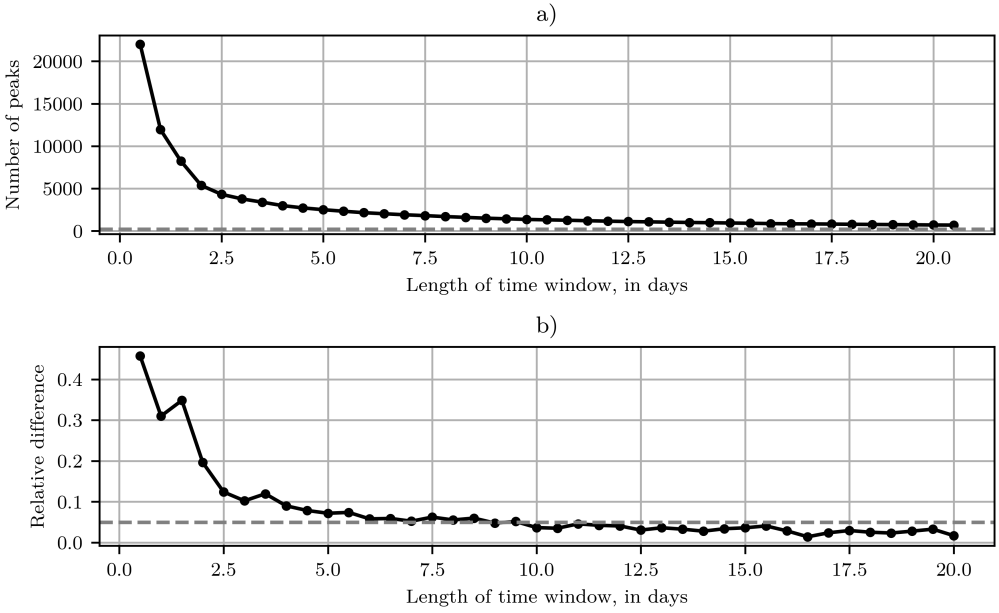

Figure 6.3: Study on time window length for filtering peaks of data on wind at 10 m height. **a)** Number of found peaks; **b)** Relative difference in number of found peaks to subsequent time window length.

the upper and lower limits for what is considered a legitimate peak and what is considered an outlier. However, the majority of possible outliers occur during hurricanes for which in this analysis outliers were not removed from the data set. The peaks appear to be fairly equally distributed in the domain, indicating that the time window of 9 days is sufficient to capture extreme events. A total of 1506 peaks were used for the study.

The threshold of $10.1379\,\mathrm{m\,s^{-1}}$ was found to be the most suitable, with a corresponding p-value of 0.0778 and 133 peaks exceeding this threshold. The shape parameter resulted to 0.4418 with the 95% confidence interval ranging from 0.138 to 0.745, indicating that the corresponding GPD excess model is unbounded [18]. The scale parameter was calculated to be 0.6659. The diagnostic plots presented in figure 6.5 show some deviations between the excess model and empirical data, particularly in the p-p plot (figure 6.5 a)) and the q-q plot (figure 6.5 b)). The p-p plot shows that the excess model overestimates lower values and underestimates higher values. The q-q plot indicates that the most rare peaks are underestimated by the excess model. However, the return-level plot (figure 6.5 c)) shows that 98.5% of the peaks lie within the estimated 95%-confidence interval (CI) of the return level, suggesting that the excess model is a good fit to the data. For some specific return periods the corresponding extreme wind speeds are presented in table 6.2.

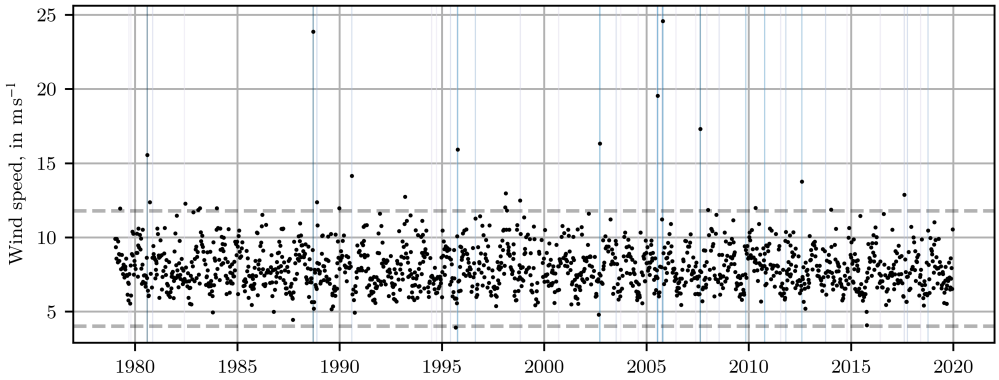

Figure 6.4: Identified peaks, together with the limits between peaks and outliers (horizontal lines) and occurrences of hurricanes (vertical lines).

Table 6.2: Return levels of extreme wind speeds at height of 10 m.

Return period, in years	Extreme wind speed, in $m\,s^{-1}$	95% CI, in $m\,s^{-1}$
0.50	10.497	10.170 . . . 10.824
1.00	11.166	10.404 . . . 11.927
2.00	12.074	10.880 . . . 13.268
3.00	12.749	11.321 . . . 14.178
4.00	13.308	11.723 . . . 14.892
5.00	13.792	12.093 . . . 15.492
10.00	15.642	13.569 . . . 17.715
15.00	17.017	14.618 . . . 19.417
20.00	18.154	15.389 . . . 20.918
25.00	19.141	15.972 . . . 22.309
30.00	20.022	16.421 . . . 23.623
40.00	21.566	17.055 . . . 26.077
50.00	22.906	17.464 . . . 28.349
75.00	25.707	17.963 . . . 33.451
100.00	28.022	18.076 . . . 37.967

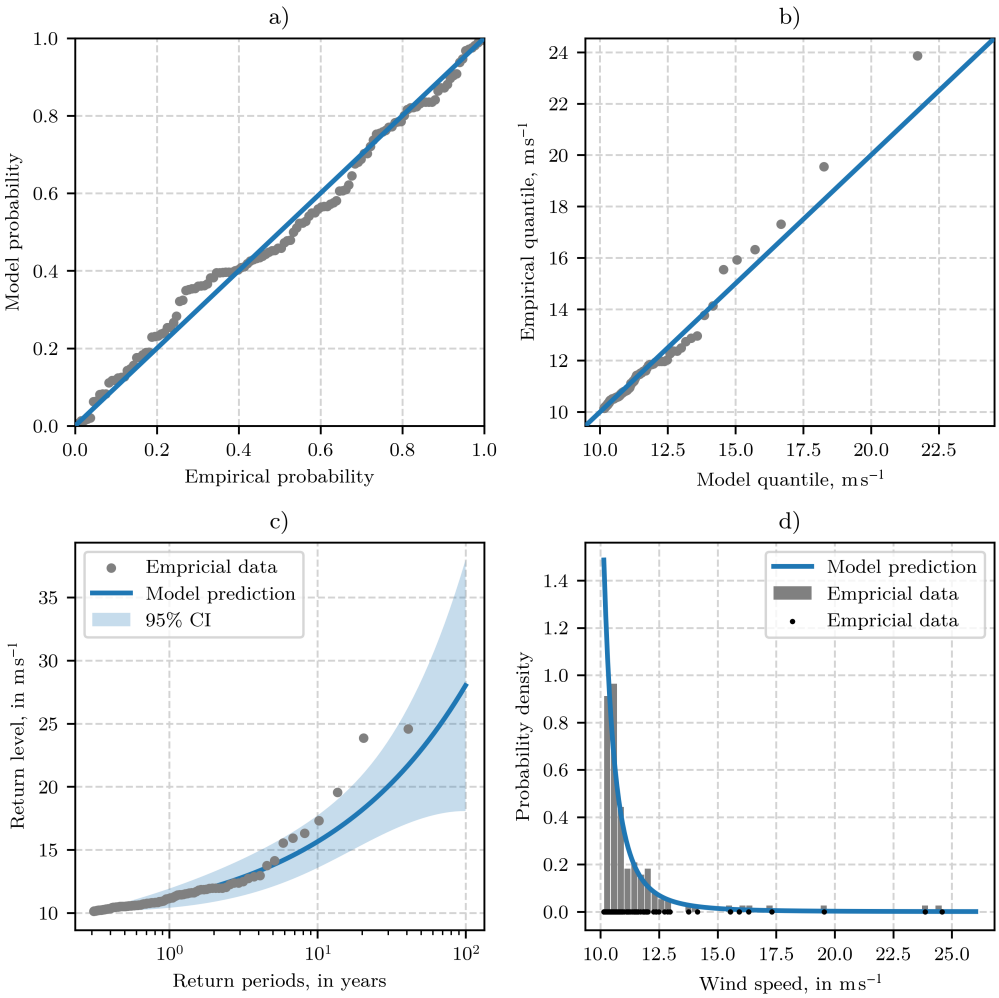

Figure 6.5: Diagnostic plots for the GPD excess model fit. **a)** p-p plot; **b)** q-q plot; **c)** return level plot; **d)** density plot.

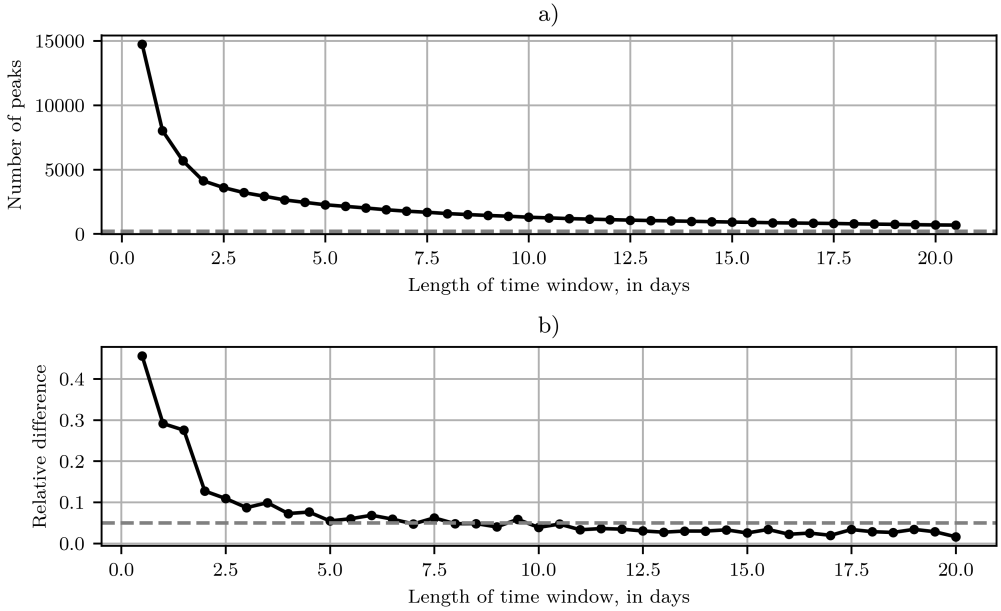

Figure 6.6: Study on time window length for filtering peaks of data on significant wave height. **a)** Number of found peaks; **b)** Relative difference in number of found peaks to subsequent time window length.

6.3.2 Significant Wave height

The data provided by the ERA5 reanalysis model, developed by the ECMWF describe the hourly significant wave height of combined wind sea and swell. For the analysis, the same node as for the analysis of the wind (N20.418° W87.114°) was selected as it is the closest node to a possible site identified by Alcérreca-Huerta et al. [1].

The results of the study regarding the time window length are shown in figure 6.6. The figure reveals that the relative difference in figure 6.6 b) dips for the first time below the 5% mark at a time window length of 7 days, corresponding to 168 (numerical) observations. The resulting peaks are shown with black dots in figure 6.7. The upper and lower limits for what is considered a legitimate peak and what is considered an outlier are represented by horizontal dashed gray lines. The thin vertical lines indicate hurricanes which passed the node within a radius of 2°, where the color intensity represents the maximum wave height was during the passage of the hurricane. Similarly to the analysis of the wind at a height of 10 m, many of the peaks which would be considered as outliers correlate with the occurrence of hurricanes, wherefore no peak was filtered out for this study. All 1760 peaks are well distributed, suggesting that the time window length of 7 days is suitable for this analysis.

Following the methodology described in section 6.2, the most suitable threshold was estimated to 1.5189 m with a corresponding p-value of 0.0576 and 179 peaks above the threshold. The shape parameter resulted to 0.3817 with the 95% confidence interval ranging from 0.065 to 0.698, resulting

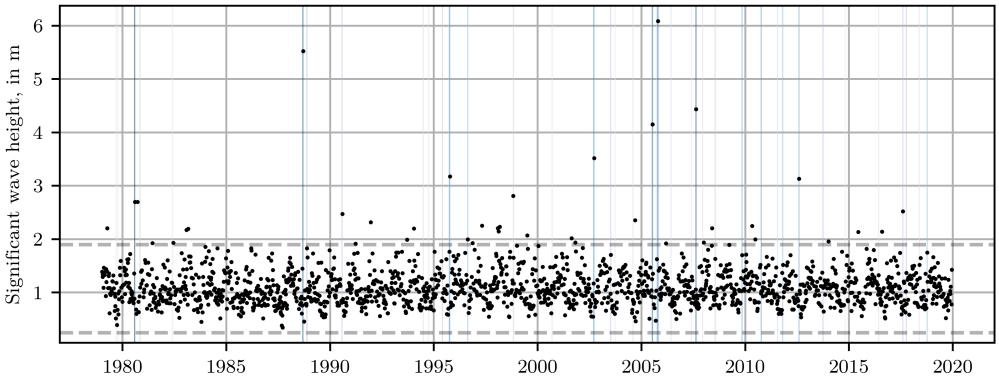

Figure 6.7: Identified peaks of significant wave height together with the limits between peaks and outliers (horizontal lines) and close hurricanes (vertical lines).

in an unbound excess model [18]. The scale parameter was calculated to be 0.2023. The p-p plot shown in figure 6.8 a) has a z-shaped deviation. This results in overestimating low values and underestimating higher values, particularly for the most extreme values the q-q plot in figure 6.8 b) supports these findings. With 98.3% the vast majority of the peaks are withing the estimated 95%-CI of the return level (see figure 6.8 c)). Despite the differences, the excess model is a good fit for the numerical data. For selected return periods the corresponding extreme significant wave heights are presented in table 6.3.

6.3.3 Currents

The data on the current are taken from the HYCOM and evaluated at N20.40° and W87.12°, the closest node to the data on wind and wave as provided by the ERA5-reanalysis model of the ECMWF. The current was examined at the surface and at a depth of 50 m. Characteristic values for the currents at the sea bed are provided by Flores [40], who suggests $v_{bot} = 0.3\,\mathrm{m\,s^{-1}} \ldots 0.4\,\mathrm{m\,s^{-1}}$. The overall prevailing current direction is NNE with a share of 94%, while they stay 96% in the direction between N and NE as stated by Flores [40]. For the specific node analyzed, the HYCOM model predicts the surface current mostly in eastern direction as can be seen in figure 6.9 a). The current at a depth of 50 m (see figure 6.9 b)) is also closely confined, but appears to be dependent on the current speed. For lower current speeds, the current has a heading of east-northeast, while for higher currents, it has a higher eastward component.

Currents at Surface

The study on the time window length for peak identification shows the same behavior as wind and waves (see figure 6.10). The relative difference constantly decreases as shown in figure 6.10 (b) and falls for the first time below the 5% mark at a time window length of 8 days, equivalent to 64 (numerical) observations. The resulting peaks are shown with black dots in figure 6.11 while

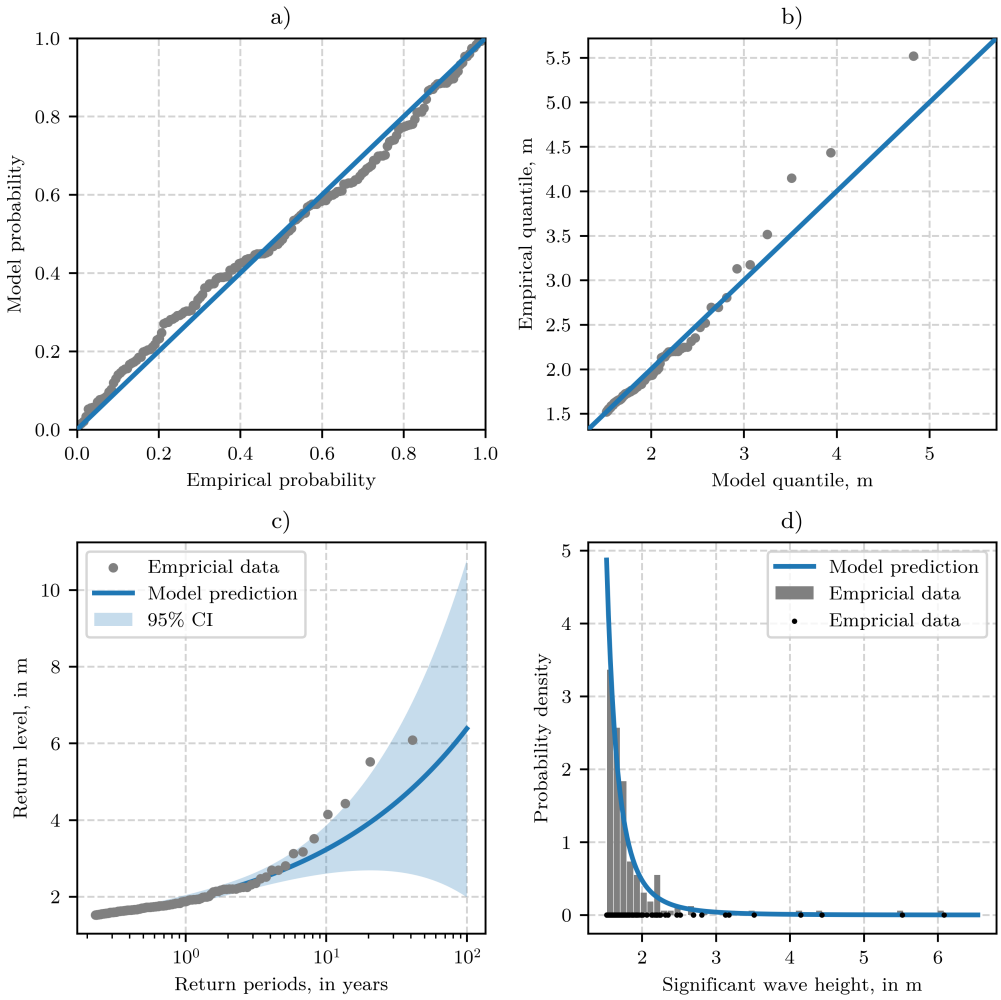

Figure 6.8: Diagnostic plots for the GPD excess model fit to the significant wave height. **a)** p-p plot; **b)** q-q plot; **c)** return level plot; **d)** density plot.

Table 6.3: Return levels of extreme significant wave height.

Return period, in years	Extreme significant wave height, in m	95%-CI, in m
0.25	1.537	1.507 ... 1.567
0.50	1.703	1.624 ... 1.782
1.00	1.919	1.797 ... 2.041
2.00	2.201	2.045 ... 2.357
3.00	2.404	2.209 ... 2.599
4.00	2.568	2.321 ... 2.814
5.00	2.708	2.402 ... 3.014
10.00	3.229	2.602 ... 3.856
15.00	3.604	2.669 ... 4.539
20.00	3.907	2.687 ... 5.128
25.00	4.167	2.680 ... 5.653
30.00	4.396	2.658 ... 6.133
40.00	4.791	2.590 ... 6.992
50.00	5.129	2.503 ... 7.755
75.00	5.822	2.253 ... 9.391
100.00	6.383	1.988 ... 10.778

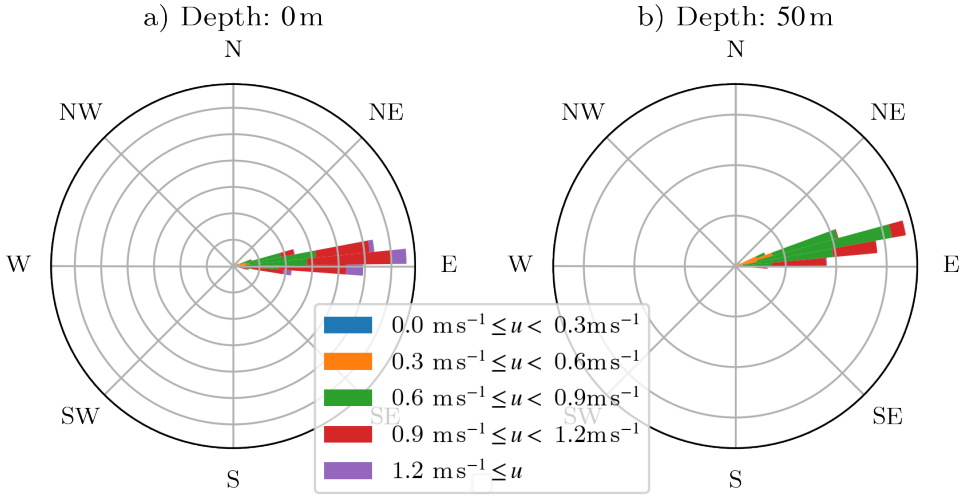

Figure 6.9: Histogram of current as modeled with HYCOM. **a)** Current at the water surface; **b)** Current at a depth of 50 m. Both values for the node at N20.40° and W87.12°.

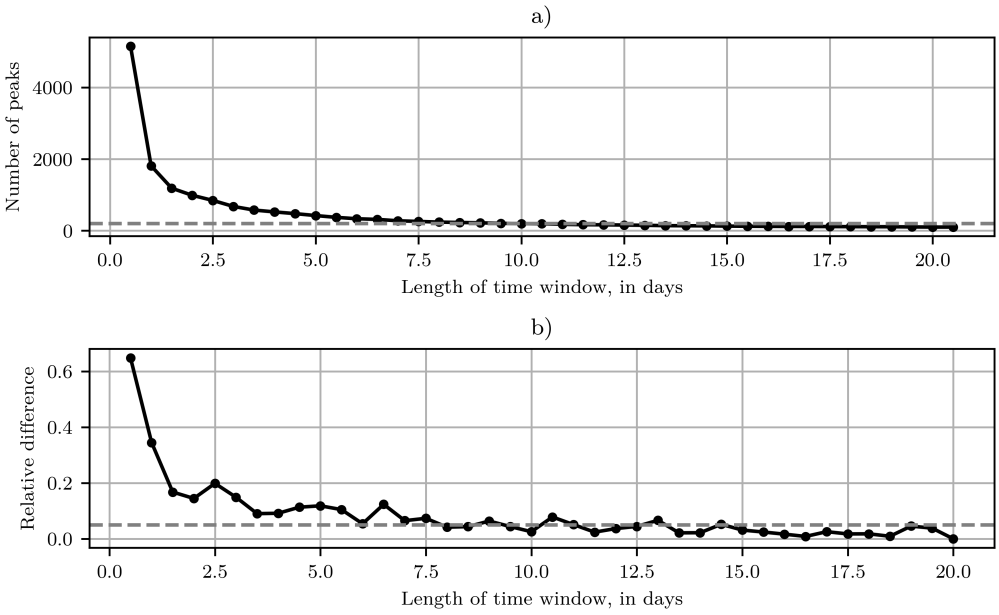

Figure 6.10: Study on time window length for filtering peaks of data on current speed at surface. **(a)** Number of found peaks **(b)** Relative difference in number of found peaks to subsequent time window length.

the red dots indicate outliers which have been filtered out. The upper and lower limits for what is considered a legitimate peak and what is considered an outlier are represented by horizontal dashed gray lines. The thin vertical lines indicate hurricanes which passed the node within a radius of 2°. The more intense their color is, the greater their maximum wind speed was during their passage. In contrast to wind and wave, only a few outliers correlate with the occurrence of hurricanes for which the outliers were filtered out at this node. In total 736 peaks were found with 9 outliers above the upper threshold and 3 outliers below the lower threshold. The distribution of the peaks appears to be random for which the time window length of 8 days is considered as adequate.

The best threshold was estimated to $1.1519\,\mathrm{m\,s^{-1}}$ with a p-value of 0.0520, resulting in 379 peaks over threshold. The corresponding shape parameter is -0.4044 with its 95 %-CI between -0.519 and -0.290. Due to the negative CI of the shape parameter it is safe to assume that a bound excess model is the best fit [18]. The scale parameter was calculated to 0.2080. Following the p-p plot in figure 6.12 a), the excess model resembles the numerical observations quite good, with a slight overestimation of the values at the lower end, also visible in the density plot (see figure 6.12 d)). At the upper end, the model deviates from the empirical data, as can be seen in figure 6.12 b) and c). Nevertheless all peaks are within the 95 %-CI. For some specific return periods the corresponding extreme significant wave heights are presented in table 6.4.

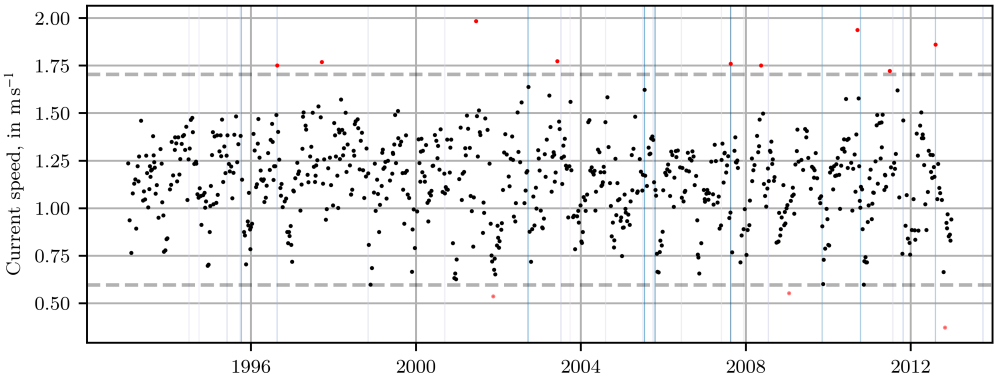

Figure 6.11: Identified peaks of current speed at surface together with the limits between peaks and outliers (horizontal lines) and close hurricanes (vertical lines).

Table 6.4: Return levels of extreme current speed at surface.

Return period, in years	Extreme significant wave height, in m	95%-CI, in m
0.25	1.392	1.269 ... 1.515
0.50	1.459	1.310 ... 1.608
1.00	1.510	1.345 ... 1.674
2.00	1.548	1.375 ... 1.721
3.00	1.566	1.389 ... 1.742
4.00	1.577	1.399 ... 1.755
5.00	1.585	1.406 ... 1.763
10.00	1.604	1.424 ... 1.785
15.00	1.614	1.433 ... 1.794
20.00	1.620	1.439 ... 1.800
25.00	1.624	1.444 ... 1.804
30.00	1.627	1.447 ... 1.806
40.00	1.631	1.451 ... 1.810
50.00	1.634	1.455 ... 1.813
75.00	1.639	1.460 ... 1.817
100.00	1.642	1.464 ... 1.820

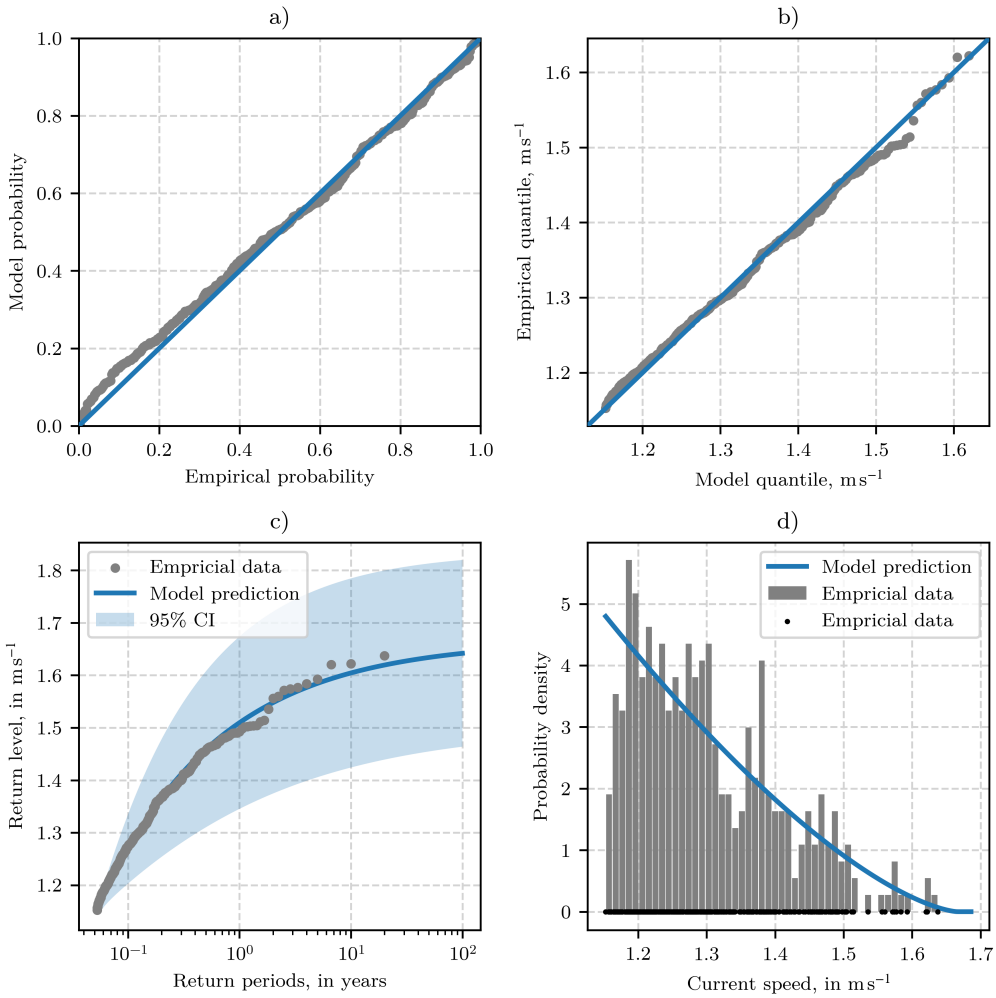

Figure 6.12: Diagnostic plots for the GPD excess model fit to the current speed at surface. **a)** p-p plot; **b)** q-q plot; **c)** return level plot; **d)** density plot.

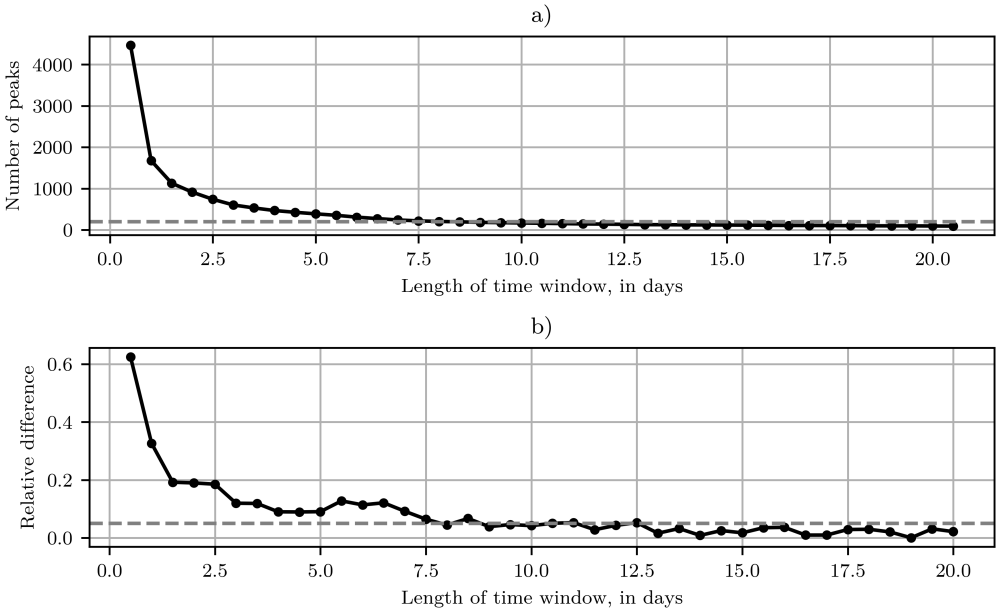

Figure 6.13: Study on time window length for filtering peaks of data on current speed at a depth of 50 m. **a)** Number of found peaks; **b)** Relative difference in number of found peaks to subsequent time window length.

Currents at a Depth of 50 meters

For the currents at a depth of 50 m, the study on the time window length is depicted in figure 6.13. As expected, the optimum window length is 8 days. The relative difference between a time window length at the subsequent one (see figure 6.13 b)) decreases with minor fluctuations. As illustrated in figure 6.14, only 3 outliers were found at the upper end and one at the lower end. Given the fact, that only one of those three outliers coincides with the occurrence of a hurricane, all outliers were filtered out. Hurricanes which passed at a distance of no more than 2° are marked with vertical lines with the color intensity representing the hurricane's maximum wind speed during the passage. At the depth of 50 m, 694 peaks were found which seem to be randomly distributed in the domain.

A suitable threshold was calculated to $0.9823\,\mathrm{m\,s^{-1}}$ with a p-value of 0.0527, resulting in 250 peaks. The shape parameter and its 95 %-CI was estimated to -0.3730 and -0.460 to -0.286, respectively, indicating a bound excess model similarly to surface currents. The corresponding scale parameter is 0.1542. The diagnostic plots in figure 6.15 show a good fit, although higher values are slightly overestimated by the excess model (see figure 6.15 b) and c)). All peaks were found within the estimated 95 percent-CI of the return level. For some specific return periods the corresponding extreme currents speeds are presented in table 6.5.

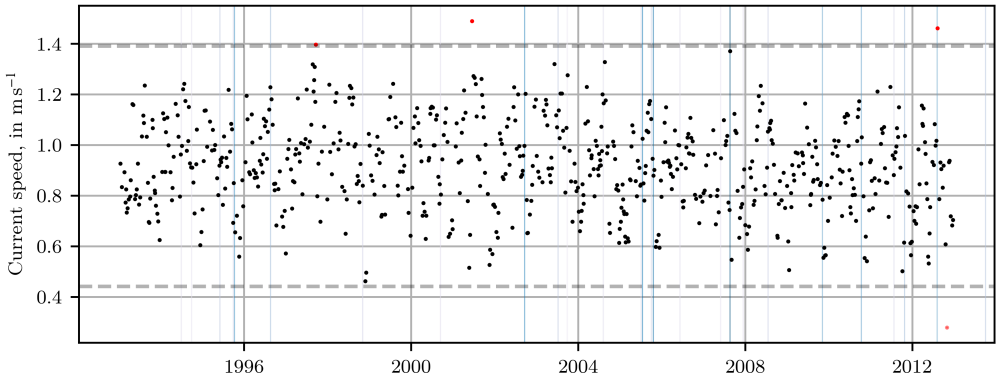

Figure 6.14: Identified peaks of current speed at a depth of 50 m together with the limits between peaks and outliers (horizontal lines), close hurricanes (vertical lines) and outliers (red dots).

Table 6.5: Return levels of extreme current speed at a depth of 50 m.

Return period, in years	Extreme current speed, in m s^{-1}	95%-CI, in m
0.25	1.125	1.039 ... 1.212
0.50	1.187	1.069 ... 1.305
1.00	1.235	1.095 ... 1.374
2.00	1.271	1.117 ... 1.426
3.00	1.289	1.128 ... 1.449
4.00	1.300	1.136 ... 1.464
5.00	1.307	1.141 ... 1.474
10.00	1.327	1.156 ... 1.499
15.00	1.337	1.163 ... 1.511
20.00	1.343	1.168 ... 1.518
25.00	1.347	1.172 ... 1.523
30.00	1.350	1.174 ... 1.527
40.00	1.355	1.178 ... 1.532
50.00	1.358	1.181 ... 1.535
75.00	1.364	1.186 ... 1.541
100.00	1.367	1.189 ... 1.544

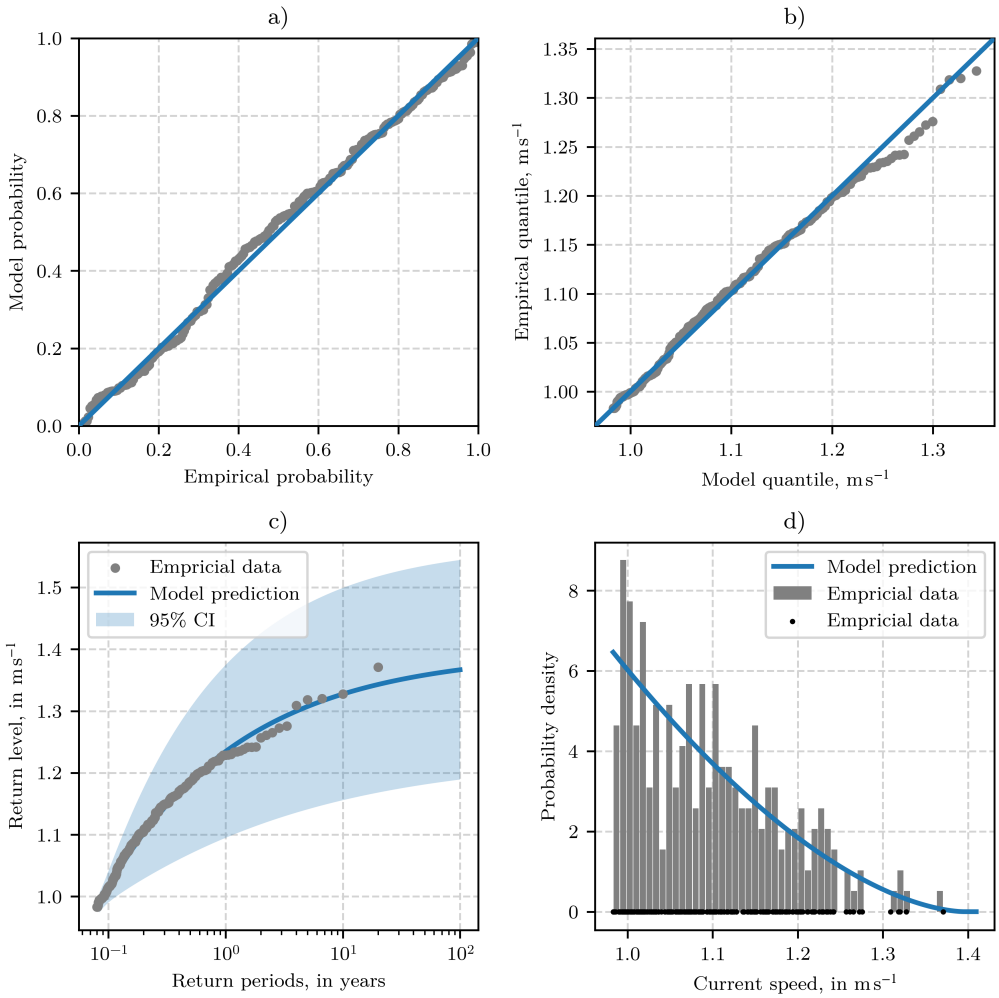

Figure 6.15: Diagnostic plots for the GPD excess model fit to the current speed at a depth of 50 m. **a)** p-p plot; **b)** q-q plot; **c)** return level plot; **d)** density plot.

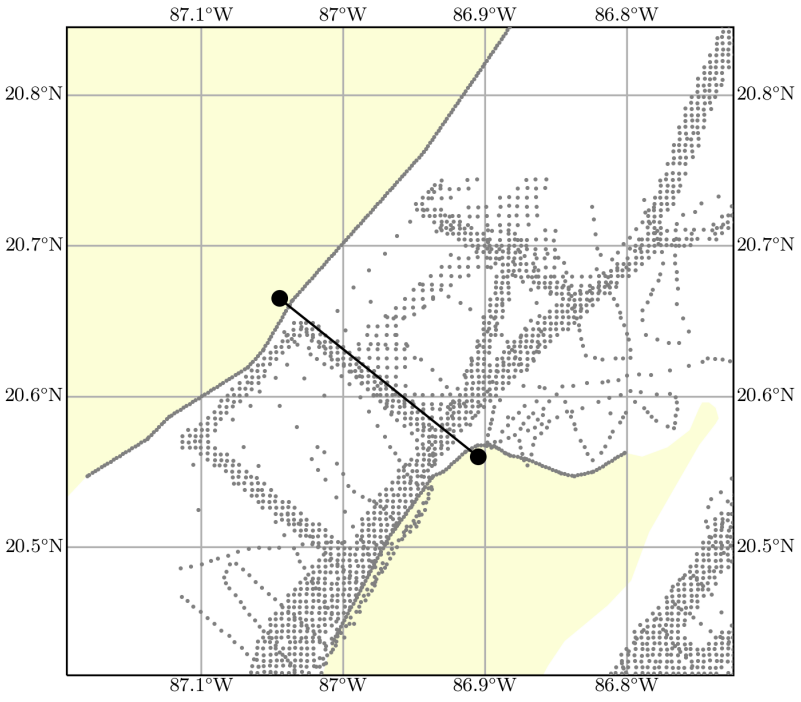

Figure 6.16: Position of the used transect in the Cozumel Channel and the position of data points used for interpolation.

6.3.4 Bathymetry

The position of the transects is shown in figure 6.16. It starts on the mainland coast close to *Plaza del Carmen* and ends near *Punta Norte* on Cozumel Island. The gray dots indicate the data points which have been used for interpolation. They result from measurements taken during the expedition CEMIE-O 1 in 2019, from the nautical chart 922-004 published by the Mexican Navy, and NaturalEarth in case of the coast line. After interpolation with the inverse distance weighted interpolation (IDW) method, the depth has been filtered with a Savitzky–Golay filter in order to eliminate strong fluctuations. The results are shown in figure 6.17. The Cozumel Channel shows a pronounced valley with a relatively flat plain at approximately 450 m of depth. The valley is delimited by steep slopes on either side, with an inclination ranging between 5 and 10 degrees and with peaks over 20 degrees. Although the wide valley in the center of the channel provides space for a lot of turbines, the slopes are interesting for installation as they significantly reduce the length of the mooring lines and the required length of subsea cables. During early phases of harnessing the Cozumel Current, it is expected that turbines are installed at the slopes of the Channel in much

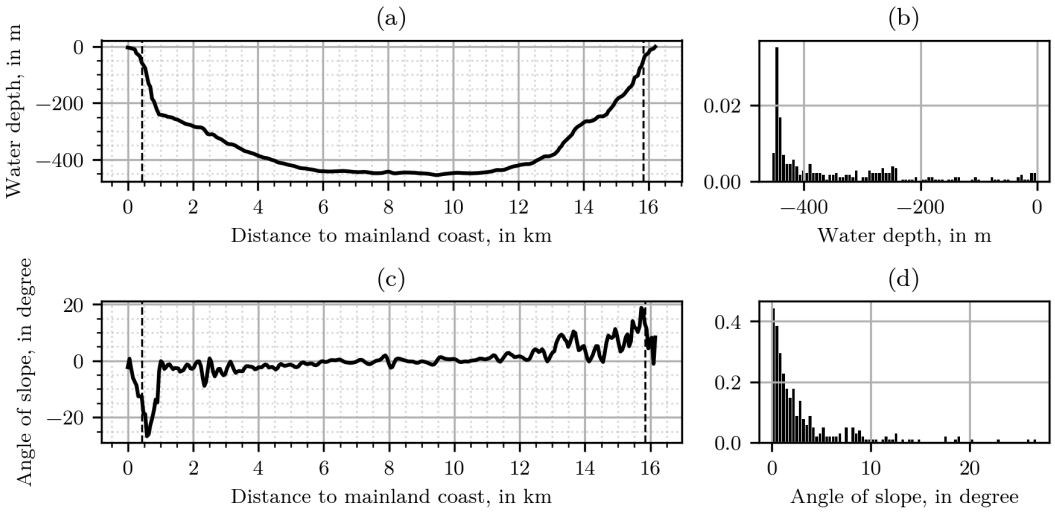

Figure 6.17: Bathymetry of the transect in the Cozumel Channel with the black, dashed lines indicating the positions with depths of 50 m. **a)** Water depth,; **b)** Density distribution of water depth; **c)** Angle of the slope; **d)** Density distribution of absolute angle of the slope.

shallower waters and closer to the coast.

6.3.5 Storm Surge

No exact data are available on the storm surge, however, observations during the passage of Hurricane Gilbert in 1988 suggest that the storm surge may vary between 3 m and 6 m for the coast of *Quintana Roo*, including the Cozumel Channel [10]. Thus, the maximum storm surge can be considered with 6 m due to a hurricane with return period of 125 years.

6.3.6 Tides

The tidal range is generally consistent throughout the Caribbean. On the Mexican coast, a mixed mainly semidiurnal tide is encountered with an astronomical tidal range of approximately 20 cm to 30 cm. [61, 62]. This prediction is based on harmonic amplitudes and epochs for six tidal constituents. Comprehensive data is available from measurements by the *Servicio Meteorológico Nacional* (*Mexican* National Weather Service) at a site near Puerto Morelos (N20°52′6″, W86°52′) and Cozumel (N20°31′37.2″, W86°56′24.6″) [105].

6.3.7 Sea Level Rise

The study conducted by Ruiz-Ramírez et al. [91] reported a sea level rise of 2.8 mm y^{-1} for the entire coast in the Mexican Caribbean between 1993 and 2015. However, more regional estimates were obtained for two specific locations during the same period. The sea level rise in *Puerto Morelos*

was found to be $0.6\,\mathrm{mm\,y^{-1}}$, while *Isla Cozumel* experienced a sea level rise of $1.0\,\mathrm{mm\,y^{-1}}$.

6.4 Geological and Geotechnical Data

The site of interest has not been subject to comprehensive geological or geotechnical surveys, but previous studies have explored the geology of Cozumel, the Mexican Caribbean, and the Gulf of Mexico.

The upper most layer or the layer immediately below the ground surface across the entire Island of Cozumel can be characterized as *Caliche II* crust, according to the findings of Spaw [106]. Since slopes generally transport sediment from higher to lower regions in the oceans [98], the upper most layer in the pronounced slope at the eastward side of the Cozumel Channel can be expected to have similar sediments to these on the coast of Cozumel Island. Although marine sediments are similar to land based sediments, there are a few difference such as the pore water presenting a higher saturation of dissolved gases. According to Schwab et al. [98], the sediments found in the Gulf of Mexico and the western Caribbean is mainly Carbonate Ooze with skeleton remains greater than 30%, while close to Cozumel Island terrigenous sediment can be expected. An extensive study on the modern sediments in the Gulf of Mexico has been performed by Balsam and Beeson [7] analyzing 186 top core and grab samples, a lot of which were located on the shelf north of the Yucatán Peninsula and the Campeche Bank which is in the wake of the Yucatan Straight. According to the findings, the sediment on the shelves near Yucatán is mainly composed of calcareous sands while the sediment on the slopes can be mainly classified as carbonate mud (micrite). Inspection of the reefs around the southern part of Cozumel Island, showed the sea floor being covered in calcareous sediment, coarse sand, and coral debris, which eventually will be transported down the insular slope [77]. Gischler and Lomando [44] studied reefs south of Cozumel Island, which are composed of grainstone, wackestone and packstone. Similar to the reefs in the northern region of the mainland of Belize, Tertiary and Quaternary limestones are present. The foundation of the reefs in this region was reported to be limestone, according to Purdy [87], Mazzullo et al. [70], and Shinn et al. [103]. For the Elmer Reef in the north of Belize, limestone was found 1.6 m below the reef's top, with coral framestone, partially lithified gravelly sands, and unconsolidated sediments on top of the limestone [70]. Measurements of samples of limestone taken at the main land close to Cozumel have been conducted by Santiago Sierra [94], reporting density, unconfined compressive strength, and Young's modulus. A work based on measurements to relate tensile strength to the compressive strength of limestone has been done by Nazir et al. [80] and is defined by

$$q_{t,r} = \left(\frac{q_{u,r}}{9.25}\right)^{1/0.947} \tag{6.10}$$

.

The limestone in the region of the Yucatan Channel has a density of $2110.2\,\mathrm{kg\,m^{-3}}$, a uniaxial unconfined compressive strength of 27.73 MPa, and a minimum Young's modulus of 4.3185 GPa [94]. The coefficient of subgrade reaction can be assumed to be $80\,\mathrm{MN\,m^{-3}}$ [8].

Chapter 7

System Design

The design of the position keeping system for a MCEC is performed mainly via an automated optimization process based on the genetic algorithm described in chapter 5. To ensure efficacy, it is important to start with a sound design concept. The choices behind the design concepts used and the considerations made during this process are discussed in this chapter.

7.1 General Design Considerations

For submerged mooring systems, design of platform and mooring system are strongly coupled. A decision made for one will inevitably impact the other's optimum. To systematically evaluate the options, the design process is separated into the following sub-problems:

- Height-control system
- Rotor alignment
- Buoyancy providing system
- Elevation system for maintenance purpose
- Mooring line configuration

Those problems will be addressed separately in the following although some solutions will overlap an consequently solve more than one design problem. Other solutions depend on the choices taken for another problem, as e.g. the elevation system depends on the mooring configuration.

7.1.1 Height-control system

The height-control system mainly controls the vertical position of the platform within the water column. Maintaining a constant depth of the system despite environmental changes is important for ensuring productivity and safety of the system. In the upper section of the water column, wind

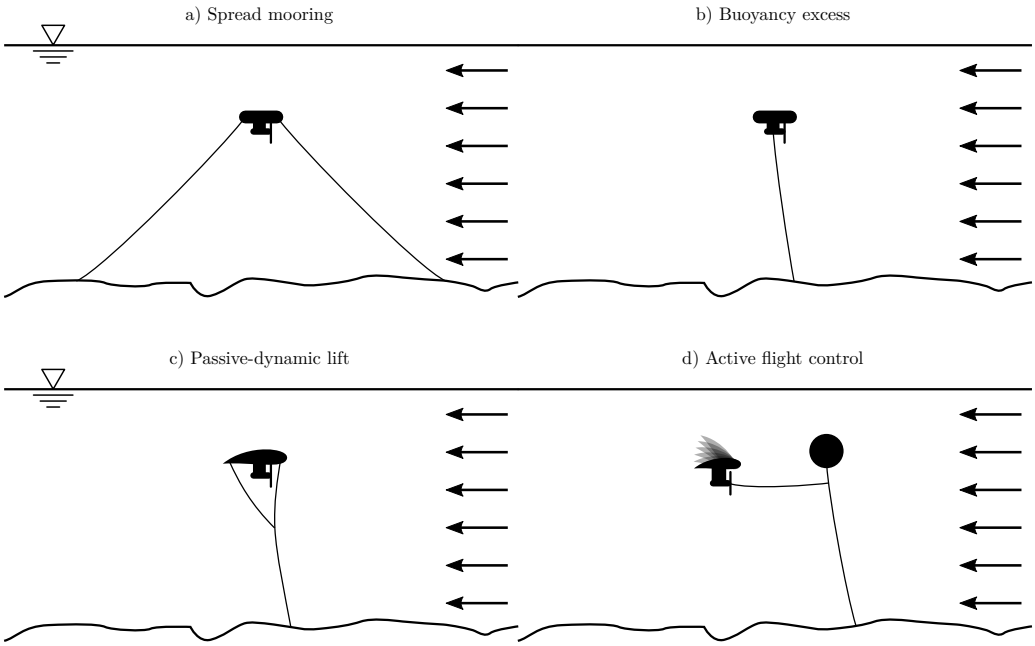

Figure 7.1: Concepts for height control systems.

and wave induced currents might have a significant impact on the conditions. Accurate knowledge of the design depth and its variability over the lifespan is also necessary for designing pressurized compartments and estimating the fatigue life of various components. In figure 7.1 various systems to control the platform's height are shown, which are discussed below.

Multiple Mooring Lines One straightforward and mechanically simple approach for maintaining a constant platform height above seabed, or depth below surface, is a mooring system with multiple lines as depicted in figure 7.1 a). In this configuration, a slight excess of buoyancy causes the platform to rise towards the surface, while a minimum of two mooring lines prevent the system from floating upwards. The system's buoyancy is enough to maintain all mooring lines under tension, even in the most severe load cases, ensuring the platform maintains a constant height regardless of the load conditions.

Excess of Buoyancy Another simple approach is a system that utilizes a single mooring line with an excess of buoyancy, illustrated figure 7.1 b). In this system, horizontal and vertical movements are coupled, as the platform's possible positions are roughly situated on the surface of a sphere surrounding the anchor point. Therefore, the tension in the mooring line controls both horizontal and vertical movements. To significantly reduce the mooring offset and maintain the platform's position, even in the severe conditions, a substantial excess in buoyancy is required.

Passive Lift Control An elegant, yet slightly more complex solution involves using integrated foils in the platform's structure with a single mooring line, as shown in figure 7.1 c). With a slight

buoyancy excess, the platform can maintain its position during low or no loads. During high-load phases, the position can be regulated using the dynamic lift of the foil-shaped members of the platform. Under loading, the surfaces contributing to the dynamic lift increase the tension in the mooring line due to the increased flow. Furthermore, a reduction in the pitch of the platform (nose up) generates more lift which further reduce the mooring offset. It is crucial to ensure that the pitch angle is decreased to prevent downforce, which could push the platform towards the sea floor. A significant change in the pitch angle could also lead to performance loss in the turbine.

Active Lift Control/Flight-Control System Alternatively to the passive-dynamic lift, an active flight control system could be used as depicted in figure 7.1 d). This approach requires a nearly neutrally buoyant platform and a mechanism for adjusting the platform's static buoyancy or dynamic lift. Since the platform is nearly neutrally buoyant, the flight control system only needs to counteract environmental forces. If the leading mooring line is sufficiently long, surfacing the platform for maintenance would be a simple task. However, the active control requires more moving parts, which reduces the overall system reliability. Additionally, the mooring radius is highly dependent on the length of the leading mooring line. Like all systems with a single mooring line, the lack of redundancy in the mooring line and anchor poses a risk and requires greater safety factors.

7.1.2 Rotor Alignment

As this system is designed for a horizontal-axis turbine, it should be installed with its rotational axis parallel to the current, resulting in the current passing through the rotor area perpendicularly. In the industry, two configurations are commonly used for horizontal turbines. The first configuration places the rotor *upwind* of the rotor's body and is more prevalent, particularly in the wind industry. The second configuration can sometimes be observed on pod drives of large ships, which require high maneuverability, or in concept studies for newer wind turbines.

Upstream Upstream turbines position the rotor ahead of the turbine's body and are the most common among wind and ocean current turbines. This configuration has the advantage of providing undisturbed flow to the rotor. However, the platform, or at least parts of it, is subject to cyclic loading due to the rotor wake. In wind turbines, this phenomenon is often referred to as rotor shedding, as the frequency of loading on each member depends on rotational frequency, number of blades, and the number of elements in the turbine's wake. Blades have a relatively low flexural stiffness, which leads to high deflections under great load. Depending on the distances between the platform and the rotor plane, the blade's tips might get close to the platform, further increasing the cyclic loads and the risk of damage due to tip vortex cavitation.

Downstream Especially the problem with reduced distance due to flex of the blades can be avoided by placing the rotor plane downstream. For wind and marine currents, downstream turbines are rather rare, yet are very common for ship propulsion systems. Just as the platform has to operate

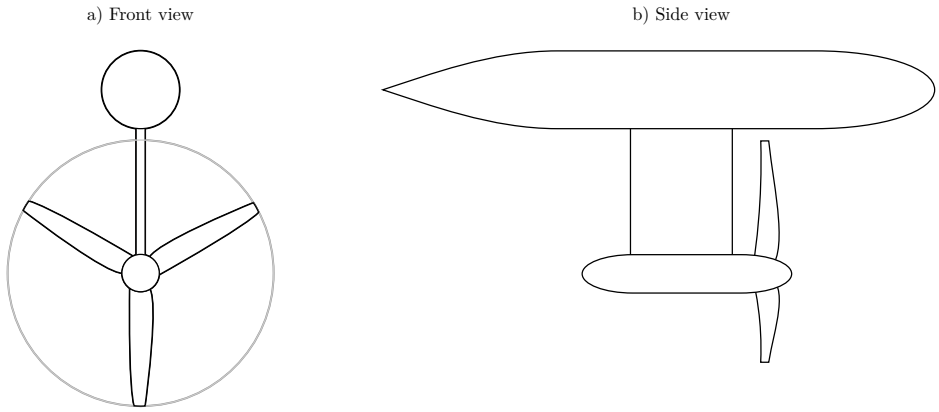

Figure 7.2: Possible arrangement for a single hull system with hull above turbine. **a)** Front view; **b)** Side view.

in the rotors wake on upstream turbines, downstream turbines place the rotor in the wake of the turbine housing and its struts. Depending on the design of the platform, this results in a highly unsteady inflow, potentially increasing vibration and noise, cyclic loading, and the possibility for cavitation of the turbine blades. The produced noise or vibration is a result of the cyclic loading due to circumferential speed gradients in the current field. Its frequency depends directly on the number of struts, the number of blades and the rotor's rotational frequency and can hardly be modified during operation. Special care has to be taken on the structural blade design and the control mechanism to avoid resonance or to block certain rotational frequencies by the control system of the turbine if it results impossible to avoid resonance.

7.1.3 Buoyancy Providing System

Since the turbine itself is not neutrally buoyant, the platform must provide the required buoyancy. This is typically accomplished through hydrodynamically shaped floaters or hulls that are integrated into the platform's structure. Various formulae have been developed to create streamlined underwater bodies, such as torpedoes or autonomous underwater vehicle (AUV)s, which will be discussed later. However, one mayor question is the number and geometrical arrangement of the hulls within the platform's structure. While the number of hulls can principally be infinite, more than three hulls might not significantly improve the platform's properties, reducing the possibilities to one, two, or three hulls. Furthermore, they should be arranged symmetrically (with respect to the x-z plane) with their main axis parallel to the current's flow to reduce drag. These constraints limit the number of options to only a few, which are discussed below. Nonetheless, several parameters, such as the hull's relative position in forward (x), sideways (y), and vertical (z) directions can still be modified, to suit the project's specific requirements.

Single Hull To satisfy the symmetry, the single hull should be placed either above or below the turbine, symmetrically placed in the x-z plane of the rotor as depicted in figure 7.2. A mayor

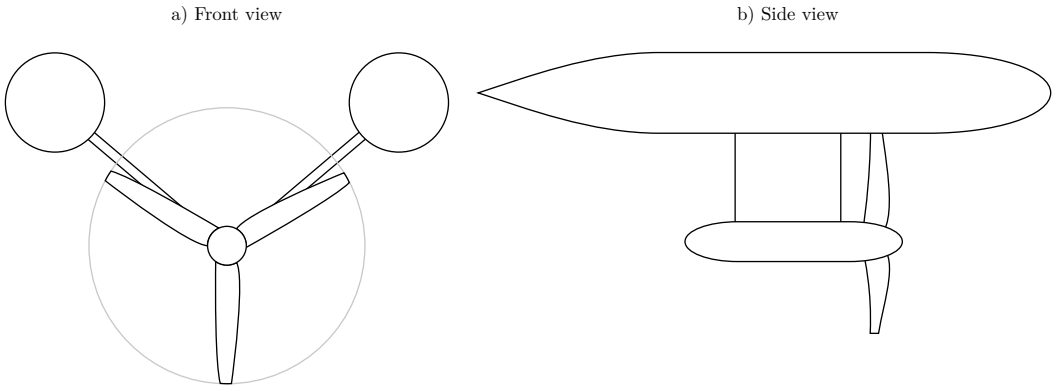

Figure 7.3: Possible arrangement for a double hull system with hull above turbine. **a)** Front view; **b)** Side view.

problem with this arrangement is that it does not provide a restoring moment through the mooring line, causing the platform to tilt to either the starboard or port side. As a result, the orientation of the platform becomes less well-defined, making difficult to predict loads on the entire system.

Double Hull A double hull system is a better choice in terms of providing a restoring moment via the mooring lines. In this arrangement, the hulls are placed at an equal height and an equal distance from the x-z plane, as shown in figure 7.3. Compared to single hull systems, the double hull system allows for greater freedom in positioning the hulls, making it easier to avoid the rotor's swept area. Additionally, maintenance at the surface is made easier as the platform's roll is reduced and the turbine can be placed closer to the surface, improving accessibility for service in water.

Placing the hulls at center line as variation of the double hull system offers no significant benefits over double hull systems as described above, but carries the drawbacks of both the single and the double hull systems.

Triple Hull A combination of the single hull systems with the hull at center line and the double hull systems with the hull each at the turbine's sides could potentially improve some characteristics of the platform. In such a system, the center hull does not necessarily need to be of the same size as the ones on the sides and could house some of the mechanical and/or electronic parts that do not fit into the turbine's housing. In the system shown in figure 7.4, two main hulls and a third auxiliary hull are used. Alternatively, the third hull could be increased in size to house the turbine as well as a buoyancy tank. However, the advantage of increased redundancy is offset by the disadvantage of a greater complexity due to more tanks and hulls. The benefits of increased redundancy might be rather small in comparison to a well-designed two hull system. Moreover, this arrangement does not provide any significant improvement regarding the platform's mooring offset and orientation.

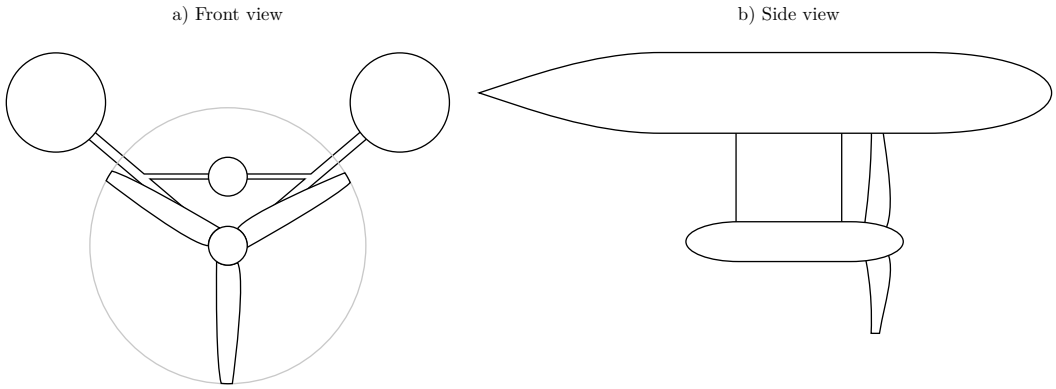

Figure 7.4: Possible arrangement for a triple hull system with hull above turbine. **a)** Front view; **b)** Side view.

7.1.4 Elevation System for Maintenance

Not least because of the permanent currents, in water survey and maintenance while the platform is submerged is challenging. The best and safest option is to elevate the platform to the surface and conduct the necessary service either on the surface or by lifting the platform out of the water. Elevating the platform to the surface is relatively easy in principle as the platform requires either a slight excess in buoyancy or an active flight system. However, lowering the platform to its design depth without heavy equipment poses a significant challenge, especially for smaller systems like marine renewable energy platforms. Unlike large systems from oil and gas, off-the-shelf tensioning systems such as chain jacks, wire winches, and in-line tensioners are typically unsuitable for smaller systems. Nevertheless, the functional principle of these larger systems can be applied to such smaller systems, which is discussed below.

Winch One or more small-scale winches can be integrated into the platform's structure to facilitate maintenance. Since the turbine requires connectivity to the grid even when the platform is not operating, supply of electricity is not a problem. During operation, one or more mooring lines would be required to be stored on the winch, with the excess in length of the order of magnitude of the design depth of the system. For maintenance, the break of the winch would be released and due to the platform's buoyancy, it would rise to the water surface. To lower the platform back to its design depth, the mooring line would be hauled in, and the brake finally engaged. Depending on the size of the buoyancy tanks, significant force might be required to haul the mooring line, for which ballast tanks might be necessary. These tanks would be flooded after finishing service at water surface to reduce the platform's buoyancy. Once the final position is reached, the ballast tanks would be evacuated, for example, by pressurized gas tanks or a temporary gas line to the surface.

To reduce system complexity while maintaining redundancy, a single winch could be considered if two or more mooring lines have to be lengthened for maintenance. However, this would require positioning the winch at the center line of the platform to reduce the heel. Furthermore, the mooring

lines need to be fed and guided through the structure, as the fairleads and the attachment point of the winch would not be close.

In-Line Tensioner In-line tensioners can be particularly useful for systems with a single mooring line, as they allow for external mechanical power to be used for shortening the mooring line. After maintenance, a service vessel would pull the free end of the mooring line to tension it and then lower the platform to its planned position. Before raising the platform again for the next maintenance cycle, the mooring lines must be picket up by the service vessel or designed to be accessible from the water surface at all times. However, in-line tensioners may not be feasible for systems with multiple mooring lines or when the required tools are not available during maintenance cycles. In particular, achieving a specific heel and trim angle can be a challenge for multiple mooring lines.

7.1.5 Mooring Line Configuration

The mooring line configuration can vary from a single line to four mooring lines. In this section, the advantages and disadvantages of a configuration with one, two, three, and four mooring lines are discussed.

Single Mooring Line Configuration In a single mooring line configuration, the platform connects to a single anchor, with the mooring line bridled at its top end and connected to the platform at various points. If designed correctly, the platform is able to swivel around the anchor pointand align itself always with the direction of the current. This configuration requires less installation complexity and material, but lacks redundancy in the system, which could increase the material of the single anchor. Depending on the exact circumstances and requirements, this might not necessarily result in a reduced cost and thus needs a closer look whether this concept might be the better choice for a project.

Two Mooring Line Configuration The implementation of a two mooring line configuration for the system requires one mooring line upstream and one mooring line downstream of the platform, each connected to their respective anchor. Bridled sections at the top end of both mooring lines control the heel and heading of the platform. That way, each mooring line connects to both forward and both aft ends of the platform, respectively.

In comparison to the mooring configuration with a single mooring line, the mooring offset can be reduced without the need for great forces in the mooring lines. Especially in farms with various turbines, the mooring offset has to be either very narrowly defined or the distance between the devices has to be increased significantly to avoid contact or entanglement of the mooring line. Additionally, the trim of the platform is more closely defined. Nevertheless, the platform looses its ability to follow the current's direction on its own. This would either require a more advanced tracking system or accept the loss in performance due to the current not coming directly from the front.

Three Mooring Line Configuration The third mooring configuration uses three mooring lines with two anchors upstream of the platform and one anchor located on the center line aft of the platform. The forward mooring lines connect the anchor directly to the corresponding fairleads, while the aft mooring lines connects to both aft fairleads via a bridled section at its top end.

The two forward mooring lines lead to better behavior of the platform under currents coming from either side of the platform and not straight from the front. Furthermore, they help significantly control the heel of the platform. In comparison to the two mooring line configuration, an additional anchor is needed. As turbines are typically installed in a farm, sharing anchors might be an option, depending on the conditions of the sea floor and the layout of the farm.

Four Mooring Line Configuration To furthermore control the platform's position, an additional mooring line can be added at the aft end of the platform. Each fairlead located at the four ends of the hulls connects to an anchor placed radially outwards, with two anchors upstream of the platform and two anchors downstream of the platform.

Similar to the three mooring line configuration, sharing anchors might be possible, if the conditions of the farm allow for it. The additional anchor and mooring line increase the redundancy of the system as in case of a line loss, three of four lines absorb the forces, while for the three mooring line configuration, the forces are distributed between the two remaining mooring lines.

7.2 Design Concept

The description of the design concept for the complete mooring system can be found below. This concept was used as basis for the subsequent optimization process, described in chapter 8. Its final review to ensure compliance with the important design codes is documented in chapter 9.

7.2.1 Turbine

In recent years, various concepts have been developed for MCEC that can be classified based on the alignment of the main rotary axis with respect to the current. The rotor of many recently developed devices share the same basic design with wind turbines as both types extract kinetic energy from a fluid. The majority of these devices have their main rotational axis in the horizontal plane, which is parallel to the current. However, there have been efforts to design cross-flow turbines with an axis of rotation perpendicular to the current, resulting in a vertical axis of rotation that eliminates the need to track the current's direction. Despite this, current designs continue to primarily use a horizontal axis of rotation.

Available Designs

Different MCECs suitable for this zone and the projected conditions are available, however all of them show a lack of detailed information publicly available. One such device is being developed by the Mexican company *Potencia Industrial*.

A small MCEC has been developed by *Schottel HYDRO* with a diameter of 5 m, while a bigger version with 6.3 m in diameter seems to be in development. *Sustainable Marine Energy* provides two platform options to moor the turbine to the sea floor: the *PLAT-I* for surface mooring or *PLAT-O* for full submersion of the device. However, the latter seems to be abandoned as no updates have been published in recent years. The turbine is optimized for higher energy currents typically found in confined tidal currents or rivers, and adoptions might be necessary for low energetic ocean currents.

The University of Strathclyde in Glasgow, Scotland is developing a turbine optimized for slow ocean currents with speeds up to $1.5\,\mathrm{m,s^{-1}}$ found in regions like the Philippines or the Cozumel Channel in Mexico. However, no final design is available as the turbine is still in the early stages of technological readiness.

Finally, at the Institute of Engineering of the National Autonomous University of Mexico (UNAM), Mexico, two prototypes for low energetic ocean currents are under development. The first is a cross-flow turbine, and an early prototype at scale has already undergone testing in a circulation tank, towing tank, and natural conditions. The second development is a parallel flow turbine, similar to the prototype developed by the University of Strathclyde, but in a much earlier stage of development as tank test have not been carried out yet.

Estimation of Turbine Parameter

Due to the lack of verified data of a turbine suitable for the Cozumel Channel, the platform will be developed based on a conservative estimate for a parallel flow turbine.

Key Coefficients A key parameter used for characterizing a parallel flow turbine is the power coefficient (C_P) that is defined by

$$C_P = \frac{2P}{\rho A_S v_\infty^3} \quad , \tag{7.1}$$

where P denotes the power at the shaft, ρ the water's density, A_S the swept area of the rotor, and v_∞ is the undisturbed velocity of the current at hub height [93]. The power coefficient is a function of the tip speed ratio

$$\lambda = \frac{\omega R}{v_\infty} \quad , \tag{7.2}$$

where ω is the angular velocity of the rotor and R its tip radius. The torque coefficient (C_Q) is directly related to the power coefficient and tip speed ratio by their ratio ($C_Q = C_P \lambda^{-1}$) [93], thus can be calculated by

$$C_Q = \frac{2Q}{\rho A_S v_\infty^2 R} \quad , \tag{7.3}$$

where Q is the torque at the shaft. The thrust coefficient is typically calculated by

$$C_T = \frac{2T}{\rho A_S v_\infty^2} \quad , \tag{7.4}$$

Table 7.1: Expected and estimated principal data of a reference 5 m-turbine.

Description	Symbol	Unit	Value
Rotor diameter	D	m	5
Total length	L	m	2.0
Hub diameter	d	m	0.3
Mass	m	kg	1200
Displaced volume	V	m^3	0.15
Maximum power coefficient	C_P	–	0.45
Maximum thrust coefficient	C_T	–	0.8
Maximum torque coefficient	C_Q	–	0.075
Design TSR	λ	–	6.5

where T is the thrust generated by the turbine [93].

Mass and Volume The *Schottel Tidal Generator* is a tidal turbine developed with a diameter of 5 m Schottel Hydro [96, 97]. The turbine supposedly operates at high velocities as its cut-in velocity is $0.7\,\mathrm{m\,s^{-1}}$ and its cut-out velocity is $4.6\,\mathrm{m\,s^{-1}}$. As a turbine in the Cozumel Channel will work at much lower current speeds, the rotational speeds are equally lower, possibly requiring a bigger, thus heavier generator. The *Schottel Tidal Generator* has a mass of approximately 800 kg to 1000 kg. Therefore, the reference mass of the turbine for the platform design is estimated conservatively to 1200 kg, while the reference volume is assumed to be $0.15\,\mathrm{m^3}$.

Power and Thrust Considering that the use case of the aforementioned turbine is similar, it's coefficients are expected to be quite similar. During field trials, the power coefficient of the turbine *SIT250* was found to be $C_P = 0.44$ at a tip speed ratio (TSR) of $\lambda \approx 5.0$ and the thrust coefficient was found to be $C_T = 0.78$ at $\lambda \approx 5.5$ [108]. As conservative estimation, the power coefficient is taken as $C_P = 0.45$ and the thrust coefficient as $C_T = 0.8$, both at $\lambda = 6.5$, as suggested by Encarnacion et al. [37]. The torque coefficient was then estimated to $C_Q = 0.070$. The results are summarized in table 7.1.

Power Control Mechanism For sake of this work, no pitch control is considered. Nevertheless, it is assumed that the frequency of the generator is adjusted to maintain the turbine always in its optimal working conditions as described in table 7.1. This might be achieved via a frequency converter.

7.2.2 Platform

As the turbine itself is not neutrally buoyant it has to be mounted on a platform which provides the necessary buoyancy for maintaining its position. Single hull, double hull, and triple hull systems

have been considered and are discussed in detail in section 7.1.3. Single hull systems, such as the one shown in figure 7.2, stand out for their simplicity, as they have much less parts and consequently in much less joints. Independently on the technology used for joining one or more parts, each joint is prone to failure due to different effects, including fatigue, corrosion and stress concentration. However, dual hull systems can reach further upstream without significantly increasing the pitching moment due to the hulls drag. They also offer the possibility to connect various mooring lines or a bridled mooring line to compensate the reaction moment due to the generators torque or moments by current not coming directly from front. For a system with three hulls, the advantages as stated in section 7.1.3 do not offset its disadvantages in comparison to a two-hull system. As the volume of a body increases with the third power of its longitude and the surface only with the second power, fewer but bigger hulls tend to have a lower drag then more but smaller hulls.

Shape of Hull

The purpose of the hull is providing buoyancy while simultaneously minimizing their drag. Myring [78] developed the so called Myring-profiles for the nose- and tail-section, which provide the possible shape of low-drag bodies for fully submerged, cylindrical bodies. The nose shape is defined by the position dependent radius (r_N) as

$$r_N = \frac{1}{2} d_H \left(1 - \left(\frac{x}{L_N} - 1 \right)^2 \right)^{1/n} \quad , \tag{7.5}$$

with its derivation defined by

$$\frac{\mathrm{d}r_N}{\mathrm{d}x} = \frac{1}{2} d_H \frac{2 \left(\frac{x}{L_N} - 1 \right) \left(\frac{2L_N x - x^2}{{L_N}^2} \right)^{1/n - 1}}{n L_N} \tag{7.6}$$

where x denotes the distance from the nose's tip, d_H the maximum diameter of the hull, L_N the length of the nose and n the shape parameter. The tail's position dependent radius (r_T) is given by

$$r_T = \frac{1}{2} d_H - \left(\frac{3 d_H}{2 {L_T}^2} - \frac{\tan\theta}{L_T} \right) x^2 + \left(\frac{d_H}{{L_T}^3} - \frac{\tan\theta}{{L_T}^2} \right) x^3 \quad , \tag{7.7}$$

with its derivation given by

$$\frac{\mathrm{d}r_T}{\mathrm{d}x} = -2 \left(\frac{3 d_H}{2 {L_T}^2} - \frac{\tan\theta}{L_T} \right) x + 3 \left(\frac{d_H}{{L_T}^3} - \frac{\tan\theta}{{L_T}^2} \right) x^2 \quad , \tag{7.8}$$

where x is the distance from the front end of the tail (counting towards the tail's aft end), L_T the length of the tail, d_H the maximum diameter of the hull, and θ is half the included angle at the tail's tip.

Uppal et al. [117] did some research on the optimal parameter for the nose and tail section for an autonomous underwater vehicle with a total length of 1.4 m and in the range of 0.6 m s^{-1} to 1.4 m s^{-1}. A fineness ratio of 0.1 was used, with a relative nose length of $^5/_{28} L_{OA}$ and a relative tail

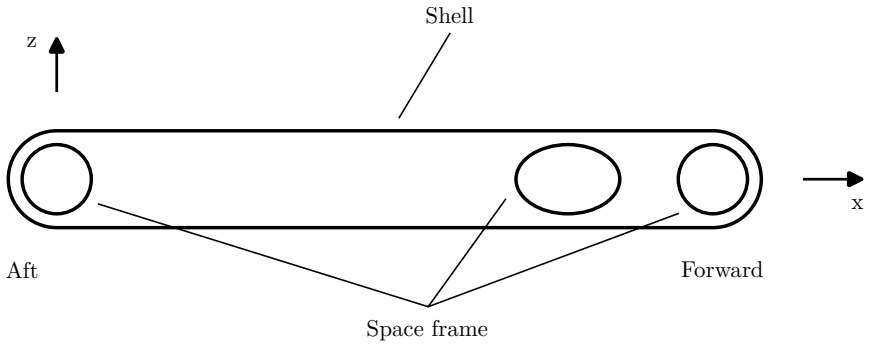

Figure 7.5: Exemplary cross-section of strut.

length $^{9}/_{28}L_{OA}$, where L_{OA} is the length over all of the hull. The optimal nose shape parameter was found to be 3, while a tail angle (θ) of 15° gave the lowest volumetric drag coefficient of $C_{dV} = 0.0382$, $C_{dV} = 0.0415$ and $C_{dV} = 0.0476$ for speeds of $v = 1.4\,\mathrm{m\,s^{-1}}$, $v = 1.0\,\mathrm{m\,s^{-1}}$ and $v = 0.6\,\mathrm{m\,s^{-1}}$, respectively.

The equations for volume (V_H) and surface (S_H) of the hull can be derived by

$$V_H = \pi \int_0^{L_N} r_N^2 \,\mathrm{d}x + \frac{\pi}{4} {d_H}^2 \left(L_{OA} - L_N - L_T\right) + \pi \int_0^{L_T} r_T^2 \,\mathrm{d}x \tag{7.9}$$

and

$$S_H = 2\pi \int_0^{L_N} r_N \sqrt{1 + \left(\frac{\mathrm{d}r_N}{\mathrm{d}x}\right)^2} \,\mathrm{d}x + \pi d_H \left(L_{OA} - L_N - L_T\right) + 2\pi \int_0^{L_T} r_T \sqrt{1 + \left(\frac{\mathrm{d}r_T}{\mathrm{d}x}\right)^2} \,\mathrm{d}x \quad . \tag{7.10}$$

Strut Design

The strut connects both hulls and provides the mounting point of the turbine, transmitting the forces exerted on the turbine to the hulls and in turn to the mooring lines. It primarily comprises a steel space frame placed between both hulls. The shell of the strut follows the shape of the space frame, with the cross-section shaped as depicted in figure 7.5.

7.2.3 Mooring System

As discussed in chapter 2, the offshore industry currently employs various types of systems . Catenary systems are simple and easy to install, but they become less efficient on deeper installations due to their weight, and their mooring system's footprint is significantly larger compared to other systems. Additionally, catenary systems do not provide vertical restoring forces required for subsurface moorings. Tension leg platforms, on the other hand, require a significant excess in buoyancy and are not suitable for fully submerged platforms. For this reason, a taut mooring system will be used for the platform in this work. In total, two different system configurations will be compared,

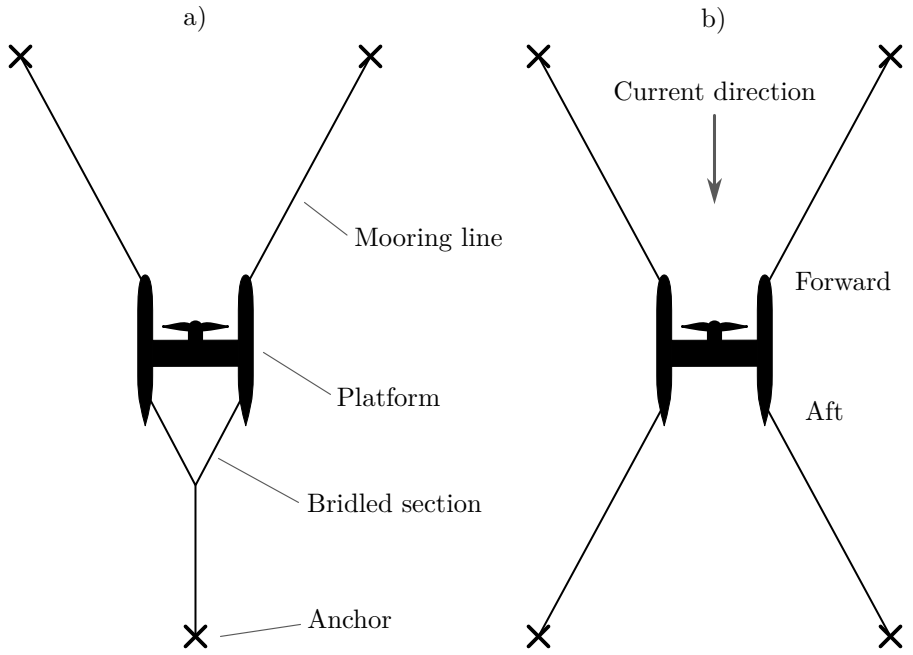

Figure 7.6: Mooring concepts used as basis for optimization. **a)** Three mooring line configuration; **b)** Four mooring line configuration.

one with three mooring lines and one with four mooring lines.

Both configurations (see figure 7.6) consist of four fairleads, one at each of the hull's ends, which connect to the mooring lines. At the forward ends of the structure, the fairleads are directly connected to the anchor via a mooring line. In the three mooring line configuration, the aft fairleads connect to a bridled section that joins into a single aft mooring line at the centerline of the platform. In contrast, the four mooring line configuration has two aft mooring lines, each directly connecting the fairlead to the corresponding anchor.

All mooring lines and bridled section are composed of steel wire with the same diameter. Although the mooring lines in a taut system should never make contact to the sea floor, for the last two meters of each mooring line connecting to an anchor, studless chain is used as precautionary measure.

7.2.4 Elevation System

To raise the platform to the water surface and lower it back to design depth, a combined system of ballast tanks and winches for the aft mooring lines is chosen. The mooring lines are attached to the platform via four fairleads. Since three are sufficient to define the platform's position in space, two mooring lines have to be adjusted in length. The complete process of reaching design depth is depicted in figure 7.7. In the first stage the ballast tanks are flooded to reduce the platforms overall buoyancy and decrease the required power of the winches (see figure 7.7 b)). Afterwards, the

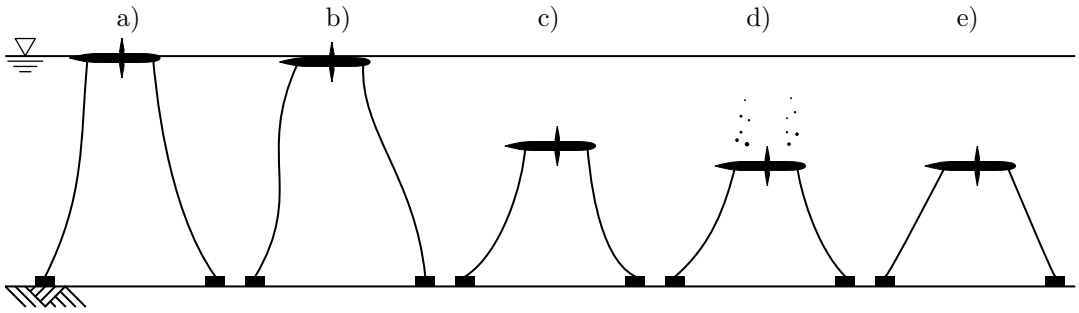

Figure 7.7: Procedure for reaching design depth after installation or service. **a)** Platform floating on surface for maintenance; **b)** Ballast tanks flooded to reduce buoyancy; **c)** Hauling in aft mooring lines with winch; **d)** Evacuating ballast tanks with pressurized gas when design depth reached; **e)** Turbine in operation.

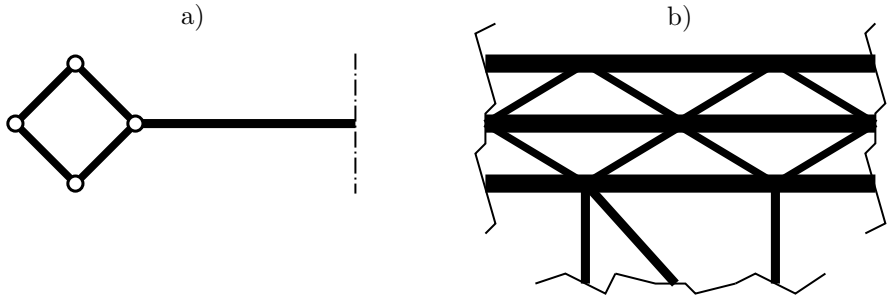

Figure 7.8: Sketch of space frame of internal structure of the platform. **a)** View from behind, with internal structure of port hull visible; **b)** Top view with section of port hull visible.

winches lower the platform by reducing the length of the aft mooring lines (figure 7.7 c)) until the design depth is reached. The ballast tanks are evacuated by the help of small tanks with pressurized gas, carried within the structure. These can be either exchanged during service or recharged if the service vessel can be equipped with the necessary devices. This method helps reducing the power requirements on the winches. They can be smaller, lighter, and especially cheaper than the winches which would be required for lowering the platform without reducing its buoyancy. Furthermore, the ballast tanks do not need to be design to withstand excessive pressure, as they are supposed to be at ambient pressure at all times.

7.2.5 Internal Structure of Platform

In case an outer shell is needed for a structure or a vessel, it is typically also designed to considerably contribute to the overall strength of the object. However, it is also possible to separate this specific task from the outer shell, what requires additional structural members to transmit forces and moments. Several approaches exist to design such structures, but due to their efficient use of material for a given strength, space frames or space trusses are widely used.

The cross section of the space frame within the hulls is of quadratic shape with the corners

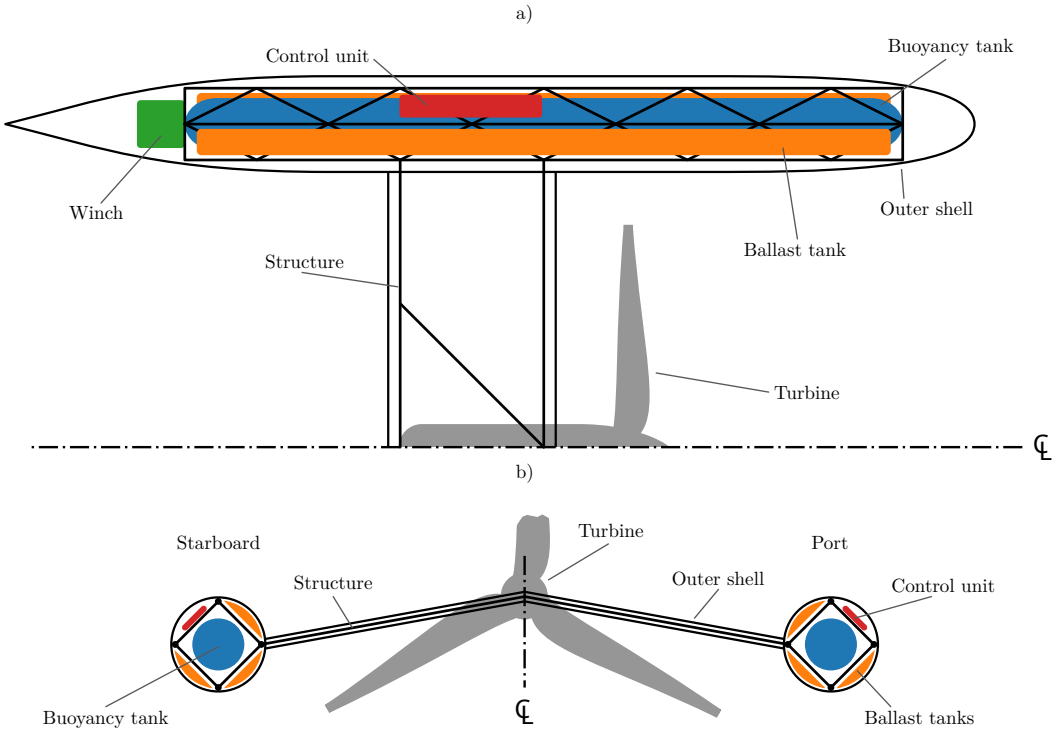

Figure 7.9: Layout of platform. The space frame and the outer shell are depicted in black, The buoyancy tanks in blue, the ballast tanks in orange, the position of the winch is marked in green, the placement of the control units in red and the position of the turbine in gray. **a)** Top view; **b)** Front view.

aligned vertically and horizontally. This way, the space frame of the strut can connect to nodes of the hull's space frame. A sketch of the principal arrangement of the members is shown in figure 7.8. The structure of the space frame is similar to the Warren truss configuration.

7.2.6 Compartments and Layout of Platform

The general layout of the platform is shown in figure 7.9. To counteract the submerged weight of the structure, two buoyancy tanks are fitted within the structure of the hulls. This design feature provides protection against external forces during unexpected events, such as collisions with other vessels or objects and the platform is more likely to keep its ability to surface without the need for special equipment. The ballast tanks are placed between the outer shell and the structure. The number of the ballast tanks is subject to optimization. The upper outer face of the space frames is left blank for control equipment to be placed. This location was chosen as it provides the best accessibility during service. Equipment for controlling emergency functions may be placed on the strut close to the turbine, as this position is best protected against external influence.

Buoyancy Tanks

To maximize the volume of the buoyancy tanks, the tanks span from the aft end to the forward end of the structure. The tanks are of cylindrical shape with half-spherical ends. The displaced volume (V_{bt}) can be calculated by

$$V_{bt} = \frac{\pi}{4} d_{bt}^2 \left(L_S - d_{bt}\right) + {}^1\!/_6 \pi d_{bt}^3 \quad , \tag{7.11}$$

where L_S is the length of the structure in the hulls and d_{bt} the outer diameter of the buoyancy tank. The outer surface of a single buoyancy tank (S_{bt}) is given by

$$S_{bt} = \pi d_{bt} \left(L_S - d_{bt}\right) + \pi d_{bt}^2 \quad . \tag{7.12}$$

Ballast Tanks

The ballast tanks need to fit between the outer shell and the structure, maintaining the required clearance to both. Since the ballast tanks are assumed to be pressurized to the same pressure as the environment, their shape can be complex in comparison to the buoyancy tanks. Both ends of the ballast tanks are flat, while the cross section is supposed to maximize the space between structure and shell.

Due to the variety of combinations of dimensions of the structural members and the outer diameter of the hull, the easiest approach is to approximate the cross-sectional area (A_{blst}) with polygons. First, a circular segment is drawn with the outer diameter

$$d_{blst} = d_H - t_{shell} - c_{shell} \quad , \tag{7.13}$$

where d_H is the outer diameter of the hull, t_{shell} the thickness of the shell, and c_{shell} the minimal clearance between the shell and all internal components. The apothem of the cross section can be calculated based on the node radius of the space frame and is defied by

$$a_{blst} = \frac{r_n}{\sqrt{2}} + {}^1\!/_2 d_{II} + c_{struc} \quad , \tag{7.14}$$

where r_n is the node radius of the space frame of the hull, d_{II} the outer diameter of the diagonal members in the space fame of the hull, and c_{struc} the minimal clearance between the structure and other components. From this circular segment, the space occupied by the longitudinal structural members in the space frame of the hull is subtracted. Important for this step is the correct placement of the longitudinal structural members and considering the structural clearance (c_{struc}) together with their diameter (d_I).

7.2.7 Mooring Winch

The mechanism for lifting the platform to the surface relies on automatic winches which are suitable for under water operation. Suitable systems are fabricated by various suppliers such as *InterOceanSystems LLC* and *Okeanus*. Both suppliers are able to fabricate the winches with required

dimensions and required power to haul in the aft mooring lines in acceptable time.

7.3 Design Criteria

7.3.1 Load Cases

To the best of the authors knowledge, no mandatory or recommended load cases explicitly for OCTs have been made available to date. However, the IEC 62600-2 [54] defines load cases for tidal energy converter (TEC), which are comparable to ocean current turbines in several regards. Given the specific conditions of the installation site and the lack of data from a turbine provider, the design of the mooring system is based on a subset of the load cases defined in the code.

The loads on the system are governed by the magnitude of the current and its direction. Wave and wind conditions are defined; however, their effect on the mooring system is limited to three load cases because the platform is submerged during operation.

The details on the environmental conditions and the relevant limit states are summarized in table 7.2. A description of each group of load cases can be found in the following sections. For load cases other that the first and the last, the last letter indicates the direction of the current, while wind and waves are always assumed to come directly from the front (180°): *A* indicates a current from 180°, *B* indicates a current from 150°, and *C* indicates a current from 210°.

LC1: Static Equilibrium The first load case considers the equilibrium condition of the mooring system at design depth. Although this load cases is not explicitly defined in IEC 62600-2 [54], it was added to the list as it gives useful insights in the basic behavior of the system.

LC2: Normal Operation This group of load cases describes the normal operation of turbine and mooring system. The platform operates at its design depth with the 1-year current and 1-year wind. While the wind comes directly from the front (180°), the ocean current varies between 180° (LC2A), 150° (LC2B), and 210° (LC2C). For these load cases the ULS, FLS, and SLS are considered.

LC3: Parked and Survival For these load cases, the turbine is supposed to be in survival mode with its brakes applied. The loads are calculated for a 100-year current, 50-year waves, and 5 year wind and reviewed for the ULS, and SLS. Wind and waves come directly from the front while the current changes between 180° (LC3A), 150° (LC3B), and 210° (LC3C).

LC4: Parked These load cases assume a parked turbine with its brakes applied, but in contrast to group LC3 not in survival mode, resulting in the return levels of 1-year for the current, wind, and the waves. The loads are evaluated according to the ULS, FLS, and SLS.

Table 7.2: Complete load case matrix.

	Depth m	**Current** $\mathrm{m\,s^{-1}}$	**Angle** °	**Wave** m	**Wind** $\mathrm{m\,s^{-1}}$	**ULS**	**FLS**	**SLS**	**ALS**
LC1	50	–	–	–	–	•		•	
LC2A	50	1.38	180	–	12	•	•	•	
LC2B	50	1.38	150	–	12	•	•	•	
LC2C	50	1.38	210	–	12	•	•	•	
LC3A	50	1.55	180	8	16	•		•	
LC3B	50	1.55	150	8	16	•		•	
LC3C	50	1.55	210	8	16	•		•	
LC4A	50	1.38	180	2	12	•	•	•	
LC4B	50	1.38	150	2	12	•	•	•	
LC4C	50	1.38	210	2	12	•	•	•	
LC5A	50	1.55	180	3	16				•
LC5B	50	1.55	150	3	16				•
LC5C	50	1.55	210	3	16				•
LC6A	50	1.55	180	3	16				•
LC6B	50	1.55	150	3	16				•
LC6C	50	1.55	210	3	16				•
LC7A	50	1.55	180	3	16				•
LC7B	50	1.55	150	3	16				•
LC7C	50	1.55	210	3	16				•
LC8A	50	1.55	180	3	16				•
LC8B	50	1.55	150	3	16				•
LC8C	50	1.55	210	3	16				•
LC9	0	1.19	180	0.5	5	•			

LC5: Loss of Stability/Leakage In these load cases, the platform is supposed to have lost one of its starboard ballast tanks. While the main buoyancy tanks are protected by the structure, the ballast tanks are close to the outer surface and might be damaged by external factors or not flooded with air after reaching design depth. While the current is the 100-year return level, the wind and the waves have a return period of 5-years. The loads are evaluated according to the ALS.

LC6: Loss of Stability/Leakage Similar to the load case group LC5, the platform is supposed to have lost its port ballast tanks. The return level for the current in 100-years, and for wind and waves 5-years, while the loads are evaluated according to the ALS.

LC7: Loss of Line Under these load cases, the effect of losing the forward starboard mooring line is evaluated according to the ALS. While it is also possible to loose the starboard aft mooring line (or bridled line), the forward mooring lines experiences a much greater load due to the current coming from the front. Equally to the load cases LC5 and LC6, the current is set to its 100-year return level, and wind and waves to their respective 5-year return level.

LC8: Loss of Line Equally to a loss of the starboard mooring line in LC7, the loss of the forward port mooring line is considered under the conditions of the ALS. Therefore, the platform experiences the 100-year current, 5-year waves, and 5-year wind.

LC9: Maintenance The last load case considers maintenance of the platform at the water surface under the ULS. The turbine is supposed to have its brakes applied with the current, wind, and waves for maintenance. Transportation of the platform can happen in very different conditions, in case the platform is towed to the construction site, the maximum current is expected to not exceed $1.19\,\mathrm{m\,s^{-1}}$, which is equal to the conditions expected for maintenance. In case the construction site is at a considerable distance of the port it would be far more feasible to load the platform on a vessel instead of towing it to the construction site.

7.3.2 Additional Environmental Conditions

Aside from the primary environmental conditions defined in section 7.3.1, corrosion and marine growth have to be taken into account. In case no specific data are available, corrosion of $0.3\,\mathrm{mm\,year^{-1}}$ should be considered for the suspended part of mooring lines in tropical waters, as stated in DNVGL OS-E301 [32]. For a design life of 20 years this results in a total corrosion allowance of 6 mm. According to PEMEX NRF-003:2000 [83], a thickness of the marine growth of 35 mm should be applied to all structural members. A typical density for marine growth is $1325\,\mathrm{kg\,m^{-3}}$ [32]. Due to its specific shape, the mass of the marine growth on chains is twice the value obtained with the nominal diameter.

Table 7.3: Partial load safety factors for ULS and a safety level of SL2.

Load case	Design category	Partial load safety factor
LC1	Normal	1.35
LC2A	Normal	1.35
LC2B	Normal	1.35
LC2C	Normal	1.35
LC3A	Extreme	1.35
LC3B	Extreme	1.35
LC3C	Extreme	1.35
LC4A	Normal	1.35
LC4B	Normal	1.35
LC4C	Normal	1.35
LC9	Transport	1.5

7.3.3 Requirements of Limit States

The criteria for evaluating the system's performance depend on the analyzed limit state. More information on the limit states can be found in section 3.2.4. The default safety level of a marine structure should be SL2 [54]. The risk for humans due to failure of the structure or the mooring system is very low, as the platform is supposed to not be boarded, neither during operations nor during service of the platform. The environmental damage could be considered as small during an accident, as only small amounts of lubricants are required in the winches and the turbine itself. However, the loss of the structure leads to economic and political consequences wherefore the safety level is not lowered to SL3 but maintained at SL2.

Ultimate Limit State The partial load safety factor which is applied to the loads defined in the ULS depend on both, the design category and the source of the loading. Since in the simulations loads of different sources are applied at the same time, the maximum partial load safety factor is chosen for each design category. The safety factors for each load case are summarized in table 7.3. For evaluating the stresses and buckling of the structure, a material factor of 1.1 was selected.

According to IEC 62600-10 [53], the analysis of the mooring system should be based on a safety factor of 1.67 for loads estimated with a dynamic mooring analysis. For loads estimated with a quasi-static mooring analysis a safety factor of 2.0 should be considered. The evaluation of the anchor holding capacity is based on intact conditions and redundancy checks. ULS assumes an intact system wherefore the safety factor for anchor piles under axial loading is 2.0 and under lateral loading is 1.6 [53].

Accidental Limit State According to IEC 62600-2 [54], the partial load safety factor for the ALS should be taken as 1.0 for analyzing accidental loads on the structure, while the material factor

is given by 1.1.

The mooring lines should be evaluated with a safety factor of 1.25 when based on a dynamic mooring analysis, and with a safety factor of 1.43 when based on a quasi-static analysis, as mentioned in IEC 62600-10 [53]. The holding capacity of anchor piles under accidental loads (i.e. redundancy check) should be evaluated with a safety factor of 1.5 for axial loading and 1.2 for lateral loading, as given in IEC 62600-10 [53].

Fatigue Limit State For estimating the fatigue life of offshore steel structures, ISO 19902 [55] introduces a fatigue damage design factor and a local experience factor. The fatigue damage design factor should be 2.0 for inspectable components that are non-critical and 5.0 for inspectable and critical components. The local experience factor takes into account the experience with structures of similar type or in similar conditions and is 1.0 if no evidence suggests otherwise.

According to the requirements of API RP-2SK [5], the fatigue life of the mooring system of floating offshore structure should be designed with a safety factor of at least 3. The typical design life of renewable offshore structure such as offshore wind turbines is 20 years. Assuming the same design life for the MCEC, the mooring system should withstand the cyclic loads of 75 years.

Serviceability Limit State The conditions for serviceability are typically defined by the operator of the platform and the manufacturer of the turbine. In general, the platform should avoid hitting other objects that are in proximity, not overstretch the power cable and avoid extreme rotations. To keep the offset of the platform within a reasonable range, the platform should stay within 10 m of the original position. Heel of the platform is not as critical as the other rotations since it is in line with the rotational axis of the turbine. In order to avoid excessive bending of the power cable, 20° will be considered as the limit for heel, while trim and heading should be limited to 10° as their impact on the turbine's performance is greater.

With the exception of resonance, accelerations are not of a concern for the platform as no humans will board the structure. Furthermore, the platform is supposed to operate out of the influence of wind and waves, which are typical environmental factors that introduce high accelerations.

Chapter 8

Optimization of Design Concept

The optimization process of the design of the position-keeping system is an iterative process due to recursive dependencies. For instance, adjusting the platform's buoyancy increases the diameter of both hulls which itself changes the geometry of the internal space frame. Any changes in the geometry, such as the position of the turbine, can significantly impact the equilibrium position of the platform, potentially changing the loads in the mooring lines. To tackle this problem, a genetic optimization algorithm and coupled mooring analysis and structural finite element analysis were used. Since genetic optimization algorithms rely on evaluating a great number of different individuals, it is crucial to have a time-efficient analysis of the different designs. The mooring systems were analyzed based on quasi-static principles using straight, linear-elastic mooring lines, while the structural deformations and stresses were calculated via a finite element analysis based on beam elements. This approach enabled the optimization of both, the platform and mooring system simultaneously.

The different parameters and their allowed range of values which formed part of the optimization process are described in section 8.1 while a description of the numeric models used si given in section 8.2. The automated optimization process by means of the genetic algorithm can be found in section 8.3 and the subsequent manual fine-tuning in section 8.4.

Performance The performance of the individuals is evaluated via the mass of the whole system, the achieved safety factor, the maximum angle, and the net buoyancy deviation. The achieved safety factor (S_F) is calculated by

$$S_F = \frac{1/\gamma_M R_k}{\gamma_f F_k} \quad , \tag{8.1}$$

where F_k is the characteristic load, and R_k the characteristic resistance of the used material, γ_f the load factor, and γ_M the material factor. For the mooring lines, the load is the tension within the line and the resistance the MBL as estimated with the formulae in Ma et al. [68], see equation (4.9). In the case of the structure, the load is the stress in the structural members and the resistance their yield strength. For buckling, the load is set to the buckling factor as calculated by *Abaqus*. Lastly,

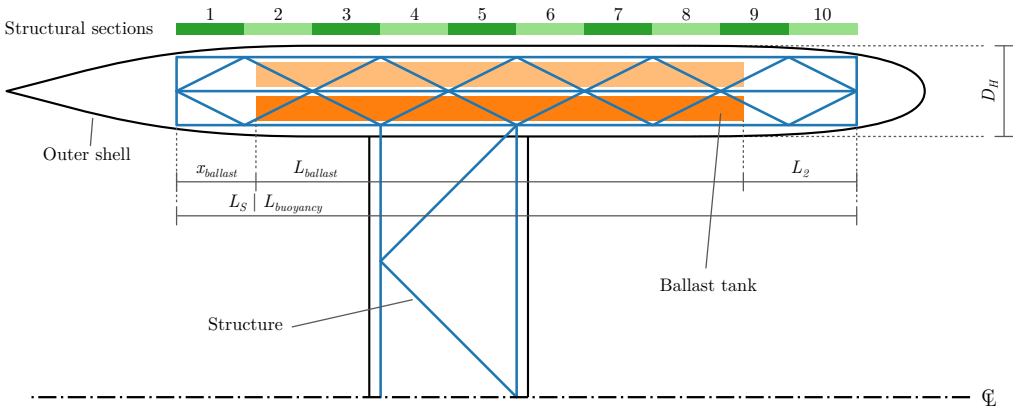

Figure 8.1: Top view of the port side of the platform concept with the outer shell marked in black, the structure in blue, and the different segments of the structure in green. The exemplary position of one ballast tank per side is shown in orange. Not to scale.

the minimum of all three factors is taken. The maximum angle is determined by the highest value among heel, trim, or heading of the platform at equilibrium. The net buoyancy deviation is the difference between the design net buoyancy of 50 kg and the calculated net buoyancy. Any design proposals with net buoyancy smaller than the minimum net buoyancy of 20 kg are discarded. The net buoyancy ($\tilde{B}$) is calculated by

$$\tilde{B} = (V_{PL} - n_{BLLST} V_{BLLST} + V_{MLs})\rho_w - (m_{PL} + m_{MLs}) \quad , \tag{8.2}$$

where V_{PL} denotes the displaced volume of the complete platform, V_{BLLST} the displaced volume of a single ballast tank, n_{BLLST} the number of ballast tanks, V_{MLs} the displaced volume of all mooring lines, ρ_w the density of the water, m_{PL} the total mass of the platform, and m_{MLs} the mass of all mooring lines.

8.1 Parameter Subject to Optimization

8.1.1 Principals

The main parameter changed by the algorithm is the outer diameter of the hull. Several variables depend on this diameter, such as the length of both hulls, the volume of the buoyancy tanks, and the maximum volume available to the ballast tanks. Another parameter that can be changed is the number of the hull segment, the strut is connected to (see figure 8.1). Since the strut spans over two segments, the parameter refers to the aftmost segment of both. In the example of the figure, the strut would be connected to segment 4. The number of hull segments is fixed to 10 as it was found that this maximizes the available space inside the hull for a given hull diameter and fixed aspect ratio of these segments. Therefore, the strut is allowed to connect to every structure between the 1st to the 9th section, including both boundaries.

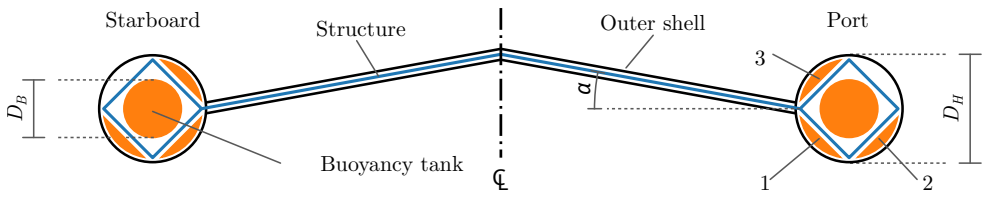

Figure 8.2: Front view of the platform concept with the outer shell marked in black, the structure in blue, and the position of the tanks in orange. The ballast tanks are numbered on the port side.

8.1.2 Mooring System

The mooring system consists of three and four mooring lines respectively, that connect each of the four corners of the platform to three or four anchors, depending on the system configuration (see figure 8.3). The main part of the mooring lines consists of steel wire, while the last two meters connecting to the anchor are steel chains. The diameter of both segments can be changed independently by the algorithm, however, the dimensions are the same for all mooring lines to reduce the complexity of the resulting system. The initial strain of the wire rope can be adjusted for the forward mooring lines and for the aft mooring line(s) independently. Though, both forward mooring lines have the same initial strain, which is equally true for the aft mooring line(s). The strain of the forward mooring lines is not necessarily the same as the strain of the aft mooring line(s). Additionally, the mooring footprint (χ_m) can be adjusted in the range of 0.8 to 2. The mooring footprint is given as the ratio between the platform's height above the sea bed at its initial position ($L_{ML,v}$, see figure 8.3) and the horizontal distance of the anchor from the corresponding fairlead ($L_{ML,h}$):

$$\chi_{ML} = \frac{L_{ML,h}}{L_{ML,v}} \tag{8.3}$$

In the case of the mooring system with three mooring lines, the aft mooring line is bridled at the top to connect to both aft ends of the platform (figure 8.3 b)). The length of the bridled section (L_{bridle}) is variable and is defined as the fraction of the length of a straight line connecting the anchor to the center point between both aft fairleads ($L'_{ML,aft}$, see figure 8.3 b)). The relative length ($\chi_{ML,bridle}$) was changed between 0.1 and 0.5 and was defined by

$$\chi_{ML,bridle} = \frac{L_{bridle}}{L'_{ML,aft}} \quad . \tag{8.4}$$

The position of the bridle point ($\vec{\boldsymbol{p}}_{bridle}$) can be found by

$$\vec{\boldsymbol{p}}_{bridle} = \chi_{ML,bridle} \left(\vec{\boldsymbol{p}}_{A,aft} - \begin{bmatrix} 1 \\ 0 \\ 1 \end{bmatrix} \vec{\boldsymbol{p}}_{FL,aft,stb} \right) \quad , \tag{8.5}$$

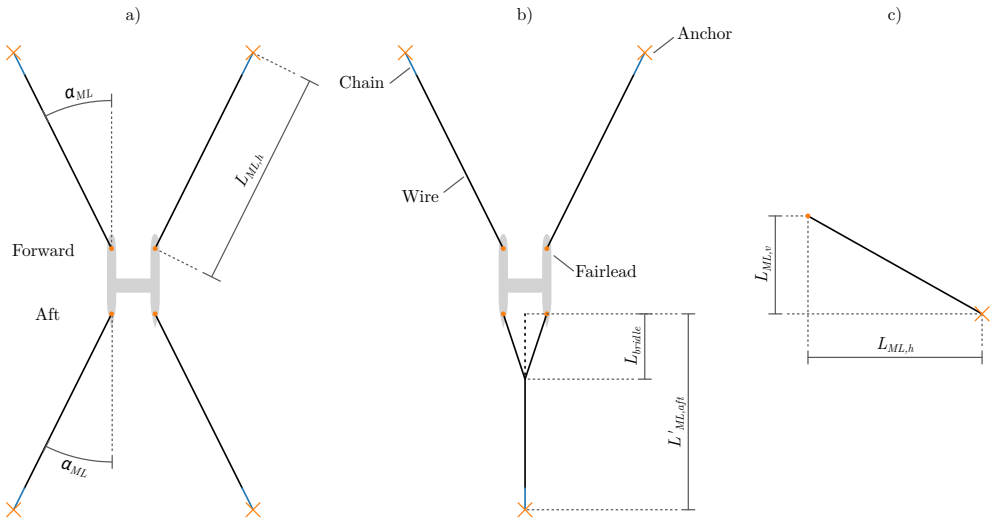

Figure 8.3: Concept of the mooring systems for optimization in top view. The segment of the mooring line which is composed of wire is shown in black, while the chain segment is shown in blue. The anchors are marked with orange crosses while the fairleads are marked with orange dots. For better orientation, the shadow of the platform is shown in light gray. The lengths in b) are measured parallel to the line. **a)** Mooring system with four lines. **b)** Mooring system with three lines and bridled section. **c)** Side view of a single mooring line. Not to scale

where $\vec{p}_{A,aft}$ is the position vector of the aft anchor point and $\vec{p}_{FL,aft,stb}$ the position vector of the aft starboard fairlead. Since the platform is symmetric to the center line, the center point between both aft fairleads can be calculated by simply dropping the y coordinate of one of both fairleads.

8.1.3 Structural

The type of frames used for the hulls and for the strut can be changed individually, with both hulls sharing the same (but mirrored) frame type. For the hull, four different frame types are available as displayed in figure 8.4. The two possible hull types for the strut are shown in figure 8.5. The dimensions of all four types of structural members can be changed as well and is selected from a list that is explained in more detail in section 8.1.3. A limitation is that the diagonal members cannot have a higher serial number than the corresponding girder.

Hollow Steel Profiles for Space Frame

The algorithm selects profiles for the space frame according to the definitions outlined in the norm EN 10210. The thickness range of the round profiles is shown in table 8.1, while the complete list can be found in table B.1.

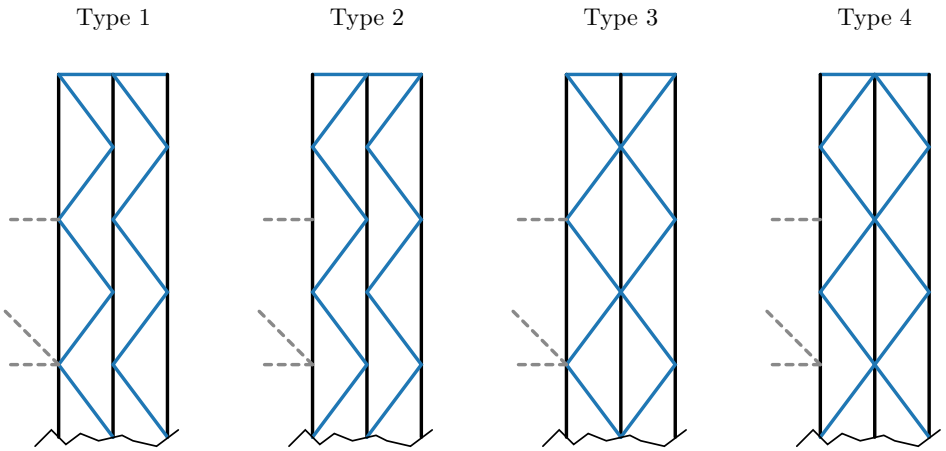

Figure 8.4: Possible configurations of space frame of hulls for the optimization algorithm. The forward end of the starboard hull is shown in the top view. The possible connection with the structure of the strut is shown with dotted gray lines. Vertical lines (shown in black) indicate structural members of type 1 and blue lines indicate structural members of type 2.

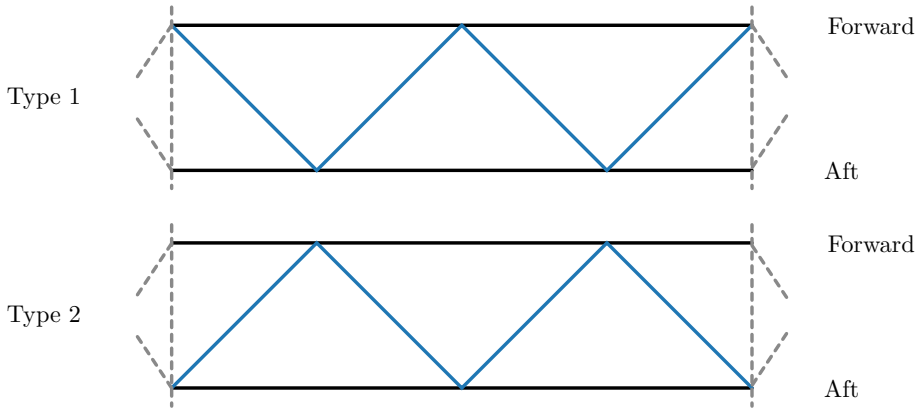

Figure 8.5: Possible configurations of space frame of the strut for the optimization algorithm, shown in top view. The possible connection with the structure of the hull is shown with dotted gray lines. Horizontal lines (shown in black) indicate structural members of type 3 and blue lines indicate structural members of type 4.

Table 8.1: Diameter and thickness range of structural members. All values are given in mm.

Diameter	**Thickness range**	**Diameter**	**Thickness range**
30.0	2.6 . . . 10.0	88.9	3.2 . . . 25.0
31.8	2.6 . . . 10.0	95.0	3.6 . . . 28.0
33.7	2.6 . . . 11.0	101.6	3.6 . . . 28.0
38.0	2.6 . . . 12.5	108.0	3.6 . . . 30.0
42.4	2.6 . . . 14.2	114.3	3.6 . . . 32.0
44.5	2.6 . . . 14.2	121.0	4.0 . . . 32.0
48.3	2.6 . . . 16.0	127.0	4.0 . . . 36.0
51.0	2.6 . . . 16.0	133.0	4.0 . . . 40.0
54.0	2.6 . . . 16.0	139.7	4.0 . . . 45.0
57.0	2.9 . . . 16.0	146.0	4.5 . . . 45.0
60.3	2.9 . . . 17.5	152.4	4.5 . . . 45.0
63.5	2.9 . . . 17.5	159.0	4.5 . . . 55.0
70.0	2.9 . . . 17.5	165.1	4.5 . . . 55.0
76.1	2.9 . . . 20.0	168.3	4.5 . . . 55.0
82.5	3.2 . . . 25.0		

8.1.4 Ballast Tanks

The number of ballast tanks per hull can be modified between one and three (see figure 8.2), resulting in two to six ballast tanks in total. Furthermore, the length and the longitudinal position can be changed for all ballast tanks simultaneously. The length (L_{BST}) is given as a fraction of the length of the buoyancy tanks (L_{BT}) or nominal length of the structure (L_S) as

$$L'_{BST} = \frac{L_{BST}}{L_{BT}} \quad . \tag{8.6}$$

The position of the ballast tank (x_{BLLST}) is given as a fraction of the length difference between the buoyancy tank and the ballast tank (see figure 8.1) by

$$x'_{BST} = \frac{x_{BLLST}}{L_{BT} - L_{BST}} \quad , \tag{8.7}$$

where x'_{BST} is the relative position of the ballast tanks in the x-direction and which is controlled by the algorithm.

8.2 Numerical Model

8.2.1 Preliminary Estimations

The principal dimensions together with mass and buoyancy are reviewed before analyzing the mooring system and the structure of the platform to avoid unnecessary calculations. If the model is unable to float, there is no need to estimate the forces in the mooring line or stresses in the structure of the platform.

The overall length of the hulls (L_{OA}) is defined by the fineness ratio (χ_h) and the outer diameter of the hull (d_H):

$$L_{OA} = 2\chi_h d_H \tag{8.8}$$

Since the segments of the space frame are supposed to be quadratic, the node radius (r_n) has to be of the length of each segment. In this work, the number of segments is set to 10, wherefore the node radius is indirectly defined by the hull's outer diameter (d_H). Accounting for the thickness of the structural elements of type I, a given clearance between shell and structure, and the thickness of the hull itself, the resulting, required node radius is found numerically with the function `root_scalar`. This function is part of the *scipy.optimize*-module of Python 3 that was used in version 1.8.0 [120]. This function determines two positions along the x-axis of the hull where the radius of the tail section and the nose section is equal, with the distance between these positions being 10 times the resulting node radius.

The masses of the buoyancy tanks and the shell are estimated by multiplying the (outer) surface area with the respective thickness and density of the material used. The surface area of the hull is defined in equation (7.10), while the surface area of the buoyancy tank is defined by equation (7.12).

For the structural members, mass and volume are calculated using the corresponding cross-section and the distance between nodes. Since this method does not account for overlapping of the members, it results in slightly overestimating both volume and mass.

8.2.2 Quasi Static Mooring Analysis

Dynamic mooring analyses are computationally expensive. For the mooring analysis during genetic optimization, a quasi-static mooring analysis was performed with the Python package OffshorePy. This module was developed at the Institute of Engineering, National Autonomous University of Mexico, and is described in more detail together with verification and validation in chapter 4.

The platform is modeled with a `RigidBody`, its mass and displaced volume are set to the values calculated beforehand. Fairleads and anchor points are placed directly on the structure and on the sea bed, respectively, and connected via segmented (and bridled, in the case of the three mooring line configuration) mooring lines. For each connection between two segments, a neutrally buoyant float is added, while the line composition is according to the concepts described in section 7.2.3.

The environmental conditions are then adjusted for each load case and the system is solved with a maximum of 250 iterations. If no solution could be found after 250 iterations, but the current maximum angle is within the range of $-75°$ to $75°$, the solving is resumed for another 1000 iterations.

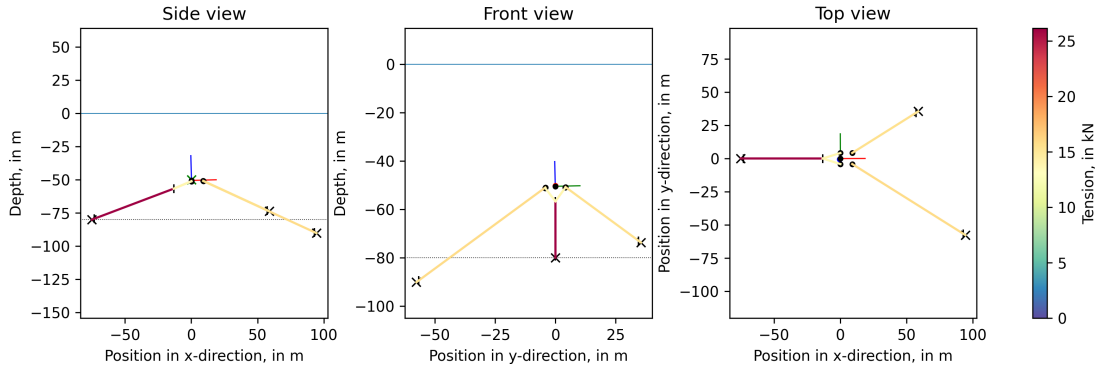

Figure 8.6: Plot of exemplary three mooring line configuration of the system. Note that the sea floor is displayed at the depth directly below the platform and not inclined as indicated by the anchor points.

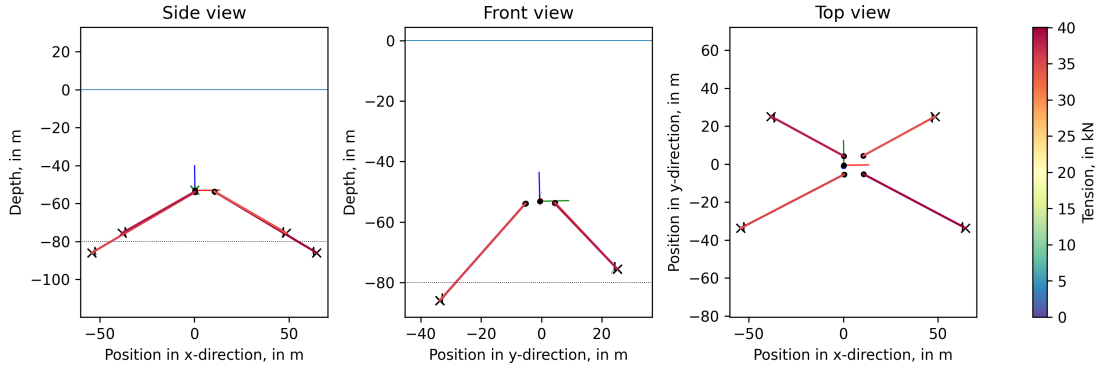

Figure 8.7: Plot of exemplary four mooring line configuration of the system. Note that the sea floor is displayed at the depth directly below the platform and not inclined as indicated by the anchor points.

The system is always solved with the option `zero_matrix` set to `solve` to avoid intermediate states of the system with no restoring forces and thus an empty stiffness matrix. The design proposal is rejected in case an `EquilibriumError` was raised during solving the system, i.e., no solution could be found in either 250 or 1250 iterations. Exemplary plots for the three mooring line configuration and the four mooring line configuration can be seen in figures 8.6 and 8.7, respectively. Note that the sea floor is not displayed inclined as it is assumed for the calculations, but displayed horizontally at the depth directly below the platform's initial position.

8.2.3 Abaqus

The model for the structural analysis was created by using the scripting interface of Abaqus in Python. A script template was created to generate a generic platform. For each design proposal and each load case, a copy of the template is created and the necessary variables such as dimensions, rotations, and loads are adjusted. For each load case, a separate working directory was created. Abaqus

was then executed from Python using the command `abaqus cae nogui=<path_to_script>`, where `<path_to_script>` describes the absolute path to the python script.

The origin of the coordinate system was placed at the very aft of the platform's structure, with y and z centered at the center line. The x-axis was facing forward, the y-axis facing to port, and the z-axis facing upwards.

Mesh The nodes were numbered consecutively starting with the starboard hull, then the port hull, and lastly the strut. For each of the three elements, the numbering started at the aftmost plane. Within each cross-section of the hulls, the numbering started with the lowest node on the center line and proceeded with the node towards the center line. In the case of the strut, the numbering of the nodes started at the starboard hull and ended at the port hull.

Depending on the shape of the structure, the nodes were then connected accordingly with wire elements and organized into four different wire sets, each set for one type of structural member. The cross-sectional profiles of the beams were created with element profiles by using the outer radius and the thickness of the material. To each wire element, the corresponding pipe profile was assigned. For their orientation, the *n1 vector* in positive y-direction was used for all elements on the hulls and the *n1 vector* in positive x-direction was used for all elements of the strut. For the steel used, the linear elastic isotropic material model was chosen with a density of $7850\,\mathrm{kg\,m^{-3}}$, a Poisson ratio of 0.3, and a Young's modulus of 210 GPa. To account for the buoyant force on the elements, the gravitational acceleration was later adjusted to match the correct submerged weight of the structure.

The mesh was then generated over the wire elements with B32 beam elements of size 0.05 m and a deviation factor of 0.1.

Loads and Boundary Conditions The mooring forces of the starboard and port forward moorings were applied to the foremost bottom node on each hull. The force of the buoyancy tanks was applied to the nodes directly above the tank except for the foremost and sternmost nodes. The turbine force is applied to the foremost node of the strut on the center line. The displacement of the aftmost node on the center line was fixed in the y-direction, while the attachment points of the forward mooring lines were fixed in the x-direction, and the z-movement was inhibited at all four attachment points of the mooring lines. The gravity was set to $9.81\,\mathrm{m\,s^{-2}}$.

Load Steps The structure of the platform is evaluated for two different load steps. The first step was the buckling analysis while the second step was used to evaluate the load-bearing capacity of the structure. During the buckling analysis, the first 10 eigenvalues were calculated with 50 vectors and a maximum of 100 iterations.

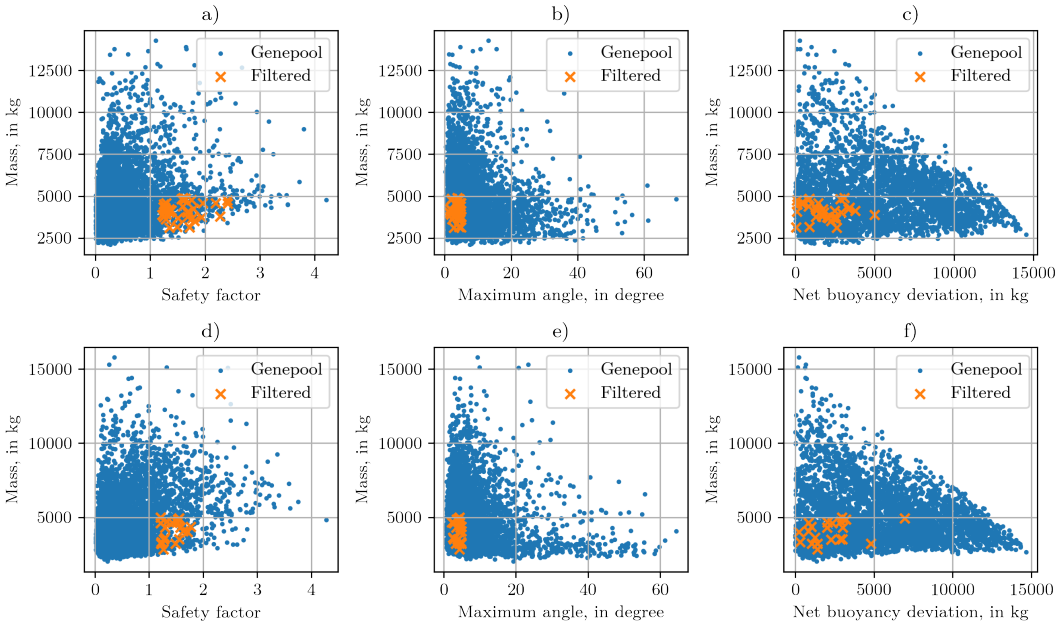

Figure 8.8: Performance of complete gene pool of mooring concepts. **a)-c)** Three-mooring line configuration; **d)-f)** four-mooring line configuration. The complete gene pool is represented by the blue dots, while the orange crosses indicate design proposals that have been filtered regarding maximum mass, maximum inclination, and minimum safety factor.

8.3 Automated Optimization

The optimization was carried out for both, the three-mooring line configuration and the four-mooring line configuration. The results of the process for both configurations can be found in figure 8.8. The design proposals have been filtered to have a maximum mass of 5000 kg, a maximum inclination of 5° in either direction, and a minimum safety factor of 1.2. The performance of all filtered design proposals can be found in table 8.2 for the three-mooring line configuration and in table 8.3 for the four-mooring line configuration. The number following the G in the name of a design proposal indicates its generation and the number following the I indicates the design proposal within its generation. 35 design proposals with these qualities were found with a three-mooring line configuration and 21 design proposals with a four-mooring line configuration. Qualitatively, there was no big difference in the complete gene pool between the three and four-mooring line configurations. The maxima were in the same order of magnitude: The maximum mass was found to be 14 277 kg and 15 774 kg, the maximum safety factor was 4.21 and 4.28, and the net buoyancy deviation peaked at 14 528 kg and 14 667 kg, respectively. The former value correlates to the three-mooring line configuration while the latter value correlates to the four-mooring line configuration. The maximum angle peaked at around 70° since this was a condition for the algorithm to consider this design proposal valid. The filtered design proposals, however, did present slight differences, especially regarding the safety factor. For the three-mooring line configuration, a few

Table 8.2: Filtered design proposals and their performance for the three-mooring line configuration. SF: Safety factor; A: Maximum pitch, list, or yaw angle; B: Net buoyancy deviation.

	Mass	SF	A	B		Mass	SF	A	B
G026I000	3150.80	1.72	4.95	59.96	G109I024	3900.33	1.29	1.95	1676.21
G028I022	4890.93	1.60	3.90	3101.98	G115I021	4765.96	1.75	1.92	811.61
G028I023	4033.93	1.35	1.38	1797.70	G116I021	4746.97	2.41	3.98	92.40
G028I029	4585.51	2.19	3.05	1454.42	G125I031	3747.02	1.94	4.98	1991.58
G029I022	4082.77	1.69	4.68	92.41	G126I012	4132.73	1.37	2.24	2483.97
G030I002	3172.10	1.49	4.38	891.89	G127I014	3691.51	1.77	4.25	2106.10
G033I016	4127.67	1.26	4.03	3777.51	G129I003	3535.02	1.81	4.35	2248.65
G033I020	4588.84	1.30	4.61	374.50	G129I004	4383.11	1.59	4.85	832.33
G037I028	4227.08	1.29	1.71	3340.04	G129I012	3114.80	1.35	2.74	2610.75
G042I030	4811.44	1.57	4.42	2839.74	G132I015	4238.88	1.79	4.07	1334.22
G043I015	3627.72	1.29	2.21	2565.40	G134I000	3886.98	1.22	3.10	4982.99
G044I005	4217.75	1.35	3.90	1761.15	G139I031	4573.55	1.96	4.92	462.05
G062I015	4306.97	1.27	3.82	3420.90	G142I029	4553.19	2.42	3.86	476.47
G062I026	3760.22	1.25	2.76	1291.57	G144I020	3680.95	1.50	3.98	2380.66
G081I005	4158.72	1.38	4.46	1344.46	G146I007	3783.28	2.28	4.88	1707.39
G093I026	4515.65	1.24	3.49	135.52	G146I028	4040.68	1.67	4.52	2882.30
G108I012	4334.50	1.24	4.20	1271.85	G149I028	3772.75	1.68	4.74	2524.39
G109I002	4852.75	1.64	2.15	893.52					

design proposals with a safety factor greater than 2 were found.

From the filtered design proposals, G111I007 (Four mooring lines) presented a good balance between all four metrics. The mass of the system was high and the net buoyancy deviation was also at the higher end. The maximum inclination of the platform, however, was relatively low. Despite the safety factor being low in comparison to the factors found for the three-mooring line configuration, it was among the highest for the four-mooring line configuration. Another good candidate for further optimization was G146I007 (Three mooring lines) due to its much higher safety factor and lower net buoyancy deviation.

8.4 Manual Optimization

For manual optimization, good knowledge of the influence of the parameter is key. In a parametric study, most of the parameters used in the automated optimization were investigated. Each parameter was changed within a reasonable range and increment. Based on the findings, certain parameters were updated and the resulting individual was evaluated after each change in the parameter. The parametric study was performed for each parameter individually, ignoring the fact

Table 8.3: Filtered design proposals and their performance for the four-mooring line configuration. SF: Safety factor; A: Maximum pitch, list, or yaw angle; B: Net buoyancy deviation.

	Mass	**SF**	**A**	**B**		**Mass**	**SF**	**A**	**B**
G002I021	4079.46	1.63	4.84	852.03	G051I022	4328.09	1.29	4.57	2009.24
G019I007	3236.80	1.23	4.33	1401.57	G060I027	4993.51	1.21	4.37	2963.45
G022I003	3240.73	1.49	4.94	1047.13	G111I007	4663.74	1.52	2.20	2034.12
G022I014	2863.36	1.26	4.29	1392.51	G132I021	3331.61	1.23	4.81	299.64
G034I011	4945.88	1.56	4.08	6938.49	G137I000	3511.37	1.27	3.82	2270.18
G035I011	4614.93	1.22	2.75	2353.10	G142I002	4374.23	1.77	4.90	1016.94
G035I018	3536.90	1.55	4.01	2855.94	G145I014	4024.44	1.71	4.30	231.34
G036I030	3651.00	1.29	2.53	1246.35	G150I011	4642.01	1.43	4.46	830.84
G041I022	4724.12	1.33	4.27	2887.71	G161I023	3238.37	1.22	3.31	4794.10
G042I019	3541.02	1.27	2.78	2975.88	G162I009	4313.40	1.58	3.42	3011.61
G047I009	4863.75	1.53	3.52	3208.63					

that the parameters do not change the design proposal independently. After a few iterations, a new study had to be conducted to see the effect on other parameters. After several repetitions, a design was found as no improvement could be found without or at a reasonable cost.

In the following, the process for the design based on G146I007 in a three-mooring line configuration and based on G111I007 in a four-mooring line configuration are described in more detail.

8.4.1 Three-Mooring Line Configuration

The results of the initial parametric study of the design proposal G146I007 for the three-mooring line configuration can be found in figures 8.9 to 8.11. Despite the mass and net buoyancy deviation changing a lot for the hull diameter, their variability was typically very low in comparison to the adjusted safety factor and the maximum inclination. For the sake of simplicity, both, the mass of the system and the net buoyancy deviation, were ignored during the manual optimization. Increasing the relative length of the ballast tanks to 1.0 increased the adjusted safety factor but more importantly lowered the maximum inclination by a quite significant amount (see figure 8.10 b) and c)). While the same held true for the relative position of the ballast tanks, this parameter lost its significance once the relative length of the ballast tanks approaches 1.0 (see figure 8.10 f) and g)). Via the mooring footprint it was also possible to increase the adjusted safety factor while reducing the maximum inclination (see figure 8.10 j) and k)). By increasing the initial strain of the aft lines figure 8.11 f) and g)) and by decreasing the wire diameter of the mooring lines figure 8.11 j) and k)), the same effect could be achieved.

The history of the parameters which were changed can be seen in table 8.4, where each changed parameter is underlined in the next version. In the first iteration of the manual optimization process, the mooring footprint was changed from 1.42 to 1.8 and the relative length of the ballast tank was

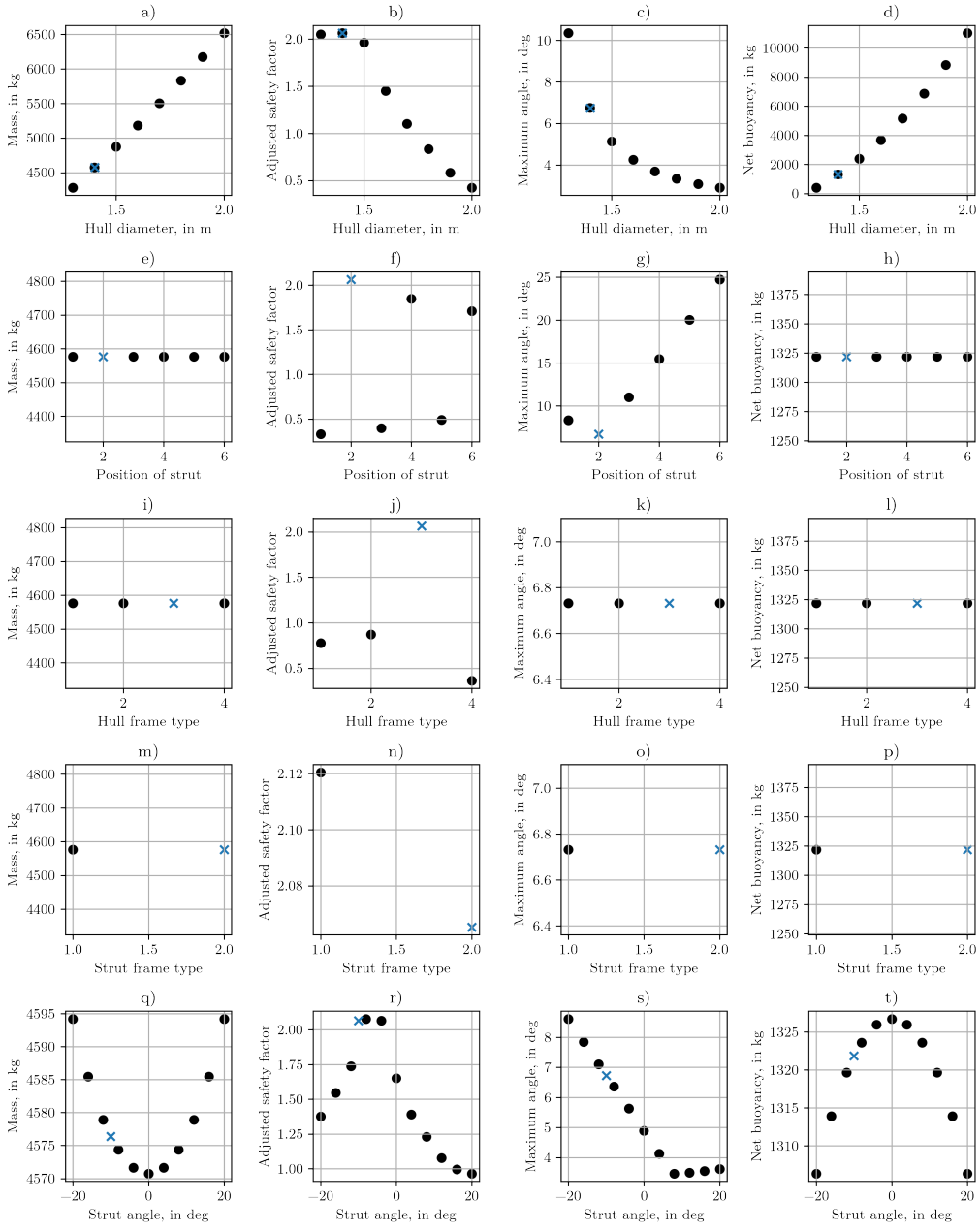

Figure 8.9: Parametric study on G146I007 in three-mooring line configuration.

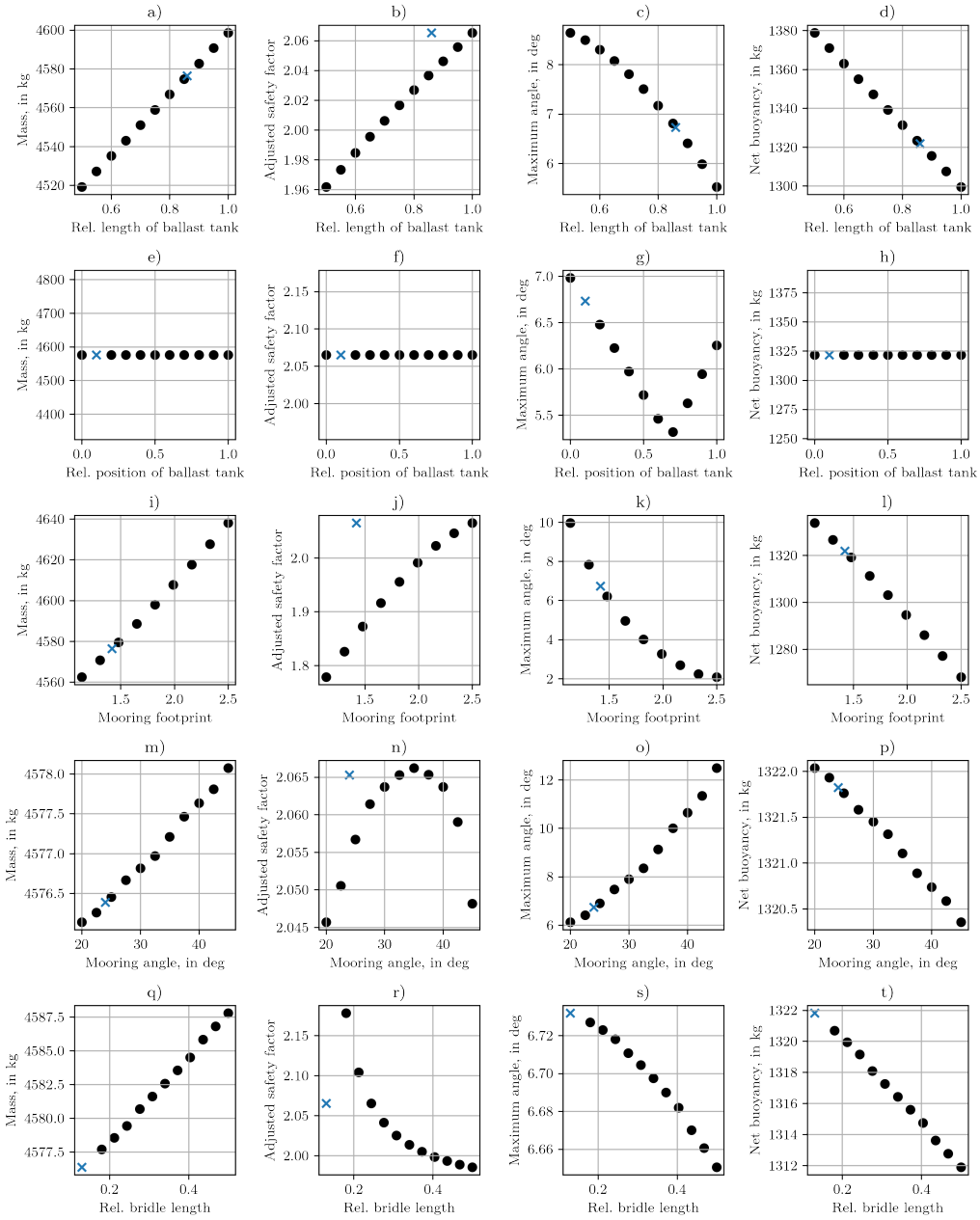

Figure 8.10: Parametric study on G146I007 in three-mooring line configuration (cont.).

increased from 0.86 to 1.0. In the next iteration, the mooring footprint was increased again from 1.8 to 2.5, the mooring angle adjusted from 24° to 25°, and the relative length of the bridle from 0.13 to 0.18. During the third iteration, the strut angle was modified from −10° to −4°, and the mooring angle again from 25° to 32.5°, to finally change the wire diameter in the last iteration from 0.0114 m to 0.0185 m.

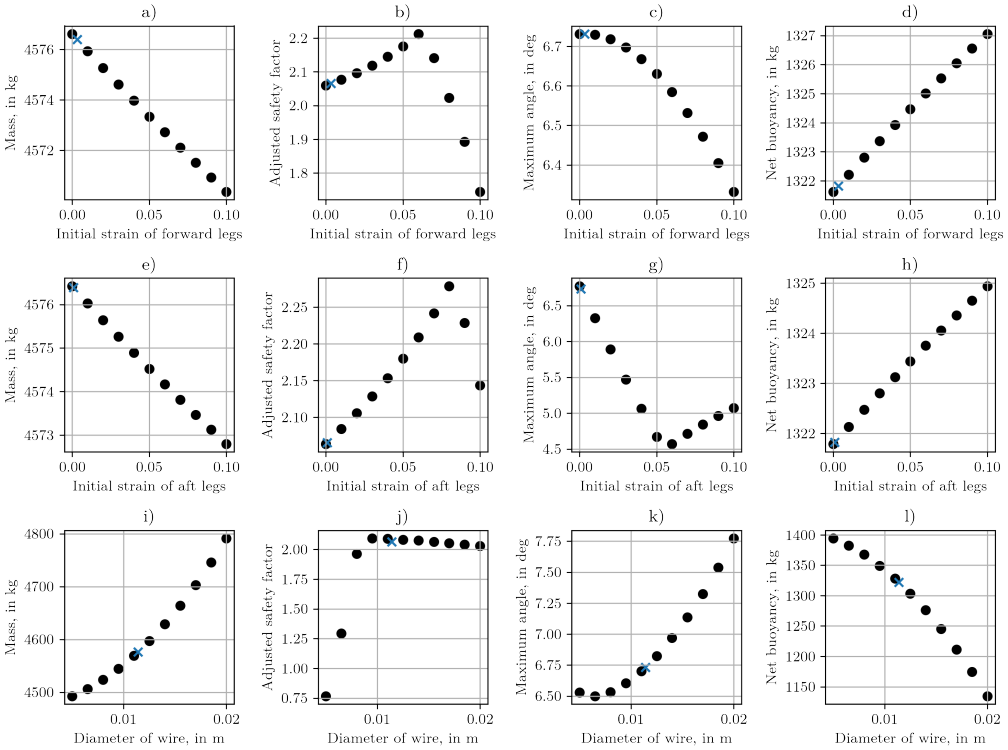

Figure 8.11: Parametric study on G146I007 in three-mooring line configuration (cont.).

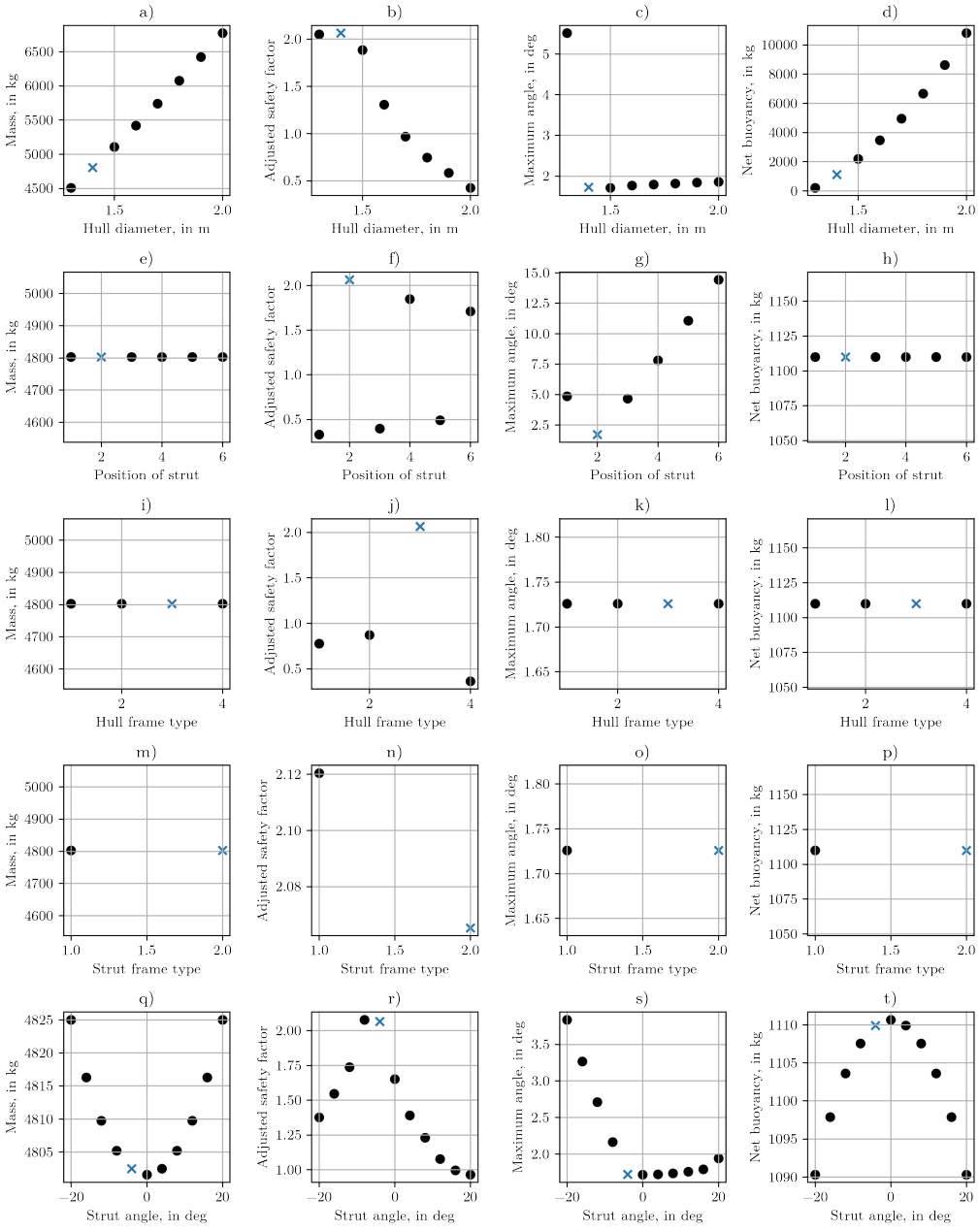

Figure 8.12: Parametric study on manually optimized G146I007 in three-mooring line configuration.

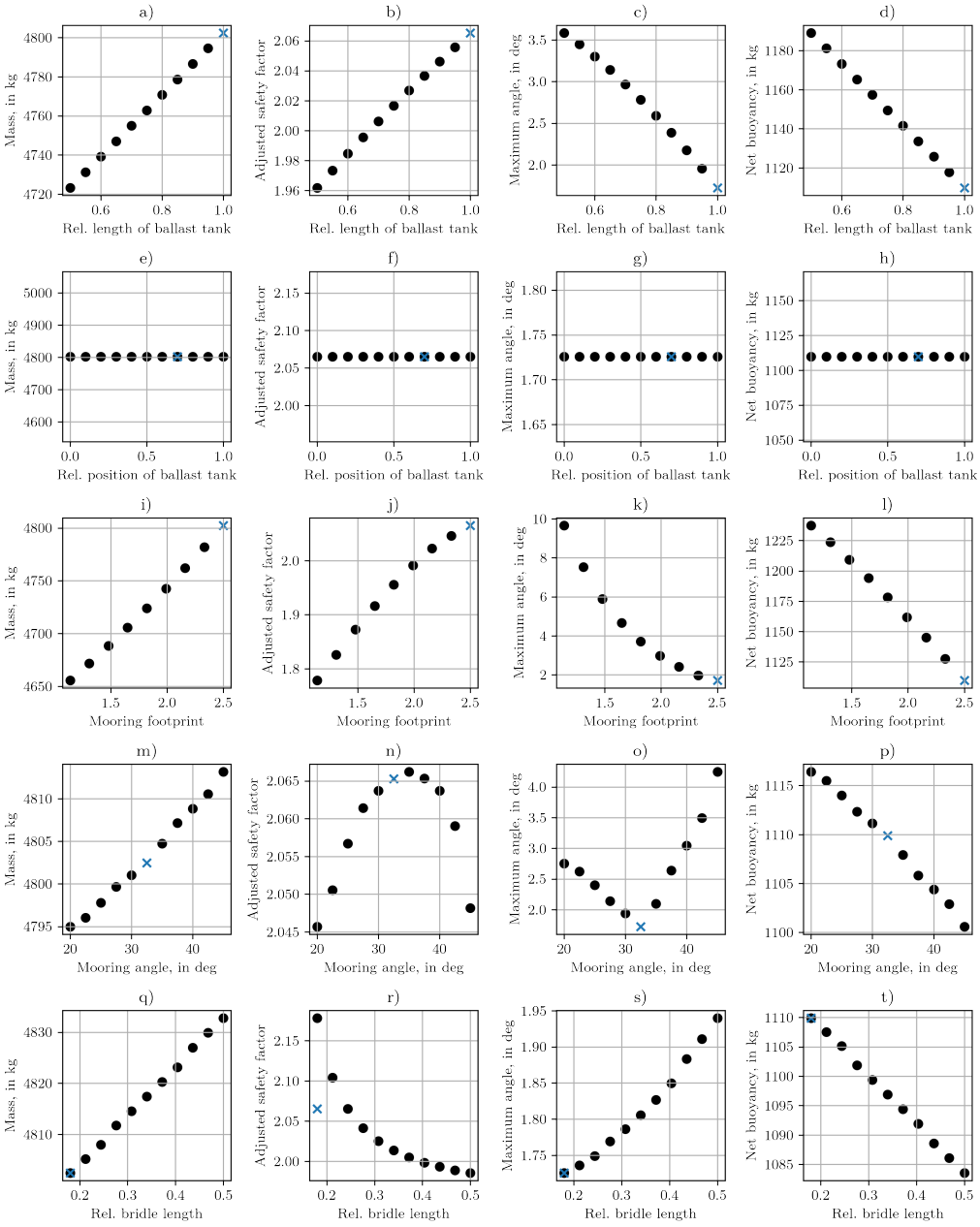

Figure 8.13: Parametric study on manually optimized G146I007 in three-mooring line configuration (cont.).

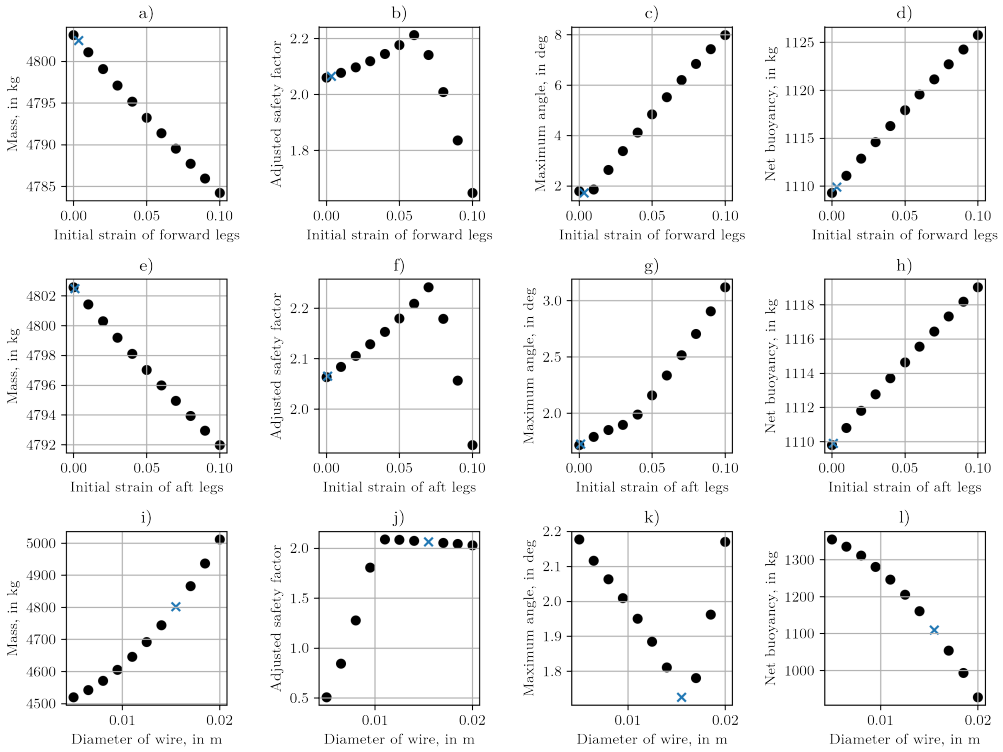

Figure 8.14: Parametric study on manually optimized G146I007 in three-mooring line configuration (cont.).

Table 8.4: Parameter changed during manual optimization of three-mooring line configuration

Parameter	**Basis**	**I1V1**	**I1V2**	**I2V1**	**I2V2**	**I2V3**	**I3V1**	**I3V2**	**Final**
Hull diameter	1.4	1.4	1.4	1.4	1.4	1.4	1.4	1.4	1.4
Position of strut	2	2	2	2	2	2	2	2	2
Frame type of hull	3	3	3	3	3	3	3	3	3
Frame type of strut	2	2	2	2	2	2	2	2	2
Strut angle	-10.0	-10.0	-10.0	-10.0	-10.0	-10.0	-4.0	-4.0	-4.0
Structural member 1	131	131	131	131	131	131	131	131	131
Structural member 2	180	180	180	180	180	180	180	180	180
Structural member 3	430	430	430	430	430	430	430	430	430
Structural member 4	138	138	138	138	138	138	138	138	138
Ballast tanks: number	1	1	1	1	1	1	1	1	1
Rel. length	0.86	0.86	1.0	1.0	1.0	1.0	1.0	1.0	1.0
Rel. position	0.1	0.1	0.1	0.1	0.1	0.1	0.1	0.1	0.1
Mooring footprint	1.42	1.8	1.8	2.5	2.5	2.5	2.5	2.5	2.5
Mooring line angle	24.0	24.0	24.0	24.0	25.0	25.0	25.0	32.5	32.5
Initial forward strain	0.0033	0.0033	0.0033	0.0033	0.0033	0.0033	0.0033	0.0033	0.0033
Initial aft strain	0.0009	0.0009	0.0009	0.0009	0.0009	0.0009	0.0009	0.0009	0.0009
Length of bridle	0.13	0.13	0.13	0.13	0.13	0.18	0.18	0.18	0.18
Mooring wire diameter	0.0114	0.0114	0.0114	0.0114	0.0114	0.0114	0.0114	0.0114	0.0185
Mooring chain diameter	0.0180	0.0180	0.0180	0.0180	0.0180	0.0180	0.0180	0.0180	0.0180

The analysis of the final design proposal can be found in figures 8.12 to 8.14. As can be seen, mass, safety factor, and net buoyancy deviation did change within a reasonable range, with the exception of the hull diameter, which had a great influence on both, mass and net buoyancy deviation (see figure 8.12 a) to d)). However, for the chosen value mass, the adjusted safety factor, and net buoyancy deviation were quite close to their optimum while the maximum inclination was minimized. This was also true for the other parameter except for the relative bridle length. This parameter still had some potential to be optimized by lowering the maximum inclination while increasing the adjusted safety factor. Ultimately the relative length of the bridle was not decreased, in part due to the fact, that the parameter was increased beforehand. Additionally, the performance of the design was satisfactory as the adjusted safety factor is relatively high and the gain in the maximum inclination would have been minimal. Therefore, the iterative process was stopped at this point and the design proposal was analyzed in more depth in chapter 9.

8.4.2 Four-Mooring Line Configuration

The result of the initial parametric study of the design proposal G111I007 for the four-mooring line configuration can be found in figures 8.15 and 8.16. Similar to the three-mooring line configuration, the impact on the mass and the net buoyancy deviation was negligible in contrast to the adjusted safety factor and the maximum inclination. For the manual optimization, those two metrics were ignored, concentrating solely on increasing the adjusted safety factor and minimizing the maximum inclination. Increasing the strut angle to 10° would have lead to a negligible change in the safety factor but to a significant reduction in the maximum inclination (see figure 8.15 r) and s)). The same held true for changing the relative position of the ballast tank to 0.6 (see figure 8.16 f) and g)), the mooring angle to 20° (see figure 8.16 n) and o)), and the initial strain of the forward lines to 0.2 (see figure 8.16 r) and s)). Before a new parameter study was performed, the strut angle was changed from $-2°$ to 10°, the relative position of the ballast tank from 0.45 to 0.6, the mooring wire diameter from 0.0085 m to 0.0125 m, the mooring footprint from 1.38 to 1.6, and the mooring angle from 24° to 20°. During the second iteration, the strut angle was changed from 10° to $-8°$ and the hull diameter from 1.539 m to 1.639 m. In the last and third iteration, the relative length of the ballast tank was changed from 0.75 to 0.9, the mooring angle was changed again from 20° to 27.5° and finally, the mooring footprint was increased from 1.6 to 1.7.

The parametric study of the final version can be seen in figures 8.17 and 8.18, for which an acceptable balance between the four parameters, but especially the safety factor and the maximum inclination were found. Both are located either at an extreme value (e.g., figure 8.17 g)) or a transition point (e.g., figure 8.17 c)).

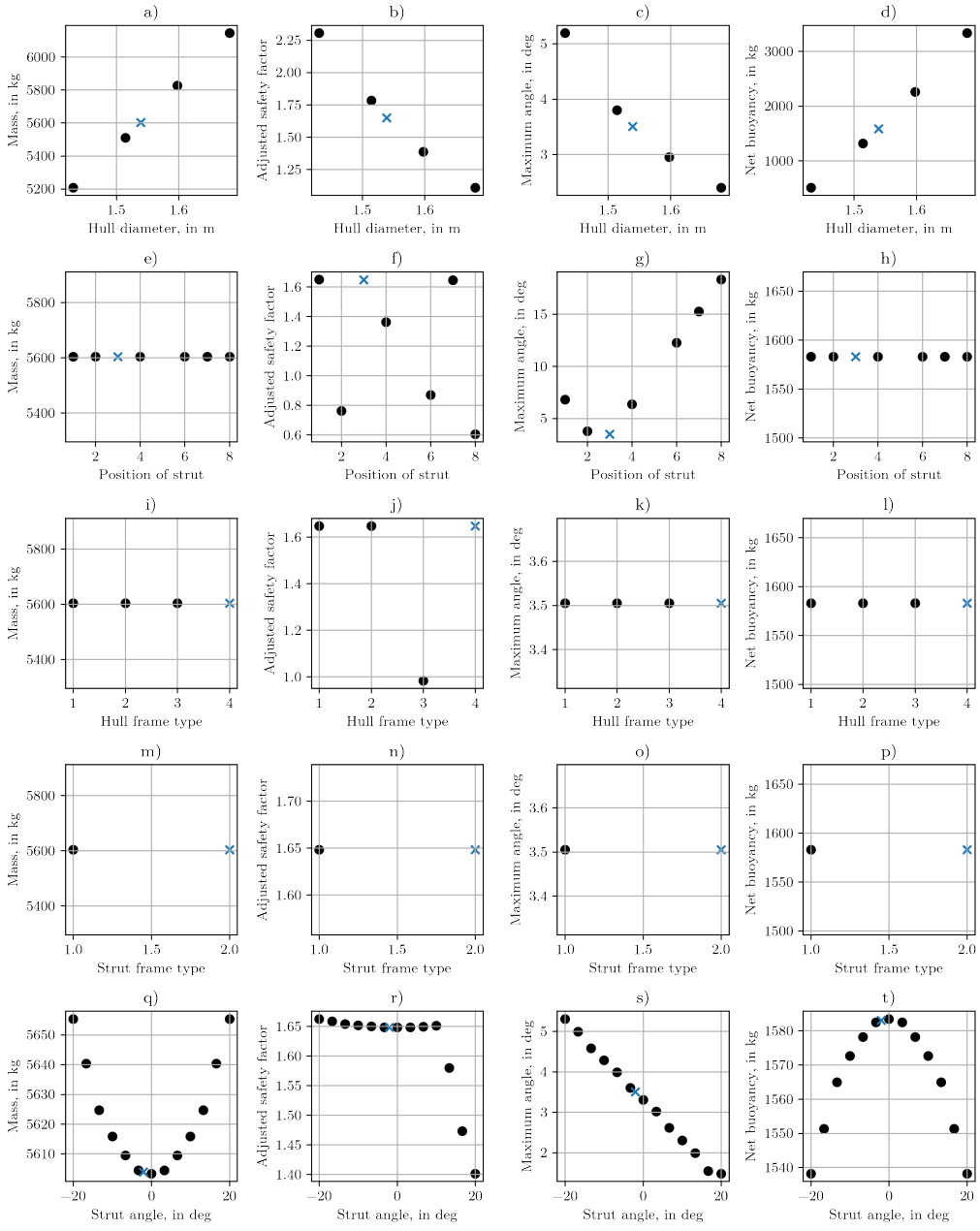

Figure 8.15: Parametric study on G111I007 in four-mooring line configuration.

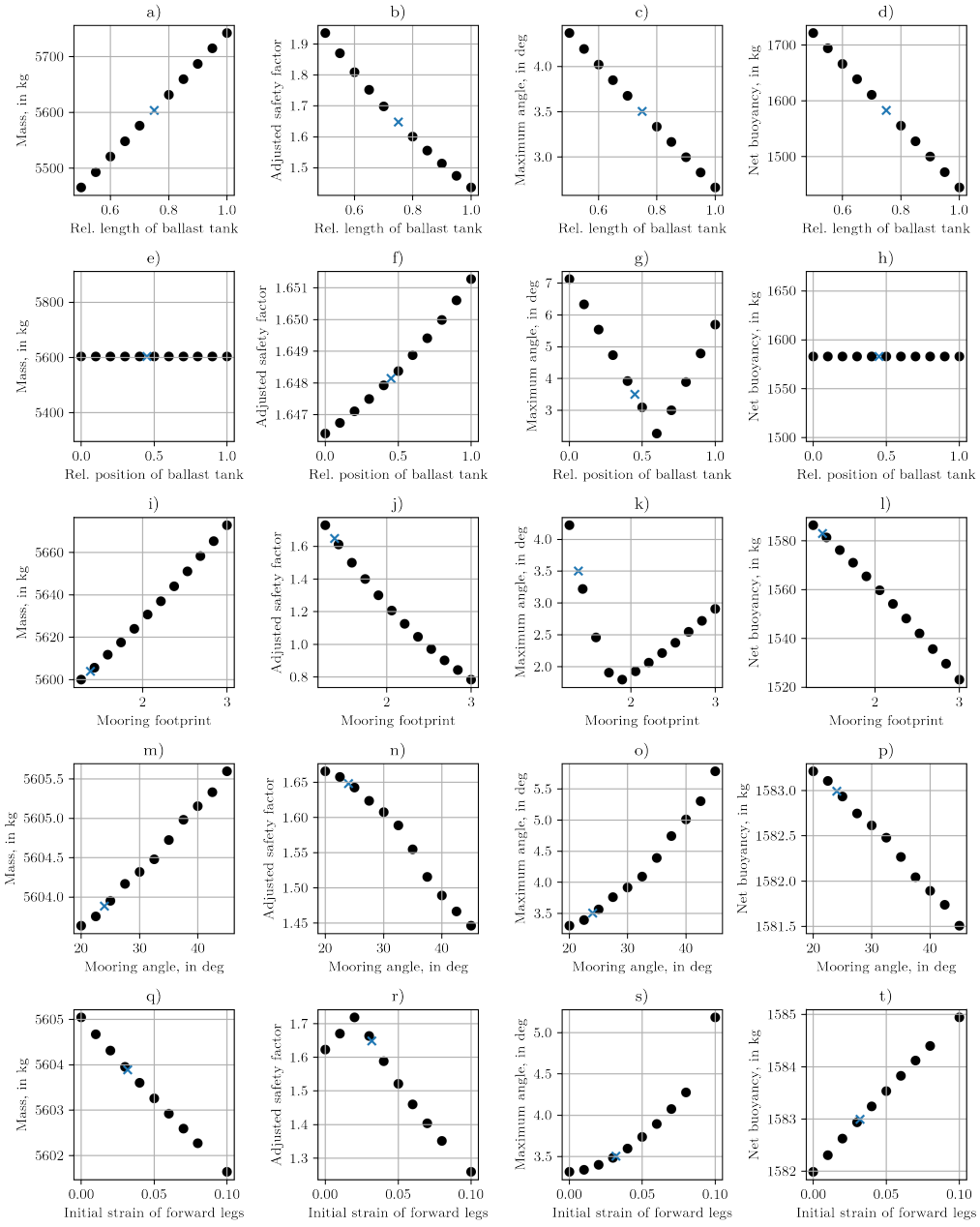

Figure 8.16: Parametric study on G111I007 in four-mooring line configuration (cont.).

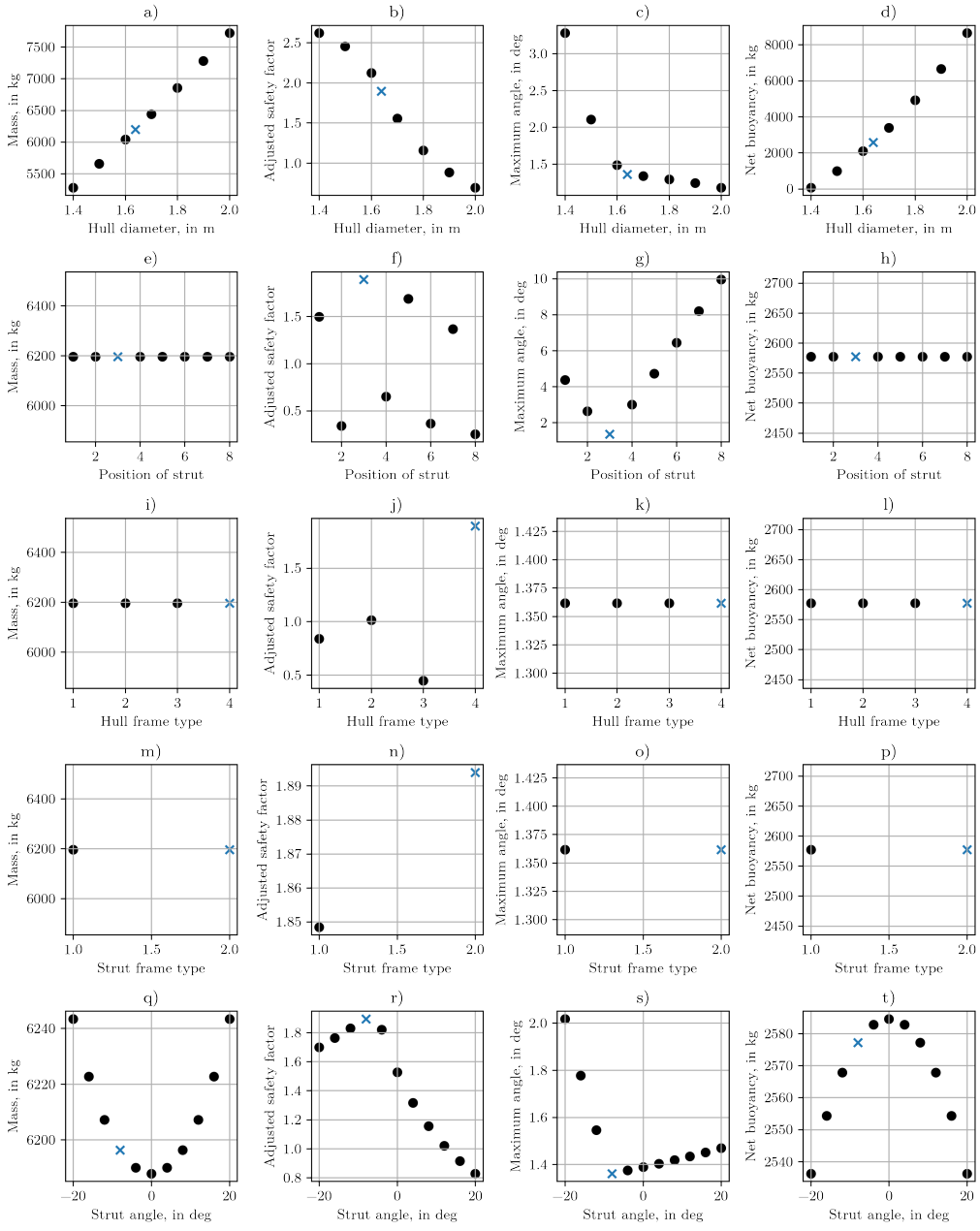

Figure 8.17: Parametric study on manually optimized G111I007 in four-mooring line configuration.

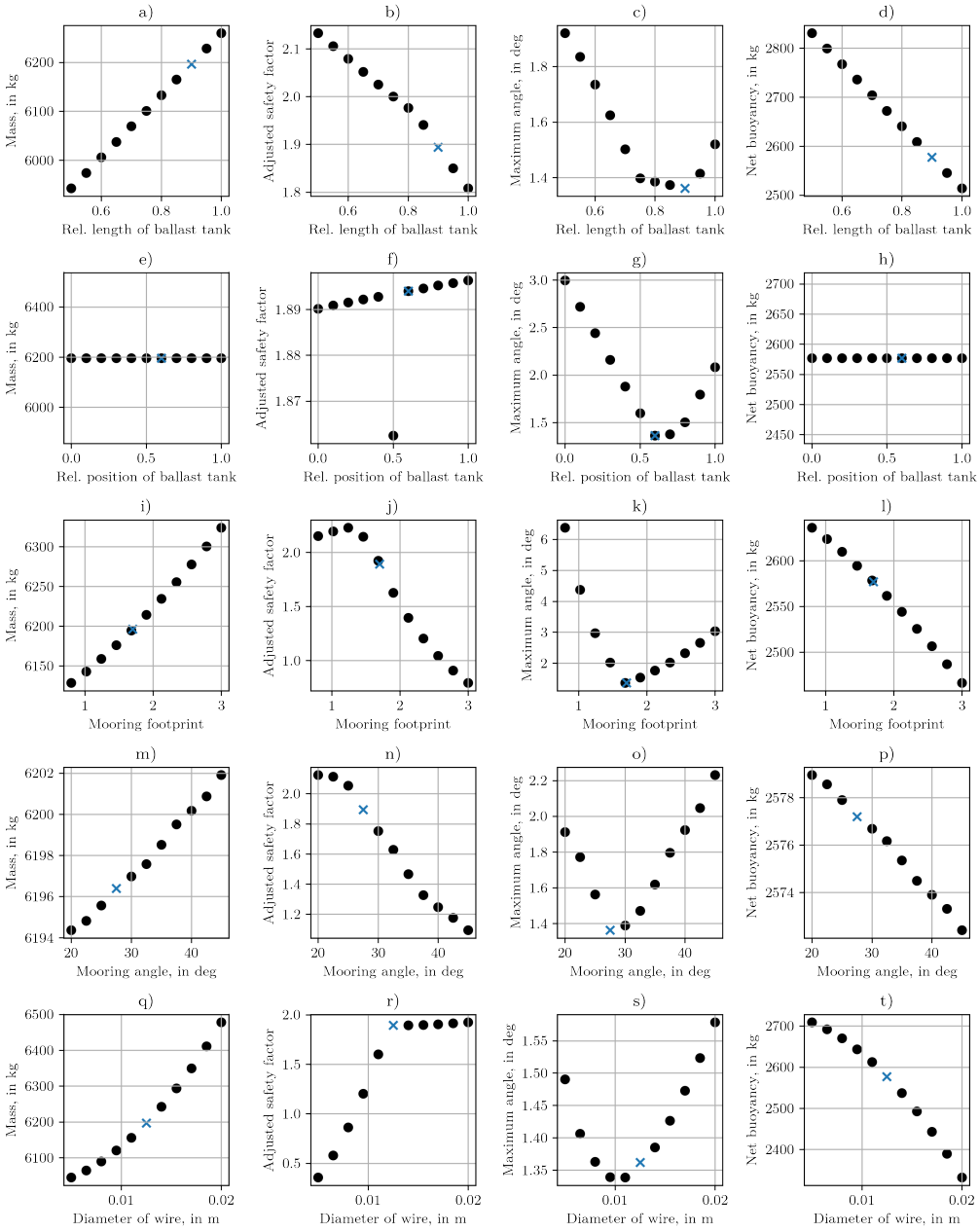

Figure 8.18: Parametric study on manually optimized G111I007 in four-mooring line configuration (cont.).

Table 8.5: Parameter changed during manual optimization of four-mooring line configuration

Parameter	**Basis**	**I1V1**	**I1V2**	**I1V3**	**I1V4**	**I1V5**	**I2V1**	**I2V2**	**I3V1**	**I3V2**	**Final**
Hull diameter	1.539	1.539	1.539	1.539	1.539	1.539	1.539	1.639	1.639	1.639	1.639
Position of strut	3	3	3	3	3	3	3	3	3	3	3
Frame type of hull	4	4	4	4	4	4	4	4	4	4	4
Frame type of strut	2	2	2	2	2	2	2	2	2	2	2
Strut angle	-2.0	10.0	10.0	10.0	10.0	10.0	-8.0	-8.0	-8.0	-8.0	-8.0
Structural member 1	226	226	226	226	226	226	226	226	226	226	226
Structural member 2	279	279	279	279	279	279	279	279	279	279	279
Structural member 3	353	353	353	353	353	353	353	353	353	353	353
Structural member 4	235	235	235	235	235	235	235	235	235	235	235
Ballast tanks: number	3	3	3	3	3	3	3	3	3	3	3
Rel. length	0.75	0.75	0.75	0.75	0.75	0.75	0.75	0.75	0.9	0.9	0.9
Rel. position	0.45	0.45	0.6	0.6	0.6	0.6	0.6	0.6	0.6	0.6	0.6
Mooring footprint	1.38	1.38	1.38	1.38	1.6	1.6	1.6	1.6	1.6	1.6	1.7
Mooring line angle	24.0	24.0	24.0	24.0	24.0	20.0	20.0	20.0	20.0	27.5	27.5
Initial forward strain	0.0319	0.0319	0.0319	0.0319	0.0319	0.0319	0.0319	0.0319	0.0319	0.0319	0.0319
Initial aft strain	0.0251	0.0251	0.0251	0.0251	0.0251	0.0251	0.0251	0.0251	0.0251	0.0251	0.0251
Mooring wire diameter	0.0085	0.0085	0.0085	0.0125	0.0125	0.0125	0.0125	0.0125	0.0125	0.0125	0.0125
Mooring chain diameter	0.0159	0.0159	0.0159	0.0159	0.0159	0.0159	0.0159	0.0159	0.0159	0.0159	0.0159

Chapter 9

Review of Final Design

After optimizing the design concepts, one design proposal was found for the three-mooring line configuration and one for the four-mooring line configuration. Both proposals looked promising since they comply with the requirements for the load cases they were checked against. These limit states, however, resemble solely a subset of the required load cases as defined in IEC 62600-2 [54]. Furthermore, the mooring analysis is based on a quasi-static analysis. While it is possible to design the mooring system based on this type of analysis, it is recommended to perform a dynamic mooring analysis to gain more detailed knowledge of the stresses and positions involved. Furthermore, there are load cases that cannot be simulated with the quasi-static mooring analysis tool used.

In this chapter, the three-mooring line design proposal is analyzed in more depth with the proprietary mooring analysis software *ProteusDS*. The results were used to verify the compliance of the design with the design codes. A free decay test was used to determine the natural frequency of the structure for surge, sway, and heave, a fatigue analysis of the mooring system was performed, and a suitable pile anchor for weak rock was designed. The applied design criteria such as allowable mooring offset and partial safety factors, as well as the load cases considered, can be found in chapter 7.

9.1 Methodology

The dynamic mooring analysis was run based on the load cases defined in section 7.3.1. While for the optimization process, only a few load cases were selected to speed up the process, in this dynamic analysis all defined load cases are used.

9.1.1 Dynamic Analysis of Mooring System

A base model with all required objects and features was created in ProteusDS. The platform was modeled by a *RigidBody* connected to four *DCabels*. Each cable was attached to the platform at the position of the respective fairlead and coupled via a connection object of type *RigidBodyDCable-*

PointConnection. In the case of the forward mooring lines, the remaining end was fixed in space as it is supposed to be connected to the anchor at the sea floor, while the two aft mooring lines of the bridled section were connected to the center aft mooring line via a *DCableDCablePointConnection*. Similar to the forward mooring lines, the lower end of the aft center mooring line was fixed in space to model the anchor. The segments of each mooring line were defined in segment mode 1 according to the specifications. The properties of the used materials were later changed int the `lib.ini`-file to the exact values of the analyzed design.

The shape of the outer shell was created with openSCAD. The result was exported to .stl and then converted to a wavefront `.obj` file which is readable by ProteusDS. For converting the `.stl` file to an `.obj` file, the positions of all vertices were rounded to 1×10^{-3} m. Vertices with the same coordinates were joined and the polygons thus reduced to lines were deleted. Hydrodynamic and aerodynamic loading were switched on for the outer shell, but hydrostatic loads were ignored as the buoyancy is created by the tanks and not the outer shell itself. The tanks themselves were modeled by simple cylinders with same volume and length but different diameter. They were placed at the centroid of the corresponding tank. As these tanks are protected by the outer shell, they only contributed to hydrostatic loading while all dynamic loading was switched off. The buoyancy of all other features such as the structure, the turbine, and the outer shell, were modeled by cuboids of corresponding volume, placed at the position of the feature.

For the first load case LC1, the final position of the corresponding quasi-static mooring analysis was loaded to reduce time for settling of the platform's position. For all subsequent load cases, load case LC1 from the dynamic mooring analysis was loaded and afterwards adjusted to the requirements by the load case.

Environment The current was set to a power law profile applied to the lower 50% of depth. The exponent was 0.143, with heading and magnitude of current as defined in the respective load case. While the water depth was set to the mean depth of 80 m, the inclined bottom was modeled with a custom wavefront file. Waves and wind were only simulated for the load case LC9 at a depth of 0 m, as their effect does not extend down to design depth of the platform. The waves were calculated as Stokes waves of second order with the wave height according to equation (6.8). A constant uniform wind profile was applied with the wind driven current profile as defined in DNV RP C205 [23], reaching down to 20 m of depth. The environmental transition time was set to 5 s for current, waves, and wind with all other environmental parameter were left at their default value.

Simulation The simulation was run for 35 s in simulated time at an output interval of 0.1 s with the standard $4^{\text{th}}/5^{\text{th}}$ Runge-Kutta integrator. The truncation error was set to 0.001 and the time step was limited to 1×10^{-15} s to 1 s and initially set to 0.001 s.

9.1.2 Estimation of Inertia

The inertia of the platform was calculated with respect to the origin of its local reference frame. For irregularly shaped objects such as the shell, the tanks, or the water trapped inside the platform,

the inertia was calculated numerically. Therefore stl files were created with openSCAD for surfaces with additive inertia and surfaces with subtractive inertia. The mass, the centroid, and the inertia of the surfaces were calculated by means of the numpy-stl library (version 2.17.1) for Python [118]. Depending on the type of surface, the reference of the inertia was shifted to the platforms origin with the parallel axes theorem and added to or subtracted from the total inertia. Validation of simple geometric shapes showed, that the numerical solution is equal to the analytical solution with negligible error.

The inertia of the space frame was calculated analytically by calculating the inertia of each structural member, shifting the inertia by means of the parallel axes theorem and tilting the reference axes according to the inclination of the member. The principal moments of inertia of a tubular member are given by [47]

$$J_1 = {}^1\!/_2 m \left({r_o}^2 + {r_i}^2\right) \tag{9.1}$$

$$J_2 = J_3 = {}^1\!/_4 m({r_o}^2 + {r_o}^2 + {}^1\!/_3 l^2) \quad , \tag{9.2}$$

where J_1 is the moment of inertia about its longitudinal axis, J_2 and J_3 about its radial axes, m is the mass of the member, r_o its outer radius, r_i its inner radius, and l its length. To adjust the inertia matrix according to the inclination of the member, the angles between the principal axis and the axis of the reference frame were computed. The entries of the inertia matrix (J_{ij}) in the reference frame of the platform are defined by [47]

$$J_{xx} = J_1 \cos^2 \alpha_{x1} + J_2 \cos^2 \alpha_{x2} + J_3 \cos^2 \alpha_{x3} \tag{9.3}$$

$$J_{yy} = J_1 \cos^2 \alpha_{y1} + J_2 \cos^2 \alpha_{y2} + J_3 \cos^2 \alpha_{y3} \tag{9.4}$$

$$J_{zz} = J_1 \cos^2 \alpha_{z1} + J_2 \cos^2 \alpha_{z2} + J_3 \cos^2 \alpha_{z3} \tag{9.5}$$

$$J_{xy} = J_1 \cos \alpha_{x1} \cos \alpha_{y1} + J_2 \cos \alpha_{x2} \cos \alpha_{y2} + J_3 \cos \alpha_{x3} \cos \alpha_{y3} \tag{9.6}$$

$$J_{xz} = J_1 \cos \alpha_{x1} \cos \alpha_{z1} + J_2 \cos \alpha_{x2} \cos \alpha_{z2} + J_3 \cos \alpha_{x3} \cos \alpha_{z3} \tag{9.7}$$

$$J_{yz} = J_1 \cos \alpha_{y1} \cos \alpha_{z1} + J_2 \cos \alpha_{y2} \cos \alpha_{z2} + J_3 \cos \alpha_{y3} \cos \alpha_{z3} \quad , \tag{9.8}$$

where α_{ji} is the angle between the i-th principal axis and j-th axis of the reference frame.

9.1.3 Structural Analysis

The structural analysis was performed similar to the analysis performed during optimization, which is described in chapter 8. Additionally to the effects considered, the effect of the trapped water and inertia forces of the platform were incorporated. The trapped water was modeled with point masses at each node, together with a point force to counteract their weight. To consider inertia of the platform, both, the linear and rotational, accelerations were adjusted to the values estimated by ProteusDS for the rigid body. To cope with stresses at the connection between strut and hull, the connections with the hull at the corresponding nodes were fitted with stiffener plates. The plates were of trapezoidal shape, had a thickness of 0.03 m, a base length of 0.8878 m and an angle

at either side of 45°. These values are given with respect to the center line of the beams.

9.1.4 Design of Pile Anchor

The relevant design codes for marine applications define various methodologies for designing piles and pile anchors in sand or clay. Methodologies for piles in weak rock, however, are hardly available. A methodology for pile anchors in weak rock, similar to which can be found in the Cozumel Channel, has been proposed by Bañuelos-García et al. [8]. The estimation of the pull-out and lateral capacity were enhanced in this work regarding the aforementioned paper and are described in the following.

Guidance on the design of ground anchors and soil nails is given by Juran and Elias [60], as they touch on durability considerations, performance criteria, and approaches to ensure the stability of the different components. A method for estimating the shaft friction of anchor piles driven in weak rock has been presented by Terente et al. [110]. The method is based on pile testing data which suggested that current methods significantly underestimate the holding capacity of driven piles. Serrano and Olalla [100] calculated the pull-out resistance of anchors in different materials based on the failure criterion of Hook and Brown. Xu et al. [123] reviewed the state of the art of shear mechanism of rock-socketed piles and estimation of the shaft friction. Pullout forces due to skin friction of pre-bored anchor piles were evaluated in the study of Park et al. [81] and compared to different design standards. Different methods for estimating the unit skin friction were compared to measurements by McVay et al. [73]. They found, that estimating the unit skin friction based on the unconfined compressive strength and the split tensile strength gives the best results. In case only the unconfined compressive strength is available, results based on the method of Gupton and Logan gave the best results, while calculations based on standard penetration tests gave the worst results. A similar work on different methods for estimating the skin friction of piles in limestone based on the unconfined compressive strength has been published by Alshenawy et al. [3].

The design of anchors is typically divided into different – more or less – independent tasks: Vertical and horizontal capacity of the anchors. The common assumption of uncoupled behavior between vertical and horizontal load capacity of the soil i.e. uncoupled interaction between soil and structure in horizontal and vertical direction leads to this separation in the design process [88]. Typically, the design of anchors is divided into issues due to installation and issues due to operation, which both have to be considered for evaluating structural integrity [88]. As the pile anchor in rock is typically installed in pre-drilled holes in the rock and then grouted in place, the stresses during installation are neglected.

For a given diameter of the pile (d_a), the minimum wall thickness (t_a) can be calculated based on API RP 2A-WSD [4] by

$$t_a = 6.35 \times 10^{-3} + \frac{d_a}{100} \quad . \tag{9.9}$$

Note that in contrast to the formula given in API RP 2A-WSD [4] the diameter should be given in m and not in mm. The embedded length (L_e) is then calculated following Poulos and Davis [85]

by

$$L_e = 4\left(\frac{E_s I}{n_H}\right)^{1/5} \quad , \tag{9.10}$$

where E_s is the Young's modulus of the steel used, I is the second moment of area of the pile's cross-section, and n_H the horizontal coefficient of subgrade reaction [8].

Structural Capacity

The structural capacity of the pile anchor is analyzed according to Bañuelos-García et al. [8]. However, the material factors are taken according to IEC 62600-2 [54]. Since pile anchors for floating structure are only subject to tension and bending forces, buckling is not part of the expected failure modes and therefore not analyzed. The structural capacity to axial loads is calculated by

$$Q_{sa} = \frac{1}{\gamma_M}\sigma_y A_c \quad , \tag{9.11}$$

where γ_M is the material factor corresponding to the load case and required safety level, σ_y the yield strength of the material used, and A_c the cross-sectional area of the anchor pile. The structural capacity to withstand lateral loads (Q_{sl}) can be estimated by

$$Q_{sl} = \frac{\sigma_{cr} A_c}{2\gamma_M} \quad , \tag{9.12}$$

where the critical stress for shear loads (σ_{cr}) is defined by the maximum of

$$\sigma_{cr} = \frac{1.6E_s}{\left(\frac{d_a}{t'_a}\right)^{5/4}\sqrt{\frac{L_e}{d_a}}} \leq 0.6\sigma_y \quad , \tag{9.13}$$

and

$$\sigma_{cr} = \frac{0.78E_s}{\left(\frac{d_a}{t'_a}\right)^{3/2}} \leq 0.6\sigma_y \quad , \tag{9.14}$$

where t'_a is the adjusted wall thickness. In case the pile is welded via electric resistance, the adjusted wall thickness is calculated by $t'_a = 0.93t_a$, otherwise the adjusted wall thickness is equal to the (nominal) wall thickness of the pile (t_a).

Axial Holding Capacity

The vertical holding capacity or pull-out capacity (Q_{ha}) of a pile in rock is based on the skin friction (Q_f) and the submerged weight of the anchor, calculated by

$$Q_{ha} = Q_f + W_P \quad . \tag{9.15}$$

Different methods are available to estimate the pull-out capacity of piles in soft rocks such as limestone, yet they all rely on the following relation:

$$Q_f = \tau_f A_s \quad , \tag{9.16}$$

where τ_f is the resistance of the shaft to friction and A_s the outer surface area of the shaft. According to the guideline ROM 0.5-05 [86], the resistance of the shaft to friction for rocks is calculated by

$$\tau_f = 0.1 p_{vs} \quad , \tag{9.17}$$

with the vertical pressure for sinking in rock (p_{vs}) defined by

$$p_{vs} = 3 \times 10^{-3} \sqrt{q_{u,r}} f_D f_A \leq 15\,\mathrm{MPa} \quad , \tag{9.18}$$

where $q_{u,r}$ is the compressive strength of the rock (in Pa), f_D a factor to consider the rock quality designation (RQD), and f_A a factor to consider alteration of the rock due to weathering. The design code ROM 0.5-05 [86] includes also a factor for considering inclination of the load, which, however, should be taken as 1 for the cases considered in this work. The factor considering RQD should be the minimum of

$$f_D = 2\sqrt{\frac{s}{d_a}} < 1 \tag{9.19}$$

and

$$f_D = 0.2\sqrt{\frac{\chi_{RQD}}{d_a}} < 1 \quad , \tag{9.20}$$

where d_a is the diameter of the anchor, s the lithoclase spacing, and χ_{RQD} the RQD in percent. The factor for alteration of the rock due to weathering (f_A) shall be taken as 1.0 for weathering of type I, as 0.7 for weathering of type II, and as 0.5 for weathering of type III. For more information on the types of rock weathering see [86, chapter 2.2.9.7].

Additionally to the holding capacity of the anchor in the rock, the maximum allowable axial forces for the connection between steel and grout shall be reviewed. This analysis can be performed according to relevant design codes such as API RP 2A-WSD [4]. For plain connections between steel and grout (i.e. without shear keys), the maximum allowable axial stress is limited to 0.138 MPa and 0.184 MPa, for operation environmental conditions and design environmental conditions, respectively. In case shear keys are used, they should be either a semi circular welded bead, a flat bar with fillet welds, or a round bar with fillet welds. The maximum allowable axial stress is calculated by

$$\tau_f = 138 \times 10^3 + 0.5 q_{u,g} \frac{h}{s} \tag{9.21}$$

for operation environmental conditions, and

$$\tau_f = 184 \times 10^3 + 0.67 q_{u,g} \frac{h}{s} \tag{9.22}$$

for design environmental conditions, where τ_f is the maximum allowable load transfer stress, $q_{u,g}$ the unconfined compressive strength of the grout used, h the outstand of the shear key, and s the spacing of the shear keys or their pitch height if they are arranged in a continuous helix. The unconfined compressive strength of the grout used must satisfy the following condition:

$$17.25\,\text{MPa} \leq q_{u,g} \leq 110\,\text{MPa}$$

For more requirements on the design of shear keys for grouted connections see API RP 2A-WSD [4, chapter 7.4.4.c].

Lateral Holding Capacity

The lateral holding capacity of piles is typically analyzed by means of p-y curves based on the approach first introduced by Winkler. The p-y curves for weak rock such as limestone and the differential equation to model interaction between the pile and the soil are described by Reese [89]. To avoid issues with adhesion under axial loads, the rock is supposed to be loaded until yielding of the rock is reach and the elastic region of the corresponding p-y curve is left. The differential equation describing the pile as beam and its interaction with soil via linear elastic springs is solved with the finite difference method and is given by

$$EI\frac{\mathrm{d}^4 y}{\mathrm{d}z^4} + F_v\frac{\mathrm{d}^2 y}{\mathrm{d}z^2} + k_{ir}y = 0 \quad , \tag{9.23}$$

where E is the Young's modulus of the used steel, I the second moment of inertia of the pile's cross-section, y the lateral deflection of the pile, z the depth below groundline, F_v the vertical load on the pile (if analyzed at the same time), and k_{ir} the initial linear stiffness of the rock at depth z according to the corresponding p-y curve.

At the tip of the pile, the shear force and the bending moment are supposed to be zero, while at the pile's top end at the groundline the shear force is equal to the horizontal load (F_h) and the bending moment equal to the applied moment (M_0). The moment at the groundline is calculated by

$$M_0 = s_{pe}F_h \quad , \tag{9.24}$$

where s_{pe} is the height above groundline of the padeye. Considering these boundary conditions and the distance between nodes of the uniform grid (h), the nonzero entries of the stiffness matrix ($\boldsymbol{K}$) can be derived. Analyzing the axial and lateral capacity of the anchor pile separately as suggested by Randolph and Gourvenec [88] (i.e. $F_v = 0$ for this analysis) leads to the equation system given

by

$$i = 0: \quad \left(2\frac{EI}{h^4} + k_{ir}\right) y_0 - 4\frac{EI}{h^4} y_1 + 2\frac{EI}{h^4} y_2 = \frac{2F_h}{h^2}\left(1 + s_{pe}\right) \tag{9.25}$$

$$i = 1: \quad -2\frac{EI}{h^4} y_0 + \left(5\frac{EI}{h^4} + k_{ir}\right) y_1 - 4\frac{EI}{h^4} y_2 + \frac{EI}{h^4} y_3 = -\frac{F_h s_{pe}}{h^2} \tag{9.26}$$

$$2 \leq i \leq n-2: \quad \frac{EI}{h^4} y_{i-2} - 4\frac{EI}{h^4} y_{i-1} + \left(+\frac{EI}{h^4} + k_{ir}\right) y_i - 4\frac{EI}{h^4} y_{i+1} + \frac{EI}{h^4} y_{i+2} = 0 \tag{9.27}$$

$$i = n-1: \quad \frac{EI}{h^4} y_{n-3} - 4\frac{EI}{h^4} y_{n-2} + \left(5\frac{EI}{h^4} + k_{ir}\right) y_{n-1} - 2\frac{EI}{h^4} y_n = 0 \tag{9.28}$$

$$i = n: \quad 2\frac{EI}{h^4} y_{n-2} - 4\frac{EI}{h^4} y_{n-1} + \left(-2\frac{EI}{h^4} + k_{ir}\right) y_n = 0 \quad , \tag{9.29}$$

where k_{ir} is the stiffness of the rock at the corresponding depth, i is the number of the node, n the number of nodes, and h the distance between nodes, defined as

$$h = \frac{L_e}{n} \quad . \tag{9.30}$$

According to Reese [89], the stiffness of weak rock (k_{ir}) can be calculated based on the initial Young's modulus of the rock (E_{ir}) and the depth below the ground line (z) by

$$k_{ir} = \begin{cases} \left(100 + \frac{400z}{3d_a}\right) E_{ir} & , \text{ for } 0 \leq z \leq 3d_a \\ 500 E_{ir} & , \text{ for } z > 3d_a \end{cases} \quad , \tag{9.31}$$

where d_a is the outer diameter of the anchor pile. The ultimate resistance of the rock is given by

$$p_{ur} = \begin{cases} \alpha_r q_{u,r} d_a \left(1 + 1.4\frac{z}{d_a}\right) & , \text{ for } 0 \leq z \leq 3d_a \\ 5.2\alpha_r q_{u,r} d_a & , \text{ for } z > 3d_a \end{cases} \quad , \tag{9.32}$$

where α_r is the strength reduction factor (see Reese [89]), and $q_{u,r}$ the compressive strength of the rock. The elastic limit deflection of the rock is defined as

$$y_A = \left(\frac{p_{ur}}{2\left(r_{rm} d_a\right)^{0.25} k_{ir}}\right)^{4/3} \quad , \tag{9.33}$$

where r_{rm} is a constant describing the properties of the rock, ranging between 0.0005 and 0.00005 (see Reese [89]).

To find the horizontal load associated to a deflection reaching the elastic limit of the rock, the equation system is solved for an arbitrary horizontal load which then is used to extrapolate (or interpolate) the maximum load. The horizontal holding capacity can then be calculated by

$$Q_{hl} = y_{A,0} \frac{F_h}{y_0} \quad , \tag{9.34}$$

where $y_{A,0}$ is the elastic limit deflection of the rock at groundline, F_h is the arbitrary horizontal load for which the system was solved, and y_0 the lateral deflection at groundline due to the arbitrary force F_h.

9.1.5 Fatigue Life of Mooring Lines and Components

Estimating the annual fatigue damage per environmental state of mooring lines or mooring components is typically based on either T-N curves (i.e. in API RP-2SK [5]) or on S-N curves (i.e. DNVGL OS-E301 [32]). Following the guidance of API RP-2SK [5], the T-N curves for tension-tension fatigue are defined by

$$nR^m = k \quad , \tag{9.35}$$

where n is the number of load cycles leading to failure, R the ratio of tension range to MBL, and m and k are the slope and intercept of the T-N curve, respectively. When calculating the fatigue life of mooring line components, stress concentration factors should be considered. The damage is typically calculated as the combined damage of so called *low frequency* and *wave frequency* tensions which are computed under mean loading due to other environmental conditions such as wind and currents. API RP-2SK [5] suggests four methods for combining damage due to low frequency and wave frequency tensions. Simple summation (Method 1) gives acceptable estimates for the fatigue life when either damage due to wave frequency or damage due to low frequency tensions are dominant. This is the case when the ratio between the wave frequency standard deviation tension and the low frequency standard deviation tension satisfies one of the following conditions:

$$\frac{\sigma_{wf}}{\sigma_{lf}} \geq 1.5 \quad ; \qquad \frac{\sigma_{wf}}{\sigma_{lf}} \leq 0.5$$

Method 2 is based on a combined spectrum of low frequency and wave frequency tensions and gives conservative results which tend to significantly overestimate the fatigue damage. To adjust the combined spectrum method, a narrow-banded correction factor was introduced for Method 3. The most accurate yet computationally very expensive method is Method 4 which is based on time domain cycle counting. Since in this work and under operating conditions no wave frequency tensions are present, the method of simple summation is used. Ignoring the damage due to waves, the annual fatigue damage due to environmental state i is defined by

$$D_{F,i} = \frac{n_{i,lf}}{k} \left(\sqrt{2} R_{i,lf}\right)^m \Gamma\left(1 + m/2\right) \quad , \tag{9.36}$$

where $n_{i,lf}$ is the number of low frequency cycles per year for environmental state i, $R_{i,lf}$ the ratio between low frequency standard deviation tension range and MBL, and Γ the gamma function. The number of low frequency cycles per year for environmental state i is calculated by

$$n_{i,lf} = f_{i,lf} T_i \quad , \tag{9.37}$$

where $f_{i,lf}$ is the zero up-crossing frequency of the tension spectrum in environmental state i, and T_i the time per year spent in environmental state i. With $3.155\,76 \times 10^7$ seconds per year, the time per year spent in environmental state i can be obtained by

$$T_i = 3.155\,76 \times 10^7\, P_i \quad , \tag{9.38}$$

where P_i is the probability for environmental state ii [5].

Low Frequency RMS Tension Range

As stated, for the fatigue calculations only the low frequency fatigue damage is considered. This damage is typically caused by low frequency wave loads, as wind and currents are considered by the mean load, which in turn has influence on the stiffness of the mooring system. However, at design depth of the platform, no wave or wind loads are present, wherefore the low frequency fatigue damage is calculated based on the cyclic current range and the tensions caused by this range in the mooring lines. To find the low frequency component of the current, empirical data are analyzed with a discrete Fourier transform (DFT) and the resulting amplitudes are compared. In case the available data were not obtained with a sufficient sample frequency, the root mean square (RMS) of the difference in current speed between consecutive peaks is evaluated as well. Additionally, the natural frequencies of the platform for surge, sway, and yaw motions should be considered, if supported by the data and available in the result of the DFT. The frequency which causes the most damage is then selected and used for the fatigue analysis.

For the analysis, the following procedure is applied. The natural frequency (f_n) of the complete system is determined by a free decay test simulated with ProteusDS (see section 9.3). For the empirical data of the current for the construction site, the DFT is computed and the frequencies are selected which cause the most damage. The current amplitude ($\hat{u}_k$) corresponding to frequency f of the DFT can be calculated by

$$\hat{u}_k = \frac{2}{n}|X_k| \quad , \tag{9.39}$$

where n is the number of samples and X_k the k-th coefficient of the DFT. The current amplitude ($\hat{u}_k$) based on the difference in current speed between constecutive samples is given by

$$\hat{u}_k = \frac{u_{i+1} - u_i}{2} \quad , \tag{9.40}$$

where u_i is the current for sample i and u_{i+1} the current for sample $i+1$. The mooring system is then analyzed for a higher current (u_h) and a lower current (u_l), resulting in two tensions per load case and mooring line The currents are defined by

$$u_h = u_{LC,i} + \hat{u}_k \quad \text{and} \quad u_l = u_{LC,i} - \hat{u}_k \quad , \tag{9.41}$$

where ($u_{LC,i}$) is the current corresponding to the load case for which the fatigue damage is estimated. For each mooring line the low frequency RMS tension range ($R_{i,lf}$) is calculated as the absolute

difference of both resulting tensions in the line by

$$R_{i,lf} = |T_{lf,h} - T_{lf,l}| \quad , \tag{9.42}$$

where $T_{lf,h}$ is the tension corresponding to u_h, and $T_{lf,l}$ the tensions corresponding to u_l. This analysis is performed for each mooring line, note, that the higher tension is not necessarily caused by the higher current.

The probability for each load case (P_i) is determined based on the return value of the current's magnitude and the probability for the direction. For each magnitude of current, different angles are analyzed. To determine the probability of the direction, the mode of the direction is determined with a histogram for the empirical data and with a bin width of 0.5°. A second histogram is created with a bin width of 5°, centered around the mode. The sum of the probability for the analyzed directions of the current is then adjusted to 100% while maintaining the relation between the directions.

The approach is based on quasi-static calculations. However, as the current is typically assumed to be constant for low frequency fatigue damage estimations the error is expected to be negligible.

9.2 Dynamic Mooring Analysis

A dynamic mooring analysis was run for the three-mooring line configuration. The design proposal resulting from the automated and manual optimization was analyzed with ProteusDS for all 23 load cases as defined in section 7.3.1. For more information on ProteusDS the reader is referred to section 3.3.1 or the manual [35]. The simulations were not able to find static or quasi-static equilibrium within a reasonable simulation time. Therefore, the mean value (in case of position and rotation) and maximum value (in case of tensions) of the last 20 s was selected. For all load cases analyzed, the last 20 s of simulation time do include several periods of oscillation around the mean value. The results of the calculation can be found in the following figures.

Mooring Offset The displacement from its initial position (i.e., mooring offset) can be found in figure 9.1. Noticeable is the altering yet expected y-displacement in figure 9.1. Load cases with the current coming from starboard (ending with B) showed a pronounced deflection in positive y-direction, while the load cases with the current coming from port (ending with C) showed a deflection in the negative y-direction of the same magnitude, yet marginally larger in absolute terms. An exception from this behavior was LC5B which showed with 1.06 m a significantly higher deflection in y-direction than its direct counterpart LC5C with −0.44 m. This is believed to be the result of the missing starboard ballast tank, which leads to a greater deflection in port direction. This is supported by the fact, that the deflections in the load cases with missing port ballast tank showed a qualitatively equal, but opposite behavior. Thus, in LC6B the deflection resulted to 0.40 m and in LC6C to −1.06 m. The deflections during the load cases with the current coming from the front showed noticeable deflection in the opposite direction of the missing ballast tank,

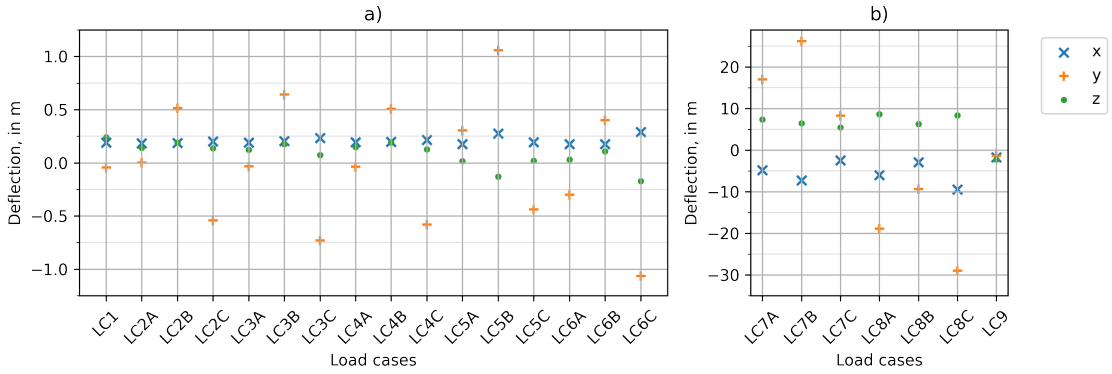

Figure 9.1: Mooring offset of platform in three mooring line configuration.

as for LC5A a deflection of 0.30 m and for LC6A a deflection of −0.30 m was estimated. For the load cases with the starboard mooring line missing (LC7A through LC7C), the platform naturally deflected to port with its maximum offset in the y-direction for LC7B, where it saw current coming from starboard. Analogously, in the load cases with the port mooring line missing (LC8A through LC8C), the platform was pushed to starboard, peaking for LC8C with the current originating from the platform's port side.

Except for the load cases LC7A through LC8C (line loss), the platform was pulled against the current. Despite the constant offset from its initial position, the platform was hardly moved in the x-direction by the presence of the current. For load case LC1 without current a deflection of 0.191 m in the x-direction was estimated while for LC2A a deflection of 0.18 m was determined, both measured from the initial position. The influence of the current was visible yet barely of importance as it was in the order of magnitude of a centimeter. For the load cases with a missing tank and the current coming from the side of the missing tank, a higher forward offset of the platform was detected. For LC5B the platform moved 0.28 m ahead of its initial position, whereas a movement of 0.29 m was calculated for LC6C.

The z-offset of the platform was also slightly above its initial position with 0.24 m for LC1. Outliers could be detected for the cases with a missing ballast tank, especially for the current coming from the same direction. For those cases, the z-offset got below 0 (−0.13 m for LC5B and −0.17 m for LC6C). For the load cases with missing lines, the platform rose to 5.47 m (LC7C) and 8.62 m (LC8A). Notably is the fact, the minimum offsets in each group were achieved for the cases with the current coming from the side with the intact mooring line (LC7C and (LC8B).

Platform Rotation The rotation of the platform for each load case can be found in figure 9.2. In synchronization with the maximum y-offsets, the heel angle of the platform peaks as well. For the load cases with the current coming from starboard, the platform lowered its starboard side, and vice versa for the load cases with the current coming from port. Expectably this was even more pronounced for LC5B (missing starboard ballast tank with current from the same direction) and

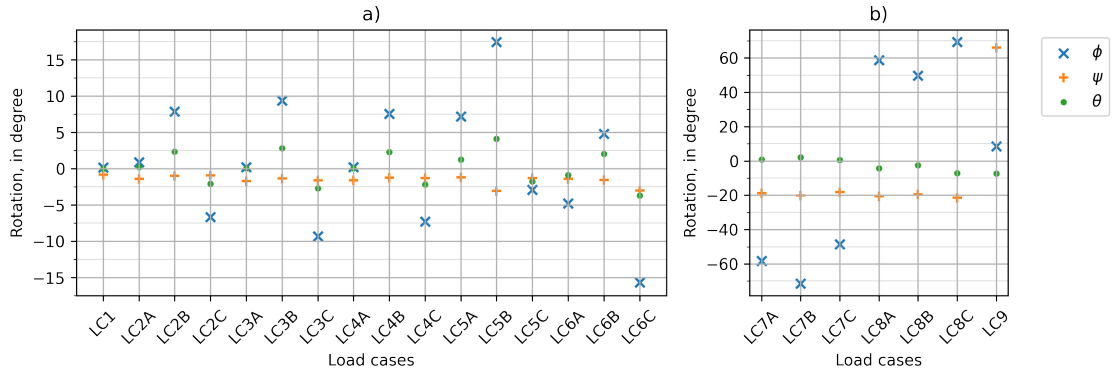

Figure 9.2: Mean rotation of platform in three mooring line configuration.

LC6C (missing port side ballast tank with current from the same direction). The heel angles for the cases with a missing mooring line were very high.

The pitch angle of the platform was rather small, with its peaks found for the load cases with missing lines (LC7A through LC8C) and the cases LC5B and LC6C. Yet, the maximum pitch angle could be found for LC9 when the platform was at the water surface for maintenance. The angle of 66.0° was very high which suggests unfavorable conditions for maintaining the platform. However, as service vessels are required, the platform can be moored to those, hence avoiding extreme motions and especially relative movement between platform and service vessel.

The yaw angle of the platform was relatively close to 0° for the load cases with the current coming from the front. Exceptions were the load cases with missing tanks (LC5A and LC6A), the load cases with missing lines, and the load case for maintenance. For the load cases with the current coming from the sides, the platform tended to yaw towards the other side, as can be seen by the altering yaw angle for load cases B and load cases C. The missing ballast tanks seemed to have shifted the yaw angled towards the opposite side of the missing tank. Thus, in LC5B the yaw angle (4.1°) was much greater than the angles found for the load cases LC2B, LC3B, and LC5B. Similarly, for LC6C, the absolute yaw angle (−3.7°) was greater than for comparable load cases.

Tensions in the mooring lines he maximum tensions in mooring lines are depicted in figure 9.3. As can be seen, the maximum tension could be found in the aft center mooring line for the load cases LC1 through LC6C. For the load cases with missing lines, the remaining forward line was the most loaded, while for the load cases under maintenance, the mooring lines were generally unloaded with the forward port side mooring line seeing the greatest load. For conditions with no current, the aft center mooring line was exposed to nearly double the load to the two forward-facing mooring lines (107.7 kN for aft center, 62.7 kN for forward starboard, and 63.5 kN for forward port). This is expected, as the force by the two forward lines has to be compensated by the aft center mooring line while the mooring angle of the forward lines slightly increases their load.

Due to the current in the load cases LC2A, LC3A, and LC4A, the load on the forward lines

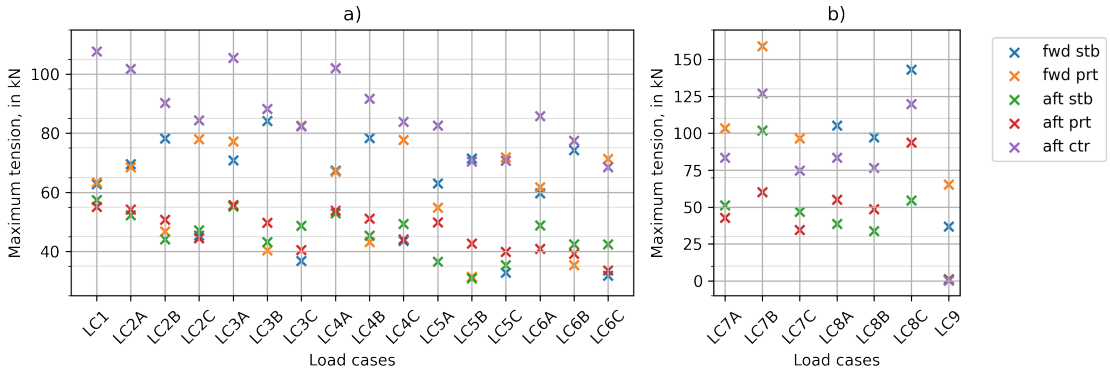

Figure 9.3: Maximum tension in mooring lines of platform. *fwd* refers to the mooring lines connected to the forward end of the platform, *prt* to the port side mooring lines, *stb* to the mooring lines on starboard side, and *ctr* to the one at center line.

increased while the load on the aft mooring lines on port and starboard decreased. For the corresponding load cases with the current coming from the side, the mooring line on the same side saw an increase in its load.

The conditions for the load cases with missing mooring lines (LC7A through LC8C) lead to a pronounced increase in the load on the remaining forward line, with a peak in the load for the load cases with the current coming from the side of the missing line. The load in the forward port side line peaked at 158.9 kN (LC7B) slightly higher than the load in the forward starboard line with 143.1 kN (LC8C). For the four remaining load cases in the scenarios, the peak loads were comparable for the load case with the current coming from the front and for the load cases with the current coming from the same side as the missing line. The loads were estimated to 103.3 kN and 105.3 kN for the load cases LC7A and LC8A, respectively. For the load cases LC7C and LC8B, the loads were calculated to be slightly lower with 96.5 kN and 97.3 kN, respectively.

Ultimate Limit State

The maximum load for the relevant load cases was found to be 109.45 kN. This load was detected in the aft center mooring line during the load case LC1. The ratio between the MBL of 360 kN and the load is 3.289. Since this ratio is significantly higher than the required adjusted safety factor of 2.171, the mooring design satisfies the demands of IEC 62600-10 [53] for the ULS.

The maximum stress was determined to 296 MPa and the minimum buckling factor to 4.8. Considering the corresponding partial load safety factor and material factor, steel of type S450 or similar is sufficient to comply with the design codes.

Serviceability Limit State

The SLS is evaluated for the load cases LC1 through LC4C. Regarding the absolute mooring offset (i.e, displacement from initial position) the platform stayed well within 0.6 m, with the maximum

deflections of 0.56 m and −0.58 m detected in the y-direction for LC3B and LC4C, respectively (see figure 9.1 a)).

The maximum inclinations of the platform for the load cases evaluated were 9.8° and −9.2°. Both heel angles were detected for the load cases LC3B and LC3C, respectively. They are well within the defined limits, however, as these angles are relative to the rotational axis of the turbine they are expected to have negligible influence on the turbine's performance. The maximum heading was estimated to 2.9° and −2.8° for LC3B and LC3C, respectively, and showed a significantly lower deviation. The maximum pitch angle was determined to −1.4° for LC3C.

Accidental Limit State

For the accidental limit state, the maximum load was determined to 162.51 kN for the forward port mooring line. In this condition (LC7B), the forward starboard mooring line was missing with the current flowing in the direction of 150° (i.e. from starboard). The maximum stress was determined to 397 MPa, while the minimum buckling factor was found to be 3.2, for which steel of type S450 or similar is sufficient to satisfy the design requirements.

9.3 Natural Frequency

A free decay test simulated in ProteusDS was used to determine the natural frequency of the platform for surge, sway, and heave. From its initial position the linear velocity of the platform was changed to $3\,\mathrm{m\,s^{-1}}$ for each direction separately. The deflection from its mean position for each direction are shown in figure 9.4 a), c), and e). A discrete Fourier transformation was then performed on the deflection to find the magnitude of the individual components and the peak frequency. The fast Fourier transformation-algorithm was used as provided by the Python-module `numpy` in version 1.22.4 [48]. As depicted in figure 9.4 b), d), and f), the magnitudes of the components have a clear peak at around 14.8 s for surge, at 16.8 s for sway, and at 15.1 s for heave.

9.4 Fatigue Life

The fatigue life of the mooring system and the platform is calculated following the methodology outlined in section 3.2.3, which is based on relevant design codes such as IEC 62600-10 [53] and API RP-2SK [5].

9.4.1 Low Frequency Tension Range

The low frequency tension range is based on changes in the current speed since the influence of wind and waves is negligible for the design depth of the system.

Current Range Since empirical data for the current are only available at a sample period of 30 min and 60 min (see section 6.1), the RMS for the difference in current speed between consecutive

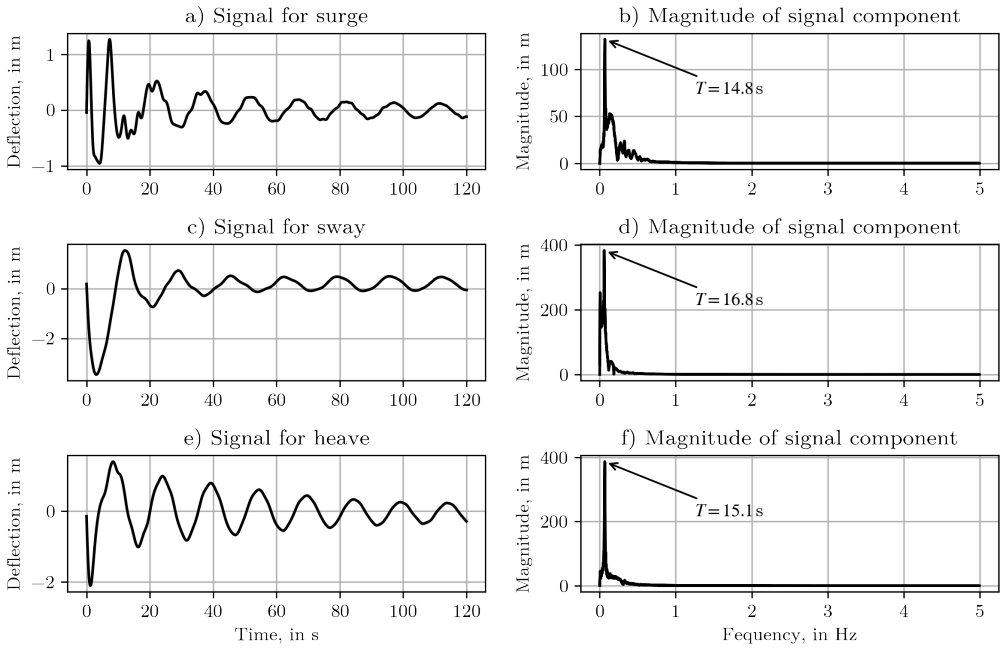

Figure 9.4: Results of free decay test to determine natural frequency of the system. **a), c), e)** show the signal for each direction; **b), d), f)** show the magnitude of the components of the signal, obtained through discrete Fourier transformation.

peaks is calculated as well as the most common time span between two peaks. The current amplitude based on measurements by the CANEK-project with 30 min sample period can be seen in table 9.1. The amplitude for a period of 60 min was obtained as half the height difference of consecutive peaks while the remaining values were obtained from the DFT. Since the current amplitude with a period of 60 min is significantly higher than all other values, a low frequency current range of $8.476 \times 10^{-2}\,\mathrm{m\,s^{-1}}$ with a period of 60 min is used.

Tension Range The tension range was calculated based on the same quasi-static model as described in section 8.2. For each load case, the mooring system was analyzed at the reference current speed, half the current range above the reference speed, and half the current range below the reference speed. The tensions obtained for each mooring line and material type can be found in tables 9.2 to 9.6. The tension denoted with *high* corresponds to the higher current speed and is not necessarily the higher obtained tension. Vice versa, tensions denoted with *low* were caused by the lower current speed. Especially for the forward mooring lines under current coming from the front, the higher tension was caused by the lower current speed. The current direction is reported in the global reference frame of the numerical model with 180° corresponding to the peak current direction in the earth's reference frame. The maximum ratio of mean tension to MBL was 0.31 for the wire.

Table 9.1: Current amplitudes for low frequency fatigue life analysis.

Period in days	**Current Amplitude** in $\mathrm{m\,s^{-1}}$
$^1/_{12}$	4.238×10^{-2}
0.5	4.51×10^{-3}
1.0	7.16×10^{-3}
2.0	8.13×10^{-3}
7.0	1.38×10^{-2}
14.0	1.18×10^{-2}
28.0	2.44×10^{-2}

Table 9.2: Tensions for fatigue life analysis of forward starboard mooring line.

				Tensions			
LC	**Mat.**	**Speed** in $\mathrm{m\,s^{-1}}$	**Dir.** in °	**Mean** in N	**High** in N	**Low** in N	**Range** in N
LC2A	Wire	1.38	180	1.10×10^4	1.08×10^4	1.11×10^4	3.04×10^2
LC2A	Chain	1.38	180	9.26×10^3	9.10×10^3	9.42×10^3	3.18×10^2
LC2B	Wire	1.38	150	1.55×10^4	1.56×10^4	1.54×10^4	2.52×10^2
LC2B	Chain	1.38	150	1.40×10^4	1.41×10^4	1.38×10^4	2.60×10^2
LC2C	Wire	1.38	210	7.37×10^3	7.03×10^3	7.72×10^3	6.87×10^2
LC2C	Chain	1.38	210	5.42×10^3	5.03×10^3	5.79×10^3	7.63×10^2

LC: Load case; Mat.: Material; Dir.: Direction

Table 9.3: Tensions for fatigue life analysis of forward port mooring line.

				Tensions			
LC	**Mat.**	**Speed** in $\mathrm{m\,s^{-1}}$	**Dir.** in °	**Mean** in N	**High** in N	**Low** in N	**Range** in N
LC2A	Wire	1.38	180	1.04×10^4	1.02×10^4	1.05×10^4	2.97×10^2
LC2A	Chain	1.38	180	9.49×10^3	9.33×10^3	9.64×10^3	3.03×10^2
LC2B	Wire	1.38	150	6.64×10^3	6.28×10^3	6.99×10^3	7.05×10^2
LC2B	Chain	1.38	150	5.65×10^3	5.28×10^3	6.01×10^3	7.37×10^2
LC2C	Wire	1.38	210	1.50×10^4	1.51×10^4	1.48×10^4	2.60×10^2
LC2C	Chain	1.38	210	1.42×10^4	1.43×10^4	1.40×10^4	2.63×10^2

LC: Load case; Mat.: Material; Dir.: Direction

Table 9.4: Tensions for fatigue life analysis of aft center mooring line.

				Tensions			
LC	**Mat.**	**Speed**	**Dir.**	**Mean**	**High**	**Low**	**Range**
		in $\mathrm{m\,s^{-1}}$	in °	in N	in N	in N	in N
LC2A	Wire	1.38	180	2.62×10^4	2.65×10^4	2.59×10^4	6.60×10^2
LC2A	Chain	1.38	180	2.54×10^4	2.58×10^4	2.51×10^4	6.63×10^2
LC2B	Wire	1.38	150	2.56×10^4	2.59×10^4	2.53×10^4	6.06×10^2
LC2B	Chain	1.38	150	2.48×10^4	2.51×10^4	2.45×10^4	6.10×10^2
LC2C	Wire	1.38	210	2.56×10^4	2.59×10^4	2.53×10^4	5.90×10^2
LC2C	Chain	1.38	210	2.48×10^4	2.51×10^4	2.45×10^4	5.93×10^2

LC: Load case; Mat.: Material; Dir.: Direction

Table 9.5: Tensions for fatigue life analysis of aft starboard mooring line.

				Tensions			
LC	**Mat.**	**Speed**	**Dir.**	**Mean**	**High**	**Low**	**Range**
		in $\mathrm{m\,s^{-1}}$	in °	in N	in N	in N	in N
LC2A	Wire	1.38	180	1.34×10^4	1.35×10^4	1.32×10^4	3.34×10^2
LC2B	Wire	1.38	150	1.26×10^4	1.27×10^4	1.25×10^4	2.29×10^2
LC2C	Wire	1.38	210	1.35×10^4	1.37×10^4	1.33×10^4	3.67×10^2

LC: Load case; Mat.: Material; Dir.: Direction

Table 9.6: Tensions for fatigue life analysis of aft port mooring line.

				Tensions			
LC	**Mat.**	**Speed**	**Dir.**	**Mean**	**High**	**Low**	**Range**
		in $\mathrm{m\,s^{-1}}$	in °	in N	in N	in N	in N
LC2A	Wire	1.38	180	1.43×10^4	1.45×10^4	1.41×10^4	3.51×10^2
LC2B	Wire	1.38	150	1.44×10^4	1.46×10^4	1.42×10^4	3.97×10^2
LC2C	Wire	1.38	210	1.35×10^4	1.36×10^4	1.34×10^4	2.45×10^2

LC: Load case; Mat.: Material; Dir.: Direction

Table 9.7: Adjusted probabilities for load cases for fatigue life analysis.

Load Case	Direction	Observations	Adjusted Probability
	in °	–	–
LC2A	34.75	10538	9.984×10^{-1}
LC2B	64.75	12	1.137×10^{-3}
LC2C	4.75	5	4.737×10^{-4}

Table 9.8: Annual fatigue damage estimation of forward starboard mooring line.

LC	Mat	TTR	Probability	n cycles	Damage	Total Damage
LC2A	Wire	9.876×10^{-4}	9.984×10^{-1}	8751.9	5.594×10^{-11}	
LC2B	Wire	8.190×10^{-4}	1.137×10^{-3}	10.0	2.962×10^{-14}	5.671×10^{-11}
LC2C	Wire	2.229×10^{-3}	4.737×10^{-4}	4.2	7.409×10^{-13}	
LC2A	Chain	1.034×10^{-3}	9.984×10^{-1}	8751.9	1.150×10^{-7}	
LC2B	Chain	8.441×10^{-4}	1.137×10^{-3}	10.0	7.131×10^{-11}	1.159×10^{-7}
LC2C	Chain	2.478×10^{-3}	4.737×10^{-4}	4.2	7.516×10^{-10}	

LC: Load case; Mat: Material; TRR: Tension range ratio R

9.4.2 Probabilities of Load Cases

Since the effect of the environmental conditions at design depth of the platform is the same for LC2 and LC4 (see section 7.3.1), fatigue life analysis was only performed for LC2A, LC2B and LC2C. The direction, the number of observations, and the adjusted probability can be seen in table 9.7. As can be seen, the current direction was nearly always 34.75° (i.e. flowing in direction of north-east to north) while current hardly flows in the other two directions.

9.4.3 Fatigue Life of System

According to API RP-2SK [5], the intercept parameter of the T-N curves for wire rope depends on the ratio between mean load and MBL, which was found to be 0.13 at maximum. For the wire rope, the T-N curve defined by the intercept $k = 687$ and the slope $m = 4.09$ was used, while for the chain, the T-N curve defined by $k = 316$ and $m = 3.0$ was used. The number of cycles (in the tables denoted with *n cycles*) was calculated according to equations (9.37) and (9.38). The annual damage per load case and total annual damage per mooring line segment are defined by equations (3.9) and (9.36). The results of the calculations per mooring line and load case are shown in tables 9.8 to 9.12. As can be seen, the segment most susceptible to fatigue damage is the chain segment of the aft center mooring line. Considering a safety factor of 3, the expected fatigue life of this mooring line is 320 204 years. Hence it is safe to consider that the mooring lines are unlikely

Table 9.9: Annual fatigue damage estimation of forward port mooring line.

LC	Mat	TTR	Probability	n cycles	Damage	Total Damage
LC2A	Wire	9.639×10^{-4}	9.984×10^{-1}	8751.9	5.066×10^{-11}	
LC2B	Wire	2.289×10^{-3}	1.137×10^{-3}	10.0	1.982×10^{-12}	5.266×10^{-11}
LC2C	Wire	8.434×10^{-4}	4.737×10^{-4}	4.2	1.392×10^{-14}	
LC2A	Chain	9.835×10^{-4}	9.984×10^{-1}	8751.9	9.907×10^{-8}	
LC2B	Chain	2.392×10^{-3}	1.137×10^{-3}	10.0	1.624×10^{-9}	1.008×10^{-7}
LC2C	Chain	8.538×10^{-4}	4.737×10^{-4}	4.2	3.075×10^{-11}	

LC: Load case; Mat: Material; TRR: Tension range ratio R

Table 9.10: Annual fatigue damage estimation of aft center mooring line.

LC	Mat	TTR	Probability	n cycles	Damage	Total Damage
LC2A	Wire	2.144×10^{-3}	9.984×10^{-1}	8751.9	1.331×10^{-9}	
LC2B	Wire	1.967×10^{-3}	1.137×10^{-3}	10.0	1.068×10^{-12}	1.333×10^{-9}
LC2C	Wire	1.914×10^{-3}	4.737×10^{-4}	4.2	3.979×10^{-13}	
LC2A	Chain	2.152×10^{-3}	9.984×10^{-1}	8751.9	1.038×10^{-6}	
LC2B	Chain	1.980×10^{-3}	1.137×10^{-3}	10.0	9.207×10^{-10}	1.041×10^{-6}
LC2C	Chain	1.924×10^{-3}	4.737×10^{-4}	4.2	3.520×10^{-10}	

LC: Load case; Mat: Material; TRR: Tension range ratio R

Table 9.11: Annual fatigue damage estimation of aft starboard mooring line.

LC	Mat	TTR	Probability	n cycles	Damage	Total Damage
LC2A	Wire	1.083×10^{-3}	9.984×10^{-1}	8751.9	8.163×10^{-11}	
LC2B	Wire	7.436×10^{-4}	1.137×10^{-3}	10.0	1.997×10^{-14}	8.170×10^{-11}
LC2C	Wire	1.190×10^{-3}	4.737×10^{-4}	4.2	5.689×10^{-14}	

LC: Load case; Mat: Material; TRR: Tension range ratio R

Table 9.12: Annual fatigue damage estimation of aft port mooring line.

LC	Mat	TTR	Probability	n cycles	Damage	Total Damage
LC2A	Wire	1.140×10^{-3}	9.984×10^{-1}	8751.9	1.008×10^{-10}	
LC2B	Wire	1.290×10^{-3}	1.137×10^{-3}	10.0	1.902×10^{-13}	1.010×10^{-10}
LC2C	Wire	7.950×10^{-4}	4.737×10^{-4}	4.2	1.093×10^{-14}	

LC: Load case; Mat: Material; TRR: Tension range ratio R

to fail due to fatigue.

9.5 Anchor Design

For anchoring MCECs various types of anchors may be suitable, depending on the exact conditions of the construction site and the loads exerted by the mooring lines. For rocky sea floor, as it is expected for the region analyzed in this work, pre-bored pile anchors and gravity anchors are well suited. However, the slope reduces the holding capacity of gravity anchors. Furthermore, the slope is exposed to sediment movement from the higher regions to the lower regions [77, 98].

In this section, the structural capacity and holding capacity of pre-bored pile anchors is analyzed according to the methodology described in section 9.1.4. Based on the dynamic simulations, the design loads considering the individual load factors for each load case were calculated and compared against the capacities.

The design loads (F_d) for analyzing the structural integrity of the anchor are computed according to equation (3.1). In the case of the geotechnical design, the characteristic load was modified with the safety factor and design factor as stated in equation (3.7), with both factors according to IEC 62600-10 [53]. The design loads corresponding to each load case are summarized in table 9.13. As can be seen for this specific mooring arrangement, the anchor design is governed by the load case in equilibrium conditions under no current (LC1). The maximum load in the aft center mooring line is reduced under current. Considering the appropriate factors for the corresponding limit state, all four design loads are superior of this load case in comparison to all other analyzed load cases.

Due to the lack of characterization of the soil in the Channel of Cozumel, characteristics of the assumed limestone are taken from measurements on the mainland. Approximate relations between different values as they can be found in literature. According to Santiago Sierra [94], the density of the limestone was found to be 2110.2 kg m^{-3} with a uniaxial unconfined compressive strength of 27.73 MPa and a minimum Young's modulus of 4.3185 GPa. The tensile strength of limestone was estimated to 6.907 02 MPa following equation (6.10), as published by Nazir et al. [80]. The rock quality was assumed to be 50% with type I weathering. The strength reduction factor (α_r) was taken as 1, and the rock constant (r_{rm}) as 5×10^{-5}.

Considering these values, two pile anchors were designed, one with shear keys and one without. For the steel, a Young's modulus of 210 GPa, a density of 7850 kg m^{-3}, and a yield stress of 235 MPa was assumed. The used grout had a shear stress of 0.138 MPa and a compressive strength of 17.25 MPa. To satisfy the design requirements, the anchor without shear keys required a diameter of 115 mm, a thickness of 13 mm, and an embedded length of 1.714 m. Considering shear keys with a height of 2.4 mm and a pitch of 24.0 mm, the required diameter was reduced to 60 mm, the thickness to 12 mm, and the required embedded length to 1.083 m.

Following the methodology described in section 9.1.4, the structural capacity in axial direction of the anchor without shear keys was determined to $Q_{sa} = 889.956$ kN, the structural capacity in lateral direction was estimated to $Q_{sl} = 266.987$ kN, the holding capacity in axial direction to $Q_{ha} = 85.505$ kN, and the holding capacity in lateral direction to $Q_{hl} = 903.873$ kN. For the anchor

Table 9.13: Loads for the design of a suitable pile anchor.

	Structural		**Geotechnical**	
	axial	lateral	axial	lateral
LC1	44.060 kN	115.624 kN	84.856 kN	178.146 kN
LC2A	33.142 kN	86.146 kN	63.830 kN	132.729 kN
LC2C	32.814 kN	86.162 kN	63.198 kN	132.753 kN
LC2B	34.340 kN	88.476 kN	66.135 kN	136.318 kN
LC3A	33.420 kN	86.792 kN	64.365 kN	133.725 kN
LC3C	33.283 kN	88.808 kN	64.100 kN	136.830 kN
LC3B	33.890 kN	87.411 kN	65.270 kN	134.677 kN
LC4A	34.785 kN	90.482 kN	66.993 kN	139.410 kN
LC4C	33.990 kN	89.659 kN	65.463 kN	138.142 kN
LC4B	35.574 kN	91.781 kN	68.513 kN	141.411 kN
LC5A	20.582 kN	53.939 kN	40.136 kN	84.145 kN
LC5C	5.814 kN	14.939 kN	11.337 kN	23.305 kN
LC5B	24.713 kN	67.382 kN	48.190 kN	105.115 kN
LC6A	20.688 kN	54.302 kN	40.342 kN	84.711 kN
LC6C	33.833 kN	87.446 kN	65.974 kN	136.415 kN
LC6B	21.918 kN	57.227 kN	42.739 kN	89.274 kN
LC7A	21.291 kN	52.820 kN	41.518 kN	82.399 kN
LC7C	39.758 kN	86.206 kN	77.529 kN	134.481 kN
LC7B	9.174 kN	22.559 kN	17.889 kN	35.192 kN
LC8A	27.835 kN	70.054 kN	54.278 kN	109.285 kN
LC8C	11.903 kN	30.304 kN	23.211 kN	47.274 kN
LC8B	29.269 kN	74.349 kN	57.075 kN	115.984 kN
LC9	15.351 kN	16.192 kN	29.566 kN	24.948 kN

with shear keys, the structural capacity in axial direction was calculated to $Q_{sa} = 386.587\,\text{kN}$, the structural capacity in lateral direction to $Q_{sl} = 115.976\,\text{kN}$, the holding capacity in axial direction to $Q_{ha} = 161.083\,\text{kN}$, and the holding capacity in lateral direction to $Q_{hl} = 219.690\,\text{kN}$. It was found, that for the anchor with shear keys, the holding capacity in axial direction was limited by the structural capacity in lateral direction, while for the anchor without shear keys, the adhesion to the grout was the limiting factor.

9.6 Required Mooring Equipment

Aside from the components analyzed above, additional equipment is required. To join the anchor chain to the wire rope, one wire rope socket and a shackle are required. For connecting the forward wire rope to the structure, a joining shackle, an anchor shackle, a swivel, and a wire rope socket are required. At the lower end, the mooring chain requires an anchor shackle to be connected to the anchor pile. Each shackle requires a matching cottor pin. The upper ends of the aft wire ropes are directly connected to the mooring winch. To connect all three aft mooring lines a master link (or sling link) is required together with six joining shackles, three swivels, and three wire rope sockets. If no suitable master link is available, a triangular mooring plate can be used to which the joining shackles are connected. Considering the maximum detected load and the required ASF, all mooring components should be rated for 260 kN. To lower the platform to it's design depth, the winches must be able to store 50 m of wire rope and provide a minimum pull of 11 kN.

Chapter 10

Conclusions

A tool for quasi-static analysis of submerged mooring systems has been presented in chapter 4. It is provided as a Python 3 package and makes use of the widely used numpy package for handling arrays, matrices, and the corresponding mathematical operations. The system is limited to lines that can be approximated by straight lines and the model is unable to estimate hydrodynamic forces. The only forces considered by the model are hydrostatic buoyancy and weight of all objects, forces due to linear elastic strain of the mooring lines. and forces explicitly stated by the user. The calculation is based on three main types of objects. Rigid bodies have six DOFs, while points provide three DOFs. Point objects are divided into fairleads, that are coupled to the corresponding rigid body, anchor points that are fixed in space, and floats that can freely move in space. Mooring lines are represented by line objects which have to be connected to a point object, and thus do not contribute to the global displacement vector. The package has been verified with simple hand calculations to ensure the correctness of the implementation. Furthermore, two laboratory experimental series have been performed to gain knowledge on the error that can be expected. The experiments took place in the open circulation tank in the Institute of Engineering of the UNAM. A buoy was moored with four lines at approximately half the water depth and the magnitude of the current was altered during the experiments. It was measured with a Vectrino just upstream of the buoy while the position of the buoy was tracked using a high-speed camera and later analyzed with ImageJ/Trackmate. While the vertical deflection of the buoy could not be reliably reproduced by the numerical model, the deflection in the x-direction (i.e., in direction of the current) and the trim of the buoy (i.e., rotation around the horizontal axis perpendicular to the current) showed good agreement with the experiments. The errors found are believed to be a result of the experimental setup and the quality of the current in the circulation tank, as high deviations from the mean velocity and unsteady disturbance of the surface were reported. Additionally, the estimation of the tension in the mooring lines was validated with full-scale experiments and numerical predictions with SSMOOR available in the literature. The mean tensions in the mooring line were predicted with a relative error of -7.3% and +4% respectively. Despite the fact of the error for the deviation of the buoy in the laboratory experiments, the low error regarding the mean tensions in the mooring line proves that

the presented Python package for quasi-static analysis of submerged mooring systems is a valuable tool for evaluating this kind of systems in early design phases. Especially the low computational effort required to find a solution sets it apart from commercial software for dynamic mooring analysis, enabling fast review and iteration of design concepts.

Additionally, a genetic algorithm was developed (see chapter 5) to be used in conjunction with the quasi-static mooring analysis tool. The algorithm can optimize a given function for single or multiple objectives, the latter by searching the Pareto-optimal front. The template of the genome is defined in an XML file by giving parameters, their possible range, and their type. Supported types are integers, floating numbers with a defined number of decimal points, and a list of which the parameter is set to a specific item. Additionally to the template, a function for evaluating the individuals has to be provided to the algorithm, returning the objectives and whether the individual satisfies or not the requirements. The algorithm has been tested with the Griewank-function and showed quick and efficient behavior in finding the global minimum.

The Chanel of Cozumel has been analyzed regarding extreme values of wind, waves, and the current, which is described in chapter 6. The analysis of the wind and the waves is based on reanalysis data ERA5 database provided by the ECMWF. The wind speeds have also been analyzed based on the data available in the HURDAT2 database, maintained by the NHC of the United States of America. The current has been based on the HYCOM model and was analyzed at the surface and a depth of 50 m. The methodology for analyzing extreme wind speeds due to hurricanes was taken from available literature, while extreme currents, waves, and wind were estimated based on the POT approach and the GPD with automated threshold selection. The methodology was derived from methods available in the literature, e.g., the threshold selection was not developed by the author of this work. The adapted method was presented in a scientific article and can be found in appendix C. Additionally, a summary of available data in the literature on different environmental conditions such as sea level rise, geotechnical properties of the region, tides, and storm surge is given. A significant discrepancy between the extreme wind speeds due to hurricanes and due to the wind speed at a height of 10 m was found. The data suggest wind speeds of $41.37\,\mathrm{m\,s^{-1}}$ due to a hurricane with a return period of 10 years, while the 10-year wind speed based on ERA5-data was estimated to $15.64\,\mathrm{m\,s^{-1}}$. However, the GPD excess model showed good agreement with the (numerical) observations as between 98.3% and 100% of all observations were found within the corresponding 95% confidence interval. For wind and wave an unbound excess model was found, while for the current at surface and a depth of 50 m a bound model was predicted.

The different design considerations for the platform have been documented and a design concept was elaborated, its description can be found in chapter 7. This design concept was then optimized with the genetic optimization algorithm, while the evaluation of the design proposals was carried out with the Python package for quasi-static mooring analysis and Abaqus for the structural analysis, as can be seen in chapter 8. An optimal design proposal was then selected from the set of optimized proposals and manually fine-tuned with the help of a parametric study. This procedure was carried out for two design concepts with the main difference in the usage of three anchors for the first concept and four anchors for the second concept. Both concepts have been evaluated regarding

their mass, the obtained safety factor, the maximum angle of the platform, and the net buoyancy. The final parametric study of the three-mooring line concept showed interesting behavior. For example, a small increase in the out diameter of the hulls has only a small effect on the safety factor and the maximum angle while the effect on mass and net buoyancy is nearly linear. The angle of the strut showed a small range to obtain a high safety factor, while its influence on net buoyancy and mass is negligible over the analyzed domain. The mooring footprint showed a clear advantage of larger footprints regarding achieved safety factor, maximum angle, and net buoyancy. The angle between the forward mooring lines and the center line showed only a significant effect on the maximum angle, for which an optimum angle could be determined. The three-mooring line concept was finally analyzed based on a dynamic mooring analysis performed with ProteusDS (see chapter 9). The fatigue life of the mooring lines was estimated and two different pile anchor designs suitable for weak rock were designed. Due to the slope and the sediment transport from higher to lower regions found in the Cozumel Channel, dead weight and drag embedment anchors are not suitable. Suction and gravity installed anchors are typically not the best choice for rocky sea bed and their installation is challenging as the slope and the predominant currents may deflect the anchor and alter its ultimate capacity. The recommended anchors are proprietary rock anchors, or (micro-) pile anchors. Therefore, an improved methodology pile anchors suitable for anchoring OCT in regions with the sea floor made up of soft rock was presented. This methodology is based on available scientific literature and international design codes and guidelines. It was found, that the load relevant for the design of the anchor is encountered during equilibrium conditions without current in the aft center mooring line. Current from the front tends to reduce the load on the mooring line, while the safety factors according to the relevant design codes increase the characteristic design load to exceed the loads experienced during line loss. The mooring system, the platform, and the design anchor show good agreement with the relevant, international design codes.

Despite the shorter and therefore stiffer mooring lines on the port side of the platform, no significant effect on the platform was detected during normal operation, which would require its mitigation. Even under heavy loads from the front, the heel of the platform was not significantly influenced. In contrast to the concept with four mooring lines, for the concept with three mooring lines a much higher inclination during line loss was reported. Neither of the concepts would be operable under such conditions, wherefore the acceptability of such deflections depends on other factors such as the permissible strain of the power cable or the stresses in the remaining mooring lines. Due to the reduced number of anchors, the three-mooring line concept seems favorable. This however might be subject to change, as a different construction site, updated parameters of the installed turbine, or requirements of a complete array have great influence.

10.1 Future Research

At the time of writing this work, no turbine ready for deployment is able to efficiently harness the current in the Cozumel Channel. The design of the platform is based on values that can be expected

from a turbine. However, these values may change for the final design of the prototype which requires analysis if the assumptions are still valid and could lead to adjusting several parameters of the platform, the mooring system, or the anchor.

The analysis tool for subsurface mooring systems was only validated with laboratory experimental data and a single full-scale experiment. Further effort could be made with different scales and a more controlled environment, to gain further knowledge on the relative error of the model regarding deflections, rotations, and the involved tensions. Furthermore, the model relies on straight mooring lines, yet could easily be extended by catenary mooring lines considering the drag of the current at different depths. Simple hydrostatic calculations based on the theory of small angles and the metacentric height could also be introduced to extend the tool to bodies floating on the surface. More advanced hydrostatic calculations including effects such as the Froude-Krylov force could be based on polygonal meshes provided by STL files or wavefront obj-files. This would additionally open up the possibility to estimate the hydrodynamic drag by coupling the analysis to a potential flow solver and estimate the friction based on empirical formulae.

The design methodology for the pile anchor in weak rocks it was not validated with laboratory-scale or full-scale experiments and the properties on the rock are based on literature for the region, based on mostly land based specimen. Independently on the use case of the anchor, common recommendation when designing piles for rocks is to verify the assumptions made during design with full-scale tests. For future research, extensive research on anchor design is recommended. This should include taking rock samples from the specific site, ideally taken from under water, to analyze them regarding the key properties for the methodology such as Young's modulus, the unconfined compressive strength or the rock quality designation. The local stratification such as thickness and composition of the sediment layer on top of the rock should also be determined. After evaluation of the specimen in laboratory, full-scale pull-out tests are recommended for validating the design methodology and the laboratory experiments. Due to the small expected dimensions of the anchors, laboratory experiments could be replaced by full-scale, land-based test close to the construction site. In the example, two tubular pile anchors were designed. Especially for the case which is limited by the structural capacity, a solid pile anchor (sometimes also referred to as *micropile*) could be considered to decrease the outer diameter and therefore the effort which has to be made during pre-drilling the rock. Another approach to pile anchor installation in rock is to equip the tip of the pile with a drill head. Such a design might decrease the time required for installation which is favorable if the current presents a significant challenge to the installation of pile anchors.

The platform was designed to house an OCT with its axis parallel to the ocean current and a diameter of 5 m. For smaller diameters, the platform might be scaled down to achieve a more effective material usage. Turbines with significantly larger diameter, however, require the platform to be adjusted in its size. Not only due to the reduced clearance between rotor and hulls, but also due to possibly changed weight and therefore weigth distribution. The Institute of Engineering is currently developing a cross-flow turbine for Cozumel Channel, following the Gorlov design. To mount such a turbine to the current concept of the platform, two turbines might be mounted to the platform at the position a parallel-axis turbine would be placed. One turbine would be pointing upwards and

the other turbine would be pointing downwards in a cantilever configuration. Such a configuration would introduce significant stress in the rotational axes of the turbines, though. A mechanically more favorable design for cross-flow turbines might be to connect the hulls with two struts, an upper and a lower strut. Between both struts, two counter-rotating turbines could be mounted side by side, reducing the mechanical requirements on the shaft and increasing serviceability on the turbines.

Bibliography

[1] Juan Carlos Alcérreca-Huerta, Job Immanuel Encarnacion, Stephanie Ordoñez-Sánchez, Mariana Callejas-Jiménez, Gabriel Gallegos Diez Barroso, Matthew Allmark, Ismael Mariño-Tapia, Rodolfo Silva Casarín, et al. "Energy Yield Assessment from Ocean Currents in the Insular Shelf of Cozumel Island". In: *Journal of Marine Science and Engineering* 7.5 (2019), pp. 1–18. DOI: 10.3390/jmse7050147.

[2] Mohammed A. Almoghayer, David K. Woolf, Sandy Kerr, and Gareth Davies. "Integration of Tidal Energy into an Island Energy System – A Case Study of Orkney Islands". In: *Energy* 242 (Mar. 2022), p. 122547. DOI: 10.1016/j.energy.2021.122547.

[3] Abdulhafiz Alshenawy, Wagdi Hamid, and Ahmed Alnuaim. "Skin Friction Behavior of Pile Fully Embedded in Limestone". In: *Arabian Journal of Geosciences* 11.2 (2018). DOI: 10.1007/s12517-018-3386-9.

[4] American Petroleum Institute. *Recommended Practice for Planning , Designing and Constructing Fixed Offshore Platforms — Working Stress Design (API RP 2A-WSD)*. American Petroleum Institute, 2002.

[5] American Petroleum Institute. *Design and Analysis of Stationkeeping Systems for Floating Structures (API-RP-2SK)*. American Petroleum Institute, 2005.

[6] American Petroleum Institute. *Geotechnical and Foundation Design Considerations (API RP 2GEO)*. 2011.

[7] William L Balsam and Jana Payne Beeson. "Sea-Floor Sediment Distribution in the Gulf of Mexico". In: *Deep Sea Research Part I: Oceanographic Research Papers* 50.12 (2003), pp. 1421–1444. DOI: 10.1016/j.dsr.2003.06.001.

[8] Francisco Bañuelos-García, Michael Ring, Edgar Mendoza, and Rodolfo Silva. "A Design Procedure for Anchors of Floating Ocean Current Turbines on Weak Rock". In: *Energies* 14.21 (2021), p. 7347. DOI: 10.3390/en14217347.

[9] Juan F. Bárcenas Graniel, Jassiel V. H. Fontes, Hector F. Gomez Garcia, and Rodolfo Silva. "Assessing Hydrokinetic Energy in the Mexican Caribbean: A Case Study in the Cozumel Channel". In: *Energies* 14.15 (2021), p. 4411. DOI: 10.3390/en14154411.

[10] Eric Gustavo Bautista Godínez, Rodolfo Silva Casarín, and Paulo Salles A. de Almeida. "Predicción de Marea de Tormenta Generada Por Ciclones Tropicales". In: *Ingenieria Hidraulica en Mexico* 18.2 (2003), pp. 5–19.

[11] H. Berteaux, A. Bocconcelli, C. Eck, S. Kery, and P. Wansek. *The Dynamoor Experiment*. Tech. rep. AD-A265 553. Woods Hole, MA, USA: Woods Hole Oceanographic INstitution, 1993.

[12] Il. Bivol, P. Jeffcoate, L. Johanning, R. Nicoll, J. Steynor, and V. Venugopal. "PLAT-O # 2 at FloWave : A Tank-Scale Validation of ProteusDS at Modelling the Response of a Tidal Device to Currents (Part 2)". In: *Conference: Asian Wave and Tidal Energy Conference*. 2018.

[13] Bridon-Bekaert Ropes Group. *Offshore Oil & Gas - Advanced Rope Solucions for the Offshore Oil & Gas Exploration, Construction and Production Industries*. 2018.

[14] I.G. Bryden, C.R. Bullen, M.S. Baine, and O. Paish. "An Assessment of Tidal Streams as Energy Sources in Orkney and Shetland". In: *Underwater Technology - Journal of the Society for Underwater Technology* 21.2 (1995), pp. 21–29.

[15] Raymond J. Castelli and Ke Fan. "O-Cell Test Results for Drilled Shafts in Marl and Limestone". In: *Deep Foundations 2002*. Orlando, Florida, United States: American Society of Civil Engineers, 2002, pp. 807–823.

[16] Gabriela Chávez, Julio Candela, and José Ochoa. "Subinertial Flows and Transports in Cozumel Channel". In: *Journal of Geophysical Research C: Oceans* 108.2 (2003), pp. 19–1. DOI: 10.1029/2002JC001456.

[17] Günther Clauss, Eike Lehmann, and Carsten Östergaard. *Meerestechnische Konstruktionen*. Berlin, DE: Springer-Verlag Berlin Heidelberg GmbH, 1988.

[18] Stuart Coles. *An Introduction to Statistical Modeling of Extreme Values*. London, UK: Springer-Verlag, 2001.

[19] Dassault Systèmes Simulia Corp. *Abaqus 6.14: Theory Guide*. Providence, RI, USA: Dassault Systèmes Simulia Corp., 2014.

[20] Det Norske Veritas. *Foundations (DNV-CN-30.4)*. DNV, 1992.

[21] Det Norske Veritas. *Geotechnical Design and Installation of Suction Anchors in Clay (DNV-RP-E303)*. DNV, 2005.

[22] Det Norske Veritas. *Certification of Tidal and Wave Energy Converters (DNV-OSS-312)*. DNV, 2008.

[23] Det Norske Veritas. *Environmental Conditions and Environmental Loads (DNV-RP-C205)*. DNV, 2010.

[24] Det Norske Veritas. *Fatigue Design of Offshore Steel Structures (DNV RP-C203)*. DNV, 2010.

[25] Det Norske Veritas. *Buckling Strength of Shells (DNV-RP-C202)*. DNV, 2013.

[26] Det Norske Veritas. *Design of Offshore Wind Turbine Structures (DNV-OS-J101)*. DNV, 2014.

[27] Manhar R. Dhanak and Nikolaos I. Xiros. *Springer Handbook of Ocean Engineering*. Berlin, DE: Springer Nature, 2016.

[28] Jason G. Digalakis and Konstantinos G. Margaritis. "An Experimental Study of Benchmarking Functions for Genetic Algorithms". In: *International Journal of Computer Mathematics* 79.4 (2002), pp. 403–416. DOI: 10.1080=00207160290017942.

[29] DNV GL. *Buckling (DNV GL-CG-0128)*. DNV GL, 2015.

[30] DNV GL. *Certification of Tidal Turbines and Arrays (DNVGL SE-0163)*. DNV GL, 2015.

[31] DNV GL. *Offshore Mooring Chain (DNVGL-OS-E302)*. DNV GL, 2015.

[32] DNV GL. *Position Mooring (DNVGL-OS-E301)*. DNV GL, 2015.

[33] DNV GL. *Tidal Turbines (DNVGL ST-0164)*. DNV GL, 2015.

[34] DNV GL. *Design of Offshore Steel Structures, General - LRFD Method (DNVGL-OS-C101)*. DNV GL, 2019.

[35] Dynamic Systems Analysis Ltd. *ProteusDS Manual - ProteusDS v2.45*. Victoria, BC, Canada: Dynamic Systems Analysis Ltd, 2018.

[36] Dynamic Systems Analysis Ltd. *Current Profiles - ProteusDS Documentation 2.45.0*. https://documentation.dsaocean.com/tutorials/Tutorials/PDS-AAV.html. 2020.

[37] Job Immanuel Encarnacion, Cameron Johnstone, and Stephanie Ordonez-Sanchez. "Design of a Horizontal Axis Tidal Turbine for Less Energetic Current Velocity Profiles". In: *Journal of Marine Science and Engineering* 7.7 (2019), p. 197. DOI: 10.3390/jmse7070197.

[38] Dmitry Ershov, Minh-Son Phan, Joanna W. Pylvänäinen, Stéphane U. Rigaud, Laure Le Blanc, Arthur Charles-Orszag, James R. W. Conway, Romain F. Laine, et al. *Bringing TrackMate into the Era of Machine-Learning and Deep-Learning*. Preprint. Bioinformatics, 2021.

[39] F.D. Fenton. "Nonlinear Wave Theories". In: *Ocean Engineering Science* 9 (1990).

[40] H. A. Flores. "Submarine Cables to 34,5 kV of the Carmen Beach to the Cozumel Island in Mexico. Corrosion Specification and Operative Experiences". In: *43rd International Conference on Large High Voltage Electric Systems 2010, CIGRE 2010*. Paris, FR: CIGRE, 2010, pp. 1–8.

[41] Carlos M. Fonseca and Peter J. Fleming. "Genetic Algorithms and Multiobjective Optimization: Formulation, Discussion and Generalization". In: *Genetic Algorithms: Proceedings of the Fifth International Conference* 93 (1993), pp. 25–50.

[42] Michael P Fourman. "Compaction of Symbolic Layout Using Genetic Algorithms". In: *Proceedings of the First International Conference on Genetic Algorithms and Their Applications*. Psychology Press, 1985, pp. 141–153.

[43] Carwyn Frost, Michael Togneri, Penny Jeffcoate, Thomas Lake, Cuan Boake, Ralf Starzmann, and Alison Williams. "A Comparison of Platform and Sea-Bed Mounted Flow Measurement Instrumentation for SME PLAT-I". In: *International Marine Energy Journal* 5.2 (2022), pp. 195–200. DOI: 10.36688/imej.5.195-200.

[44] Eberhard Gischler and Anthony J Lomando. "Recent Sedimentary Facies of Isolated Carbonate Platforms, Belize-Yucatan System, Central America". In: *Journal of Sedimentary Research* 69.3 (1999), pp. 747–763. DOI: 10.2110/jsr.69.747.

[45] David E Golberg. "Genetic Algorithms in Search, Optimization, and Machine Learning". In: *Addison Wesley, Reading* 1989.102 (1989), p. 36.

[46] Isaac González García. "Aplicación de La Teoría de Valores Extremos En El Análisis de Eventos Hidrometeorológicos". PhD thesis. Mexico City, MX: Nacional Autonomous University of Mexico, 2014.

[47] Karl-Heinrich Grote and Jörg Feldhusen. *Dubbel - Taschenbuch Für Den Maschinenbau*. Berlin: Springer-Verlag Berlin Heidelberg GmbH, 2011.

[48] Charles R Harris, K Jarrod Millman, Stéfan J van der Walt, Ralf Gommers, Pauli Virtanen, David Cournapeau, Eric Wieser, Julian Taylor, et al. "Array Programming with NumPy". In: *Nature* 585 (2020), pp. 357–362. DOI: 10.1038/s41586-020-2649-2.

[49] Jassiel V. Hernández-Fontes, Angélica Felix, Edgar Mendoza, Yandy Rodríguez Cueto, and Rodolfo Silva. "On the Marine Energy Resources of Mexico". In: *Journal of Marine Science and Engineering* 7.6 (2019). DOI: 10.3390/jmse7060191.

[50] Jassiel V. Hernández-Fontes, M. Luisa Martínez, Astrid Wojtarowski, José Luis González-Mendoza, Rosario Landgrave, and Rodolfo Silva. "Is Ocean Energy an Alternative in Developing Regions? A Case Study in Michoacan, Mexico". In: *Journal of Cleaner Production* 266 (2020), p. 121984. DOI: 10.1016/j.jclepro.2020.121984.

[51] H. Hersbach, P. Berrisford, G. Biavati, A. Horányi, J. Muñoz Sabater, J. Nicolas, C. Peubey, R. Radu, et al. *ERA5 Hourly Data on Single Levels from 1959 to Present*. Copernicus Climate Change Service (C3S) Data Store (CDS), 2018.

[52] IHI Corporation. "IHI Demonstrated the World's Largest Ocean Current Turbine for the FIrst Time in the World". In: *IHI Engineering Review* 52.1 (2019), pp. 6–9.

[53] International Electrotechnical Commission. *Marine Energy – Wave, Tidal and Other Water Current Converters – Part 10: Assessment of Mooring System for Marine Energy Converters (IEC 62600-10)*. International Electrotechnical Comission, 2015.

[54] International Electrotechnical Commission. *Marine Energy – Wave, Tidal and Other Water Current Converters – Part 2: Design Requirements for Marine Energy Systems (IEC 62600-2)*. 2016.

[55] International Standard. *Petroleum and Natural Gas Industries Fixed Steel Offshore Structures (ISO 19902)*. ISO, 2007.

[56] ITTC. *The Specialist Committee on Deep Water Mooring*. Tech. rep. International Towing Tank Conference, 1998.

[57] Penny Jeffcoate and Nick Cresswell. "Field Performance Testing of a Floating Tidal Energy Platform - Part 2: Load Performance". In: *Proc. of the 4th Asian Wave and Tidal Energy Conference (AWTEC)*. 2018.

[58] Penny Jeffcoate, Fabrizio Fiore, Ellery O'Farrell, Dean Steinke, Andrew Baron, Ralf Starzmann, and Sarah Bischof. "Comparison of Simulations of Taut-Moored Platform PLAT-O Using ProteusDS with Experiments". In: *Proceedings of AWTEC*. 2016.

[59] Penny Jeffcoate, John Mcdowell, and Nicholas Cresswell. "Floating Tidal Energy Site Assessment Techniques for Coastal and Island Communities". In: *Asian Wave and Tidal Energy Conference 2018*. Taipei, Taiwan, 2018.

[60] Ilan Juran and Victor Elias. "Ground Anchors and Soil Nails in Retaining Structures". In: *Foundation Engineering Handbook*. Boston, MA, USA: Springer, 1991, pp. 868–905.

[61] Björn Kjerfve. "Tides of the Caribbean Sea". In: *Journal of Geophysical Research* 86.C5 (1981), p. 4243. DOI: 10.1029/jc086ic05p04243.

[62] Björn Kjerfve. *Coastal Oceanographic Characteristics: Cancun-Tulum Corridor, Quintana Roo*. Tech. rep. Campeche, Mexico: Consultores en Ecosistemas Costeros y Marinos, 1994.

[63] J. A. Knappett, M. J. Brown, H. Aldaikh, S. Patra, C. D. O'Loughlin, S. H. Chow, C. Gaudin, and J. T. Lieng. "A Review of Anchor Technology for Floating Renewable Energy Devices and Key Design Considerations". In: *Frontiers in Offshore Geotechnics III - 3rd International Symposium on Frontiers in Offshore Geotechnics, ISFOG 2015*. Richardson 2008. 2015, pp. 887–892.

[64] Christopher W. Landsea and James L. Franklin. "Atlantic Hurricane Database Uncertainty and Presentation of a New Database Format". In: *Monthly Weather Review* 141.10 (2013), pp. 3576–3592. DOI: 10.1175/MWR-D-12-00254.1.

[65] Jorma Laurikkala, Martti Juhola, and Erna Kentala. "Informal Identification of Outliers in Medical Data". In: *5th International Workshop on Intelligence Data in Medicine and Pharmacology*. 2000, pp. 20–24.

[66] Mengyao Li. *Assessment and Mitigation of Environmental Impacts from the Bay of Fundy Tidal Energy Development, Atlantic Canada*. Tech. rep. Vancouver, Canada: The University of British Columbia, 2021.

[67] Bingchen Liang, Zhuxiao Shao, Huajun Li, Meng Shao, and Dongyoung Lee. "An Automated Threshold Selection Method Based on the Characteristic of Extrapolated Significant Wave Heights". In: *Coastal Engineering* 144.March 2018 (2019), pp. 22–32. DOI: 10.1016/j.coastaleng.2018.12.001.

[68] Kai-Tung Ma, Yong Luo, Thomas Kwan, and Yongyan Wu. *Mooring System Engineering for Offshore Structures*. Gulf Professional Publishing, 2019.

[69] Fermín Mallor, Eulalia Nualart, and Edward Omey. "An Introduction to Statistical Modelling of Extreme Values. Application to Calculate Extreme Wind Speeds." In: *Hub research paper* 36.November 2009 (2009), p. 45. DOI: 10.1198/jasa.2002.s232.

[70] S. J. Mazzullo, K. E. Anderson-Underwood, C. D. Burke, and W. D. Bischoff. "Holocene Coral Patch Reef Ecology and Sedimentary Architecture, Northern Belize, Central America". In: *PALAIOS* 7.6 (1992), pp. 591–601. DOI: 10.2307/3514871.

[71] John McDowell, Penny Jeffcoate, Lars Johanning, Tom Bruce, and Weichao Shi. "Increasing the Accuracy of Initial Feasibility Studies - Utilising Numerical Models to Estimate the LCoE of Floating Tidal Energy Platforms". In: *Applied Energy Symposium: MIT A+B*. Boston, USA, 2019.

[72] Wes McKinney. "Data Structures for Statistical Computing in Python". In: *Proceedings of the 9th Python in Science Conference*. 2010, pp. 56–61.

[73] M C McVay, F.C. Townsend, and R.C. Williams. "Design of Socketed Drilled Shafts in Limestone". In: *Journal of Geotechnical Enginee* 118 (1992), pp. 1626–1637.

[74] Dallas J. Meggitt, Eric Jackson, Jon Machin, and Robert Taylor. "Marine Micropile Anchor Systems for Marine Renewable Energy Applications". In: *OCEANS 2013 MTS/IEEE - San Diego: An Ocean in Common*. San Diego, CA, USA: IEEE, 2013, pp. 1–7.

[75] L Mitas and H Mitasova. "Spatial Interpolation". In: *Geographical Information Systems: Principles, Techniques, Management and Applications*. Ed. by P. Longley, M.F. Goodchild, D.J. Maguire, and D.W. Rhind. GeoInformation International, Wiley, 1999, pp. 481–492.

[76] Faith A. Morrison. *An Introduction to Fluid Mechanics*. Cambridge, UK: Cambridge University Press, 2013.

[77] Gerd Muckelbauer. "The Shelf of Cozumel, Mexico: Topography and Organisms". In: *Facies* 23 (1990), pp. 185–240. DOI: 10.1007/BF02536714.

[78] D. F. Myring. "Theoretical Study of Body Drag in Subcritical Axisymmetric Flow." In: *Aeronautical Quarterly* 27.3 (1976), pp. 186–194. DOI: 10.1017/s000192590000768x.

[79] M. Nachtane, M. Tarfaoui, I. Goda, and M. Rouway. "A Review on the Technologies, Design Considerations and Numerical Models of Tidal Current Turbines". In: *Renewable Energy* 157 (Sept. 2020), pp. 1274–1288. DOI: 10.1016/j.renene.2020.04.155.

[80] Ramli Nazir, Ehsan Momeni, Danial JahedArmaghani, and Mohd For Mohd Amin. "Correlation Between Unconfined Compressive Strength and Indirect Tensile Strength of Limestone Rock Samples". In: *Electron J Geotech Eng* 18.1 (2013), pp. 1767–1746.

[81] Kyungho Park, Daehyeon Kim, Gyudeok Kim, and Wooyoul Lee. "Evaluation of the Pullout Behavior of Pre-Bored Piles Embedded in Rock". In: *Materials* 14.19 (2021), p. 5593. DOI: 10.3390/ma14195593.

[82] Arthur Pecher and Jens Peter Kofoed. *Ocean Engineering & Oceanography 7 Handbook of Ocean Wave Energy*. Springer Nature, 2017.

[83] Petroleos Mexicanos. *Diseño y Evaluación de Plataformas Marinas Fijas En La Sonda de Campeche (PEMEX NRF-003:2000)*. PEMEX, 2000.

[84] Ajit C. Pillai, Philipp R. Thies, and Lars Johanning. "Mooring System Design Optimization Using a Surrogate Assisted Multi-Objective Genetic Algorithm". In: *Engineering Optimization* 51.8 (2019), pp. 1370–1392. DOI: 10.1080/0305215X.2018.1519559.

[85] H Poulos and E Davis. *Pile Foundation Analysis and Design*. Series in Geotechnical Engineering. New York, USA: John Wiley & Sons, 1980.

[86] Puertos del Estado. *Recomendaciones Geotécnicas Para Obras Marítimas y Portuarias (ROM 0.5-05)*. Madrid, Spain: Puertos del Estado, 2005.

[87] Edward G. Purdy. "Karst-Determined Facies Patterns in British Honduras: Holocene Carbonate Sedimentation Model". In: *The American Association of Petroleum Geologists Bulletin* 58.5 (1974), pp. 825–855. DOI: 10.1306/83D914A2-16C7-11D7-8645000102C1865D.

[88] Mark Randolph and Susan Gourvenec. *Offshore Geotechnical Engineering*. Spon Press, 2011.

[89] Lymon C. Reese. "Analysis of Laterally Loaded Piles in Weak Rock". In: *Journal of Geotechnical and Geoenvironmental Engineering* 123.11 (1997), pp. 1010–1017. DOI: 10.1061/(ASCE)1090-0241(1997)123:11(1010).

[90] Michael Ring, Paola Elizabeth Rodríguez-Ocampo, Rodolfo Silva, and Edgar Mendoza. "Extreme Value Analysis of Ocean Currents in the Mexican Caribbean Based on HYCOM Numerical Model Data". In: *Frontiers in Marine Science* 9 (2022). DOI: 10.3389/fmars.2022.866874.

[91] Jennifer D. Ruiz-Ramírez, Jorge I. Euán-Ávila, and Víctor H. Rivera-Monroy. "Vulnerability of Coastal Resort Cities to Mean Sea Level Rise in the Mexican Caribbean". In: *Coastal Management* 47.1 (2019), pp. 23–43. DOI: 10.1080/08920753.2019.1525260.

[92] Gianfausto Salvadori, Carlo De Michele, Nathabandu T. Kottegoda, and Renzo Rosso. *Extremes in Nature: An Approach Using Copulas*. Dordrecht, NL: Springer, 2007.

[93] Francesco Salvatore, Zohreh Sarichloo, and Danilo Calcagni. "Marine Turbine Hydrodynamics by a Boundary Element Method with Viscous Flow Correction". In: *Journal of Marine Science and Engineering* 6.2 (2018). DOI: 10.3390/jmse6020053.

[94] Francisco Augusto Santiago Sierra. "Características Del Subsuelo En La Península de Yucatán y Cimentaciones Sobre Roca Caliza". Bachelor's Thesis. Mexico City, Mexico: Universidad Nacional Autónoma de Mexico, 2010.

[95] Johannes Schindelin, Ignacio Arganda-Carreras, Erwin Frise, Verena Kaynig, Mark Longair, Tobias Pietzsch, Stephan Preibisch, Curtis Rueden, et al. "Fiji: An Open-Source Platform for Biological-Image Analysis". In: *Nature Methods* 9.7 (2012), pp. 676–682. DOI: 10.1038/nmeth.2019.

[96] Schottel Hydro. *Schottel Tidal Generator - Cost-Effective Power from Currents*. [Brochure], 2014.

[97] Schottel Hydro. *Cost-Effective Power From Currents*. [Brochure], 2017.

[98] William C. Schwab, Thomas E. Chase, William R. Normark, Pat Wilde, and Barbara A. Seekins. *Generic Assessment of Steep-Slope Seabed Environments: Identification of Sediment Cover and Evaluation of Swath Sonar Systems for OTEC Site Mapping*. Open-File Report 86-333-A. United States Department of the Interior Geological Survey, 1986.

[99] Secretaria de Marina. *Chart S.M. 922: Isla Mujeres a Isla Cozumel*. 2009.

[100] A Serrano and C Olalla. "Tensile Resistance of Rock Anchors". In: *International Journal of Rock Mechanics and Mining Sciences* 36.4 (1999), pp. 449–474. DOI: 10.1016/S0148-9062(99)00021-2.

[101] Mehdi Shafieefar and Aidin Rezvani. "Mooring Optimization of Floating Platforms Using a Genetic Algorithm". In: *Ocean Engineering* 34.10 (2007), pp. 1413–1421. DOI: 10.1016/j.oceaneng.2006.10.005.

[102] Masayuki Shimizu, Shigeki Nagaya, Tomohiro Ueno, Hiroyuki Saito, Show Murata, and Norihisa Handa. "Development and Demonstration Test for Floating Type Ocean Current Turbine System Conducted in Kuroshio Current". In: *Grand Renewable Energy Proceedings Japan Council for Renewable Energy (2018)*. Pacifico Yokohama, Yokohama, Japan: IEEE, 2018, pp. 1–6.

[103] Eugene A. Shinn, J. Harold Hudson, Robert B. Halley, Barbara Lidz, Daniel M. Robbin, and Ian G. Macintyre. "Geology and Sediment Accumulation Rates at Carrie Bow Cay, Belize". In: *Smithsonian Contributions to the Marine Science* 12 (1982), pp. 63–75.

[104] R A Skop. "Mooring Systems : A State-of-the-Art Review". In: *Journal of Offshore Mechanics and Arctic Engineering* 110 (1988).

[105] SMN. *Universidad Nacional Autónoma de México, Instituto de Geofísica, Servicio Mareografico Nacional, México*. 2020.

[106] Richard H Spaw. "Late Pleistocene Carbonate Bank Deposition: Cozumel Island, Quintana Roo, Mexico". In: *Gulf Coast Association of Geological Societies Transactions* 28 (1978), pp. 601–619.

[107] Ralf Starzmann, Inga Goebel, and Penny Jeffcoate. “Field Performance Testing of a Floating Tidal Energy Platform - Part 1: Power Performance”. In: *Proc. of the 4th Asian Wave and Tidal Energy Conference (AWTEC)*. 2018.

[108] Ralf Starzmann, Penny Jeffcoate, Stefan Scholl, Sarah Bischof, and Bjoern Elsaesser. “Field Testing a Full-Scale Tidal Turbine Part 1 : Power Performance Assessment”. In: *Proceedings of 11th European Wave and Tidal Energy Conference*. 2015, pp. 1–7.

[109] Ralf Starzmann, Nicholas Kaufmann, Penny Jeffcoate, Maricarmen Guerra, Alex Hay, and Ray Pieroway. “Effect of Fouling on the Performance of an Instream Turbine”. In: *International Marine Energy Journal* 5.3 (Dec. 2022), pp. 229–237. DOI: 10.36688/imej.5.229-237.

[110] V Terente, I Torres, J Irvine, and C Jaeck. “Driven Pile Design Method for Weak Rock”. In: *Proceedings of the 8th International Conference Offshore Site Investigation and Geotechnics*. 2015, pp. 652–657.

[111] Tethys. *PLAT-O at EMEC*. https://tethys.pnnl.gov/project-sites/plat-o-emec. 2019.

[112] The pandas development team. *Pandas-Dev/Pandas: Pandas*. Zenodo. 2020.

[113] Paul Thompson, Yuzhi Cai, Dominic Reeve, and Julian Stander. “Automated Threshold Selection Methods for Extreme Wave Analysis”. In: *Coastal Engineering* 56.10 (2009), pp. 1013–1021. DOI: 10.1016/j.coastaleng.2009.06.003.

[114] Jean-Yves Tinevez, Nick Perry, Johannes Schindelin, Genevieve M. Hoopes, Gregory D. Reynolds, Emmanuel Laplantine, Sebastian Y. Bednarek, Spencer L. Shorte, et al. “TrackMate: An Open and Extensible Platform for Single-Particle Tracking”. In: *Methods* 115 (2017), pp. 80–90. DOI: 10.1016/j.ymeth.2016.09.016.

[115] R. P. Trask and R. A. Weller. “Moorings”. In: *Encyclopedia of Ocean Sciences*. Academic Press, 2010, pp. 919–931.

[116] Tomohiro Ueno, Shigeki Nagaya, Masayuki Shimizu, Hiroyuki Saito, Show Murata, and Norihisa Handa. “Development and Demonstration Test for Floating Type Ocean Current Turbine System Conducted in Kuroshio Current”. In: *2018 OCEANS - MTS/IEEE Kobe Techno-Oceans (OTO)*. Kobe: IEEE, May 2018, pp. 1–6.

[117] Himanshu Uppal, Manoj T. Isaac, and Shameem B. M. “Numerical Investigation on the Drag Characteristics of AUV Hulls”. In: *International Journal of Mechanical and Production Engineering Research and Development* 9.3 (2019), pp. 645–654. DOI: 10.24247/ijmperdjun201971.

[118] Rick van Hattem. *Numpy-Stl*. 2022.

[119] Gabriel A. Vecchi and Thomas R. Knutson. “Estimating Annual Numbers of Atlantic Hurricanes Missing from the HURDAT Database (1878-1965) Using Ship Track Density”. In: *Journal of Climate* 24.6 (2011), pp. 1736–1746. DOI: 10.1175/2010JCLI3810.1.

[120] Pauli Virtanen, Ralf Gommers, Travis E Oliphant, Matt Haberland, Tyler Reddy, David Cournapeau, Evgeni Burovski, Pearu Peterson, et al. "SciPy 1.0: Fundamental Algorithms for Scientific Computing in Python". In: *Nature Methods* 17 (2020), pp. 261–272. DOI: 10.1038/s41592-019-0686-2.

[121] S Weller, L Johanning, P Davies, and MERiFIC Project. *Best Practice Report - Mooring of Floating Marine Renewable Energy Devices*. 2013.

[122] Liang-yu Xia, Li Zhi, and Ling Chen. "Optimization Design and Calculation of Mooring System Parameters Based on Genetic Algorithm". In: *MATEC Web of Conferences*. Vol. 153. 2018, p. 07006.

[123] Jiang Xu, Guoliang Dai, Weiming Gong, Qi Zhang, Asadul Haque, and Ranjith Pathegama Gamage. "A Review of Research on the Shaft Resistance of Rock-Socketed Piles". In: *Acta Geotechnica* 16.3 (2020), pp. 653–677. DOI: 10.1007/s11440-020-01051-2.

[124] Sheng Xu, Shan Wang, and C. Guedes Soares. "Review of Mooring Design for Floating Wave Energy Converters". In: *Renewable and Sustainable Energy Reviews* 111.August 2018 (2019), pp. 595–621. DOI: 10.1016/j.rser.2019.05.027.

[125] Aimin Zhou, Bo-Yang Qu, Hui Li, Shi-Zheng Zhao, Ponnuthurai Nagaratnam Suganthan, and Qingfu Zhang. "Multiobjective Evolutionary Algorithms: A Survey of the State of the Art". In: *Swarm and Evolutionary Computation* 1.1 (2011), pp. 32–49. DOI: 10.1016/j.swevo.2011.03.001.

[126] Zhibin Zhou, Mohamed Benbouzid, Jean-Frédéric Charpentier, Franck Scuiller, and Tianhao Tang. "Developments in Large Marine Current Turbine Technologies – A Review". In: *Renewable and Sustainable Energy Reviews* 71 (2017), pp. 852–858. DOI: 10.1016/j.rser.2016.12.113.

[127] Zhibin Zhou, Franck Scuiller, Jean Frederic Charpentier, Mohamed Benbouzid, and Tianhao Tang. "An Up-to-Date Review of Large Marine Tidal Current Turbine Technologies". In: *2014 International Power Electronics and Application Conference and Exposition*. Shanghai, China: IEEE, Nov. 2014, pp. 480–484.

[128] Xiangqian Zhu and Wan-Suk Yoo. "Numerical Modeling of a Spherical Buoy Moored by a Cable in Three Dimensions". In: *Chinese Journal of Mechanical Engineering* 29.3 (2016), pp. 588–597. DOI: 10.3901/CJME.2016.0204.021.

Appendices

Appendix A

Quasi-Static Mooring Analysis

A.1 Example for Usage of OffshorePy

In the following, two simple examples are presented to show the basic usage of OffshorePy and some of its key features.

A.1.1 Simple Mooring System

In the first example, a very simple mooring system is modeled consisting of a buoy moored via a single mooring line. The buoy is assumed to be completely submerged at all times, initially placed at a depth of 10 m. The water depth is 80 m and the water density 1025 $\mathrm{kg\,m^{-3}}$.

At first, the module hast to be loaded as well as pi for converting degrees into radians and calculating the volume of the spherical buoy:

```
import offshorepy
from numpy import pi
```

The object storing the mooring system model is created, note that the water depth only serves the purpose to draw the sea floor in the figures. The default gravitational acceleration is 9.81 $\mathrm{m\,s^2}$ and can be set via the argument `g` in case a different acceleration is required.

```
qs_system = offshorepy.MooringSystem(water_depth=80, water_density=1025)
```

Wire rope with a nominal diameter of 15 mm is used as material for the mooring line, with the material properties estimated as given in Ma et al. [68]. The method `add_material_from_library` adds a materials with the properties according to Ma et al. [68] to the model and returns the material object. The name is used for internal reference, while the `material_type` determines which equations are used to estimate the properties.

```
wire = qs_system.add_material_from_library(material_type='wire', nominal_diameter
  =0.015, name='wire 15')
```

The spherical buoy has a diameter of 2 m and a density 0.5 times the of water. If not explicitly given, the COG and the COB are assumed to be at the origin of the body. A rigid body object is

created with its position 10 m below the water surface and no rotation. Volume and mass of a rigid body are set via the according property.

```
>>> buoy = qs_system.add_rigid_body(name='buoy', position=[0,0,-10,0,0,0])
>>> buoy.volume = pi/6*2**3
>>> buoy.mass = 0.5*buoy.volume*1025
```

Lines need to be connected to two points. Therefore, the anchor point on the sea floor and the fairlead on the buoy are created. Anchor points are fixed in space and do not move, while the positions of fairleads are linked to the corresponding rigid body object. Fairleads are created by using the rigid body object and anchor points directly via the mooring system object.

```
buoy.add_fairlead(name='fairlead', rel_position=[0,0,-1])
qs_system.add_anchor_point(name='anchor', position=[0,0,-80])
```

Adding a fairlead or anchor point to the system returns the newly created object. However, all objects can also be retrieved later via their name:

```
fairlead = qs_system.get_object('fairlead')
```

Next, a line is created spanning from the fairlead to the anchor point. To refer to the points either their object or their name can be passed to the method. The same is true for the material. The newly created line is returned.

```
qs_system.add_line(name='cable', point0=fairlead, point1='anchor', material=wire)
```

The system can now be solved:

```
qs_system.solve()
```

This function return three values: The first values is the maximum error, the second value the number of required iterations and the third value a list of all indices of the iterations for which an empty stiffness matrix was found. The default behavior is to raise an error on encountering an empty stiffness matrix. This can be avoided by passing the argument `zero_matrix='solve'`. This way, on encountering an empty stiffness matrix (i.e. due to slack mooring lines) all objects are moved in the direction of their resulting force and moment vector. The system can be plotted and stored to a file with `matplotlib` by:

```
qs_system.plot(save_plot_to='example1.png', show_tensions=True)
```

The output can be seen in figure A.1, with the mooring system shown in a side view (figure A.1 a)), front view (figure A.1b)), and top view (figure A.1 c)). The option `show_tensions` plots the lines in a color according their maximum tensions. The local coordinate system of rigid bodies is indicated with red (positive x-direction), green (positive y-direction), and blue (positive z-direction) lines. The direction perpendicular to the figure's plane is additionally marked with a dot (towards the viewer) or a cross (away from the viewer). Tensions in the lines and residual forces (i.e. external forces) in all objects can be retrieved via the corresponding properties:

```
line = qs_system.get_object('cable')
print(line.tension)
print(line.residual[0])
```

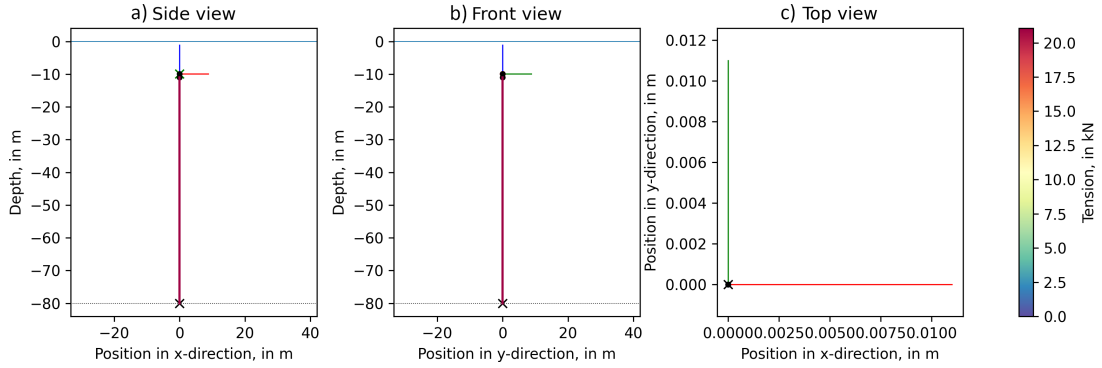

Figure A.1: Resulting mooring system of single line example.

The output would be:

```
(21059.666353338114, 20392.091353338114)
[0., 0., 21059.66635334]
```

In case of lines, the first returned value corresponds to point 0 and the second value to point 1, which are in this case the fairlead and the anchor point, respectively. The position of the buoy can be retrieved by the property `position`:

```
print(buoy.position)
```

This returns a `numpy` array with six entries, resulting in the following output:

```
[ 0.,  0., -9.92949747,  0.,  0., 0.]
```

The first three entries correspond to the position in x-, y-, and z-direction and the last three entries are the corresponding rotations in radians.

A.1.2 Multi-line Mooring System with Segmented Lines

The second example consists of a multi-line-mooring system with 12 segmented mooring lines. The lower most 10 m of each mooring line are composed of 8 mm-chain while for the rest of the mooring line 15 mm-wire rope is used. The basic model is created equal to the mooring system in example one:

```
from numpy import pi, sin, cos, radians
import offshorepy

qs_system = offshorepy.MooringSystem(water_depth=80, water_density=1025)
```

The required materials are loaded from the material library and based on the properties given in Ma et al. [68]:

```
wire = qs_system.add_material_from_library(material_type='wire', nominal_diameter
  =0.015, name='wire 15')
chain = qs_system.add_material_from_library(material_type='chain',
  nominal_diameter=0.008, name='chain 8')
```

A spherical buoy with a diameter of 2 m and a density 0.5 times the of water is created. A force of 10 000 N in positive x-direction is added to the body. The first three components are the components of the force, the last three the components of the moment. If no position of the force is given, the force is applied at the origin of the rigid body.

```
buoy = qs_system.add_rigid_body(name='buoy', position=[0,0,-15,0,0,0])
buoy.volume = pi/4*3**2*6
buoy.mass = 0.5*buoy.volume*1025
buoy.add_external_force(force=[1e4,0,0,0,0,0])
```

The fairleads are created at the angles defined below. The corresponding anchor points are 60 m radially outwards. When no name is given while creating points or lines, the objects are named automatically according to their type and a consecutive number (e.g. **Fairlead0** for the first fairlead and **AnchorPoint2** for the third anchor point). In total, 12 Fairlead-Anchor pairs are created:

```
angles = [25, 30, 35, 145, 150, 155, 205, 210, 215, 325, 330, 335]
for a in angles:
  buoy.add_fairlead(rel_position=[1.5*cos(radians(a)),1.5*sin(radians(a)),-1.5])
  qs_system.add_anchor_point(position=[60*cos(radians(a)),60*sin(radians(a)),-80])
```

The fairleads created are then connected to their corresponding anchor point via a segmented mooring line. To add a segmented line, a method of the `MooringSystem`-object is available. By passing two materials and two unstretched lengths, a mooring line with two segments is created. Since the first unstretched length is 0 and no strain is given, this segment's length is adjusted to the remaining length.

```
for i in range(len(angles)):
  qs_system.add_segmented_line(point0='Fairlead{}'.format(i), point1='AnchorPoint
  {}'.format(i), materials=[wire, chain], unstretched_lengths=[0, 10])
```

Finally the system can be solved and the result plotted:

```
qs_system.solve()
_ = qs_system.plot(save_plot_to='example02.png', show_tensions=True)
```

The resulting mooring system can be seen in figure A.2. In the front view (figure A.2 b)), the port mooring lines (i.e. right side) show a different tension than the starboard (i.e. left side) mooring lines, despite the example being symmetric to the x-z plane. Since the mooring lines are plotted in the order as they were created, the aft port mooring lines cover the forward port mooring lines. On the starboard side the forward mooring lines cover the aft mooring lines. The correct tensions can be seen in the top view (figure A.2 c)).

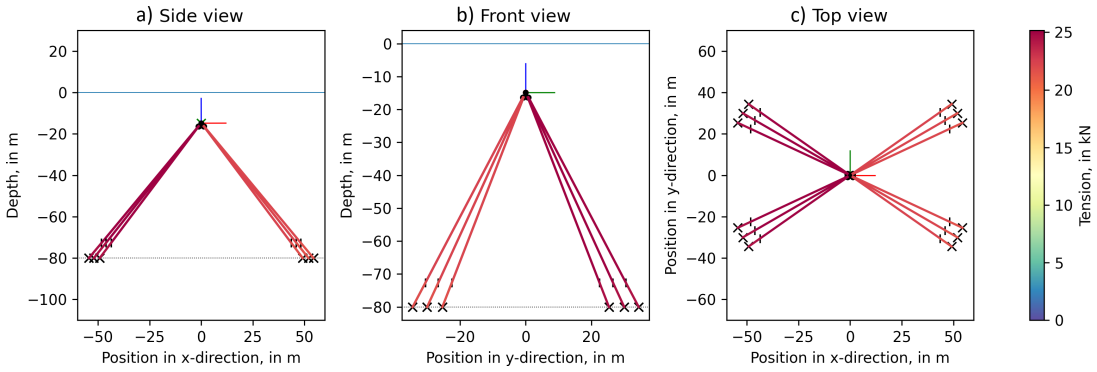

Figure A.2: Resulting mooring system of multi line example.

A.1.3 Python Code to Generate OffshorePy model for Verification

In the following the Python code to Generate offshorepy model for Verification is shown.

```
import numpy as np

import offshorepy

# DATA
water_depth = 80
water_density = 1025
water_viscosity = 1.0023e-6

buoy_diameter = 1
buoy_density = 200
buoy_depth = 40

unstretched_length = 39.5

current_speeds = [0.0, 0.5, 1, 1.5, 2]

for current_speed in current_speeds:
  # DRAG FORCE
  Rn = current_speed*buoy_diameter/water_viscosity
  if current_speed == 0:
    Cd = 0
  else:
    Cd =  24/Rn
    Cd += (2.6*Rn/5.0)/(1+(Rn/5.0)**(1.52))
    Cd += (0.411*(Rn/263000)**(-7.94))/(1+(Rn/263000)**(-8.0))
    Cd += (0.25*Rn/1e6)/(1+Rn/1e6)
  Fd = 0.5*Cd*water_density*current_speed**2 * np.pi/4*buoy_diameter**2
  Fd = np.array([1*np.sign(current_speed),0,0])*Fd

  # NUMERICAL MODEL
```

```
    qs_system = offshorepy.MooringSystem(water_depth=water_depth, water_density=
    water_density)
    qs_system.add_material_from_library('wire', 0.02, name='wire')

    # Create rigid body at the desired depth with no rotation
    buoy = qs_system.add_rigid_body(name='buoy', position=[0,0,-buoy_depth,0,0,0])
    buoy.volume = np.pi/6*buoy_diameter**3
    buoy.mass = buoy.volume*buoy_density
    # Apply external force to buoy according to its drag force. The moment is 0 and
    the force is applied at the righi body's origin
    buoy.add_external_force(np.hstack((Fd, [0,0,0])), [0,0,0])

    buoy.add_fairlead('fairlead', rel_position=[0,0,-buoy_diameter/2])
    qs_system.add_anchor_point([0,0,-water_depth], name='anchor')

    line = qs_system.add_line('fairlead', 'anchor', material='wire',
    unstretched_length=unstretched_length)

    # Solve the system with a maximum of 100 iterations and solve issues with empty
    stiffness matrix
    try:
      qs_system.solve(maxIter=100, zero_matrix='solve')
    except qsma.errors.EquilibriumError as e:
      print(e)

    # OUTPUT
    print('Current speed: {:.1f} ms-1'.format(current_speed))
    print(' Drag: {:.3e} N'.format(Fd))
    print(' Buoy, position: '+('{:.2e}m '*3+'{:.2e}rad '*3).format(*buoy.position))
    print(' Line, stretched length: {:.3e} N'.format(line.stretched_length))
    print(' Line, strain: {:.3e} N'.format(line.strain))
    print(' Line, tension at fairlead: {:.3e} N'.format(line.tension[0]))
```

A.2 Complementary Data for Experiments

In the following tables, complementary data for the experiments of the experimental series A are presented.

Table A.1: Statistical data on the current measured during the experiment series A. Given is the mean, the standard deviation (σ), the 2.5$^{\text{th}}$ ($q_{2.5}$) and the 97.5$^{\text{th}}$ quantile ($q_{97.5}$), and the mean correlation as reported by the Vectrino. Units in $\mathrm{m\,s^{-1}}$.

Experiment	**Mean**	$\boldsymbol{\sigma}$	$\boldsymbol{q_{2.5}}$	$\boldsymbol{q_{97.5}}$	**Correlation**
A01F1_A	0.000	0.026	-0.054	0.051	91.1
A02F1_B	0.003	0.020	-0.041	0.042	95.1
A03F1_C	0.007	0.014	-0.023	0.034	95.9
A04F2_A	0.108	0.018	0.075	0.140	95.1
A05F2_B	0.102	0.011	0.079	0.125	95.2
A06F2_C	0.110	0.011	0.087	0.130	95.0
A07F3_A	0.209	0.016	0.175	0.238	94.8
A08F3_B	0.211	0.012	0.185	0.234	95.3
A09F3_C	0.214	0.015	0.183	0.242	94.7
A10F4_A	0.322	0.019	0.286	0.360	94.1
A11F4_B	0.317	0.020	0.278	0.356	93.7
A12F4_C	0.316	0.019	0.278	0.354	93.2
A13F5_A	0.417	0.028	0.362	0.476	93.1
A14F5_B	0.424	0.027	0.372	0.480	92.4
A15F5_C	0.420	0.024	0.372	0.467	91.8
A16F6_A	0.536	0.032	0.478	0.600	95.1
A17F6_B	0.538	0.030	0.483	0.597	94.9
A18F6_C	0.540	0.034	0.475	0.609	94.7
A19F7_A	0.637	0.036	0.563	0.701	95.9
A20F7_B	0.631	0.033	0.569	0.695	96.0
A21F7_C	0.633	0.034	0.563	0.697	95.8

Table A.2: Signed relative error of experimental series A.

Experiment	**Speed** in $\mathrm{m\,s^{-1}}$	**x-Deflection** in m		**y-Rotation** in °	
A01F1_A	0.000	-1.000	1.803 ... -3.803	-1.000	-17.816 ... 15.816
A02F1_B	0.000	-1.000	18.298 ... -20.298	-1.000	17.199 ... -19.199
A03F1_C	0.000	-1.000	-3.447 ... 1.447	-1.000	220.294 ... -222.294
A04F2_A	0.108	0.877	1.444 ... 0.310	-0.011	0.553 ... -0.576
A05F2_B	0.102	1.386	2.195 ... 0.577	-0.181	0.346 ... -0.708
A06F2_C	0.110	3.500	4.818 ... 2.182	-0.235	0.188 ... -0.658
A07F3_A	0.209	0.113	0.245 ... -0.020	0.280	0.551 ... 0.009
A08F3_B	0.211	0.115	0.246 ... -0.015	0.288	0.555 ... 0.021
A09F3_C	0.214	0.123	0.250 ... -0.005	0.297	0.557 ... 0.036
A10F4_A	0.322	0.127	0.208 ... 0.046	0.348	0.516 ... 0.180
A11F4_B	0.317	0.079	0.159 ... -0.001	0.236	0.395 ... 0.078
A12F4_C	0.316	0.074	0.155 ... -0.006	0.263	0.427 ... 0.099
A13F5_A	0.417	-0.332	-0.307 ... -0.358	0.458	0.597 ... 0.319
A14F5_B	0.424	-0.328	-0.303 ... -0.353	0.531	0.672 ... 0.389
A15F5_C	0.419	-0.380	-0.356 ... -0.403	0.436	0.571 ... 0.300
A16F6_A	0.536	-0.435	-0.383 ... -0.486	0.493	0.700 ... 0.287
A17F6_B	0.538	-0.436	-0.385 ... -0.487	0.522	0.730 ... 0.313
A18F6_C	0.540	-0.447	-0.397 ... -0.496	0.500	0.704 ... 0.297
A19F7_A	0.636	-0.462	-0.372 ... -0.552	0.450	0.784 ... 0.116
A20F7_B	0.631	-0.473	-0.384 ... -0.563	0.424	0.758 ... 0.091
A21F7_C	0.633	-0.483	-0.395 ... -0.570	0.436	0.770 ... 0.101

Table A.3: Statistical data on the current measured during the experiment series B. Given is the mean, the standard deviation (σ), the 2.5$^{\text{th}}$ ($q_{2.5}$) and the 97.5$^{\text{th}}$ quantile ($q_{97.5}$), and the mean correlation as reported by the Vectrino. Units in $\mathrm{m\,s^{-1}}$.

Experiment	**Mean**	$\boldsymbol{\sigma}$	$\boldsymbol{q_{2.5}}$	$\boldsymbol{q_{97.5}}$	**Correlation**
B01F1_A	0.008	0.036	-0.070	0.083	67.5
B02F1_B	0.010	0.030	-0.050	0.077	69.5
B03F1_C	0.002	0.039	-0.082	0.085	52.8
B04F2_A	0.055	0.009	0.035	0.075	81.7
B05F2_B	0.066	0.021	0.028	0.112	57.8
B06F2_C	0.075	0.022	0.035	0.126	55.5
B07F3_A	0.115	0.014	0.090	0.143	64.4
B08F3_B	0.125	0.015	0.098	0.159	64.0
B09F3_C	0.121	0.014	0.096	0.153	64.6
B10F4_A	0.174	0.014	0.147	0.204	71.7
B11F4_B	0.176	0.013	0.151	0.204	70.6
B12F4_C	0.176	0.015	0.147	0.205	72.7
B13F5_A	0.218	0.014	0.190	0.245	78.6
B14F5_B	0.220	0.014	0.192	0.249	78.0
B15F5_C	0.216	0.015	0.188	0.249	79.1
B16F6_A	0.271	0.016	0.239	0.302	81.3
B17F6_B	0.276	0.016	0.244	0.308	80.5
B18F6_C	0.271	0.017	0.237	0.303	80.0
B19F7_A	0.328	0.017	0.292	0.362	84.1
B20F7_B	0.322	0.019	0.282	0.356	83.6
B21F7_C	0.317	0.020	0.278	0.356	83.6
B22F8_A	0.378	0.021	0.336	0.417	86.3
B23F8_B	0.376	0.022	0.333	0.417	86.4
B24F8_C	0.381	0.023	0.337	0.429	87.9

Table A.4: Signed relative error of experimental series B.

Experiment	**Speed**	**x-Deflection**		**y-Rotation**	
	in $\mathrm{m\,s^{-1}}$	in m		in °	
B01F1_A	0.000	-1.00	-3.80 ... 1.80	-1.00	-10.10 ... 8.10
B02F1_B	0.000	-1.03	3.93 ... -5.99	-0.99	-6.90 ... 4.92
B03F1_C	0.000	-1.09	5.31 ... -7.50	-1.02	2.57 ... -4.60
B04F2_A	0.055	-1.00	-3.81 ... 1.82	-1.00	-8.88 ... 6.89
B05F2_B	0.067	0.09	-4.32 ... 4.51	-0.65	-4.90 ... 3.60
B06F2_C	0.076	-0.35	-2.13 ... 1.43	-1.14	0.01 ... -2.29
B07F3_A	0.115	-0.84	-1.18 ... -0.51	-0.48	-3.83 ... 2.88
B08F3_B	0.126	-0.68	-0.98 ... -0.37	0.04	-2.91 ... 2.99
B09F3_C	0.121	-0.62	-0.92 ... -0.33	0.87	-3.55 ... 5.29
B10F4_A	0.174	-0.75	-0.96 ... -0.53	0.52	-3.35 ... 4.38
B11F4_B	0.176	-0.49	-0.70 ... -0.28	2.40	-1.83 ... 6.64
B12F4_C	0.176	-0.46	-0.68 ... -0.24	0.86	-1.39 ... 3.11
B13F5_A	0.218	-0.66	-0.80 ... -0.51	-0.53	-1.10 ... 0.04
B14F5_B	0.220	-0.51	-0.64 ... -0.37	-0.28	-0.85 ... 0.29
B15F5_C	0.216	-0.48	-0.62 ... -0.35	0.07	-0.76 ... 0.90
B16F6_A	0.271	-0.66	-0.75 ... -0.56	-0.35	-0.87 ... 0.18
B17F6_B	0.276	-0.48	-0.57 ... -0.39	-0.05	-0.54 ... 0.43
B18F6_C	0.271	-0.45	-0.54 ... -0.36	0.01	-0.49 ... 0.52
B19F7_A	0.328	-0.63	-0.69 ... -0.56	-0.40	-0.71 ... -0.09
B20F7_B	0.322	-0.43	-0.50 ... -0.37	-0.04	-0.37 ... 0.30
B21F7_C	0.317	-0.46	-0.53 ... -0.40	-0.06	-0.40 ... 0.28

Appendix B

Dimensions of structural members

In the following, the complete list of structural members which was used during optimization of the structure is shown. The list includes all 542 possible profiles, ordered by outer diameter and wall thickness and with all dimensions given in mm.

Table B.1: Diameter and thickness range of structural members.

i	Profile	i	Profile	i	Profile	i	Profile
0	30.0 x 2.6	1	30.0 x 2.9	2	30.0 x 3.2	3	30.0 x 3.6
4	30.0 x 4.0	5	30.0 x 4.5	6	30.0 x 5.0	7	30.0 x 5.6
8	30.0 x 6.3	9	30.0 x 7.1	10	30.0 x 8.0	11	30.0 x 8.8
12	30.0 x 10.0	13	31.8 x 2.6	14	31.8 x 2.9	15	31.8 x 3.2
16	31.8 x 3.6	17	31.8 x 4.0	18	31.8 x 4.5	19	31.8 x 5.0
20	31.8 x 5.6	21	31.8 x 6.3	22	31.8 x 7.1	23	31.8 x 8.0
24	31.8 x 8.8	25	31.8 x 10.0	26	33.7 x 2.6	27	33.7 x 2.9
28	33.7 x 3.2	29	33.7 x 3.6	30	33.7 x 4.0	31	33.7 x 4.5
32	33.7 x 5.0	33	33.7 x 5.6	34	33.7 x 6.3	35	33.7 x 7.1
36	33.7 x 8.0	37	33.7 x 8.8	38	33.7 x 10.0	39	33.7 x 11.0
40	38.0 x 2.6	41	38.0 x 2.9	42	38.0 x 3.2	43	38.0 x 3.6
44	38.0 x 4.0	45	38.0 x 4.5	46	38.0 x 5.0	47	38.0 x 5.6
48	38.0 x 6.3	49	38.0 x 7.1	50	38.0 x 8.0	51	38.0 x 8.8
52	38.0 x 10.0	53	38.0 x 11.0	54	38.0 x 12.5	55	42.4 x 2.6
56	42.4 x 2.9	57	42.4 x 3.2	58	42.4 x 3.6	59	42.4 x 4.0
60	42.4 x 4.5	61	42.4 x 5.0	62	42.4 x 5.6	63	42.4 x 6.3
64	42.4 x 7.1	65	42.4 x 8.0	66	42.4 x 8.8	67	42.4 x 10.0
68	42.4 x 11.0	69	42.4 x 12.5	70	42.4 x 14.2	71	44.5 x 2.6
72	44.5 x 2.9	73	44.5 x 3.2	74	44.5 x 3.6	75	44.5 x 4.0
76	44.5 x 4.5	77	44.5 x 5.0	78	44.5 x 5.6	79	44.5 x 6.3

continued on next page

Table B.1: Diameter and thickness range of structural members.

i	Profile	i	Profile	i	Profile	i	Profile
80	44.5 x 7.1	81	44.5 x 8.0	82	44.5 x 8.8	83	44.5 x 10.0
84	44.5 x 11.0	85	44.5 x 12.5	86	44.5 x 14.2	87	48.3 x 2.6
88	48.3 x 2.9	89	48.3 x 3.2	90	48.3 x 3.6	91	48.3 x 4.0
92	48.3 x 4.5	93	48.3 x 5.0	94	48.3 x 5.6	95	48.3 x 6.3
96	48.3 x 7.1	97	48.3 x 8.0	98	48.3 x 8.8	99	48.3 x 10.0
100	48.3 x 11.0	101	48.3 x 12.5	102	48.3 x 14.2	103	48.3 x 16.0
104	51.0 x 2.6	105	51.0 x 2.9	106	51.0 x 3.2	107	51.0 x 3.6
108	51.0 x 4.0	109	51.0 x 4.5	110	51.0 x 5.0	111	51.0 x 5.6
112	51.0 x 6.3	113	51.0 x 7.1	114	51.0 x 8.0	115	51.0 x 8.8
116	51.0 x 10.0	117	51.0 x 11.0	118	51.0 x 12.5	119	51.0 x 14.2
120	51.0 x 16.0	121	54.0 x 2.6	122	54.0 x 2.9	123	54.0 x 3.2
124	54.0 x 3.6	125	54.0 x 4.0	126	54.0 x 4.5	127	54.0 x 5.0
128	54.0 x 5.6	129	54.0 x 6.3	130	54.0 x 7.1	131	54.0 x 8.0
132	54.0 x 8.8	133	54.0 x 10.0	134	54.0 x 11.0	135	54.0 x 12.5
136	54.0 x 14.2	137	54.0 x 16.0	138	57.0 x 2.9	139	57.0 x 3.2
140	57.0 x 3.6	141	57.0 x 4.0	142	57.0 x 4.5	143	57.0 x 5.0
144	57.0 x 5.6	145	57.0 x 6.3	146	57.0 x 7.1	147	57.0 x 8.0
148	57.0 x 8.8	149	57.0 x 10.0	150	57.0 x 11.0	151	57.0 x 12.5
152	57.0 x 14.2	153	57.0 x 16.0	154	60.3 x 2.9	155	60.3 x 3.2
156	60.3 x 3.6	157	60.3 x 4.0	158	60.3 x 4.5	159	60.3 x 5.0
160	60.3 x 5.6	161	60.3 x 6.3	162	60.3 x 7.1	163	60.3 x 8.0
164	60.3 x 8.8	165	60.3 x 10.0	166	60.3 x 11.0	167	60.3 x 12.5
168	60.3 x 14.2	169	60.3 x 16.0	170	60.3 x 17.5	171	63.5 x 2.9
172	63.5 x 3.2	173	63.5 x 3.6	174	63.5 x 4.0	175	63.5 x 4.5
176	63.5 x 5.0	177	63.5 x 5.6	178	63.5 x 6.3	179	63.5 x 7.1
180	63.5 x 8.0	181	63.5 x 8.8	182	63.5 x 10.0	183	63.5 x 11.0
184	63.5 x 12.5	185	63.5 x 14.2	186	63.5 x 16.0	187	63.5 x 17.5
188	70.0 x 2.9	189	70.0 x 3.2	190	70.0 x 3.6	191	70.0 x 4.0
192	70.0 x 4.5	193	70.0 x 5.0	194	70.0 x 5.6	195	70.0 x 6.3
196	70.0 x 7.1	197	70.0 x 8.0	198	70.0 x 8.8	199	70.0 x 10.0
200	70.0 x 11.0	201	70.0 x 12.5	202	70.0 x 14.2	203	70.0 x 16.0
204	70.0 x 17.5	205	76.1 x 2.9	206	76.1 x 3.2	207	76.1 x 3.6
208	76.1 x 4.0	209	76.1 x 4.5	210	76.1 x 5.0	211	76.1 x 5.6
212	76.1 x 6.3	213	76.1 x 7.1	214	76.1 x 8.0	215	76.1 x 8.8
216	76.1 x 10.0	217	76.1 x 11.0	218	76.1 x 12.5	219	76.1 x 14.2
220	76.1 x 16.0	221	76.1 x 17.5	222	76.1 x 20.0	223	82.5 x 3.2

continued on next page

Table B.1: Diameter and thickness range of structural members.

i	Profile	i	Profile	i	Profile	i	Profile
224	82.5 x 3.6	225	82.5 x 4.0	226	82.5 x 4.5	227	82.5 x 5.0
228	82.5 x 5.6	229	82.5 x 6.3	230	82.5 x 7.1	231	82.5 x 8.0
232	82.5 x 8.8	233	82.5 x 10.0	234	82.5 x 11.0	235	82.5 x 12.5
236	82.5 x 14.2	237	82.5 x 16.0	238	82.5 x 17.5	239	82.5 x 20.0
240	82.5 x 22.2	241	82.5 x 25.0	242	88.9 x 3.2	243	88.9 x 3.6
244	88.9 x 4.0	245	88.9 x 4.5	246	88.9 x 5.0	247	88.9 x 5.6
248	88.9 x 6.3	249	88.9 x 7.1	250	88.9 x 8.0	251	88.9 x 8.8
252	88.9 x 10.0	253	88.9 x 11.0	254	88.9 x 12.5	255	88.9 x 14.2
256	88.9 x 16.0	257	88.9 x 17.5	258	88.9 x 20.0	259	88.9 x 22.2
260	88.9 x 25.0	261	95.0 x 3.6	262	95.0 x 4.0	263	95.0 x 4.5
264	95.0 x 5.0	265	95.0 x 5.6	266	95.0 x 6.3	267	95.0 x 7.1
268	95.0 x 8.0	269	95.0 x 8.8	270	95.0 x 10.0	271	95.0 x 11.0
272	95.0 x 12.5	273	95.0 x 14.2	274	95.0 x 16.0	275	95.0 x 17.5
276	95.0 x 20.0	277	95.0 x 22.2	278	95.0 x 25.0	279	95.0 x 28.0
280	101.6 x 3.6	281	101.6 x 4.0	282	101.6 x 4.5	283	101.6 x 5.0
284	101.6 x 5.6	285	101.6 x 6.3	286	101.6 x 7.1	287	101.6 x 8.0
288	101.6 x 8.8	289	101.6 x 10.0	290	101.6 x 11.0	291	101.6 x 12.5
292	101.6 x 14.2	293	101.6 x 16.0	294	101.6 x 17.5	295	101.6 x 20.0
296	101.6 x 22.2	297	101.6 x 25.0	298	101.6 x 28.0	299	108.0 x 3.6
300	108.0 x 4.0	301	108.0 x 4.5	302	108.0 x 5.0	303	108.0 x 5.6
304	108.0 x 6.3	305	108.0 x 7.1	306	108.0 x 8.0	307	108.0 x 8.8
308	108.0 x 10.0	309	108.0 x 11.0	310	108.0 x 12.5	311	108.0 x 14.2
312	108.0 x 16.0	313	108.0 x 17.5	314	108.0 x 20.0	315	108.0 x 22.2
316	108.0 x 25.0	317	108.0 x 28.0	318	108.0 x 30.0	319	114.3 x 3.6
320	114.3 x 4.0	321	114.3 x 4.5	322	114.3 x 5.0	323	114.3 x 5.6
324	114.3 x 6.3	325	114.3 x 7.1	326	114.3 x 8.0	327	114.3 x 8.8
328	114.3 x 10.0	329	114.3 x 11.0	330	114.3 x 12.5	331	114.3 x 14.2
332	114.3 x 16.0	333	114.3 x 17.5	334	114.3 x 20.0	335	114.3 x 22.2
336	114.3 x 25.0	337	114.3 x 28.0	338	114.3 x 30.0	339	114.3 x 32.0
340	121.0 x 4.0	341	121.0 x 4.5	342	121.0 x 5.0	343	121.0 x 5.6
344	121.0 x 6.3	345	121.0 x 7.1	346	121.0 x 8.0	347	121.0 x 8.8
348	121.0 x 10.0	349	121.0 x 11.0	350	121.0 x 12.5	351	121.0 x 14.2
352	121.0 x 16.0	353	121.0 x 17.5	354	121.0 x 20.0	355	121.0 x 22.2
356	121.0 x 25.0	357	121.0 x 28.0	358	121.0 x 30.0	359	121.0 x 32.0
360	127.0 x 4.0	361	127.0 x 4.5	362	127.0 x 5.0	363	127.0 x 5.6
364	127.0 x 6.3	365	127.0 x 7.1	366	127.0 x 8.0	367	127.0 x 8.8

continued on next page

Table B.1: Diameter and thickness range of structural members.

i	Profile	i	Profile	i	Profile	i	Profile
368	127.0 x 10.0	369	127.0 x 11.0	370	127.0 x 12.5	371	127.0 x 14.2
372	127.0 x 16.0	373	127.0 x 17.5	374	127.0 x 20.0	375	127.0 x 22.2
376	127.0 x 25.0	377	127.0 x 28.0	378	127.0 x 30.0	379	127.0 x 32.0
380	127.0 x 36.0	381	133.0 x 4.0	382	133.0 x 4.5	383	133.0 x 5.0
384	133.0 x 5.6	385	133.0 x 6.3	386	133.0 x 7.1	387	133.0 x 8.0
388	133.0 x 8.8	389	133.0 x 10.0	390	133.0 x 11.0	391	133.0 x 12.5
392	133.0 x 14.2	393	133.0 x 16.0	394	133.0 x 17.5	395	133.0 x 20.0
396	133.0 x 22.2	397	133.0 x 25.0	398	133.0 x 28.0	399	133.0 x 30.0
400	133.0 x 32.0	401	133.0 x 36.0	402	133.0 x 40.0	403	139.7 x 4.0
404	139.7 x 4.5	405	139.7 x 5.0	406	139.7 x 5.6	407	139.7 x 6.3
408	139.7 x 7.1	409	139.7 x 8.0	410	139.7 x 8.8	411	139.7 x 10.0
412	139.7 x 11.0	413	139.7 x 12.5	414	139.7 x 14.2	415	139.7 x 16.0
416	139.7 x 17.5	417	139.7 x 20.0	418	139.7 x 22.2	419	139.7 x 25.0
420	139.7 x 28.0	421	139.7 x 30.0	422	139.7 x 32.0	423	139.7 x 36.0
424	139.7 x 40.0	425	139.7 x 45.0	426	146.0 x 4.5	427	146.0 x 5.0
428	146.0 x 5.6	429	146.0 x 6.3	430	146.0 x 7.1	431	146.0 x 8.0
432	146.0 x 8.8	433	146.0 x 10.0	434	146.0 x 11.0	435	146.0 x 12.5
436	146.0 x 14.2	437	146.0 x 16.0	438	146.0 x 17.5	439	146.0 x 20.0
440	146.0 x 22.2	441	146.0 x 25.0	442	146.0 x 28.0	443	146.0 x 30.0
444	146.0 x 32.0	445	146.0 x 36.0	446	146.0 x 40.0	447	146.0 x 45.0
448	152.4 x 4.5	449	152.4 x 5.0	450	152.4 x 5.6	451	152.4 x 6.3
452	152.4 x 7.1	453	152.4 x 8.0	454	152.4 x 8.8	455	152.4 x 10.0
456	152.4 x 11.0	457	152.4 x 12.5	458	152.4 x 14.2	459	152.4 x 16.0
460	152.4 x 17.5	461	152.4 x 20.0	462	152.4 x 22.2	463	152.4 x 25.0
464	152.4 x 28.0	465	152.4 x 30.0	466	152.4 x 32.0	467	152.4 x 36.0
468	152.4 x 40.0	469	152.4 x 45.0	470	159.0 x 4.5	471	159.0 x 5.0
472	159.0 x 5.6	473	159.0 x 6.3	474	159.0 x 7.1	475	159.0 x 8.0
476	159.0 x 8.8	477	159.0 x 10.0	478	159.0 x 11.0	479	159.0 x 12.5
480	159.0 x 14.2	481	159.0 x 16.0	482	159.0 x 17.5	483	159.0 x 20.0
484	159.0 x 22.2	485	159.0 x 25.0	486	159.0 x 28.0	487	159.0 x 30.0
488	159.0 x 32.0	489	159.0 x 36.0	490	159.0 x 40.0	491	159.0 x 45.0
492	159.0 x 50.0	493	159.0 x 55.0	494	165.1 x 4.5	495	165.1 x 5.0
496	165.1 x 5.6	497	165.1 x 6.3	498	165.1 x 7.1	499	165.1 x 8.0
500	165.1 x 8.8	501	165.1 x 10.0	502	165.1 x 11.0	503	165.1 x 12.5
504	165.1 x 14.2	505	165.1 x 16.0	506	165.1 x 17.5	507	165.1 x 20.0
508	165.1 x 22.2	509	165.1 x 25.0	510	165.1 x 28.0	511	165.1 x 30.0

continued on next page

Table B.1: Diameter and thickness range of structural members.

i	Profile	i	Profile	i	Profile	i	Profile
512	165.1 x 32.0	513	165.1 x 36.0	514	165.1 x 40.0	515	165.1 x 45.0
516	165.1 x 50.0	517	165.1 x 55.0	518	168.3 x 4.5	519	168.3 x 5.0
520	168.3 x 5.6	521	168.3 x 6.3	522	168.3 x 7.1	523	168.3 x 8.0
524	168.3 x 8.8	525	168.3 x 10.0	526	168.3 x 11.0	527	168.3 x 12.5
528	168.3 x 14.2	529	168.3 x 16.0	530	168.3 x 17.5	531	168.3 x 20.0
532	168.3 x 22.2	533	168.3 x 25.0	534	168.3 x 28.0	535	168.3 x 30.0
536	168.3 x 32.0	537	168.3 x 36.0	538	168.3 x 40.0	539	168.3 x 45.0
540	168.3 x 50.0	541	168.3 x 55.0				

Appendix C

Publication in Frontiers in Marine Science

frontiers | Frontiers in Marine Science

ORIGINAL RESEARCH
published: 13 June 2022
doi: 10.3389/fmars.2022.866874

Extreme Value Analysis of Ocean Currents in the Mexican Caribbean Based on HYCOM Numerical Model Data

*Michael Ring**, *Paola Elizabeth Rodríguez-Ocampo*, *Rodolfo Silva* and *Edgar Mendoza**

Institute of Engineering, National Autonomous University of Mexico, Mexico City, Mexico

Comprehensive knowledge of extreme values is required for designing offshore structures and ocean current turbines. However, data on the return levels of ocean currents are rarely available. This is the case for the Mexican Caribbean, where enormous energy potential in the ocean currents has recently been detected. In this study, long-term numerical data from the Hybrid Coordinate Ocean Model for a depth of 50m was adjusted *via* linear quantile regression to short-term empirical data for a depth of 49m. The error of the results was estimated using simplified extreme value analysis. Based on the numerical data, a comprehensive extreme value analysis was conducted using the peaks over threshold method and fitting a Generalized Pareto Distribution to the data. This method relies on filtering peaks with a moving time window and an automated threshold selection based on a reparameterised scale parameter of the Generalized Pareto Distribution. The adjusted numerical model is shown to underestimate the empirical data with the error converging to almost 22% for rare events (return period > 10years). The method showed consistent results in the domain, with some anomalies only at the boundaries of the underlying numerical model. The methodology is suitable for estimating the return levels of ocean currents provided by HYCOM, although further research is needed to reduce the error of the numerical model.

Keywords: ocean current, return level, extreme value analysis, peaks over threshold, generalized pareto distribution, Caribbean Sea, HYCOM

OPEN ACCESS

Edited by:
Alvise Benetazzo,
Institute of Marine Science (CNR), Italy

Reviewed by:
Oyvind Breivik,
Norwegian Meteorological Institute, Norway
Antonio Ricchi,
University of L'Aquila, Italy

****Correspondence:***
Edgar Mendoza
EMendozaB@iingen.unam.mx
Michael Ring
MRing@iingen.unam.mx

Specialty section:
This article was submitted to Physical Oceanography, a section of the journal Frontiers in Marine Science

Received: *31 January 2022*
Accepted: *25 April 2022*
Published: *13 June 2022*

Citation:
Ring M, Rodríguez-Ocampo PE, Silva R and Mendoza E (2022) Extreme Value Analysis of Ocean Currents in the Mexican Caribbean Based on HYCOM Numerical Model Data. Front. Mar. Sci. 9:866874. doi: 10.3389/fmars.2022.866874

1 INTRODUCTION

In recent years, many projects have sought to harvest ocean energy from tidal currents. For instance, in early 2021, Sustainable Marine launched the *Pempa'q Instream Tidal Energy* project to harvest the tidal energy, using a 420 kW PLAT-I 6.4 platform, in the Bay of Fundy, Nova Scotia, Canada (Sustainable Marine, 2021). Similarly, Orbital Marine Power launched their O2 platform in the north of Scotland, UK. This platform has two turbines each with a diameter of 20m and a rated

Abbreviations: GPD, Generalized Pareto Distribution; HYCOM, Hybrid Coordinate Ocean Model; POT, Peaks over threshold; $CI_{95\%}$, 95% confidence interval.

power of 1 MW (Orbital Marine Power Ltd, 2021). The successful deployment of platforms for such technologies requires currents that are typically avoided by other industries because they are too intensive. These technologies require currents that are often too strong to be harnessed for other uses. Consequently, there is limited knowledge about the exact environmental conditions near the currents.

Fan et al. (2010) studied the currents obtained from the Hybrid Coordinate Ocean Model (HYCOM) in the Gulf of Mexico, and compared them against field measurements for the same area. Their results show inconsistencies for low-frequency motions, such as eddies, in the numerical model. The model also tends to overestimate deeper currents during loop current eddy events. Cetina et al. (2006) studied current circulation in the same area, finding that the direction of the currents may reverse for several weeks, mainly due to passing eddies within the main current stream, near Chinchorro Bank, south of Cozumel Island, in the Caribbean Sea. Other studies on subinertial flows have been carried out using short-term measurements, to characterize the currents at this site (Chávez et al., 2003), the fluctuations of the current (Ochoa et al., 2005), and their variability (Abascal et al., 2003). The strong correlation between the flow through the Cozumel Channel and that at the centre of the Yucatan Channel was found by Athie et al. (2011), who compared simultaneous measurements in both channels over 8 months in 2000 and 2001. The tidal currents in the Yucatan Channel, which separates the northern tip of the Yucatan Peninsula and the west coast of Cuba, were studied by Carrillo González et al. (2007). From their measurements, they found that the amplitude of the diurnal components of the tide is about ten times greater than the semi-diurnal components.

In relation to the modelling and characterisation of currents several relevant researches have been published. Jonathan and Ewans (2013) reviewed the behaviour of extreme value modelling for the characterization of ocean environments for the design of marine structures. They summarized basic concepts and modelling with covariates and multivariates. Extreme ocean currents in the north west Atlantic were analysed by Oliver et al. (2012), based on numerical data, using a Monte-Carlo simulation for the integration of tidal and non tidal currents. Standard statistical methods for extreme values were extended to handle the temporal dependence, directionality, and tidal non-stationarity of ocean current extremes, by Robinson and Tawn (1997). They found that the tidal current and directionality in non-extreme surge currents explain the strong directionality in the speed of extreme ocean currents. Devis-Morales et al. (2017) analysed extreme wind and wave events in the Caribbean, applying the block model, peaks over threshold (POT) method, and the individual storms method, to obtain estimates of extreme values for the Colombian Caribbean coast.

Moeini et al. (2010) compared the quality of two sources of surface winds for wave modelling in the Persian Gulf. They used measurements of the wind and wind data generated by the climatological model of the *European Center for Medium Range Weather Forecasts* as data input for the wave model. The waves were simulated with the SWAN model (for *Simulating Waves Nearshore*) and compared to empirical wave data measured 20 km away from the meteorological station which recorded the wind data. They performed extreme value analysis (EVA) based on the measured and modelled wave data and found that the wave data generated with the empirical wind data matched the empirical wave data much better than the wave data generated with the modelled wind. Niroomandi et al. (2018) simulated waves in Chesapeake Bay and validated the results with measurements. They performed an EVA comparing generalized extreme value function and Generalized Pareto Distribution (GPD). They also studied the effect of key parameters, including threshold value, time span and data length on the design wave heights. Park et al. (2020) used EVA to obtain the return levels for wave, wind and currents for the Barents Sea. Their analysis is based on hindcast data generated with the *Global Reanalysis of Ocean Waves 2012* model. They based their EVA on the Gumbel distribution, and the 2- and 3-parameter Weibull distribution and ultimately suggest using the Weibull distribution for the wind speed and current speed. Viselli et al. (2015) calculated extreme wind and waves in the Gulf of Maine, USA, by applying the POT method with short block lengths of 4 to 8 days to ensure the peaks were independent. For each block, only the maximum peak was selected, which also had to be over half a block length after the previously selected peak. This method was adapted from Simiu (2011) and aims to avoid serially related peaks. Liu et al. (2018) used the average conditional exceedance rate method to estimate extreme current speeds with multi-year return periods, based on data obtained from a platform in the South China Sea. Bore et al. (2019) used a marginal model to determine the statistical extremes of current speed, by evaluating the signal in deterministic and stochastic components. Qi and Shi (2009) used the three-parameter Weibull distribution to estimate the distribution of extreme winds, waves, and currents, using data from 30-year hindcasts to which the Weibull distribution was fitted.

Thompson et al. (2009) introduced a methodology for automatic threshold selection based on statistical parameters as described in Coles (2001). Their method was applied to extreme wave height by increasing the threshold from the 50th percentile upward, until a specific condition was satisfied. Similarly, Solari et al. (2017) presented a methodology for automatic threshold selection, defining possible thresholds by a list of peaks within a moving time window. The parameters of a GPD are calculated for each set of peaks, defined by threshold and the moving time window. For each GPD the p-value was estimated employing the right-tail weighted Anderson-Darling test. The threshold, which minimizes one minus the p-value for the specific threshold, was selected while its uncertainty is estimated using the bootstrap technique. Liang et al. (2019) selected possible thresholds which are uniformly distributed in the upper half of the data. For each threshold, a GPD is fitted to the data, and the differences in return periods values with increasing thresholds are plotted. A stable region for the return period with an increasing threshold indicates independence from the threshold, and the lower bound of the area is selected as the final threshold. Coles and Simiu

(2003) proposed the use of resampling schemes to measure uncertainties caused by the relatively short length of the numerical data of hurricane extreme values. They adapted a bootstrap method and used empirical corrections to adjust the bias in the distributions obtained. Morton and Bowers (1996) studied the multivariate point process model in extreme value analyses. As an example, they used a moored semi-submersible and its response to wind and waves (i.e., bivariate analysis) and estimated the 50-year mooring force and return period contours for a 50-year combined wind-wave condition.

The Cozumel Channel in the Mexican Caribbean Sea has significant potential for the harnessing of ocean currents (Hernández-Fontes et al., 2019; Bárcenas Graniel et al., 2021). The predominant current direction is in north east direction, especially for the higher current speeds. Since the currents in this region are mainly caused by global ocean currents, the direction rarely changes (Alcérreca-Huerta et al., 2019). When it does, it is usually caused by eddies within the ocean current that result in a relatively low flow in the opposite direction. South east of Cozumel Island the mean current speed was determined to be $0.9ms^{-1}$ with a standard deviation of $0.2ms^{-1}$. In the wake of the Cozumel Channel the mean current speed was measured as $1.3ms^{-1}$ with a standard deviation of $0.3ms^{-1}$ (Cetina et al., 2006). The oceanic climate, the biodiversity and intensive tourism are the main reason why this region is unattractive for conventional marine structures, however it is an area with great potential for harvesting energy from ocean currents.

Long-term data, for at least 20 years (Devis-Morales et al., 2017) are necessary to correctly design offshore structures that take into consideration extreme events. The current measurements are available for a depth of 49m in the Cozumel Channel, but empirical data covers less than two years. On the other hand, simulated data of high spatial resolution are available for the current in the Cozumel Channel, although the degree of error with respect to the real current in this region is not known. This paper is based on measurements from the Canek project 2009/2010 in the Channel of Cozumel. It addresses such shortcomings by comparing and adjusting the simulated data with empirical data, and subsequently performing an EVA on the numerical data. The analysis was applied to the northern part of the Mexican Caribbean, marked in red in **Figure 1**. The study area extends from the south of Cozumel Island to *Cabo Catoche*, north of Cancún, and to the east of the continental shelf. Although the numerical model overestimates the current, the EVA results are expected to give valuable predictions for extreme currents.

2 MATERIALS AND METHODS

2.1 Data Sources

Empirical and numerical data were used for the theoretical analysis presented here. Both sources provide data on the eastward and northward components of the ocean currents in the study area for different depths and different temporal resolutions. The Canek project, which has carried out similar measurements in the past (Chávez et al., 2003), was responsible for the measurements of the current in the Cozumel Channel. The Canek research project, also known as the *Estudio de la circulación y elintercambio a través del Canal de Yucatán* (Study of circulation and exchange through the Yucatan Canal) has been coordinated by the *Centro de Investigación Científica y Educación Superior de Ensenada* since its foundation in 1996. The data were obtained using a stationary, long-range acoustic Doppler current profiler at N20°32.218′ W087°02.738′ [see **Figure 1B**] anchored at a depth of approximately 400m, and measuring every half hour, from 9th April 2009 to 14th May 2011. The data on depth were recorded in 16 cells, with the shallowest cell at a depth of 49m. For the numerical data, the HYCOM was chosen because of its good temporal range and resolution, and excellent spatial resolution, compared to other products. In this study, the data of the reanalysis model HYCOM + NCODA GOMu0.04 experiment 50.1 are used, which are publicly available in https://www.hycom.org/data/gomu0pt04/expt-50pt1. The model provides the current components at 40 depths for the Mexican Caribbean (among other regions), covering 1st January 1993 to 31st December 2012, at a temporal resolution of three hours and a spatial resolution of 0.04 in both eastern and northern directions. Numerical current data are reported at a depth of 50m while the empirical data describe the current at 49m.

2.2 Validating and Adjusting Numerical Data With Empirical Data

Interpolation of HYCOM data to match the Canek data was carried out using the griddata function, available in the *SciPy*-module (version 1.6.1) for Python 3 (Virtanen et al., 2020). The four nodes of the numerical model were used as input, which surround the location of the measured field data. Due to the different sampling frequencies of the data sources, the data with higher frequency (i.e., the empirical data) had to be reduced. The data provided by the Canek project were sampled every 30 min and every hour, depending on the date. As the HYCOM numerical data reports the instantaneous value every three-hours, the empirical data were reduced by discarding every time step which is not available in the numerical data.

A linear quantile regression was performed on the current speed, using the quantreg model, as provided by the *statsmodels* module (version 0.12.2) for Python 3 (Seabold and Perktold, 2010). The linear regression was estimated for the empirical data proportional to the numerical data with the intercept set to zero.

To estimate the error produced by the numerical data, a simplified EVA was performed for both data sets, the empirical data in its original form and the numerical data in its adjusted form but reduced to the temporal range of the empirical data set. The analysis is described in detail in section 2.3. However, due to the low number of observations available in both sets, the methodology had to be modified. As a threshold, the 0.5th-quantile was used in contrast to the suggested automated threshold selection. However, the same range of possible thresholds was used to estimate the confidence interval. The (signed) relative error between empirical and numerical data is

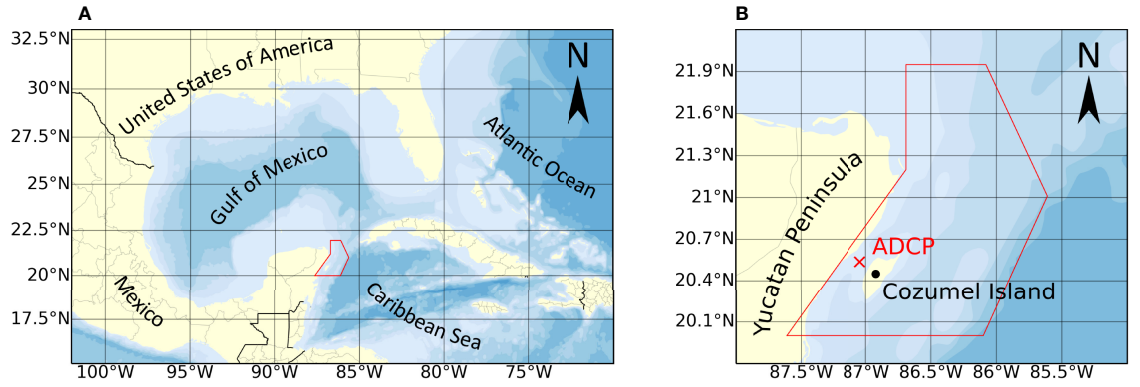

FIGURE 1 | **(A)** Study area within the Mexican Caribbean and **(B)** position of the acoustic Doppler current profiler (ADCP).

defined as

$$e_r = 1 - \frac{u_m}{u_e}, \quad (1)$$

where u_e is the empirical current speed and u_m is the speed as predicted by the numerical model. Besides the mentioned modules for Python 3 (Van Rossum and Drake, 2009), substantial parts of the data processing have been carried out with the NumPy-module in version 1.20.1 (Harris et al., 2020) and the pandas-module in version 1.2.2 (Wes McKinney, 2010).

2.3 Extreme Return Levels With Peaks Over Threshold

The methodology used assumes that for a random variable (x) the excess over a suitable threshold (u) can be modelled by a GPD. Liang et al. (2019) define the cumulative density function of the GPD as

$$F(x) = \begin{cases} 1 - \left(1 + \xi \frac{x-u}{\sigma}\right)^{(-1/\xi)} & \text{for } \xi \neq 0 \\ 1 - \exp\left(-\frac{x-u}{\sigma}\right) & \text{for } \xi = 0 \end{cases}, \text{ with } x \geq u \ , \quad (2)$$

Where $\boldsymbol{x}$ represents the random variable, $\boldsymbol{u}$ the threshold, ξ the shape parameter, and σ the scale parameter.

The procedure can be summarized as follows, where the automated threshold selection method is based on the work of Thompson et al. (2009):

1. Selection of peaks using a moving time window.
2. Detection and filtering of outliers using the quartile method.
3. Identification of potential thresholds between the 25th and 98th percentiles, or the 100th highest peak, whichever is less.
4. For each potential threshold u_j:

(a) Fit a GPD through all peaks for which $x_i > u_j$.

(b) Determine a reparameterised scale parameter (σ_i^*) and its difference ($\Delta\sigma_i^*$) tothe next higher threshold (u_j+1).

(c) Fit the normal distribution with zero mean through the difference of the reparameterised scale parameter corresponding to the current and all greater thresholds ($\Delta\sigma_i^* | u_i \geq u_j$).

5. Selection of the lowest threshold for which the p-value of the normal distribution through the difference of the reparameterised scale parameter is greater than a significance level of 5%.
6. Estimation of the return levels based on the selected threshold.

To consider the phenomenon as random, the realization of each variable should be independent. However, with the temporal resolution provided, the data analysed in this study is not random. To select only values independent of temporally close values (later called *peaks*), a moving time window was used, as suggested in Solari et al. (2017). The time window is of fixed length, depending on the variable type, and moves consecutively through the time series. If the value in the centre of the time window is the maximum of that time window, this value is selected as an independent peak.

Outliers may be present in the set of selected peaks, which would alter the final excess model. For the automated and semi-automated detection of outliers, a great variety of methods are available (Hodge and Austin, 2004). One of the simplest methods suitable for univariate data is based on quartiles and presented in Laurikkala et al. (2000). The authors define an upper (u_u) and lower threshold (u_l), beyond which all peaks are considered as outliers and are consequently discarded. Both thresholds are defined by

$$u_l = q_1 - 1.5(q_3 - q_1) \quad (3)$$

$$u_u = q_3 + 1.5(q_3 - q_1) \ , \quad (4)$$

where q_1 is the first quartile (25th percentile) and q_3 is the third quartile (75th percentile).

From the previously selected peaks, potential thresholds are selected, as suggested in Thompson et al. (2009). The potential thresholds are equally spaced between 25th and 98th percentile. If less than 100 peaks are found above the 98th percentile, the 100th

largest peak is selected as the upper limit of the range for potential thresholds.

For each threshold, all peaks $x_i > u_j$ are selected, and a GPD is fitted through those peaks. The shape (ξ_j) and scale (σ_j) parameters of the GPD are determined by the function genpareto.fit, which is part of the SciPy.stats-package. The location parameter is held fixed to the corresponding threshold u. The reparameterised scale parameter, which is defined by

$$\sigma_j^* = \sigma_j - \xi_j u_j \ , \tag{5}$$

should be constant above a suitable threshold, following Coles (2001). This relationship was extended by Thompson et al. (2009) by fitting a normal distribution with a mean of zero through the difference of the reparameterised scale parameter for the current and all greater thresholds. This difference is defined by

$$\Delta\sigma_j^* = \sigma_{j+1}^* - \sigma_j^* \ . \tag{6}$$

The first threshold for which the corresponding normal distribution has a p-value ≥ 0.05 is selected for calculating the return levels. As a test for normality, the Kolmogorov-Smirnov test is used, as implemented in the ks_1samp function of the SciPy.stats-package. The return level X_m (Coles, 2001) can be calculated as

$$x_m = \begin{cases} u + \frac{\sigma}{\xi}\left((m\zeta_u)^{\xi} - 1\right) & \text{for } \xi \neq 0 \\ u + \sigma \log\left(m\zeta_u\right) & \text{for } \xi = 0 \end{cases} \ . \tag{7}$$

The average number of peaks m during a return period (T_B) is defined by

$$m = \frac{n_p}{n_y} T_B \ , \tag{8}$$

where n_p is the total number of peaks and n_y the number of years for which data is available.

The exceedance probability of threshold $\hat{\zeta}_u$, the complete Variance-Covariance Matrix V and the variance of return level Var ($\hat{x}_m$) are estimated, as stated in the following equations (Coles, 2001), where the values with a hat indicate the estimation of the corresponding value.

$$\hat{\zeta}_u = \frac{n_{pot}}{n_p} \ , \tag{9}$$

where n_{pot} is the number of peaks over threshold

$$V = \begin{bmatrix} \frac{\hat{\zeta}_u}{n_p}\left(1 - \hat{\zeta}_u\right) & 0 & 0 \\ 0 & \mathrm{Var}\left(\hat{\sigma}\right) & \mathrm{Cov}\left(\hat{\sigma}, \hat{\xi}\right) \\ 0 & \mathrm{Cov}\left(\hat{\xi}, \hat{\sigma}\right) & \mathrm{Var}\left(\hat{\xi}\right) \end{bmatrix} \ , \tag{10}$$

$$\mathrm{Var}\left(\hat{x}_m\right) = \nabla \hat{x}_m^T \, V \, \nabla \hat{x}_m \ , \tag{11}$$

with

$$\nabla \hat{x}_m = \left[\frac{\partial x_m}{\partial \zeta_u}, \frac{\partial x_m}{\partial \sigma}, \frac{\partial x_m}{\partial \xi}\right]^T = \begin{bmatrix} \sigma m^{\xi} \zeta_u^{\ \xi - 1} \\ \xi^{-1}\left((m\zeta_u)^{\xi} - 1\right) \\ -\sigma\xi^{-2}\left((m\zeta_u)^{\xi} - 1\right) + \sigma\xi^{-1}(m\zeta_u)^{\xi}\log\left(m\zeta_u\right) \end{bmatrix} \tag{12}$$

3 RESULTS

3.1 Numerical Data Accuracy

The empirical and numerical data used have different temporal resolutions. Therefore, the empirical data from the Canek project were downsampled by discarding all time steps that are unavailable in the data provided by the numerical model. In **Figure 2** the unadjusted numerical data show a clear bias towards overestimation. The numerical data were adjusted by the linear regression model, which was estimated with a quantile regression using the 0.5^{th}-quantile, and is defined by

$$u'_m = 0.791831 u_m \ , \tag{13}$$

where u'_m is the adjusted current speed. The adjusted numerical data reflect the empirical data much better. The effect of the model adjustment is strongly reflected by the mean relative error, that is reduced from −0.255 to 0.006. The mean absolute relative error of 0.288 and the root mean squared relative error of 0.365 are reduced to 0.153 and 0.206, respectively. Of greater concern, however, is the missing tail of the probability distribution of both numerical data in Figurs 2A, as these are of great importance for EVAs. Especially in the adjusted data, this leads to a pronounced underestimation of higher current speeds (i.e., rare events) as seen in the deviation from the diagonal in **Figure 2B**.

To quantify the effect of the missing tail on the extreme value estimations, a simplified EVA was performed. Due to the short time range, the length of the time window was reduced to 7 days (i.e., 56 observations). Additionally, the 0.5^{th}-quantile was selected as the threshold rather than the proposed automated threshold selection. As expected from the results presented in **Figure 2B**, the adjusted numerical model shows an underestimation of extreme values, as can be seen in **Figure 3A**. Nevertheless, for rare events (return period > 10 years) the relative error converges to a value just below 0.22 (see **Figure 3B**). The large 95% confidence interval ($CI_{95\%}$) in **Figure 3A** is the result of the short temporal coverage of the data used for the analysis. It should be noted that the CI in **Figure 3B** is not $CI_{95\%}$; it is the maximum error estimated by the upper and lower bounds of the $CI_{95\%}$ in **Figure 3A**.

3.2 Extreme Value Analysis

The methodology was applied to several nodes in the Mexican Caribbean, shown as grey dots in **Figure 4**. It should be noted

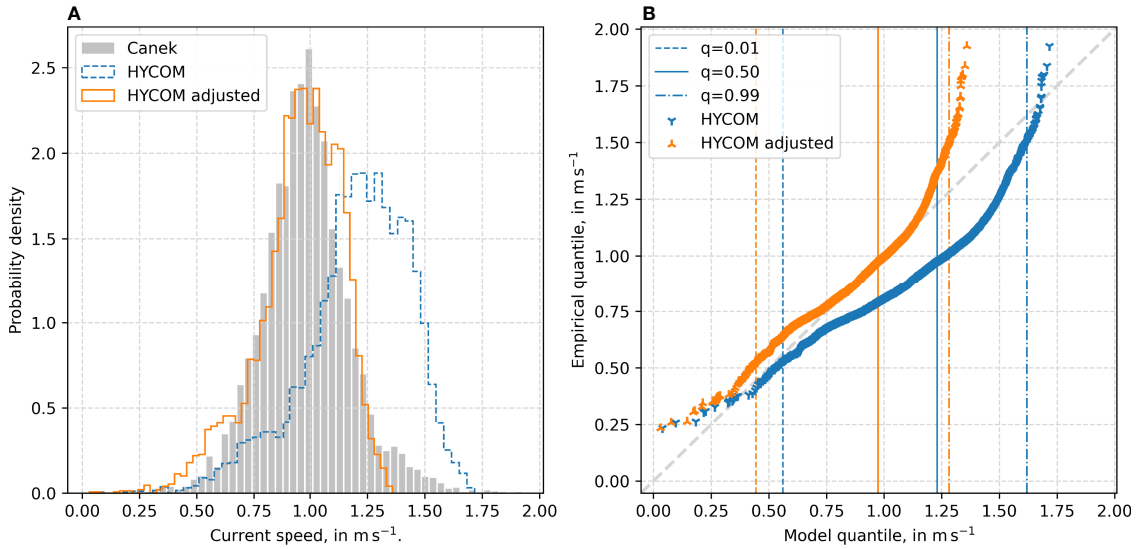

FIGURE 2 | Adjustment of the HYCOM numerical data to the Canek-project empirical data [from the ADCP shown in **Figure 1 (B)**]. **(A)** Histogram showing the numerical data before and after the adjustment. **(B)** Q-Q plot of numerical data before and after the adjustment. The 0.01st 0.5th and 0.99th-quantiles are marked for both data sets.

that not every node contains data on the current, as some are on land, or in waters of less than 50m depth. The four nodes marked in red were selected as the results suggest that it is possible to obtain a different behaviour with respect to the GPD fit. The node at position P1 (20.520° N, 86.600° W) is where the current is most concentrated off the east coast of Cozumel. The node at position P2 (20.640° N, 86.960° W), is in the Cozumel Channel, near a possible site for the installation of ocean current turbines [see Alcérreca-Huerta et al. (2019)]. That at P3 (21.040° N, 86.560° W) is in the wake of the Cozumel Channel, off the coast of Cancun, and the node at P4 (21.800° N, 86.480° W) is in the Yucatan current northeast of Cancun.

To determine the optimal length of the time window, the number of peaks identified in the windows was analysed for the nodes at P1 to P4. In **Figure 5A**, there is a steady fall in the number of peaks, but it remains above the critical number of 200. At a length of 25 days, the number of peaks for all four nodes is just below 250. The relative difference between the number of

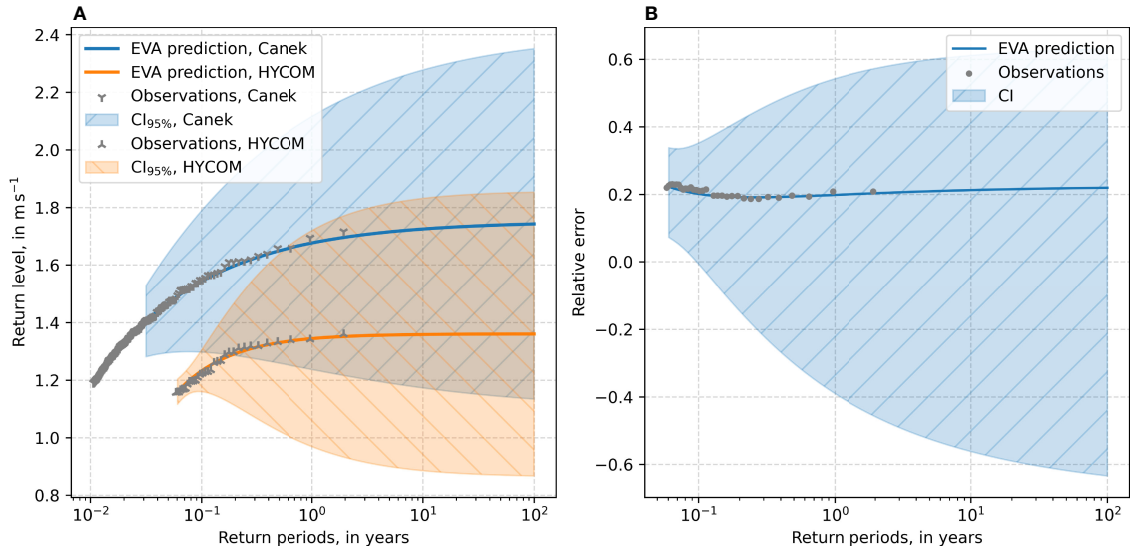

FIGURE 3 | Results of the simplified EVA for the adjusted numerical and empirical data. The adjusted numerical data are limited to the temporal range of the empirical data. **(A)** Return level plot. **(B)** Relative error of estimated return levels.

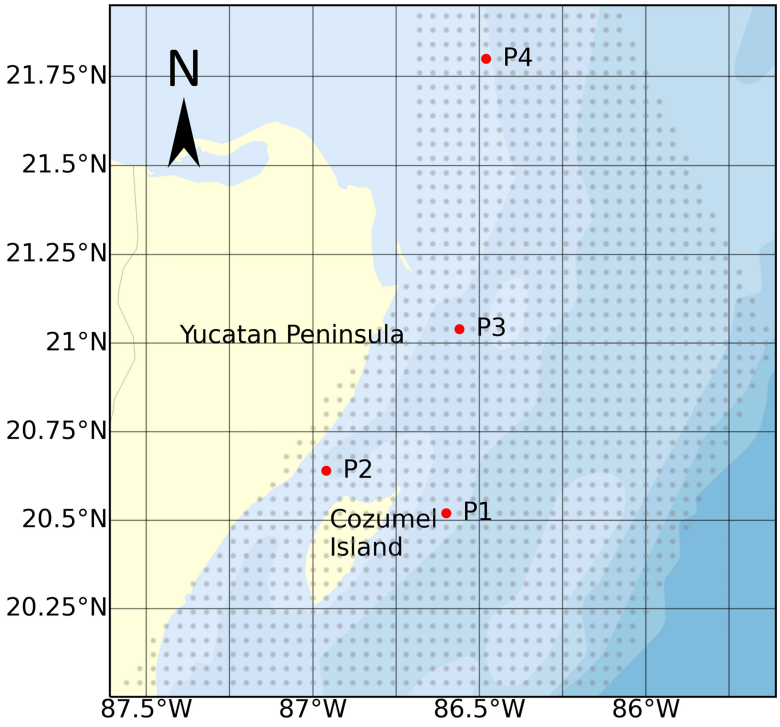

FIGURE 4 | Location of the nodes for the numerical model which lie within the study area. The nodes marked in red are positions for which more details regarding the GPD fit are presented.

peaks and the length of time window (see **Figure 5B**) shows a decreasing trend, as the length of the time window increases. From a 21 day length, the relative difference is less than 10%, dipping briefly below the 5% mark at a length of 23 days. To spread the number of peaks evenly within the time range analysed, and to avoid having too few peaks, a time window of 23 days in length was chosen.

Figure 6 shows the statistical data of the GPD fit for each node. While the north, east, and southern boundaries of the domain are determined by the node selection, the western boundary is a feature of the numerical data generated by HYCOM for this site. The number of identified peaks seems to be similar in the study region (see **Figure 6A**), with a slight decrease towards deeper waters.

Figures 6B, C) show the selected threshold for each node and the corresponding p-value for the automatic threshold selection, respectively. The value of selected thresholds tend to increase in the centre of the channel, and in the stream close to the east coast of Cozumel Island that extends northward, along the Cancun coast. This is expected, since the current becomes more intense at these locations. As it was possible to find a suitable threshold for all nodes with information on the current velocity, the p-value is over 0.05 in significance, although some inconsistencies of above 0.1, and even 0.15, are found throughout the domain.

There is no clear trend in the shape parameter of the fitted GPD in **Figure 6D**. However, it was estimated to be negative for all nodes, producing a bounded GPD. For a few nodes at the northwestern boundary, the shape parameter was estimated to be very close to zero. The scale parameter in **Figure 6E** indicates a slight increase off Cozumel Island and at the northeastern boundary, which leads to a thicker tail for the GPD in those regions (i.e., increased return levels).

Figure 6F shows the number of peaks above the threshold which lie within the estimated $CI_{95\%}$. For nearly all the nodes, the estimated $CI_{95\%}$ covers 100% of the numerical observations. As is to be expected, not all the observations are within the $CI_{95\%}$ for all the nodes. However, the number of nodes for which some observations are outside the $CI_{95\%}$ is small, while the minimum share within the analysed region is still above 90%. Despite this apparent overestimation of the $CI_{95\%}$, this suggests that the methodology of GPD fit together with the estimation of the $CI_{95\%}$ is suitable and the results of the GPD for the given input data is reliable.

Return levels for the selected return periods, on the corresponding lower and upper boundaries of the $CI_{95\%}$ are shown in **Figure 7**. The expected return level (central column) increases in the channel and the main current, which extends northwards from the east of the Cozumel Island. This trend is further pronounced in the case of the $CI_{95\%}$ upper boundary (right column of **Figure 7**), which is in agreement with the results in **Figures 6B**, **E**. The region with higher shape parameters at the northwest edge of the domain (see **Figure 6D**) is not noticeable in the estimated return level (centre column in **Figure 7**). However, in case of the CI95%-

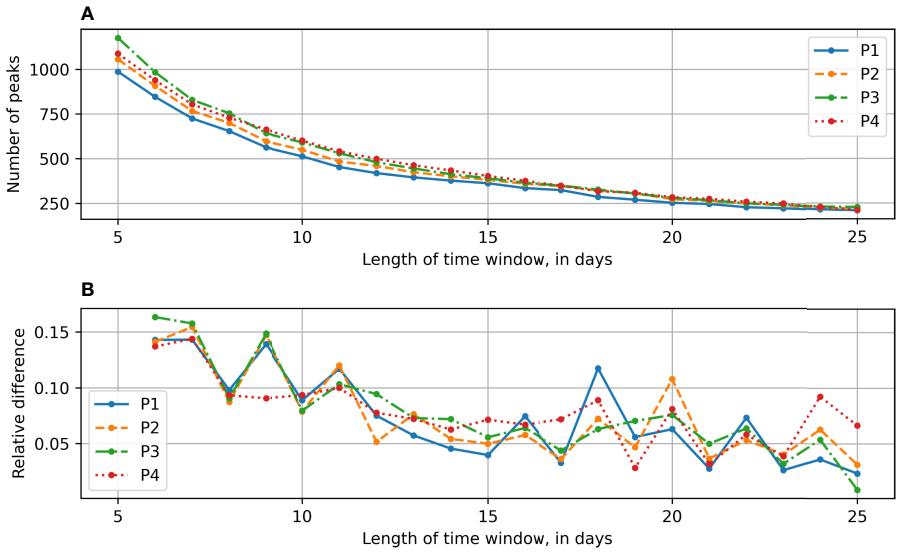

FIGURE 5 | Relation between the number of independent peaks and the length of the time window for the nodes at P1 to P4. **(A)** Number of identified peaks. **(B)** Relative difference in number of identified peaks to previous time window length.

limits, that region stands out with lower return level for the lower bound of the $CI_{95\%}$ and higher return levels for the upper limit, suggesting a much higher uncertainty. The distribution over the rest of the domain is as expected, see **Figure 6**.

The parameters for the GPD excess model for the four nodes seen in **Figure 4** are summarized in **Table 1**. Except for the node at position P4, the shape parameters are negative, with all of $CI_{95\%}$ below zero. Compared to the standard error, the shape parameter at P4 is small, giving a $CI_{95\%}$ closely centred around zero. However, this result could be due to an error in the numerical model, as mentioned above. The highest scale parameter is found at P1, which produces a thicker tail to the probability distribution. Nevertheless, the bound nature of the excess model (due to the negative shape parameter) prevents high return levels for this node. The number of peaks found for each node is similar, just above the critical threshold of 200. Slightly more than 100 peaks were found above the selected threshold. The number of peaks, and peaks above the threshold, suggests that the

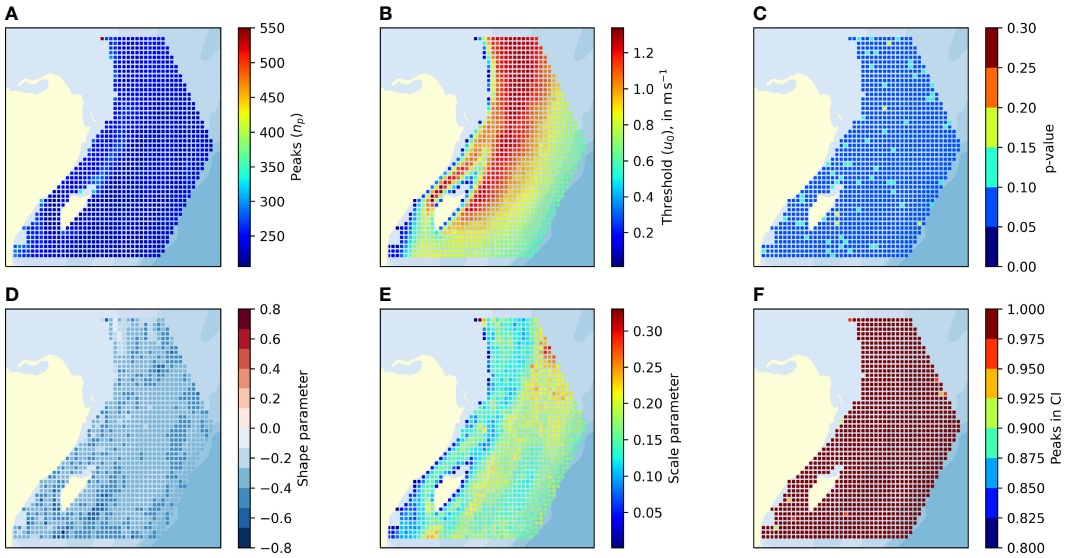

FIGURE 6 | Statistical data for the GPD fit. **(A)** Number of identified peaks. **(B)** Selected thresholds. **(C)** p-value for the selected thresholds. **(D)** Shape factor for GPD fit to POT. **(E)** Scale factor for GPD fit to POT. **(F)** Share of peaks within the $CI_{95\%}$.

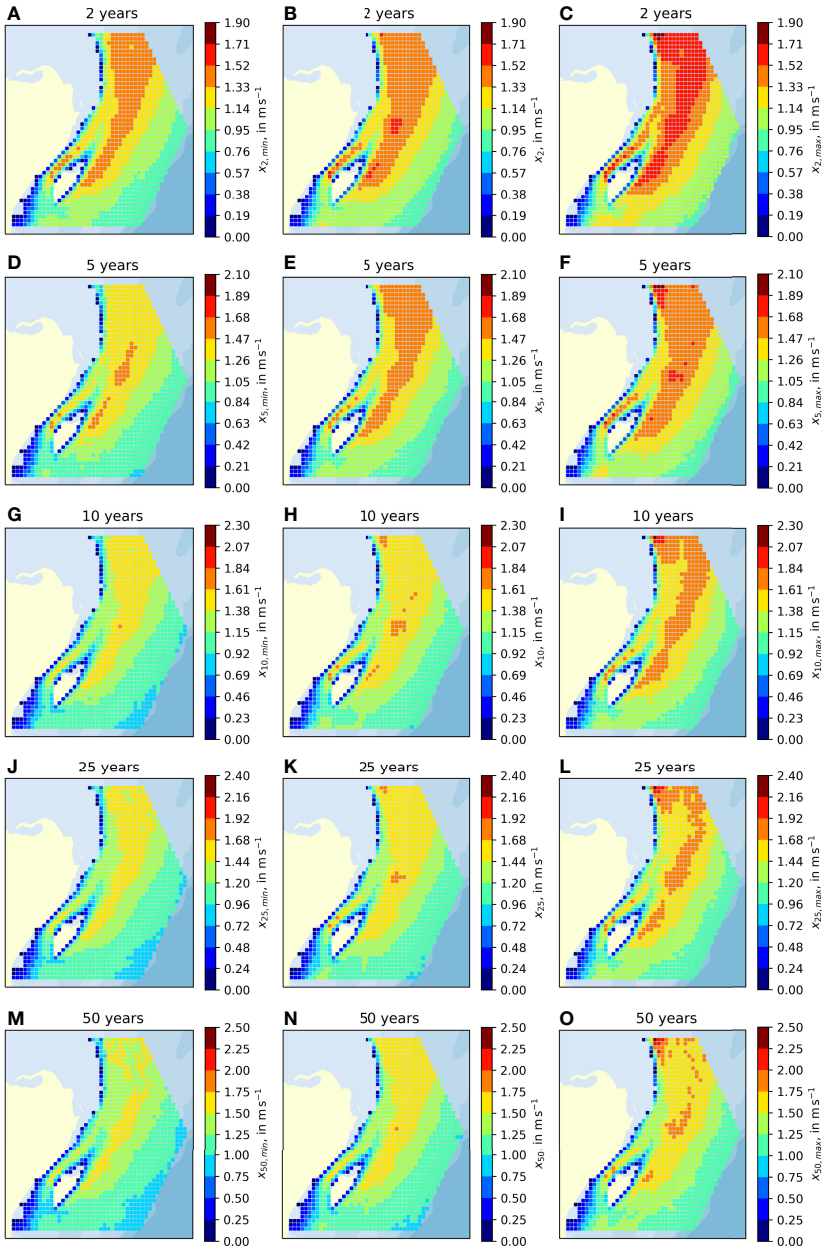

FIGURE 7 | Return levels for 50m depth for different return periods. All the figures in one row correspond to the same return period; **(A–C)** 2 years, **(D–F)** 5 years, **(G–I)** 10 years, **(J–L)** 25 years, and **(M–O)** 50 years. The left column shows the lower bound of the $CI_{95\%}$, the right column the upper bound of the $CI_{95\%}$, and the central column the predicted return level.

selected time span of 20 years is a bit short, but still sufficient to perform the EVA.

In **Figure 8**, the peaks, POT, and the thresholds are shown for the four nodes. None of these nodes have a cluster of peaks (or lack thereof), suggesting that a 23 day time window is sufficient. The distributions of peaks, together with the filtered outliers, are shown for each node in **Figure 9**. The nodes at P1 to P3 show a standard distribution of peaks. The node at P4 has a multi-modal distribution, suggesting an error, and that the conclusions drawn from the data might not be reliable. No outliers at the upper end were found for the node at P2, whereas at P1 and P4 there were one each, and at P3, two. At the lower end, a few outliers were also detected and filtered out, but due to the nature of POT methods, these tend to have no significant effect on the outcome.

Figures 10–13 present the corresponding diagnostic plots for the GPD excess model. For a detailed interpretation of this type of plot, the reader is referred to Coles (2001). Despite

TABLE 1 | Values for GPD fit for four nodes.

	Node at P1	Node at P2	Node at P3	Node at P4
Threshold (u_o) in ms^{-1}	1.2397	1.3267	1.0400	1.0784
Shape parameter (ξ)	-0.3965	-0.3171	-0.3669	-0.0839
Corresponding $CI_{95\%}$	-0.480	-0.423	-0.453	-0.280
	…	…	…	…
	-0.313	-0.211	-0.280	0.112
Scale parameter (σ)	0.1827	0.1501	0.1417	0.1088
Peaks (n_p)	222	239	242	249
POT (n_{pot})	111	114	111	102
POT in $CI_{95\%}$ of return level	100%	100%	100%	100%

slight deviations in the diagnostic plot for the node at P1 in **Figure 10**, and especially the q-q plot in **Figure 10B**, 100% of the empirical POT still lie within the $CI_{95\%}$, as seen in **Figure 10C** and tab. 1. Both plots suggest an overestimation of the GPD model. There are few peaks, especially visible in the density plot (**Figure 10D**). However, the bound excess model seems to give a good fit for the underlying numerical data. The diagnostic plots for the node at P2 (**Figure 11**) show some deviations between the numerical data and GPD excess model in the p-p plot (**Figure 11A**). Around the 0.6 mark, the GPD excess model shows a slight overestimation. This deviation is also visible in the q-q plot (**Figure 11B**) at speeds of about 1.45ms−1 and in the return level-plot (**Figure 11C**) at the same speeds. Despite these inconsistencies, the GPD excess model is a fits the data well.

The p-p plot presents some discrepancies at the 60% percentile at P3 (**Figure 12A**). The excess model also differs from the numerical data for higher speeds, as seen in **Figures 12B, C**. However, all the observations are within the estimated $CI_{95\%}$ of the return level, suggesting that the GPD excess model application is reliable.

The plots in **Figure 13** bring into doubt whether this excess model can be used to reliably estimate the extreme values of the node at P4. Although the $CI_{95\%}$ includes all the numerical observations, the p-p plot (**Figure 13A**) and especially the q-q plot (**Figure 13B**) looks unusual. A slight s-shaped deviation is present, with considerable inconsistencies above 1.2ms^{-1} in the q-q plot. Additionally, and as observed in **Figure 7**, the $CI_{95\%}$ in **Figure 13C** is quite large, while the density plot in **Figure 13D** shows a reasonable fit to the data.

4 DISCUSSION

For adjustment of the numerical data, the empirical and numerical data were filtered to match their time steps. The high relative error of -25.5% was reduced to 0.6% by linear quantile regression. However, the mean absolute relative error and the root mean square relative error cannot be reduced in the same way. This indicates that, despite the adjustment, the numerical model is not able to accurately reproduce the behaviour of the current in this region. Furthermore, the lack of the tail in the numerical data histogram proves that there is still room to improve the HYCOM numerical model. The effect of the missing tail on extreme value predictions was estimated with a simplified EVA. Despite the short time series,

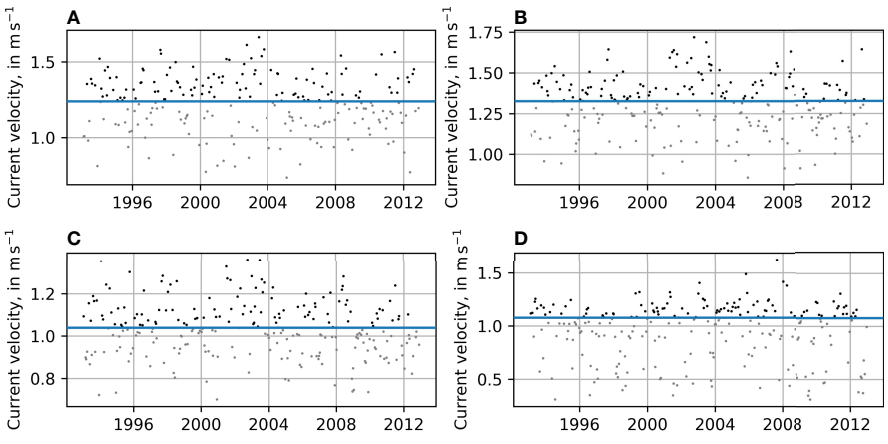

FIGURE 8 | Distribution of peaks over time for the nodes at P1 to P4, as identified by means of a 23 days moving time window. The peaks under threshold are marked with grey dots, the peaks over threshold with black dots, and the selected threshold by the blue line. **(A)** Node at P1, **(B)** Node at P2, **(C)** Node at P3, and **(D)** Node at P4.

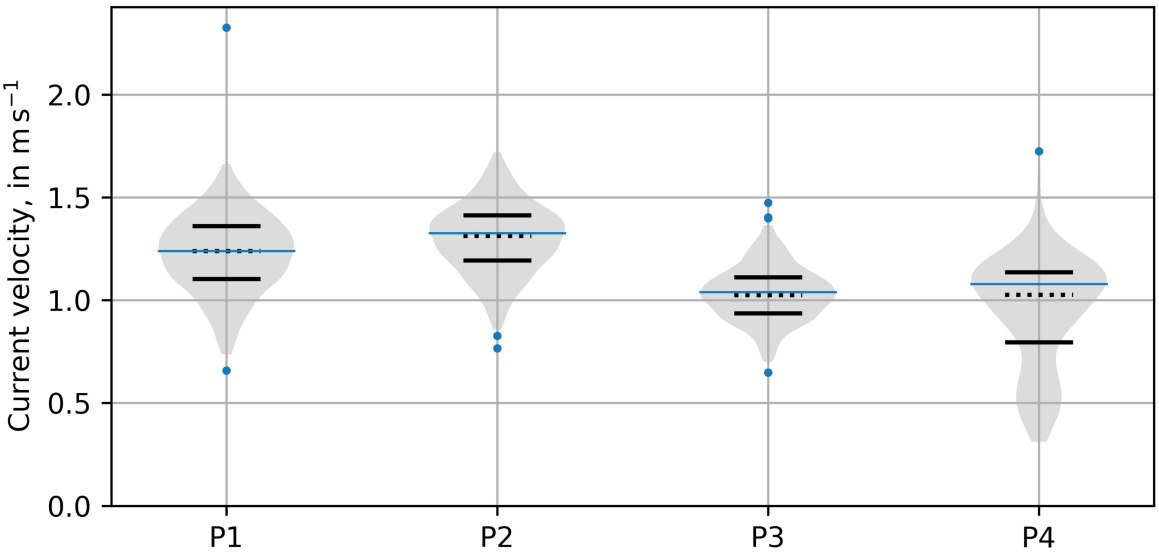

FIGURE 9 | Detected outliers and distribution of peaks for nodes at P1 to P4. The first and third quartiles are shown as solid lines and the median as a dotted line. The filtered outliers are shown as blue dots and the selected threshold as a thin blue line.

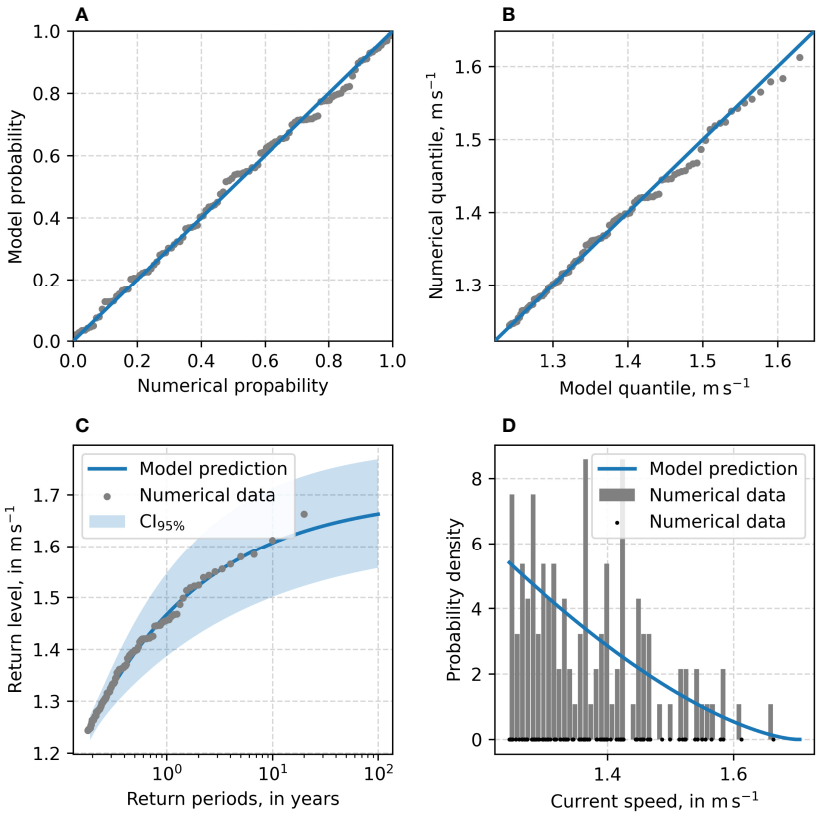

FIGURE 10 | Diagnostic plot for the GPD excess model fitted to 3-hourly current for the node at P1. **(A)** p-p plot, **(B)** q-q plot, **(C)** return level plot, and **(D)** density plot.

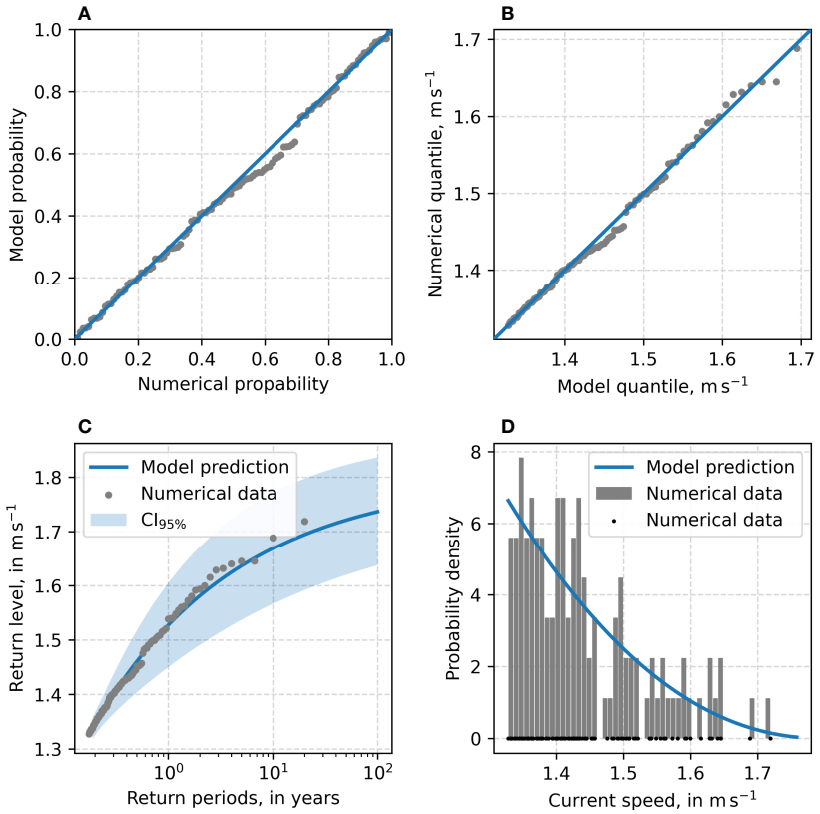

FIGURE 11 | Diagnostic plot for the GPD excess model fitted to 3-hourly current for the node at P2. **(A)** p-p plot, **(B)** q-q plot, **(C)** return level plot, and **(D)** density plot.

the error can be estimated at 22% underestimation for rare events with a return period of > 10years. However, the error presents very low variability for rare events, and the error converges to a value close to 22%. This makes it easy to account for in design processes. Nevertheless, these results should be addressed in future research in order to accurately identify the source of the error and to characterize it over a larger area, instead of a single point.

As shown by the large $CI_{95\%}$ of the simplified EVA, the temporal coverage of the empirical data is not sufficient to reliably estimate extreme values. However, the error between the extreme value predictions of empirical and numerical data is consistent. This error gives the necessary information to have sufficiently detailed knowledge on the extreme value predictions derived from the HYCOM model.

For most of the nodes, the EVA showed consistent behaviour over the domain analysed. Some inconsistencies were found, especially at the boundary of the numerical domain and on the northwest edge of the continental shelf. Besides the significant changes in the bathymetry in those regions, the ordered grid of the numerical model might not be fully capable of representing the nature of the current in boundaries that are not aligned with the grid. As can be seen for the node at P4, the estimated $CI_{95\%}$ is large, and the multimodal peak distribution suggests an unusual behaviour of the HYCOM data for this area. The results for these nodes may be unreliable, and it is suggested that the data obtained for these locations is used with special care.

The other three nodes, which had more information on the GPD fit, showed unremarkable results, as the EVA represents a good fit for the numerical observations. For most nodes, 100% of the numerical observations were found to be within the estimated $CI_{95\%}$. This share should be much closer to 95%, indicating that the estimated $CI_{95\%}$ is larger than it should be. In contrast to the assumed symmetric distribution of the $CI_{95\%}$, a log-likelihood profile could give better results and might be investigated in future studies if the overestimation of the $CI_{95\%}$ represents an issue.

The extreme values found a reasonable distance from the coast vary considerably. Therefore, it is important to carefully select a region with similar behaviour in terms of GPD fit. Basing design values on a region with heterogeneous behaviour could lead to erroneous design choices. Besides the variability, regions with similar return periods are found on either side of Cozumel Island. In terms of extreme currents, with reduced effort it may be possible to adapt energy harvesting devices designed for Cozumel Channel conditions to the conditions on the east coast of Cozumel.

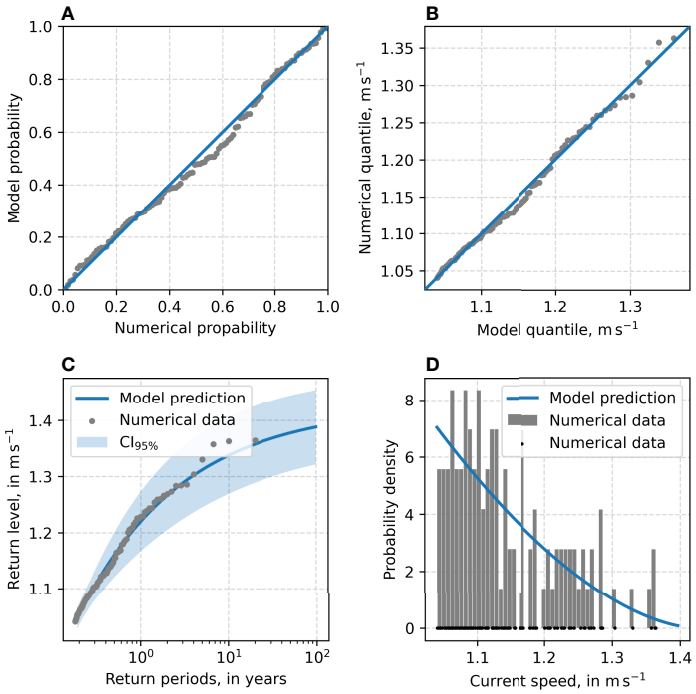

FIGURE 12 | Diagnostic plot for the GPD excess model fitted to 3-hourly current for the node at P3. **(A)** p-p plot, **(B)** q-q plot, **(C)** return level plot, and **(D)** density plot.

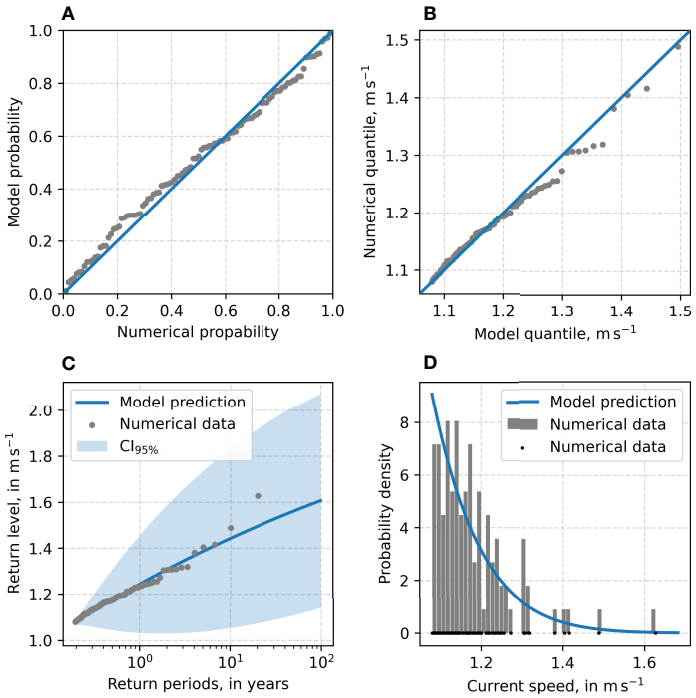

FIGURE 13 | Diagnostic plot for the GPD excess model fitted to 3-hourly current for the node at P4. **(A)** p-p plot, **(B)** q-q plot, **(C)** return level plot, and **(D)** density plot.

5 CONCLUSIONS

It was found that the HYCOM model does not accurately reproduce the current velocities in the Cozumel Channel. Adjusting the model with a linear quantile regression reduces the mean absolute relative error to 15.3%, but the lack of a tail in the distribution of the numerical data leads to an underestimation of extreme values of almost 22%.

Applied to a range of nodes within the Mexican Caribbean, the methodology showed consistently – and to some extent predictable – behaviour. In the Cozumel Channel and in the main current, the threshold and the extreme values are naturally higher than in regions with lower current intensities. The difference in return levels can be explained by the threshold and the scale parameter.

Despite the shortcomings of the numerical model, the methodology presented for estimating extreme values of ocean currents based on HYCOM data proves to be a valuable tool due to the predictability of the error for extreme values.

DATA AVAILABILITY STATEMENT

The raw data supporting the conclusions of this article are available from the corresponding author, MR, upon reasonable request.

AUTHOR CONTRIBUTIONS

Conceptualization and methodology: PR-O and MR; data processing, analysis and visualisation: MR; writing – original draft preparation: PR-O and MR; writing – review and editing: PR-O, MR, RS, and EM; supervision and project administration: RS and EM; funding acquisition: EM; All authors contributed to manuscript revision, read, and approved the submitted version.

FUNDING

This research was funded by the CONACYT-SENER-SUSTENTABILIDAD ENERGÉTICA project: FSE-2014-06-249795 "Centro Mexicano de Innovación en Energía del Océano (CEMIE Océano)".

ACKNOWLEDGMENTS

The authors would like to thank Julio Candela and Julio Sheinbaum for permission to use their empirical data and Jill Taylor for reviewing the English language. Furthermore, the first author is grateful for the financial support provided by the CONACYT doctoral fellowship.

REFERENCES

Abascal, A. J., Sheinbaum, J., Candela, J., Ochoa, J., and Badan, A. (2003). Analysis of Flow Variability in the Yucatan Channel. *J. Geophys. Res. C.: Ocean.* 108, 11–11. doi: 10.1029/2003JC001922

Alcérreca-Huerta, J. C., Encarnacion, J. I., Ordoñez-Sánchez, S., Callejas-Jiménez, M., Barroso, G. G. D., Allmark, M., et al. (2019). Energy Yield Assessment From Ocean Currents in the Insular Shelf of Cozumel Island. *J. Mar. Sci. Eng.* 7, 1–18. doi: 10.3390/jmse7050147

Athie, G., Candela, J., Sheinbaum, J., Badan, A., and Ochoa, J. L. (2011). Yucatan Current Variability Through the Cozumel and Yucatan Channels. *Cienc. Mar.* 37, 471–492. doi: 10.7773/cm.v37i4a.1794

Bárcenas Graniel, J. F., Fontes, J. V. H., Garcia, H. F. G., and Silva, R. (2021). Assessing Hydrokinetic Energy in the Mexican Caribbean: A Case Study in the Cozumel Channel. *Energies* 14, 4411. doi: 10.3390/en14154411

Bore, P. T., Amdahl, J., and Kristiansen, D. (2019). Statistical Modelling of Extreme Ocean Current Velocity Profiles. *Ocean. Eng.* 186, 106055. doi: 10.1016/j.oceaneng.2019.05.037

Carrillo González, F., Ochoa, J., Candela, J., Badan, A., Sheinbaum, J., and González Navarro, J. I. (2007). Tidal Currents in the Yucatan Channel. *Geofis. Internacional.* 46, 199–209. doi: 10.22201/igeof.00167169p.2007.46.3.39

Cetina, P., Candela, J., Sheinbaum, J., Ochoa, J., and Badan, A. (2006). Circulation Along the Mexican Caribbean Coast. *J. Geophys. Res.: Ocean.* 111, 1–19. doi: 10.1029/2005JC003056

Chávez, G., Candela, J., and Ochoa, J. (2003). Subinertial Flows and Transports in Cozumel Channel. *J. Geophys. Res. C.: Ocean.* 108, 19–11. doi: 10.1029/2002JC001456

Coles, S. (2001). "An Introduction to Statistical Modeling of Extreme Values", in *Springer Series in Statistics* (London, UK: Springer-Verlag).

Coles, S., and Simiu, E. (2003). Estimating Uncertainty in the Extreme Value Analysis of Data Generated by a Hurricane Simulation Model. *J. Eng. Mechanics.* 129, 1288–1294. doi: 10.1061/(asce)0733-9399(2003)129:11(1288

Devis-Morales, A., Montoya-Sánchez, R. A., Bernal, G., and Osorio, A. F. (2017). Assessment of Extreme Wind and Waves in the Colombian Caribbean Sea for Offshore Applications. *Appl. Ocean. Res.* 69, 10–26. doi: 10.1016/j.apor.2017.09.012

Fan, S., Dupuis, K., Harrington-Missin, L., Calverley, M., Watson, A., and Jeans, G. (2010). Validation of HYCOM Current Profiles Using MMS NTL Observations. *Proc. Annu. Offshore. Technol. Conf.* 3, 2135–2147. doi: 10.2523/20797-ms

Harris, C. R., Millman, K. J., van der Walt, S. J., Gommers, R., Virtanen, P., Cournapeau, D., et al. (2020). Array Programming With NumPy. *Nature* 585, 357–362. doi: 10.1038/s41586-020-2649-2

Hernández-Fontes, J. V., Felix, A., Mendoza, E., Cueto, Y. R., and Silva, R. (2019). On the Marine Energy Resources of Mexico. *J. Mar. Sci. Eng.* 7. doi: 10.3390/jmse7060191

Hodge, V. J., and Austin, J. (2004). A Survey of Outlier Detection Methodologies. *Artif. Intell. Rev.* 22, 85–126. doi: 10.1023/B:AIRE.0000045502.10941.a9

Jonathan, P., and Ewans, K. (2013). Statistical Modelling of Extreme Ocean Environments for Marine Design: A Review. *Ocean. Eng.* 62, 91–109. doi: 10.1016/j.oceaneng.2013.01.004

Laurikkala, J., Juhola, M., and Kentala, E. (2000). Informal Identification of Outliers in Medical Data. *In. 5th. Int. Workshop. Intell. Data Med. Pharmacol.* 1, 20–24.

Liang, B., Shao, Z., Li, H., Shao, M., and Lee, D. (2019). An Automated Threshold Selection Method Based on the Characteristic of Extrapolated Significant Wave Heights. *Coast. Eng.* 144, 22–32. doi: 10.1016/j.coastaleng.2018.12.001

Liu, M., Wu, W., Tang, D., Ma, H., and Naess, A. (2018). Current Profile Analysis and Extreme Value Prediction in the LH11-1 Oil Field of the South China Sea Based on Prototype Monitoring. *Ocean. Eng.* 153, 60–70. doi: 10.1016/j.oceaneng.2018.01.064

Moeini, M. H., Etemad-Shahidi, A., and Chegini, V. (2010). Wave Modeling and Extreme Value Analysis Off the Northern Coast of the Persian Gulf. *Appl. Ocean. Res.* 32, 209–218. doi: 10.1016/j.apor.2009.10.005

Morton, I. D., and Bowers, J. (1996). Extreme Value Analysis in a Multivariate Offshore Environment. *Appl. Ocean. Res.* 18, 303–317. doi: 10.1016/S0141-1187(97)00007-2

Niroomandi, A., Ma, G., Ye, X., Lou, S., and Xue, P. (2018). Extreme Value Analysis of Wave Climate in Chesapeake Bay. *Ocean. Eng.* 159, 22–36. doi: 10.1016/j.oceaneng.2018.03.094

Ochoa, J., Candela, J., Badan, A., and Sheinbaum, J. (2005). Ageostrophic Fluctuations in Cozumel Channel. *J. Geophys. Res. C.: Ocean.* 110, 1–16. doi: 10.1029/2004JC002408

Oliver, E. C., Sheng, J., Thompson, K. R., and Blanco, J. R. (2012). Extreme Surface and Near-Bottom Currents in the Northwest Atlantic. *Nat. Haz.* 64, 1425–1446. doi: 10.1007/s11069-012-0303-5

Orbital Marine Power Ltd. (2021). *Orbital Marine Power Launches O2: World's Most Powerful Tidal Turbine*. Available at: https://orbitalmarine.com/orbital-marine-power-launches-o2 (Accessed Date November 16, 2021).

Park, S. B., Shin, S. Y., Shin, D. G., Jung, K. H., Choi, Y. H., Lee, J., et al. (2020). Extreme Value Analysis of Metocean Data for Barents Sea. *J. Ocean. Eng. Technol.* 34, 26–36. doi: 10.26748/ksoe.2019.094

Qi, Y., and Shi, P. (2009). Calculation of the Extreme Wind, Wave And Current In Deep Water of the South China Sea. *The Proceedings of The Third (2009) ISOPE International DEEP-OCEAN TECHNOLOGY SYMPOSIUM: Deepwater Challenge (IDOT-2009)*1–7. Available at: http://publications.isope.org/proceedings/ISOPE_IDOT/ISOPE_IDOT_2009/start.htm.

Robinson, M. E., and Tawn, J. A. (1997). Statistics for Extreme Sea Currents. *J. R. Stat. Soc. Ser. C.: Appl. Stat* 46, 183–205. doi: 10.1111/1467-9876.00059

Seabold, S., and Perktold, J. (2010). "Statsmodels: Econometric and Statistical Modeling With Python", in *In 9th Python in Science Conference* 57, 61. doi: 10.25080/Majora-92bf1922-011.

Simiu, E. (2011). *Design of Buildings for Wind: A Guide for ASCE 7-10 Standard Users and Designers of Special Structures: Second Edition* (Hoboken, New Jersey, USA: John Wiley and Sons).

Solari, S., Egüen, M., Polo, M. J., and Losada, M. A. (2017). Peaks Over Threshold (POT): A Methodology for Automatic Threshold Estimation Using Goodness of Fit P-Value. *Water Resour. Res.* 53, 2833–2849. doi: 10.1002/2016WR019426

Sustainable Marine. (2021). *Sustainable Marine Unveils 'Next-Gen Platform' Ahead of World-Leading Tidal Energy Project*. Available at: https://www.sustainablemarine.com/press-releases/-sustainable-marine-unveils-%E2%80%98next-gen-platform%E2%80%99-ahead-of-world-leading-tidal-energy-project (Accessed date November 16, 2021).

Thompson, P., Cai, Y., Reeve, D., and Stander, J. (2009). Automated Threshold Selection Methods for Extreme Wave Analysis. *Coast. Eng.* 56, 1013–1021. doi: 10.1016/j.coastaleng.2009.06.003

Van Rossum, G., and Drake, F. L. (2009). *Python 3 Reference Manual* (Scotts Valley, CA: CreateSpace).

Virtanen, P., Gommers, R., Oliphant, T. E., Haberland, M., Reddy, T., Cournapeau, D., et al. (2020). {SciPy} 1.0: Fundamental Algorithms for Scientific Computing in Python. *Nat. Methods* 17, 261–272. doi: 10.1038/s41592-019-0686-2

Viselli, A. M., Forristall, G. Z., Pearce, B. R., and Dagher, H. J. (2015). Estimation of Extreme Wave and Wind Design Parameters for Offshore Wind Turbines in the Gulf of Maine Using a POT Method. *Ocean. Eng.* 104, 649–658. doi: 10.1016/j.oceaneng.2015.04.086

Wes, M. K. (2010). Data Structures for Statistical Computing in Python (Accessed Proceedings of the 9th Python in Science Conference).

Conflict of Interest: The authors declare that the research was conducted in the absence of any commercial or financial relationships that could be construed as a potential conflict of interest.

Publisher's Note: All claims expressed in this article are solely those of the authors and do not necessarily represent those of their affiliated organizations, or those of the publisher, the editors and the reviewers. Any product that may be evaluated in this article, or claim that may be made by its manufacturer, is not guaranteed or endorsed by the publisher.